UNIVERSITÄT TRIER

Shape optimization for the mitigation of coastal erosion

Vom Fachbereich IV der Universität Trier zur Erlangung des akademischen Grades
Doktor der Naturwissenschaften (Dr. rer. nat.)
genehmigte

Dissertation

von

Luka Schlegel

Trier, im Januar 2023

Gutachter:	Prof. Dr. Volker Schulz
	Prof. Dr. Bijan Mohammadi
Datum der Disputation:	02. Dezember 2022

Abstract

Coastal erosion describes the displacement of land caused by destructive sea waves, currents or tides. Due to the global climate change and associated phenomena such as melting polar ice caps and changing current patterns of the oceans, which result in rising sea levels or increased current velocities, the need for countermeasures is continuously increasing. Today, major efforts have been made to mitigate these effects using groins, breakwaters and various other structures.
This thesis will find a novel approach to address this problem by applying shape optimization on the obstacles. Due to this reason, results of this thesis always contain the following three distinct aspects:

The selected *wave propagation model*, i.e. the modeling of wave propagation towards the coastline, using various wave formulations, ranging from steady to unsteady descriptions, described from the Lagrangian or Eulerian viewpoint with all its specialties. More precisely, in the Eulerian setting is first a steady Helmholtz equation in the form of a scattering problem investigated and followed subsequently by shallow water equations, in classical form, equipped with porosity, sediment portability and further subtleties. Secondly, in a Lagrangian framework the Lagrangian shallow water equations form the center of interest.

The chosen *discretization*, i.e. dependent on the nature and peculiarity of the constraining partial differential equation, we choose between finite elements in conjunction with a continuous Galerkin and discontinuous Galerkin method for investigations in the Eulerian description. In addition, the Lagrangian viewpoint offers itself for mesh-free, particle-based discretizations, where smoothed particle hydrodynamics are used.

The method for *shape optimization* w.r.t. the obstacle's shape over an appropriate cost function, constrained by the solution of the selected wave-propagation model. In this sense, we rely on a differentiate-then-discretize approach for free-form shape optimization in the Eulerian set-up, and reverse the order in Lagrangian computations.

For a better comprehension, we would like to highlight, that each chapter explicitly states its own claim to novelty right at the start of each chapter.

Zusammenfassung

Küstenerosion beschreibt die Abtragung von Landmasse durch destruktive Meereswellen, Strömungen oder Gezeiten. Aufgrund des globalen Klimawandels und der damit verbundenen Phänomene, wie dem Abschmelzen der Polkappen oder der sich ändernden Strömungsmuster der Ozeane, die zu einem Anstieg des Meeresspiegels führen, wird der Bedarf an effektiven Gegenmaßnahmen kontinuierlich größer. Bereits heute werden große Anstrengungen unternommen, um diese Auswirkungen durch Buhnen, Wellenbrecher und verschiedene andere Hindernisse abzumildern.
Diese Arbeit versucht einen neuartigen Ansatz mittels Formoptimierung der Hindernisse zur Lösung dieses Problems. Die Ergebnisse der Arbeit unterteilen sich daher in die folgenden drei Aspekte:

Das gewählte *Modell zur Wellenausbreitung*, das die Bewegung der Wellen in Richtung Küste über verschiedene Wellenformulierungen bestimmt, die von stationären bis hin zu instationären Beschreibungen reichen und entweder mittels Eulerschen oder Lagrangeschen Ansatz beschrieben werden. In diesem Sinne werden zuerst partielle Differentialgleichungen aus der klassischen Eulerschen Sichtweise untersucht. Diese Untersuchungen umfassen die zeitunabhängige Helmholtz Gleichung in Form eines Zerstreuungsproblems als auch die Flachwassergleichungen, in klassischer Form, ausgestattet mit Porosität, der Möglichkeit zum Sedimenttransport und weiteren Feinheiten. Daraufhin werden die Flachwassergleichungen zusätzlich im Lagrangeschen Rahmen untersucht.

Die gewählte *Diskretisierung*, die abhängig von der Art der einschränkenden partiellen Differentialgleichung gewählt wird. Das bedeutet, dass das numerische Modell in Untersuchungen der Eulerschen Beschreibungen aus der Familie der finiten Elemente in Verbindung mit der stetigen Galerkin und der unstetigen Galerkin Methode gewählt wird. Darüber hinaus bietet sich die Lagrangesche Sichtweise für partikelbasierte Diskretisierungen an, die sich auf auf Smoothed Particle Hydrodynamics reduzieren.

Die *Methode zur Formoptimierung* eines Hindernisses über eine geeignete Kostenfunktion, die durch die Lösung des gewählten Wellenausbreitungsmodells eingeschränkt wird. In diesem Sinne stützen wir uns auf den Ansatz des Differenzierens und anschließendem Diskretisierens für die Freiform-Optimierung in der Eulerschen Betrach-

tungsweise und kehren die Reihenfolge für Lagrangesche Berechnungen um.

Zum besseren Verständnis möchten wir zudem darauf hinweisen, dass jedes Kapitel gleich zu Beginn explizit seinen eigenen Anspruch auf Neuartigkeit erheben wird.

Acknowledgements

I would like to express my great gratitude to my doctoral supervisor, Volker Schulz, for his guidance in very regular exchanges and for sharing his years of experience in the scientific world. In addition, I would like to praise my working group, where each and everyone contributed to a good and fruitful atmosphere for discussion and help. Christian, Michael and Marcel deserve to be explicitly named for proofreading the manuscript and for useful remarks.

I am thankful to the Deutsche Forschungsgemeinschaft for foundation of the project "Shape Optimization Mitigating Coastal Erosion" (SOMICE) within the priority program SPP 1962 "Non-smooth and Complementarity-based Distributed Parameter Systems: Simulation and Hierarchical Optimization", which enabled the cooperation with our colleagues from Dakar, Senegal. In this light, I owe thanks to Diaraf Seck such as my partner in crime Mame Gor Ngom for inspiring analytical discussions.

Finally, I would like to express my deep gratitude for the support of my parents Stefan and Stephanie, my sister Anna and my better-half Anjana. Vielen Dank!

Preface

The following information is a necessary requirement of the examination regulation.

Publications

Individual chapters inherit from individual written publications that have been made throughout the doctoral period and are digitally recorded with references [160, 158, 157, 159]. In this light, [158] and [157] are contained in Chapters 5 and 6 and have undergone the standard review process with [157] being already published. A brief relational summary can be found in the table below.

Chapter	Reference
4	[160]
5	[158]
6	[157]
8	[159]

In addition, a research article, presenting results in conjunction with Chapter 5 and [158] was published for SIAM News Online[1].
If not stated differently all figures, tables and numerical implementations presented in the respective chapters are made by the author of this work.

[1]Last visited: 10.02.2022 URL: https://sinews.siam.org/Details-Page/shape-optimization-for-the-mitigation-of-coastal-erosion-via-shallow-water-equations

Curriculum Vitae

10/2019 – Today	**Doctoral Student** at the Chair of Prof. Dr. Volker Schulz
10/2019 04/2017 – 10/2019	**Master of Science, Applied Mathematics** Study of Applied Mathematics at Universität Trier
08/2017 10/2013 – 08/2017	**Bachelor of Science, Business Mathematics** Study of Business Mathematics at Universität Trier
04/2013 08/2004 - 04/2013	**Abitur** Friedrich-Wilhelm-Gymnasium, Trier
08/2000 - 07/2004	**Grundschule** St. Martin, Gusterath-Pluwig

Contents

Chapter 1

Introduction

This chapter will describe the general motivation to investigate shape optimization for the mitigation of coastal erosion by means of vivid examples in Section 1.1, before describing the structure of the thesis in Section 1.2.

1.1 Motivation & Scope of the Thesis

In October 2003, a four meter wide breach was dug into a peninsula named Langue de Barbarie, located in the north of Dakar, Senegal near the city of Saint-Louis. With the intention to counter floodings that had continually beset the region throughout the years, the action's hope was to create a drainage channel. However, not withstanding tides, the breach rapidly expanded to 800 meters, separating the southern end of the peninsula from the main country and transforming it into an island. By January 2020, the sea had already claimed more than six kilometers of land; this alteration led to the loss of villages and tourist resorts as well as permanent changes in the peninsula's flora and fauna [145]. Waves are traveling now unhindered towards the shorelines threatening the formerly protected mainland. Satellite recordings[1] in Figure 1.1 capture this process over the years.

Similar but different was investigated in 2010, where the Mentawai earthquake shocked an entire region in the south-west of Sumatra, Indonesia, ultimately resulting in tsunami waves of heights of more than three meters flooding more than 600 meters inland. While having devastating effects on the islands' inhabitants, the behind located mainlands of Sumatra were nearly unaffected. It was investigated that the islands have served as an effective shield by absorbing most of the water waves energy [174].
Both incidents described before, although taken from very different parts of the world, demonstrate the importance of protective measures to enable long-term living in coastal regions. In general, we can state that prevention of such disasters amidst steadily rising sea levels is limited in neither time nor space, and its importance is only increasing. Ob-

[1] https://commons.wikimedia.org/wiki/File:Langue_de_Barbarie_breach_animation.gif

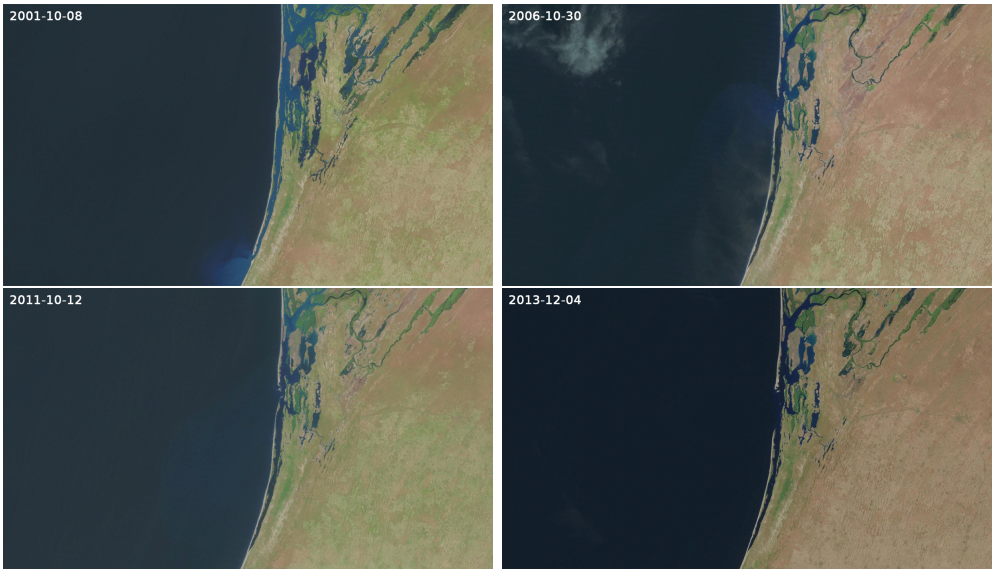

Figure 1.1: Satellite Recordings of the Langue de Barbarie from 2001 to 2013. Figure Courtesy of Yaamboo/NASA on Wikimedia Commons.

viously, this insight is not novel as previous efforts have attempted to mitigate the effects of coastal erosion via groins, breakwaters, and various other structures. Current experiments have utilized the continually increasing computational performance of numerical simulations to model the propagation of waves towards the shore and identify optimal wave-breaking offshore obstacles, that have exemplifying proven itself effective in the described incidents. Our approach focuses on these kinds of simulations and essentially involves finding an obstacle's optimal shape for a given wave, relying on shape calculus rather than a finite design space. To underline the effectiveness of our measures, we will illustrate analytical results in different scenarios with special attention to the two described events at the coastlines of Saint-Louis, Senegal and Sumatra, Indonesia.

1.2 Structure of the Thesis

The thesis is structured as follows: We start in Chapter 2 by stating different classes of partial differential equations (PDEs) that are used in the course of this work. Known regularity results are recalled and the finite element method for the calculation of numerical solutions is introduced in general and subsequently elaborated with focus on continuous and discontinuous Galerkin (CG & DG) methods. In Chapter 3 we then provide the reader with the basic tools for PDE-constrained shape and topology optimization, that are necessary to tackle the problem in the continuous and discrete setting and provide a short overview on algorithmic strategies. In a first investigation in Chapter 4 we focus on a simple objective, that is interpreted in the erosion setting and constrained to the solution of a time-harmonic wave formulation - the Helmholtz equation in form of a

scattering problem. We derive the associated continuous adjoint, shape derivative and finally topological derivative. Results are tested and verified on different domains, while relying on certain wave and obstacle specifications for different algorithmic strategies. Chapter 5 turns towards propagating waves, with the help of a time-dependent description. More precisely, the hydrodynamics are defined to be the Saint-Venant or better known as shallow water equations (SWE). Again, we derive continuous adjoint and shape derivative and verify results on different domains for different wave specifications for a rigid obstacle. In Chapter 6 we amend the formulation to porous SWE, where the discontinuous porosity factor, resembles a permeable obstacle. The discontinuity requires a careful treatment, when calculating numerical solutions, which is closely investigated. Chapter 7 extends the wave propagation for sediment transport. The coupling of Exner-type equations with SWE (SWEE) leads to an aggravation of solution strategies, which will be discussed in detail. Chapter 8 will then derive adjoints for a general class of particles, that are associated with Lagrangian fluid formulations. In the following, the smoothed particle hydrodynamics (SPH) with non-standard boundary interaction serve as discretization for fluids based on the Lagrangian form of SWE and the discrete shape derivative is derived for this specific technique. Results are again tested and numerically verified. Ultimately, Chapter 9 gives an indication of future directions of investigation and states a final conclusion.

1.3 Glossary

For the convenience of the reader, we introduce some notations and list some definitions which are central to this thesis and frequently appear. Thus, the following can be regarded as a supplemental glossary.

Geometric Notation

$\mathbb{N}$	set of natural numbers excluding zero
$\mathbb{N}^d$	set of natural numbers excluding zero of dimension $d \in \mathbb{N}$
$\overline{\mathbb{N}}_0^d$	$(\mathbb{N} \cup \{0, \infty\})^d$ of dimension $d \in \mathbb{N}$
$\mathbb{C}^d$	complex space of dimension $d \in \mathbb{N}$
$\mathbb{R}^d$	Euclidean space of dimension $d \in \mathbb{N}$
e_i	i^{th} standard coordinate vector in $\mathbb{R}^d$
$\mathbb{R}_+^d$	$\{x \in \mathbb{R}^d \vert x_i > 0 \; \forall i \in \{1, ..., d\}\}$
$\mathbb{R}^{d_1 \times d_2}$	set of $d_1 \times d_2$ matrices with entries in $\mathbb{R}$, where $d_1, d_2 \in \mathbb{N}$

$\|\cdot\|_p$	p-norm in $\mathbb{R}^d$, given by $\|x\|_p = \sqrt[p]{\sum_{i=1}^d \|x_i\|^p}$ for $p \in [1,\infty)$ and $\|x\|_\infty = \max_{1\leq i\leq d} \|x_i\|$; cases of interest are the Euclidean norm ($p=2$), supremum norm ($p=\infty$) and Manhattan norm ($p=1$)
$\|x\|$	absolute value of $x \in \mathbb{R}$

Linear algebra

Let A and B be two matrices in $\mathbb{R}^{d\times d}$ and let x and y denote two vectors in $\mathbb{R}^d$.

A^T	transpose of A
$\det(A)$	determinant of A
$\lambda(A)$	eigenvalues of A
$A : B$	Frobenius inner product, i.e. $A : B = \sum_{i,j=1}^d A_{ij}B_{ij}$
$x^T y = x \cdot y$	scalar product of x and y
$xy^T = x \otimes y$	outer product of x and y
$\mathbf{I}_d$	identity matrix in $\mathbb{R}^{d\times d}$

Sets and set operations

Let Ω and D denote two subsets of $\mathbb{R}^d$.

Ω^c	complement of Ω, i.e., $\Omega^c = \mathbb{R}^d \setminus \Omega$
$\|\Omega\|$	d-dimensional volume of Ω
$\mathrm{int}(\Omega)$	interior of Ω
$\overline{\Omega}$	closure of Ω in $\mathbb{R}^d$
$\partial\Omega$	boundary of Ω
Γ_D	Dirichlet boundary
Γ_N	Neumann boundary
$\Omega \dot\cup D$	disjoint union of the sets Ω and D
S^1	unit circle
$\mathrm{Emb}(\Omega, \mathbb{R}^d)$	manifold of smooth embeddings from Ω into $\mathbb{R}^d$
$\mathrm{Diff}(\Omega)$	Lie group of all diffeomorphism from Ω into itself
B_e	shape space
$T_c B_e$	shape tangent space

g^1	first Sobolev metric
Δ_c	Laplace-Beltrami operator
g^S	Steklov-Poincaré type metric

Differentiation

Assume $u : \Omega \times (0,T) \to \mathbb{R}$, $x \in \Omega$, $t \in (0,T)$ with sufficient regularity. Assume $J : \Omega \to \mathbb{R}$ well-defined shape functional and $V : \Omega \to \mathbb{R}^d$ sufficiently smooth vector field.

$\frac{\partial u}{\partial x_i} = \partial_{x_i} u = u_{x_i}$	spatial partial derivative of u, if exists $\lim_{h\to 0} \frac{u(x+he_i)-u(x)}{h}$
$\frac{\mathrm{d}}{\mathrm{d}t}(u) = \frac{\mathrm{d}u}{\mathrm{d}t}$	total time derivative of u for $x \in \Omega(t)$
$\frac{\mathrm{d}^+ u}{\mathrm{d}t}\Big\|_{t=0}$	total time derivative of u for $x \in \Omega(t)$ evaluated at $t = 0^+$
$D_m(u) = \dot{u}$	material or substantial derivative as total time derivative for velocity equal to the fluid velocity
$D^\alpha(u)$	spatial partial derivatives $d^\alpha = \frac{\partial^{\lvert\alpha\rvert} u}{\partial x_1^{\alpha_1} \cdots \partial x_d^{\alpha_d}}$ where α is a multi-index
x^α	multi-index notation for the monomial $x^\alpha = x_1^{\alpha_1} \cdots x_d^{\alpha_d}$
$\alpha!$	multi-index factorial $\alpha_1! \cdots \alpha_d!$
$\lvert\alpha\rvert$	multi-index order $\alpha_1 + ... + \alpha_d$
$\mathrm{div}(V) = \nabla \cdot V$	divergence operator of V
$\mathrm{div}_{\partial\Omega}(V)$	tangential divergence operator on $\partial\Omega$ of V
κ_m	additive curvature on $\partial\Omega$, i.e. $\mathrm{div}_{\partial\Omega}(n)$ for exterior normal n
∇u	gradient operator or Jacobian of u
Δu	Laplace operator of u
$\nabla_h, \nabla_h \cdot, \Delta_h$	broken gradient, divergence, Laplacian operator
$\mathrm{d}x, \mathrm{d}s, \mathrm{d}t$	differential element on $\Omega, \partial\Omega, (0,T)$
$DJ(\Omega)[V]$	shape derivative of $J(\Omega)$ in direction V
$DJ_\Omega(\Omega)[V]$	shape derivative in volume form of $J(\Omega)$ in direction V
$DJ_\Gamma(\Omega)[V]$	shape derivative in boundary form of $J(\Omega)$ in direction V
$D_T J(\Omega)(x)$	topological derivative of $J(\Omega)$ at $x \in \Omega$

Infinite Spaces

$C^{k,\gamma}(\overline{\Omega})$	k,γ-Hölder Spaces
$L^p(\Omega)$	$\{u : \Omega \to \mathbb{R} \mid u \text{ is Lebesgue measurable, } \|\|u\|\|_{L^p(\Omega)} < \infty\}$ for $\|\|u\|\|_{L^p(\Omega)} = (\int_\Omega \|u\|^p \,\mathrm{d}x)^{\frac{1}{p}}$ for $1 \leq p < \infty$
$L^p_{Loc}(\Omega)$	$\{u : \Omega \to \mathbb{R} \mid u \in L^p(V) \text{ for each } V \text{ compactly contained in } \Omega\}$
$W^{k,p}(\Omega)$	Sobolev space $\{u \in L^1_{Loc}(\Omega) : \forall \alpha \in \mathbb{N}_0^d, \|\alpha\| \leq k,\ \exists D^\alpha u \in L^p(\Omega)\}$
$W^{\sigma,p}(\Omega)$	fractional Sobolev space
$W^{k,0,p}(X)$	Sobolev space on space-time cylinder $X := \Omega \times (0,T)$
$W^{k,1,p}(X)$	Sobolev space on space-time cylinder with existing first-order weak time-derivative

Banach and Hilbert spaces

Let $\Omega \subset \overline{\Omega}$ be a bounded domain in $\mathbb{R}^d$. Further let $H(\Omega)$ denote a Hilbert space of functions $u\colon \Omega \to \mathbb{R}$.

$\langle \cdot, \cdot \rangle_{H(\Omega)}$ $= (\cdot, \cdot)_{H(\Omega)}$	inner product on $H(\Omega)$
$\\| \cdot \\|_{H(\Omega)}$	norm on $H(\Omega)$
$d(\cdot, \cdot)_{H(\Omega)}$	metric on $H(\Omega)$
$H^*(\Omega)$	dual space of $H(\Omega)$
$H^1_0(\Omega)$	set of $H^1(\Omega)$-functions which vanish on the boundary $\partial\Omega$
$H^k(\Omega)$	Sobolev space $W^{k,2}(\Omega)$ of integer order $k \in \mathbb{N}_0$, $H^0(\Omega) = L^2(\Omega)$
$C^k(\Omega)$	set of functions with continuous derivative up to order $k \in \mathbb{N}_0$
$C^\infty(\Omega)$	$\bigcap_{k=0}^\infty C^k(\Omega)$
$C^k_c(\Omega)$	$u \in C^k(\Omega)$ such that $\mathrm{supp}(u) \subset \Omega$
$T(u)$	trace of u on $\partial\Omega$
$H^{1/2}(\partial\Omega)$	set of all Dirichlet traces on $\partial\Omega$

Discretizations

$\mathcal{T}_h$	$\{\kappa_e\}_{1 \leq e \leq N_{el}}$ mesh of domain Ω with $N_{el} \in \mathbb{N}$ number of elements κ
$\mathbb{P}^k(\kappa)$	polynomials up to degree $k \in \mathbb{N}$ on $\kappa \in \mathcal{T}_h$

W_h	general finite element approximation space
u_h	canonical finite element counterpart of u on $\mathcal{T}_h$
N_j^k	j^{th} finite element shape function of polynomial order $k > 0$ on Lagrangian elements
$\mathcal{H}^k(\mathcal{T}_h)$	broken Sobolev space
$u^{\pm}$	traces of u for $\kappa \in \mathcal{T}_h$ and its adjacent element κ'
$\{\{p\}\}$	average of p
$[\![p]\!]$	jump of p
$\mathcal{F}(\cdot, \cdot, n)$	normal dependent numerical flux function

Miscellaneous

$\mathbb{1}_M$	indicator function of a set $M \subset \mathbb{R}^d$ with values $\begin{cases} 1 & \text{if } x \in M \\ 0 & \text{if } x \notin M \end{cases}$
$\text{supp}(u)$	support of a function u
δ_{kj}	Kronecker delta with values $\begin{cases} 1 & \text{if } k = j \\ 0 & \text{else} \end{cases}$
$\text{sgn}(x)$	sign function with values $\begin{cases} 1 & \text{if } x > 0 \\ 0 & \text{if } x = 0 \\ -1 & \text{if } x < 0 \end{cases}$
$d_\Omega(x)$	signed distance function with values $d_\Omega(x) = \begin{cases} d(x, \partial\Omega) & \text{if } x \in \Omega \\ 0 & \text{if } x \in \partial\Omega \\ -d(x, \partial\Omega) & \text{if } x \in \bar{\Omega}^c \end{cases}$
$\dim(V)$	dimension of vector space V
$\text{codim}(U, V)$	codimension of vector space $U \subset V$
$\mathcal{O}(\cdot)$	big $\mathcal{O}$-notation, i.e. $f = \mathcal{O}(g)$ as $x \to x_0$, such that there exists $\lvert f(x)\rvert \leq c\lvert g(x)\rvert$ for x sufficiently close to x_0
$o(\cdot)$	small o-notation, i.e. $f = o(g)$ as $x \to x_0$, provided $\lim_{x \to x_0} \frac{\lvert f(x)\rvert}{\lvert g(x)\rvert} = 0$

Chapter 2

Partial Differential Equations for Waves & Fluids

This chapter is supposed to form the basics of our conducted research on partial differential equations. We start by defining and classifying partial differential equations that are of interest in Section 2.1, before we visit the associated function spaces in Section 2.2. The chapter will end by introducing finite element methods in conjunction with the CG and DG method in Section 2.3.

2.1 Classification of PDEs

In this section we will give basic definitions of different classes of a partial differential equation (PDE). Within these classes different members often share common properties, that can be exploited in an analytical or numerical analysis, as it can be for example seen in Section 2.3. We hereby mostly follow the monograph of [72, Chapter 1]. The definitions and notations can appear slightly changed, due to consistency reasoning.

Definition 2.1. *(PDE) For integer $k \in \mathbb{N}$ and for open $\Omega \subset \mathbb{R}^d$, an expression*

$$f(D^k u(x), D^{k-1} u(x), ..., Du(x), u(x), x) = 0 \tag{2.1}$$

is called a partial differential equation (PDE) of order k. In this setting we are given

$$f : \mathbb{R}^{d^k} \times \mathbb{R}^{d^{k-1}} \times ... \times \mathbb{R}^d \times \mathbb{R} \times \Omega \to \mathbb{R} \tag{2.2}$$

and are searching for

$$u : \Omega \to \mathbb{R}. \tag{2.3}$$

The notion of (2.1) can be extended to vector-valued solution variables.

Definition 2.2. *(PDE-System) For integers $k, m \in \mathbb{N}$ and for open $\Omega \subset \mathbb{R}^d$, an expression*

$$F(D^k U(x), D^{k-1}U(x), ..., DU(x), U(x), x) = 0 \tag{2.4}$$

is called a PDE-system of order k. In this setting we are given

$$F : \mathbb{R}^{md^k} \times \mathbb{R}^{md^{k-1}} \times ... \times \mathbb{R}^{md} \times \mathbb{R}^m \times \Omega \to \mathbb{R}^m \tag{2.5}$$

and are searching for

$$U : \Omega \to \mathbb{R}^m. \tag{2.6}$$

Since this work will deal with a variation of PDEs, it appears useful to form classification criteria for different characteristic properties that are not only order-dependent.

Definition 2.3. *(Linear, Semilinear, Quasilinear, Nonlinear PDE)*
The PDE (2.1) is called

i) linear, if it has the form

$$\sum_{|\alpha| \leq k} a_\alpha(x) D^\alpha u(x) = s(x) \tag{2.7}$$

ii) semilinear, if it has the form

$$\sum_{|\alpha| = k} a_\alpha(x) D^\alpha u(x) + a_0(D^{k-1}u(x), ..., Du(x), u(x), x) = 0 \tag{2.8}$$

iii) quasilinear, if it has the form

$$\sum_{|\alpha| = k} a_\alpha(D^{k-1}u(x), ..., Du(x), u(x), x) D^\alpha u(x) + a_0(D^{k-1}u(x), ..., Du(x), u(x), x) = 0 \tag{2.9}$$

iv) nonlinear, if it it depends nonlinearly on derivatives of highest orders

for scalar source term $s : \Omega \to \mathbb{R}$ and given functions a_α with multi-index $\alpha = (\alpha_1, ..., \alpha_d) \in \mathbb{N}_0^d$, $|\alpha| = \sum_{i=1}^d \alpha_i$ and

$$D^\alpha := \frac{\partial^{|\alpha|}}{\partial^{\alpha_1} x_1 ... \partial^{\alpha_d} x_d}.$$

Remark. In Definition 2.1 Du is introduced instead of nabla-notation ∇u to denote the gradient, since it extends naturally to high-order derivatives, where instead $\nabla^2 u$ frequently denotes the Laplacian instead of the Hessian matrix.

Remark. Definition 2.3 carries over equation-wise to PDE-systems as in Definition 2.2. In this sense, we will investigate PDEs of linear type in Chapter 4 and systems of linear, quasilinear or nonlinear type in Chapters 5-8.

We will now classify second-order PDEs and time-dependent first-order PDE-Systems as these two types of equations form the center of investigations respectively in Chapters 4-8.

Second-Order PDEs

Following [72, pp. 293-294] second-order PDEs arise frequently in two distinct forms.

Definition 2.4. *([Non-]Divergence Form of Second-Order PDE) We define second-order PDEs in divergence form as*

$$f(D^2u(x), Du(x), u(x), x) = -\sum_{i,j=1}^{d} \left(a_{i,j}u_{x_i}\right)_{x_j} + \sum_{i=1}^{d} b_i u_{x_i} + cu + s = 0 \tag{2.10}$$

and in non-divergence form as

$$f(D^2u(x), Du(x), u(x), x) = -\sum_{i,j=1}^{d} a_{i,j}u_{x_i x_j} + \sum_{i=1}^{d} b_i u_{x_i} + cu + s = 0 \tag{2.11}$$

for scalar functions $a_{i,j}, b_i, c, s : \Omega \to \mathbb{R}$ for $i, j \in \{1, ..., d\}$, where the subscript at the independent variable denotes the respective partial derivative.

Equations of type (2.10) and (2.11) can be classified dependent on the coefficient matrix [40, p. 8].

Definition 2.5. *(Classification of Second-Order PDE) Equations of Definition 2.4 with symmetric coefficient matrix $A := (a_{i,j})_{i,j\in\{1,...,d\}} \in \mathbb{R}^{d\times d}$ can be classified as*

i) elliptic, if $\lambda(A)_i > 0$ for all $i \in \{1, ..., d\}$

ii) parabolic, if $\lambda(A)_i = 0$ for one $i \in \{1, ..., d\}$, while $\lambda(A)_j > 0$ for all $j \in \{1, ..., d\}\backslash i$

iii) hyperbolic, if $\lambda(A)_i < 0$ for one $i \in \{1, ..., d\}$, while $\lambda(A)_j > 0$ for all $j \in \{1, ..., d\}\backslash i$

for eigenvalue-operator $\lambda : \mathbb{R}^{d\times d} \to \mathbb{C}^d$.

Remark. Variable coefficients can cause a change of type for the PDE in the respective part of the calculation domain. For equations of two independent variables investigations simplify [78, p. 17]. For Chapters 5-7 the observation that parabolic equations can be obtained by adding a first-order time derivative of the solution to an elliptic problem is of importance [72, p. 350].

First-Order Nonlinear Conservation Systems

In Chapters 5-7 the main focus is on equations similar to the following type (cf. to [72, Section 7.3.1.] for linear first-order PDEs).

Definition 2.6. *(First-Order Nonlinear Conservation Systems) We define first-order nonlinear conservation systems to be a set of equations of type*

$$U_t + \sum_{i=1}^{d} \partial x_i F_i(U) = S \quad \text{on } \Omega \times (0, T) \tag{2.12}$$

for initial conditions

$$U = U_0 \quad \text{on } \Omega \times \{0\} \tag{2.13}$$

for solution variable and source term $U, S : \Omega \times (0,T) \to \mathbb{R}^m$*, initial conditions* $U_0 : \Omega \times \{0\} \to \mathbb{R}^m$ *such as* $F_i : \mathbb{R}^m \to \mathbb{R}^m$ *for* $i \in \{1,..,d\}$*.*

For convenience, we suppress independent variables in the notation of dependent ones in (2.12) and in the following. Certain systems of aforementioned type are commonly emphasized in the literature.

Definition 2.7. *(Hyperbolicity of First-Order Nonlinear Conservation Systems) The system of (2.12) is defined to be hyperbolic if for each* $(\tilde{x}, x, t) \in \mathbb{R}^d \times \Omega \times (0,T)$ *the matrix*

$$B(u, \tilde{x}) := \sum_{i=1}^{d} \tilde{x}_i \mathcal{J}_i(U) \tag{2.14}$$

has m *real and state-dependent eigenvalues, i.e.*

$$\lambda\left(B(u,\tilde{x})\right) = \{\lambda_1, ..., \lambda_m\} \in \mathbb{R}^m \tag{2.15}$$

for eigenvalue-operator $\lambda : \mathbb{R}^{m\times m} \to \mathbb{C}^m$ *and Jacobian matrix of the flux* $\mathcal{J}_i(U) := \partial_U F_i(U)$ *for* $i \in \{1, ..., d\}$*.*

2.2 Sobolev Spaces

In this section we formulate the basics of Sobolev spaces that turn out to be the appropriate choice of function spaces in the analysis of PDEs. Some notation and definition seem unmotivated at first glance, but turn out to be useful, especially in Chapter 3 that forms the basis for shape and topology optimization. The following is based on [65, Chapter 2] and [72, Chapter 5].

Definition 2.8. *(Lipschitz/Hölder-Continuity) Assume* $\Omega \subset \mathbb{R}^d$ *to be open, then a function* $u : \Omega \to \mathbb{R}$ *is called*

i) Lipschitz continuous if it holds

$$|u(x) - u(y)| \leq c|x - y| \tag{2.16}$$

ii) Hölder continuous if for Hölder-exponent $0 < \gamma \leq 1$ *it holds*

$$|u(x) - u(y)| \leq c|x - y|^\gamma \tag{2.17}$$

for some constant $c \geq 0$ *and all* $x, y \in \Omega$*.*

Definition 2.9. *(Hölder [semi-]norm) In the setting of Definition 2.8*

i) if $u : \Omega \to \mathbb{R}$ is bounded and continuous, we have

$$||u||_{C(\overline{\Omega})} := \sup_{x\in\Omega} |u(x)|. \tag{2.18}$$

ii) The γ^{th}-semi-norm is defined as

$$[u]_{C^{0,\gamma}(\overline{\Omega})} := \sup_{x,y\in\Omega;x\neq y} \left\{ \frac{|u(x)-u(y)|}{|x-y|^{\gamma}} \right\}. \tag{2.19}$$

iii) The γ^{th}-norm as

$$||u||_{C^{0,\gamma}(\overline{\Omega})} := ||u||_{C(\overline{\Omega})} + [u]_{C^{0,\gamma}(\overline{\Omega})}. \tag{2.20}$$

Definition 2.10. *(Hölder Space) We define for $k \in \overline{\mathbb{N}}_0$ the space*

$$C^{k,\gamma}(\overline{\Omega}) \tag{2.21}$$

to consist of all functions $u \in C^{k,\gamma}(\overline{\Omega})$ for which we have a finite norm

$$||u||_{C^{k,\gamma}(\overline{\Omega})} := \sum_{|\alpha|\leq k} ||D^{\alpha}u||_{C(\overline{\Omega})} + \sum_{|\alpha|=k} [D^{\alpha}u]_{C^{0,\gamma}(\overline{\Omega})} < \infty. \tag{2.22}$$

Remark. Hölder spaces possess convenient mathematical properties by being a Banach space [72, p. 241]. However, solutions to PDEs are often required to contain less regularity, which prohibits analytic estimates in aforementioned spaces. For this reason, we will later on introduce Sobolev spaces in Definition 2.21.

Important calculation rules hold for domains with sufficient regularity at boundary level. To characterize these suitable sets, two alternative descriptions are proposed following [65, pp. 68-75].

Definition 2.11. *(Domain of Locally Class $C^{k,\gamma}$) A domain $\Omega \subset \mathbb{R}^d$ with $\partial\Omega \neq \emptyset$ is said to be locally of class $C^{k,\gamma}$ with integer $k \in \overline{\mathbb{N}}_0$, if at $x \in \partial\Omega$ there exists*

i) a neighborhood $W(x)$ of x

ii) a bijective map $g_x : W(x) \to B \in C^{k,\gamma}(W(x), B)$ with inverse $h_x : B \to W(x) \in C^{k,\gamma}(B, W(x))$ s.t.

$$\begin{aligned} \Omega \cap W &= h_x(B_+) \\ (\mathbb{R}^d \setminus \Omega) \cap W &= h_x(B_-) \\ \Gamma_x := \partial\Omega \cap W(x) &= h_x(B_0), \quad B_0 = g_x(\Gamma_x), \end{aligned} \tag{2.23}$$

where we have used

$$\begin{aligned} B_0 &:= \{\zeta \in B : \zeta_d = 0\} \\ B_+ &:= \{\zeta \in B : \zeta_d > 0\} \\ B_- &:= \{\zeta \in B : \zeta_d < 0\} \end{aligned} \tag{2.24}$$

for open unit ball in $\mathbb{R}^d$ and by ζ_d the indicated d^{th}-component of $\zeta \in \mathbb{R}^d$.

Remark. In this setting a domain is naturally called of class $C^{k,\gamma}$, if the Definition 2.11 holds for each $x \in \partial\Omega$.

Remark. In analogy to Definition 2.11 a description for the exterior normal is obtained for domains of class C^k with $k \in \overline{\mathbb{N}}$ via the Jacobian matrices $Dg_x(y)$ and $Dh_x(\zeta', 0)$ of g_x and h_x for $y \in \Gamma_x$ with $(\zeta' = (\zeta_1, ..., \zeta_{d-1}))$ and the definition of B_0 with $\{e_1, ..., e_{d-1}\} \subset B_0$. Hence for a normal vector field necessary holds for $1 \leq i \leq d$

$$-n_x(y) \cdot Dh_x(\zeta', 0)e_i = e_d \cdot e_i = \delta_{i,d} \tag{2.25}$$

and therefore

$$n_x(y) = -Dh_x(\zeta', 0)^{-T} e_d = -Dg_x(y)^T e_d \tag{2.26}$$

This construction is also used in the following to describe the domain implicitly via level sets.

Definition 2.12. *(Local Domain Description via Level-Sets) For domain $\Omega \subset \mathbb{R}^d$ of class $C^{k,\gamma}$ with $k \in \overline{\mathbb{N}}$ and $0 \leq \gamma \leq 1$ the set Ω can be described locally by the level-sets of $C^{k,\gamma}$-function*

$$\xi_x(y) := g_x(y) \cdot e_d \tag{2.27}$$

such that

$$\begin{aligned} \Omega \cap W(x) &= \{y \in W(x) : \xi_x(y) > 0\} \\ (\mathbb{R}^d \setminus \Omega) \cap W(x) &= \{y \in W(x) : \xi_x(y) < 0\} \\ \partial\Omega \cap W(x) &= \{y \in W(x) : \xi_x(y) = 0\} \end{aligned} \tag{2.28}$$

and naturally the gradient

$$\nabla\xi_x(y) = Dg_x(y)^T e_d \neq 0 \tag{2.29}$$

is perpendicular to the zero level-set. Hence for standard unit orthonormal basis $\{e_1, ..., e_d\} \in \mathbb{R}^d$ the unit exterior normal is given by

$$n(y) = -\frac{\nabla\xi}{|\nabla\xi|} = -\frac{Dg_x(y)^T e_d}{|Dg_x(y)^T e_d|.} \tag{2.30}$$

The local construction of level-set functions can be used to define a global characterization of domain Ω.

Theorem 2.13. *(Global Domain Description via Level-Sets) For a domain $\Omega \subset \mathbb{R}^d$ of class $C^{k,\gamma}$ with $k \in \overline{\mathbb{N}}$, $0 \leq \gamma \leq 1$ and compact boundary, there exists a Lipschitz-continuous function $\xi : \Omega \to \mathbb{R}$ such that*

$$\begin{aligned} \partial\Omega &= \{x \in \mathbb{R}^d : \xi(x) = 0\} \\ \Omega &= \{x \in \mathbb{R}^d : \xi(x) > 0\} \\ \mathbb{R}^d \setminus \Omega &= \{x \in \mathbb{R}^d : \xi(x) < 0\}. \end{aligned} \tag{2.31}$$

and for a neighborhood W of $\partial\Omega$ such that the exterior normal is defined as

$$n = -\frac{\nabla\xi}{|\nabla\xi|} \tag{2.32}$$

for $\xi \in C^{k,\gamma}(W)$ with $\nabla\xi \neq 0$ on W.

Proof. Refer to [65, pp. 75-77]. □

Remark. Domains of class $C^{0,1}$ are referred to as Lipschitz domains [65, p. 69] and provide sufficient regularity for many useful statements as it can be seen in Chapter 3.

Remark. The domain description of Theorem 2.13 forms the setting for numerical methods for topology and shape optimization in Section 3.3.2.

For domains with sufficiently regular boundary two important results of integral calculus hold.

Theorem 2.14. *(Gauss-Green) For $i \in \{1, ..., d\}$, bounded Lipschitz domain $\Omega \subset \mathbb{R}^d$ and $u \in C^1(\overline{\Omega})$, it holds*

$$\int_\Omega u_{x_i}\,\mathrm{d}x = \int_{\partial\Omega} u n_i\,\mathrm{d}s \tag{2.33}$$

for the i^{th}-component of outward pointing normal vector $n \in \mathbb{R}^d$.

Proof. Refer to [7, Theorem A6.8] □

Theorem 2.15. *(Integration by Parts) In the setting of Theorem 2.14, for $u, v \in C^1(\overline{\Omega})$ the following identity holds*

$$\int_\Omega u_{x_i} v\,\mathrm{d}x = -\int_\Omega u v_{x_i}\,\mathrm{d}x + \int_{\partial\Omega} uvn_i\,\mathrm{d}s. \tag{2.34}$$

Proof. Application of Theorem 2.14. □

We will now introduce basic terminology that is necessary to formulate Sobolev spaces [72, p. 242-246].

Definition 2.16. *(Test-Function) A function $v : \Omega \to \mathbb{R}$ is called test-function if it is an element of $C_c^\infty(\Omega)$, i.e. the space of infinitely differentiable functions with compact support on Ω.*

To motivate the following definitions, more generally for $u \in C^k(\Omega)$ and $v \in C_c^k(\Omega)$, $|\alpha|$-times integration by parts leads to

$$\int_\Omega u D^\alpha v\,\mathrm{d}x = (-1)^{|\alpha|}\int_\Omega D^\alpha uv\,\mathrm{d}x.$$

A variant still holds for locally integrable functions. Before stating this result, we first introduce the concept of distributions, that is used to extend the notion of differentiability [69, Appendix B.2].

Definition 2.17. *(Distribution) For open $\Omega \subset \mathbb{R}^d$ the linear map*

$$G : C_c^\infty(\Omega) \to \mathbb{R}, \quad v \mapsto G(v) \tag{2.35}$$

is called a distribution on Ω if and only if the following property holds:
For all compact $K \subset \Omega$, there exists an integer $k \in \mathbb{N}_0$ and a constant $c > 0$ such that

$$\forall v \in C_c^\infty(\Omega), \mathrm{supp}(v) \subset K, \quad |G(v)| \leq c \sup_{x \in K, |\alpha| \leq k} |D^\alpha v(x)|. \tag{2.36}$$

Lemma 2.18. *Let $\Omega \subset \mathbb{R}^d$ open and $u \in L^1_{Loc}(\Omega)$, then the linear map defined by*

$$G_u(v) := \int_\Omega uv \, \mathrm{d}x \tag{2.37}$$

is a distribution.

Proof. Confer [69, Appendix B.2, Example B.18]. □

Definition 2.19. *(Distributional Derivative) Given distribution G on Ω, we define the distributional derivative as*

$$D_i G : C_c^\infty(\Omega) \ni v \mapsto D_i G(v) = -G(D_i v) \tag{2.38}$$

and more general as

$$D^\alpha G : C_c^\infty(\Omega) \ni v \mapsto D^\alpha G(v) = (-1)^{|\alpha|} G(D^\alpha v). \tag{2.39}$$

Definition 2.20. *(Weak Partial Derivative) Let $u \in L^1_{Loc}(\Omega)$ and let G_u be the associated distribution. If there exists $w \in L^1_{Loc}(\Omega)$, such that $D^\alpha G_u = G_w$, i.e.*

$$\int_\Omega u D^\alpha v \, \mathrm{d}x = (-1)^{|\alpha|} \int_\Omega wv \, \mathrm{d}x \tag{2.40}$$

for all test-functions $v \in C_c^\infty(\Omega)$, then w is called the weak α^{th}-derivative of u, written as

$$D^\alpha u = w. \tag{2.41}$$

For $1 \leq p \leq \infty$, for non-negative integer k, we can define function spaces, for which all members have weak derivatives of various orders in the underlying L^p-space.

Definition 2.21. *(Sobolev Space) We call the function space*

$$W^{k,p}(\Omega) := \{u \in L^1_{Loc}(\Omega) : \forall \alpha \in \mathbb{N}_0^d, |\alpha| \leq k, \ \exists D^\alpha u \in L^p(\Omega)\} \tag{2.42}$$

a Sobolev space of integer order $k \in \mathbb{N}_0$.

Remark. Standard literature on Sobolev spaces often uses functions from $L^p(\Omega)$ instead of locally integrable functions in Definition 2.21. We highlight, that this can indeed being used interchangeably, due to inclusion $L^p(\Omega) \subset L^1_{Loc}(\Omega)$ and $\alpha = (0, ..., 0) \in \mathbb{N}_0^d$ being a valid multi-index.

The obtained space for $p = 2$ has the useful property of being a Hilbert space, i.e.

$$H^k(\Omega) := W^{k,2}(\Omega). \tag{2.43}$$

Definition 2.22. *(Sobolev Norm) For $u \in W^{k,p}(\Omega)$, we define the associated norm by*

$$||u||_{W^{k,p}(\Omega)} := \begin{cases} \left(\sum_{|\alpha|\leq k} \int_\Omega |D^\alpha u|^p \, \mathrm{d}x\right)^{1/p} & (1 \leq p \leq \infty) \\ \sum_{|\alpha|\leq k} ess \ \sup |D^\alpha u| & (p = \infty), \end{cases} \tag{2.44}$$

where the essential supremum is defined for measurable $f : \Omega \to \mathbb{R}$ as

$$ess \ \sup f := \inf\{\mu \in \mathbb{R} : \ |f > \mu| = 0\}. \tag{2.45}$$

Definition 2.23. *(Sobolev Space Closure) The closure of $C_c^\infty(\Omega)$ in $W^{k,p}(\Omega)$ is denoted by*

$$W_0^{k,p}(\Omega). \tag{2.46}$$

Remark. As before, we can identify a Hilbert space for $p = 2$ as

$$H_0^k(\Omega) = W_0^{k,2}(\Omega). \tag{2.47}$$

Since functions $u \in W^{1,p}(\Omega)$ are in general not continuous, values on the boundary $\partial\Omega$ cannot be given in the usual sense. The following theorem resolves this.

Theorem 2.24. *(Trace-Operator) Assume Ω is bounded and $\partial\Omega \in C^1(\Omega)$, then there exists a bounded linear operator*

$$T : W^{1,p}(\Omega) \to L^p(\partial\Omega) \tag{2.48}$$

that will be called trace of u on $\partial\Omega$ such that

i) $T(u) = u\big|_{\partial\Omega}$ *if* $u \in W^{1,p}(\Omega) \cap C(\overline{\Omega})$,

ii) $||T(u)||_{L^p(\partial\Omega)} \leq c||u||_{W^{1,p}(\Omega)}$

for each $u \in W^{1,p}(\Omega)$, for constant c depending on p and Ω.

Proof. Refer to [72, pp. 258-259]. □

For spaces as in Definition 2.23, the following result is obtained.

Theorem 2.25. *(Trace-Zero Functions) In the setting of Theorem 2.24 it holds that*

$$u \in W_0^{1,p}(\Omega) \Leftrightarrow T(u) = 0 \quad on \ \partial\Omega. \tag{2.49}$$

Proof. Refer to [72, pp. 260-262]. □

Remark. So-called Sobolev-Slobodeckij spaces are defined for $\sigma \in (0,1)$ for $1 \leq p \leq \infty$ as [69, p. 484]

$$W^{\sigma,p}(\Omega) := \left\{ u \in L^2(\Omega) : \frac{|u(x)-u(y)|}{|x-y|^{\frac{d}{p}+\sigma}} \in L^p(\Omega \times \Omega) \right\} \tag{2.50}$$

$$W^{\sigma,\infty}(\Omega) := C^{0,\sigma}(\overline{\Omega}), \tag{2.51}$$

which lead for $s = k + \sigma$ to a fractional counterpart of Definition 2.21

$$W^{s,p}(\Omega) := \{u \in W^{k,p}(\Omega) : \forall \alpha \in \mathbb{N}_0^d, |\alpha| \leq k,\ \exists D^\alpha u \in W^{\sigma,p}(\Omega)\} \tag{2.52}$$

and we define

$$W^{s,\infty}(\Omega) := C^{k,\sigma}(\overline{\Omega}). \tag{2.53}$$

Analogously to (2.43) we obtain for $p = 2$ a fractional Hilbert space.
Sobolev-Slobodeckij spaces have a particular role in Definition 2.24 by concreting the image in (2.48) to obtain a surjective, bounded linear operator via mapping [81]

$$T : W^{1,p}(\Omega) \to H^{1-1/p,p}(\partial\Omega). \tag{2.54}$$

A weak solution to elliptic PDEs in divergence form as of Definition 2.4 can be obtained for multiplication with an arbitrary test-function $v \in H_0^1(\Omega)$ and integration over domain of class C^1. For $a_{i,j}, b_i, c, s \in L^2(\Omega)$ for $i, j \in \{1, ..., d\}$ we obtain a variational formulation for $u \in H_0^1(\Omega)$

$$\int_\Omega \sum_{i,j}^{d} a_{i,j} u_{x_i} v_{x_j} + \sum_{i=1}^{d} b_i u_{x_i} v + cuv \,\mathrm{d}x = \int_\Omega sv \,\mathrm{d}x. \tag{2.55}$$

This leads us to the definition of a general form, which builds the basis for investigations in Chapter 4 [72, Chapter 6].

Definition 2.26. *(Weak Solution of Elliptic PDE) We call $u \in H_0^1(\Omega)$ a weak solution of PDE (2.10) if*

$$a(u,v) = b(v), \quad \forall v \in H_0^1(\Omega), \tag{2.56}$$

where bilinear form $a(\cdot,\cdot)$ and linear form $b(\cdot)$ refer to left and right-hand side of (2.55).

For an overview of existence and uniqueness of weak solutions of Definition 2.26, we refer to [72, Section 6.2.].
In accordance with the remark to Definition 2.5 parabolic equations and with Definition 2.6 similarly first-order nonlinear conservation systems require solutions defined on the space-time cylinder $X := \Omega \times (0,T)$. It therefore appears natural to extend spaces of Definitions 2.21 and 2.22 for the possible existence of first-order weak partial time-derivatives [178, Chapter 3].

Definition 2.27. *(Sobolev Space on Space-Time Cylinder) In the setting of Definition 2.21 for $k \in \mathbb{N}_0$ we define*

$$W^{k,0,p}(X) := \{u \in L^1_{Loc}(X) : \forall \alpha \in \mathbb{N}_0^d, |\alpha| \leq k,\ \exists D^\alpha u \in L^p(X)\} \tag{2.57}$$

equipped with the norm for $u \in W^{k,0,p}(X)$

$$||u||_{W^{k,0,p}(X)} := \begin{cases} \left(\sum_{|\alpha|\leq k} \int\int_X |D^\alpha u|^p \,\mathrm{d}x\,\mathrm{d}t\right)^{1/p} & (1 \leq p \leq \infty) \\ \sum_{|\alpha|\leq k} ess\ \sup |D^\alpha u| & (p = \infty). \end{cases} \tag{2.58}$$

Definition 2.28. *(Sobolev Space on Space-Time Cylinder with Weak Time-Derivatives) In the setting of Definition 2.21 for $k \in \mathbb{N}_0$ we define*

$$W^{k,1,p}(X) := \{u \in L^1_{Loc}(X) : \forall \alpha \in \mathbb{N}_0^d, |\alpha| \leq k,\ \exists D^\alpha u \in L^p(X) \wedge \partial_t u \in L^p(X)\} \tag{2.59}$$

equipped with the norm for $u \in W^{k,1,p}(X)$

$$||u||_{W^{k,1,p}(X)} := \begin{cases} \left(\sum_{|\alpha|\leq k} \int\int_X |D^\alpha u|^p \,\mathrm{d}x\,\mathrm{d}t + \int\int_X |\partial_t u|^p \,\mathrm{d}x\,\mathrm{d}t\right)^{1/p} & (1 \leq p \leq \infty) \\ \sum_{|\alpha|\leq k} ess\ \sup |D^\alpha u| + ess\ \sup |\partial_t u| & (p = \infty). \end{cases} \tag{2.60}$$

Similar to before we obtain Hilbert spaces for $p = 2$. Furthermore $W^{k,0,2}(X)$ coincides with $L^2(0,T;H^k(\Omega))$ for appropriate modifications on a null-set [178, Section 3.4] and $W^{1,1,2}(X)$ with $H^1(X)$. We will rely in Chapters 5-7 on the latter. Analogously to the elliptic case we then define for $a_{i,j}, b_i, c, s \in L^2(\Omega)$ for $i,j \in \{1,...,d\}$ the variational formulation for $u \in W_0^{1,0,2}(X)$ and for all $v \in W_0^{1,1,2}(X)$

$$\int\int_X -uv_t + \sum_{i,j}^d a_{i,j} u_{x_i} v_{x_j} + \sum_{i=1}^d b_i u_{x_i} v + cuv \,\mathrm{d}x\,\mathrm{d}t = \int\int_X sv \,\mathrm{d}x\,\mathrm{d}t + \int_\Omega y_0 v(x,0)\,\mathrm{d}x, \tag{2.61}$$

where we define $u_0 \in \Omega \times \{0\}$ to be the initial condition and $v(.,T) = 0$ to get rid of $u(.,T) = 0$, which is not necessarily defined in $W_0^{1,0,2}(X)$. In this setting we can define weak solutions to parabolic PDEs [178, Section 3.3.].

Definition 2.29. *(Weak Solution of Parabolic PDE) We call $u \in W_0^{1,0,2}(X)$ a weak solution of a parabolic PDE if*

$$a(u,v) = b(v), \quad \forall v \in W_0^{1,1,2}(X) \tag{2.62}$$

with $v(.,T) = 0$, where bilinear form $a(\cdot,\cdot)$ and linear form $b(\cdot)$ refer to left and right-hand side of (2.61).

In shape derivative calculations of Chapters 5-7 we require the simultaneous existence of weak partial time-derivatives, i.e. $u, v \in W_0^{1,1,2}(X)$. In this setting, due to the trace-operator of Theorem 2.24, initial and terminal condition are well-defined for associated weak-forms. Furthermore, existence and uniqueness for parabolic problems is then most often derived for spaces such that $u \in L^2(0,T,H^1(\Omega))$ and $\partial_t u \in L^2(0,T,H^1(\Omega)^*)$ [72, Section 7.1.2], which contains $y \in W^{1,0,2}(X)$ for appropriate modification of a null-set and for which $W^{1,1,2}(X)$ builds a dense subset [178, Section 3.4.].

2.3 Finite Element Methods for PDEs

The finite element method (FEM) is a general numerical method to approximate the solution of PDEs. In Section 2.3.1 we will first sketch the common approximation space and global interpolation operator for a class of finite elements as described in monograph [69, Chapter 1]. This is followed by a description of the most widespread Galerkin methods that can be used in conjunction to solve PDEs. Hence, the continuous Galerkin (CG) method is introduced in Section 2.3.2, that is broadly applied for elliptic and parabolic equations, and the discontinuous Galerkin (DG) method in Section 2.3.3, which has gained rising attention especially for solutions to hyperbolic equations.

2.3.1 Basics of FEM

This section states necessary fundamentals for the FEM. It starts by introducing specific triplets [55, p. 93] that are subsequently elaborated.

Definition 2.30. *(Finite Element Triplet) A finite element denotes a triplet* $\{\kappa, P, \Sigma\}$ *such that*

i) $\kappa \subset \mathbb{R}^d$ *is a compact, connected Lipschitz set,*

ii) P *is a finite-dimensional vector space with elements* $p : \kappa \to \mathbb{R}^m$ *for* $m \in \mathbb{N}$ *(typically* $m = 1$ *or* $m = d$*),*

iii) Σ *is a set consisting of linear forms* $\{\sigma_1, ..., \sigma_{N_{sh}}\}$ *on elements of* P *such that*

$$P \to \mathbb{R}^{N_{sh}}, \quad p \mapsto (\sigma_1(p), ..., \sigma_{N_{sh}}(p)) \tag{2.63}$$

is bijective. The linear forms are denoted as local degrees of freedom.

From the bijectivity we can conclude the existence of a basis in P, which gives us the following definitions [69, p. 19-21].

Definition 2.31. *(Local Shape Functions) Basis elements* $\{\theta_1, ..., \theta_{N_{sh}}\} \in P$ *with*

$$\sigma_i(\theta_j) = \delta_{ij}, \quad 1 \leq i, j \leq N_{sh} \tag{2.64}$$

are called local shape functions.

Remark. In all our computations from Chapters 4-8 we will rely on so-called Lagrange finite elements, which are obtained for a set of points $\{b_1, ..., b_{N_{sh}}\} \in \kappa$, called nodes, such that for all $p \in P$ it holds that

$$\sigma_i(p) = p(b_i) \quad \forall i \in \{1, ..., N_{sh}\}. \tag{2.65}$$

In this setting local shape functions, commonly denoted as $\{N_1, ..., N_{N_{sh}}\}$, are called nodal basis of P. Additionally, throughout this thesis, we will restrict to polynomial

vector spaces with real coefficients and global degree of at most integer $k \in \mathbb{N}$, i.e. $P := \mathbb{P}_k$, that are defined for $x \in \mathbb{R}^d$ and multi-index $\alpha \in \mathbb{N}_0^d$ as

$$\mathbb{P}_k = \left\{ p(x) = \sum_{|\alpha| \leq k} c_{\alpha_1 \dots \alpha_d} x_1^{\alpha_1} \dots x_d^{\alpha_d} : c_{\alpha_1 \dots \alpha_d} \in \mathbb{R} \right\}. \tag{2.66}$$

Definition 2.32. *(Local Interpolation Operator) Assume for a finite element triplet $\{\kappa, P, \Sigma\}$ exists a normed vector space $V(\kappa)$ of functions $u : \kappa \to \mathbb{R}^m$ such that $P \subset V(\kappa)$ and linear elements $\{\sigma_1, \dots, \sigma_{N_{sh}}\}$ can be extended to $V(\kappa)^*$. Then, the local interpolation operator $\mathcal{I}_\kappa$ is defined as*

$$\mathcal{I}_\kappa : V(\kappa) \to P, \quad u \mapsto \sum_{i=1}^{N_{sh}} \sigma_i(u)\theta_i. \tag{2.67}$$

Remark. For Lagrange finite elements one can define

$$\mathcal{I}_\kappa : V(\kappa) \to P, \quad u \mapsto \sum_{i=1}^{N_{sh}} u(b_i)N_i \tag{2.68}$$

for $V(\kappa) = \left[C^0(\kappa)\right]^m$ or $V(\kappa) = \left[H^k(\kappa)\right]^m$ for $k > d/2$.

For approximate solutions to PDEs local interpolation needs to be extended to global. Due to this reason, a partition of the domain, called mesh is defined [69, cf. p. 32].

Definition 2.33. *(Mesh) Let $\Omega \subset \mathbb{R}^d$ be a Lipschitz domain and $N_{el} \in \mathbb{N}$. Then a set $\mathcal{T}_h = \{\kappa_e\}_{1 \leq e \leq N_{el}}$ of compact, connected Lipschitz sets with non-empty interior is called mesh, if*

$$\Omega = \cup_{e=1}^{N_{el}} \kappa_e \quad \textit{and} \quad \operatorname{int}(\kappa_e) \cap \operatorname{int}(\kappa_f) = \emptyset \quad \textit{for } e \neq f. \tag{2.69}$$

Remark. Elements of $\{\kappa_e\}_{1 \leq e \leq N_{\text{el}}}$ are called mesh elements or simply elements if there is no ambiguity. In the one-dimensional case each element refers to a line segment. In the two-dimensional case each element refers to either triangles, quadrilaterals or relatives. In general, the union of all elements does not need to coincide with the domain, however, for simplicity we assume this property in Definition 2.33 and from here on.

For practical implementations a mesh is most often generated from a Lagrange reference element $\hat{\kappa}$ in association with a set of geometric transformations. All calculations are then evaluated at the reference element and interpreted for the actual mesh [69, pp. 33-36].

Definition 2.34. *(Reference Finite Element Triplet, Reference Shape Functions) The triplet $\{\hat{\kappa}, \hat{P}, \hat{\Sigma}\}$ for nodal degrees of freedom $\{\hat{\sigma}_1, \dots, \hat{\sigma}_{N_{sh}}\}$ with properties of Definition 2.30 is called the reference finite element triplet and $\{\hat{N}_1, \dots, \hat{N}_{N_{sh}}\}$ with properties of Definition 2.31 are called the reference shape functions. Assuming all elements are generated from the same reference element, we define the associated geometric transformation for $e \in \{1, \dots, N_{el}\}$ as*

$$T_e : \hat{\kappa} \to \kappa_e, \quad T_e(\hat{x}) = \sum_{i \in N_{sh}} \hat{N}_i(\hat{x})\hat{\sigma}_i. \tag{2.70}$$

Remark. Typically the geometric transformations are defined to be C^1-diffeomorphisms. In one dimension the reference element is then defined as $\hat{\kappa} = [-1, 1]$. In this setting, the simplest case of linear shape functions is defined for $\hat{x} \in \hat{\kappa}$ via

$$\begin{aligned} \hat{N}_1(\hat{x}) &= (1 - \hat{x})/2, \\ \hat{N}_2(\hat{x}) &= (1 + \hat{x})/2. \end{aligned} \tag{2.71}$$

Over two neighboring reference elements, two connecting functions are commonly referred to as hat-functions. In two dimensions the reference element is most often defined as the convex hull $\hat{\kappa} = \text{conv}((0, 0), (0, 1), (1, 0))$. On this domain, in the simplest case linear shape functions are defined for $\hat{x} \in \hat{\kappa}$ as

$$\begin{aligned} \hat{N}_1(\hat{x}) &= 1 - \hat{x}_1 - \hat{x}_2, \\ \hat{N}_2(\hat{x}) &= \hat{x}_1, \\ \hat{N}_3(\hat{x}) &= \hat{x}_2. \end{aligned} \tag{2.72}$$

Remark. The reference to mesh transformations $\{T_e : \hat{\kappa} \to \kappa_e\}_{1 \le e \le N_{el}}$ are frequently restricted to affine linear maps, which account for rotation, stretching and translation. A Lagrange reference finite element and affine linear transformations once more result in Lagrange finite elements on the mesh.

Remark. FEM triplets $\{\kappa, P\kappa, \Sigma_\kappa\}$ for mesh elements $\kappa \in \mathcal{T}_h$ are defined in terms of the reference element $\{\hat{\kappa}, \hat{P}, \hat{\Sigma}\}$ for linear bijective mapping $N_\kappa : V(\kappa) \to V(\hat{\kappa})$, we define

$$\begin{cases} \kappa &= T_\kappa(\hat{\kappa}) \\ P_\kappa &= \{N_\kappa^{-1}(\hat{p}) : \hat{p} \in \hat{P}\} \\ \Sigma_\kappa &= \{\{\sigma_{\kappa,i}\}_{1 \le i \le N_{sh}} : \sigma_{\kappa,i}(p) = \hat{\sigma}_i(N_\kappa(p)), \forall p \in P_\kappa\} \end{cases} \tag{2.73}$$

such that local shape functions consist of the set

$$\{\theta_{\kappa,i} = N_\kappa^{-1}(\hat{\theta}_i)\}_{1 \le i \le N_{sh}} \tag{2.74}$$

and the local interpolation operator of Definition 2.32 is defined in terms of these.

Definition 2.35. *(Geometrically Conforming Meshes) A mesh $\mathcal{T}_h = \{\kappa_e\}_{1 \le e \le N_{el}}$ of Lipschitz domain $\Omega \subset \mathbb{R}^d$ is called geometrically conforming, if for all κ_e and κ_f for $e \neq f \in \{1, ..., N_{el}\}$, there exists a face $\hat{F} \in \hat{\kappa}$ for the $(d-1)$-dimensional intersection $F := \kappa_e \cap \kappa_f \neq \emptyset$ such that $F = T_e(\hat{F}) = T_f(\hat{F})$.*

Remark. We can further explicitly characterize the nonempty intersections for geometrically conforming meshes, such that for

i) $d = 1$: F is a common vertex,

ii) $d = 2$: F is a common vertex or edge,

iii) $d = 3$: F is a common vertex, edge or face.

Distinct elements of a mesh are characterized by Definition 2.36 for the codimension-operator denoted by $\operatorname{codim}(V,U) = \dim(V) - \dim(U)$ for finite-dimensional $U \subset V \subset \mathbb{R}^d$.

Definition 2.36. *(Cells, Faces, Edges, Vertices) Subelements of elements $\kappa_{sub} \subset \kappa \in \mathcal{T}_h$ of a Lipschitz domain $\Omega \subset \mathbb{R}^d$ are denoted as*

i) vertices for $\operatorname{codim}(\Omega, \kappa_{sub}) = d$,

ii) edges for $\operatorname{codim}(\Omega, \kappa_{sub}) = d - 1$,

iii) faces for $\operatorname{codim}(\Omega, \kappa_{sub}) = 1$,

iv) cells for $\operatorname{codim}(\Omega, \kappa_{sub}) = 0$.

Remark. Exemplifying we state that in one dimension a line segment is a cell, while in two dimensions it is a face. In addition, we note that in the former faces and vertices are the same, while in the latter edges and faces are the same.

Finally with (2.73) and (2.74) global mesh interpolation and associated solution domains can be defined, which form the basis of PDE solutions via the FEM, see [69, p. 42].

Definition 2.37. *(Global Interpolation Operator, Approximation Space) The global interpolation operator is given for domain*

$$D(\mathcal{I}_h) = \{u \in [L^1(\Omega)]^m : \forall \kappa \in \mathcal{T}_h, u\big|_\kappa \in V(\kappa)\} \tag{2.75}$$

as

$$\mathcal{I}_h : D(\mathcal{I}_h) \to W_h, \quad u \mapsto \sum_{\kappa \in \mathcal{T}_h} \sum_{i=1}^{N_{sh}} \sigma_{\kappa,i}(u\big|_\kappa)\theta_{\kappa,i}, \tag{2.76}$$

where W_h is defined to be the finite element approximation space with

$$W_h = \{u_h \in [L^1(\Omega)]^m : \forall \kappa \in \mathcal{T}_h, u\big|_\kappa \in P_\kappa\}. \tag{2.77}$$

Remark. For W_h as in (2.77) and for Banach space V, W_h is said to be V-conformal if $W_h \subset V$. In Section 2.3.2 we will restrict to H^1-conformal spaces for the CG-method by

$$V_h = \{v_h \in W_h : \forall \hat{F} \in \mathcal{F}_h^i, [\![v_h]\!]_{\hat{F}} = 0\} \subset [H^1(\Omega)]^m, \tag{2.78}$$

which is shown in [69, Proposition 1.74] for Lagrange reference element, the set of interior faces $\mathcal{F}_h^i$ and jump operator as in Definition 2.51. DG-spaces are non-conformal, due to this reasoning a broken variant of (2.43) is introduced in Section 2.3.3.

Remark. The numerical analysis of discretizations includes various quality seals ranging from consistency, coercivity and stability to convergence orders and error estimates. For a comprehensive overview we refer to [69, Chapters 2, 3, 10].

2.3.2 Continuous Galerkin for Elliptic Problems

In this section we will look at the elliptic reaction-diffusion equation, which will serve as a paragon for a numerical handle of similar PDEs, e.g. in Chapter 4 we will deal with a comparable wave description.
In what follows we return to an important class of second-order PDEs in the form of equation (2.11). We hereby denote Dirichlet and Neumann boundaries as $\Gamma_D \subset \partial\Omega$ and $\Gamma_N \subset \partial\Omega$ respectively for a Lipschitz domain Ω [69, cf. Chapter 3.1].

Definition 2.38. *(Strong Form Reaction-Diffusion Equation) The reaction-diffusion equation is defined in strong form for $s \in C^0(\Omega)$ and $u \in C^2(\Omega) \cap C^0(\overline{\Omega})$ as*

$$-\Delta u + cu = s \quad \text{in } \Omega \tag{2.79}$$

with associated boundary conditions

$$\begin{aligned} u &= g_0 \quad \text{on } \Gamma_D \\ \partial_n u &= g_1 \quad \text{on } \Gamma_N. \end{aligned} \tag{2.80}$$

In this setting $u : \Omega \to \mathbb{R}$ is the dependent variable, the second-order derivative term is referred to as diffusion term, by $c > 0$ the reaction term is controlled, $g_0 : \Gamma_D \to \mathbb{R}$ and $g_1 : \Gamma_N \to \mathbb{R}$ determine Dirichlet and Neumann boundaries, while $s : \Omega \to \mathbb{R}$ represents the source term.
From equation (2.79) we obtain a weakened variant by the same procedure as in Definition 2.26.

Definition 2.39. *(Weak Form Reaction-Diffusion Equation) The weak form of the reaction-diffusion equation (2.79) is defined for $u \in H^1_{\Gamma_D, g_0}(\Omega), s \in L^2(\Omega), g_1 \in L^2(\Gamma_N)$ and $g_0 \in H^{1/2}(\Gamma_D)$ as*

$$\int_\Omega \nabla u \cdot \nabla v \, \mathrm{d}x - \int_{\Gamma_N} g_1 v \, \mathrm{d}x + \int_\Omega cuv \, \mathrm{d}x - \int_\Omega sv \, \mathrm{d}x = 0 \quad \forall v \in H^1_{\Gamma_D, 0} \tag{2.81}$$

with Sobolev space

$$H^1_{\Gamma_D, g_0}(\Omega) = \{u \in H^1(\Omega) : u_{\Gamma_D} = g_0\} \subset H^1(\Omega). \tag{2.82}$$

In this case, u is called a weak solution of (2.79).

For a FEM and for some particle methods, as introduced in Chapter 8, the weak form builds the starting point for numerical investigations.
The key idea in this section follows so-called Galerkin methods to replace the solution and test function space with finite-dimensional spaces V_h of dimension M and $\tilde{V}_h$ of dimension N. These approximation spaces are constructed as described in Section 2.3.1, while members of the CG method are continuous across interior boundaries of elements, enforcing zero jumps on interior facets. In this setting the solution is an element of

a conformal finite element spaces V_h with basis $\{\theta_i\}_{i\in\{1,\dots,M\}}$ and accordingly for test functions it holds $v_h \in \tilde{V}_h$ with basis $\{\phi_j\}_{j\in\{1,\dots,N\}}$ as in Definition 2.37 with

$$u_h(x) = \sum_{i=1}^{M} \theta_i(x) u_i \tag{2.83}$$

and

$$v_h(x) = \sum_{j=1}^{N} \phi_j(x) v_j \tag{2.84}$$

for coordinate vectors $\{u_i\}_{1\le i\le M}$ and $\{v_j\}_{1\le j\le N}$. Replacing functions in (2.81) with its discrete counterpart, we obtain

$$\int_\Omega \nabla u_h \cdot \nabla v_h \,\mathrm{d}x - \int_{\Gamma_N} g_1 v_h \,\mathrm{d}s + \int_\Omega c u_h v_h \,\mathrm{d}x = \int_\Omega s v_h \,\mathrm{d}x \quad \forall v_h \in \tilde{V}_h. \tag{2.85}$$

Substituting (2.83) and (2.84) into (2.85), testing with the trivial basis, and collecting Dirichlet degrees of freedom in a set $\mathcal{D} \subset \{1,\dots,M\}$ and the remaining in a set $\mathcal{N} \subset \{1,\dots,M\} \setminus \mathcal{D}$, we obtain for each $j \in \{1,\dots,N\}$

$$\begin{aligned} &\sum_{i\in\mathcal{N}} \left[\int_\Omega \nabla\theta_i \cdot \nabla\phi_j \,\mathrm{d}x + c\int_\Omega \theta_i\phi_j \,\mathrm{d}x\right] u_i \\ &= -\sum_{i\in\mathcal{D}} \left[\int_\Omega \nabla\theta_i \cdot \nabla\phi_j \,\mathrm{d}x + c\int_\Omega \theta_i\phi_j \,\mathrm{d}x\right] g_{0,i} + \int_\Omega s\phi_j \,\mathrm{d}x + \int_{\Gamma_N} g_1\phi_j \,\mathrm{d}x. \end{aligned} \tag{2.86}$$

We hence observe that this gives a system of linear equations and we next define the corresponding matrices.

Definition 2.40. *(Stiffness Matrix) The matrix that is obtained by integrating*

$$A_{ij} = \int_\Omega \nabla\theta_i \cdot \nabla\phi_j \,\mathrm{d}x, \quad i \in \{1,\dots,M\}, j \in \{1,\dots,N\} \tag{2.87}$$

is called stiffness matrix.

Definition 2.41. *(Mass Matrix) The matrix that is obtained by integrating*

$$B_{ij} = \int_\Omega \theta_i\phi_j \,\mathrm{d}x, \quad i \in \{1,\dots,M\}, j \in \{1,\dots,N\} \tag{2.88}$$

is called mass matrix.

Definition 2.42. *(Force Vector) The vector that is obtained by integrating*

$$b_j = \int_\Omega s\phi_j \,\mathrm{d}x + \int_{\Gamma_N} g_1\phi_j \,\mathrm{d}x, \quad j \in \{1,\dots,N\} \tag{2.89}$$

is called the force vector.

Remark. The case of $V_h = \tilde{V}_h$ is referred to as as Galerkin discretization, whereas $V_h \neq \tilde{V}_h$ as Petrov-Galerkin discretization.

Remark. For parabolic problems with weak solutions as in Definition 2.29, we refer to Section 2.3.3 for a numerical treatment.

2.3.3 Discontinuous Galerkin for Elliptic & Hyperbolic Problems

The following serves as an introduction to DG-methods, as presented in [57] and [69, Section 3.2.4]. In Section 2.3.1 it is stated that these methods are non-conformal to classical Sobolev spaces [94, p. 28]. Hence, it is common to redefine spaces and operators such that the restriction to each element $\kappa \in \mathcal{T}_h$ corresponds to their continuous counterpart [94, p. 23].

Definition 2.43. *(Broken Sobolev Space) Let $\mathcal{T}_h$ be a mesh of some $\Omega \subset \mathbb{R}^d$. Then the broken Sobolev space, whose restriction to each element $\kappa \in \mathcal{T}_h$ belongs to the Sobolev space $H^k(\kappa)$, is defined as*

$$\mathcal{H}^k(\mathcal{T}_h) = \{v \in L^2(\Omega) : v\big|_\kappa \in H^k(\kappa), \kappa \in \mathcal{T}_h\}, \tag{2.90}$$

Definition 2.44. *(Traces, Trace Space) In the setting of Definition 2.35 suppose $v \in \mathcal{H}^1(\mathcal{T}_h)$ such that $v\big|_\kappa \in H^1(\kappa)$, then we define by $v^\pm \in L^2(\partial\kappa)$ the traces of $\kappa \in \mathcal{T}_h$ and its adjacent element κ'. In addition, we define by $T(\mathcal{T}_h) := \Pi_{\kappa\in\mathcal{T}_h} L^2(\partial\kappa)$ the space of traces of $v \in \mathcal{H}^1(\mathcal{T}_h)$.*

Definition 2.45. *(Broken Gradient) The operator $\nabla_h : \mathcal{H}^1(\mathcal{T}_h) \to [L^2(\mathcal{T}_h)]^d$ defined as $(\nabla_h v)\big|_\kappa := \nabla(v\big|_\kappa)$ for standard gradient w.r.t. the Euclidian metric $(\nabla v)_i = \partial_{x_i} v$ for $i \in \{1, ..., d\}$ is called the broken gradient.*

Definition 2.46. *(Broken Divergence) The operator $\nabla_h \cdot : [\mathcal{H}^1(\mathcal{T}_h)]^d \to L^2(\mathcal{T}_h)$ defined as $(\nabla_h \cdot V)\big|_\kappa := \nabla \cdot (V\big|_\kappa)$ for vector-valued and standard divergence w.r.t. the Euclidian metric $\nabla \cdot V = \sum_i \partial_{x_i} V$ for $i \in \{1, ..., d\}$ is called the broken divergence.*

Definition 2.47. *(Broken Laplacian) The operator $\Delta_h : \mathcal{H}^2(\mathcal{T}_h) \to L^2(\mathcal{T}_h)$ defined as $(\Delta_h v)\big|_\kappa := \Delta(v\big|_\kappa)$ for vector-valued and standard Laplacian w.r.t. the Euclidian metric $\Delta v = \sum_i \partial^2_{x_i} v$ for $i \in \{1, ..., d\}$ is called the broken Laplacian.*

Remark. For the discretization of resulting equations via DG-method the finite element triplet $\{\hat{\kappa}, \hat{P}, \hat{\Sigma}\}$ is defined in terms of local degrees of freedom as [69, pp. 42-43]

$$\hat{\sigma}_i : V(\hat{\kappa}) \to P, \quad \hat{v} \mapsto \hat{\sigma}_i(\hat{v}) = \frac{1}{|\hat{\kappa}|} \int_{\hat{\kappa}} \hat{v}\mathcal{K}_i \, \mathrm{d}s, \quad 1 \le i \le N_{sh}, \tag{2.91}$$

where $N_{sh} = \dim(\hat{P})$, $\mathcal{K}_i$ is a smooth function on $\hat{\kappa}$ and $|\hat{\kappa}|$ denotes its Lebesgue-measure. The procedure described in Section 2.3.1 then leads to finite element triplets $\{\kappa, P, \Sigma\}$ and local shape functions $\theta_{\kappa,i}$ for all $\kappa \in \mathcal{T}_h$. In accordance to Definition 2.37 the approximation space is defined for $m = 1$ and the global interpolation operator is specified as

$$\mathcal{I}_{DG,h} : L^1(\Omega) \to W_h, \quad u \mapsto \sum_{\kappa\in\Omega} \sum_{i=1}^{N_{sh}} \frac{1}{|\kappa|} \left(\int_\kappa u\mathcal{K}_{\kappa,i} \, \mathrm{d}s \right) \theta_{\kappa,i}. \tag{2.92}$$

In the following we restrict ourselves to the polynomial space (2.66), i.e. $P := \mathbb{P}_k$, in the finite element triplet.

DG for Elliptic Problems

In this section a solution via DG-methods to the viscous part ($c = 0$) of the reaction-diffusion equation from Definition 2.38 is investigated, i.e.

$$\begin{aligned} -\Delta u &= f && \text{in } \Omega \\ u &= g_0 && \text{on } \Gamma_D \\ \partial_n u &= g_1 && \text{on } \Gamma_N. \end{aligned} \tag{2.93}$$

Discretizations are based on rewriting (2.93) as

$$\begin{aligned} \sigma &= \nabla u && \text{in } \Omega \\ -\nabla \cdot \sigma &= f && \text{in } \Omega \\ u &= g_0 && \text{on } \Gamma_D \\ \partial_n u &= g_1 && \text{on } \Gamma_N. \end{aligned} \tag{2.94}$$

If $u \in \mathcal{H}^2(\mathcal{T}_h)$ and $\sigma \in \left[\mathcal{H}^1(\mathcal{T}_h)\right]^d$, we obtain after multiplication with test-functions $v \in \mathcal{H}^1(\mathcal{T}_h)$ and $\tau \in \left[\mathcal{H}^1(\mathcal{T}_h)\right]^d$ as well as summation and integration over single elements $\kappa \in \mathcal{T}_h$ by applying integration by parts on each element

$$\begin{aligned} \sum_{\kappa \in \mathcal{T}_h} \int_\kappa \sigma \cdot \tau \,\mathrm{d}x &= -\sum_{\kappa \in \mathcal{T}_h} \left(\int_\kappa u \nabla_h \cdot \tau \,\mathrm{d}x - \int_{\partial\kappa} u^+ \tau^+ \cdot n^+ \,\mathrm{d}s \right) \\ \sum_{\kappa \in \mathcal{T}_h} \int_\kappa \sigma \cdot \nabla_h v \,\mathrm{d}x &= \sum_{\kappa \in \mathcal{T}_h} \left(\int_\kappa f v \,\mathrm{d}x + \int_{\partial\kappa} v^+ \sigma^+ \cdot n^+ \,\mathrm{d}s \right), \end{aligned} \tag{2.95}$$

where n^+ is the outward normal to element κ in accordance with Definition 2.44. Since u and v can have inter-element discontinuities, commonly numerical flux functions are introduced, i.e. for $\hat{u} : \mathcal{H}^2(\mathcal{T}_h) \to T(\mathcal{T}_h)$ and $\hat{\sigma} : \mathcal{H}^2(\mathcal{T}_h) \times \left[\mathcal{H}^1(\mathcal{T}_h)\right]^d \to \left[T(\mathcal{T}_h)\right]^d$ such that $\hat{u}$ depends on u while $\hat{\sigma}$ depends on u and σ. We obtain

$$\begin{aligned} \sum_{\kappa \in \mathcal{T}_h} \int_\kappa \sigma \cdot \tau \,\mathrm{d}x &= -\sum_{\kappa \in \mathcal{T}_h} \left(\int_\kappa u \nabla_h \cdot \tau \,\mathrm{d}x - \int_{\partial\kappa} \hat{u}(u) \tau^+ \cdot n^+ \,\mathrm{d}s \right), \\ \sum_{\kappa \in \mathcal{T}_h} \int_\kappa \sigma \cdot \nabla_h v \,\mathrm{d}x &= \sum_{\kappa \in \mathcal{T}_h} \left(\int_\kappa f v \,\mathrm{d}x + \int_{\partial\kappa} v^+ \hat{\sigma}(u, \sigma) \cdot n^+ \,\mathrm{d}s \right). \end{aligned} \tag{2.96}$$

In the analysis of PDEs two properties are decisive for numerical fluxes [69, Definition 3.40/3.42].

Definition 2.48. *(Consistency of Numerical Flux) Numerical fluxes $\hat{u}$ and $\hat{\sigma}$ are said to be consistent if for any $u \in H^2(\Omega) \cap H_0^1(\Omega)$ it holds on interior faces that*

i) $\hat{u}(u) = u\big|_{\mathcal{F}_h^i}$,

ii) $\hat{\sigma}(u, \nabla u) = \nabla u\big|_{\mathcal{F}_h^i}$,

which lets solution u satisfy (2.96).

Definition 2.49. *(Conservativeness of Numerical Flux) The numerical fluxes $\hat{u}$ and $\hat{\sigma}$ are conservative if they are single-valued.*

Remark. Defining the numerical fluxes $\hat{u}$ and $\hat{\sigma}$ differently leads to different DG discretizations w.r.t. stability and accuracy [16, 94]. Formulation (2.96), based on rewriting (2.93) as a first-order system, dates back to [48] and is often used to solve diffusive equations via DG. Solutions to (2.96) have the disadvantage of solving an additional equation associated to the newly introduced variable in (2.94). Some proposed alternatives to circumvent this drawback are shortly discussed in the following.

Setting $\tau = \nabla_h v$ and applying integration by parts we obtain for the first equation in (2.96) that

$$\sum_{\kappa\in\mathcal{T}_h} \int_\kappa \sigma \cdot \nabla_h v \,\mathrm{d}x = \sum_{\kappa\in\mathcal{T}_h} \left(\int_\kappa \nabla_h u \cdot \nabla_h v \,\mathrm{d}x + \int_{\partial\kappa} (\hat{u} - u^+) \nabla_h v^+ \cdot n^+ \,\mathrm{d}s \right). \tag{2.97}$$

This expression is substituted in the second equation of (2.96) such that we obtain a so-called primal flux formulation [16], where we are solving for a single solution variable $u \in \mathcal{H}^2(\mathcal{T}_h)$ in

$$\hat{B}(u, v) = \sum_{\kappa\in\mathcal{T}_h} \int_\kappa f v \,\mathrm{d}x \quad \forall v \in \mathcal{H}^2(\mathcal{T}_h) \tag{2.98}$$

with bilinear form $\hat{B} : \mathcal{H}^2(\mathcal{T}_h) \times \mathcal{H}^2(\mathcal{T}_h) \to \mathbb{R}$ given by

$$\hat{B}(u, v) = \sum_{\kappa\in\mathcal{T}_h} \left[\int_\kappa \nabla_h u \cdot \nabla_h v \,\mathrm{d}x + \int_{\partial\kappa} \left((\hat{u} - u^+) \nabla_h v^+ \cdot n^+ - \hat{\sigma} v^+ \cdot n^+ \right) \mathrm{d}s \right]. \tag{2.99}$$

This element-based view can be written in terms of interior $\mathcal{F}_h^i$ and exterior $\mathcal{F}_h^e$ faces. For the sum over each element, each associated boundary is visited twice, i.e. exemplifying for the first boundary term we obtain

$$\begin{aligned} &\sum_{\kappa\in\mathcal{T}_h} \left[\int_{\partial\kappa} (\hat{u} - u^+) \nabla_h v^+ \cdot n^+ \,\mathrm{d}s \right] \\ &= \sum_{\hat{F}\in\mathcal{F}_h^i} \int_{\hat{F}} \left((\hat{u}^+ - u^+) \nabla_h v^+ \cdot n^+ + (\hat{u}^- - u^-) \nabla_h v^- \cdot n^- \right) \mathrm{d}s + \sum_{\hat{F}\in\mathcal{F}_h^e} \int_{\hat{F}} (\hat{u} - u) \nabla_h v \cdot n \,\mathrm{d}s. \end{aligned} \tag{2.100}$$

If we set $n = n^+$ and hence $-n = n^-$ we can additionally rewrite it as

$$\sum_{\hat{F}\in\mathcal{F}_h^i} \int_{\hat{F}} \left((\hat{u}^+ - u^+) \nabla_h v^+ \cdot n - (\hat{u}^- - u^-) \nabla_h v^- \cdot n \right) \mathrm{d}s + \sum_{\hat{F}\in\mathcal{F}_h^e} \int_{\hat{F}} (\hat{u} - u) \nabla_h v \cdot n \,\mathrm{d}s. \tag{2.101}$$

At this point, we introduce average and jump of a scalar field v and a vector field V as well as the associated jump identity, that are necessary for further computations [94, pp. 37-38].

Definition 2.50. *(Interior Average) The average of a scalar field v and a vector field V on an interior facet is defined as*

$$\begin{aligned} \{\{v\}\} &= \frac{1}{2}(v^+ + v^-), \\ \{\{V\}\} &= \frac{1}{2}(V^+ + V^-). \end{aligned} \tag{2.102}$$

Definition 2.51. *(Interior Jump) The jump of a scalar field v and a vector field V on an interior facet is defined as*

$$\begin{aligned} [\![v]\!] &= (v^+ - v^-)n, \\ [\![V]\!] &= (V^+ - V^-) \cdot n. \end{aligned} \tag{2.103}$$

Definition 2.52. *(Exterior Average) The average of a scalar field v and a vector field V on an exterior facet is defined as*

$$\begin{aligned} \{\{v\}\} &= v^+, \\ \{\{V\}\} &= V^+. \end{aligned} \tag{2.104}$$

Definition 2.53. *(Exterior Jump) The jump of a scalar field v and a vector field V on an exterior facet is defined as*

$$\begin{aligned} [\![v]\!] &= v^+ n, \\ [\![V]\!] &= V^+ \cdot n. \end{aligned} \tag{2.105}$$

Lemma 2.54. *(Jump Identity) The jump identity states*

$$[\![Vv]\!] = [\![V]\!]\{\{v\}\} + \{\{V\}\} \cdot [\![v]\!]. \tag{2.106}$$

Proof. Simple insertion of (2.102)-(2.105) leads to the assertion. □

We can express (2.101) in jump notation as

$$\sum_{\hat{F} \in \mathcal{F}_h^i} \int_{\hat{F}} [\![(\hat{u} - u)\nabla_h v]\!] \, \mathrm{d}s + \sum_{\hat{F} \in \mathcal{F}_h^e} \int_{\hat{F}} [\![\hat{u} - u]\!] \cdot \{\{\nabla_h v\}\} \, \mathrm{d}s. \tag{2.107}$$

Using the jump identity on the first term leads to

$$\sum_{\hat{F} \in \mathcal{F}_h^i \cup \mathcal{F}_h^e} \int_{\hat{F}} [\![(\hat{u} - u)]\!] \cdot \{\{\nabla_h v\}\} \, \mathrm{d}s + \sum_{\hat{F} \in \mathcal{F}_h^i} \int_{\hat{F}} [\![\nabla_h v]\!]\{\{(\hat{u} - u)\}\} \, \mathrm{d}s. \tag{2.108}$$

The same operations on the remaining terms in (2.99) lead to

$$\begin{aligned} \hat{B}(u, v) = &\sum_{\kappa \in \mathcal{T}_h} \int_\kappa \nabla_h u \cdot \nabla_h v \, \mathrm{d}x \\ &+ \sum_{\hat{F} \in \mathcal{F}_h^i \cup \mathcal{F}_h^e} \int_{\hat{F}} [\![(\hat{u} - u)]\!] \cdot \{\{\nabla_h v\}\} \, \mathrm{d}s + \sum_{\hat{F} \in \mathcal{F}_h^i} \int_{\hat{F}} [\![\nabla_h v]\!]\{\{(\hat{u} - u)\}\} \, \mathrm{d}s \\ &- \sum_{\hat{F} \in \mathcal{F}_h^i \cup \mathcal{F}_h^e} \int_{\hat{F}} [\![v]\!] \cdot \{\{\hat{\sigma}\}\} \, \mathrm{d}s - \sum_{\hat{F} \in \mathcal{F}_h^i} \int_{\hat{F}} [\![\hat{\sigma}]\!]\{\{v\}\} \, \mathrm{d}s. \end{aligned} \tag{2.109}$$

Based on expression (2.109) various DG-discretizations can be derived by specifying fluxes $\hat{u}$ and $\hat{\sigma}$ for the DG-approximation space and interpolation operator [16][94, pp. 41-46], e.g. the symmetric interior penalty (SIP) [15], the non-symmetric interior penalty method (NIP) [153] such as the method of Baumann-Oden [29] and Bassi-Rebay [26]. We restrict ourselves in the following and in Chapters 5-7 to the former.

Definition 2.55. *(SIP-DG) The SIP-DG method is given by specification of numerical fluxes in (2.109) as*

$$\begin{array}{llll} \hat{u} = \{\{u_h\}\}, & \hat{\sigma} = \{\{\nabla_h u_h\}\} - \delta^{IP}(u_h) & on & \mathcal{F}_h^i, \\ \hat{u} = g_0, & \hat{\sigma} = \nabla_h u_h - \delta_\Gamma^{IP}(u_h) & on & \mathcal{F}_h^e \subset \Gamma_D, \\ \hat{u} = u_h, & \hat{\sigma} = g_1 n & on & \mathcal{F}_h^e \subset \Gamma_N, \end{array} \tag{2.110}$$

where

$$\begin{aligned} \delta^{IP}(u_h) &= C_{IP}\frac{k^2}{h}[\![u_h]\!], \\ \delta_\Gamma^{IP}(u_h) &= C_{IP}\frac{k^2}{h}(u_h - g_0)n, \end{aligned} \tag{2.111}$$

for constant $C_{IP} > 0$, maximum mesh diameter $h > 0$ and polynomial degree $k > 0$. From this we can rewrite (2.109) as

$$\begin{aligned} \hat{B}(u_h, v_h) = &\sum_{\kappa \in \mathcal{T}_h} \int_\kappa \nabla_h u_h \cdot \nabla_h v_h \,\mathrm{d}x \\ &+ \sum_{\hat{F} \in \mathcal{F}_h^i \cup (\mathcal{F}_h^e \subset \Gamma_D)} \int_{\hat{F}} \left[-[\![v_h]\!] \cdot \{\{\nabla_h u_h\}\} - [\![\nabla_h v_h]\!]\{\{u_h\}\} + C_{IP}\frac{k^2}{h}[\![u_h]\!][\![v_h]\!] \right] \mathrm{d}s \\ &+ \sum_{\hat{F} \in \mathcal{F}_h^e \subset \Gamma_D} \int_{\hat{F}} g_0 n \cdot \nabla_h v_h \,\mathrm{d}s - \sum_{\hat{F} \in \mathcal{F}_h^e \subset \Gamma_D} \int_{\hat{F}} C_{IP}\frac{k^2}{h} g_0 v_h \,\mathrm{d}s - \sum_{\hat{F} \in \mathcal{F}_h^e \subset \Gamma_N} \int_{\hat{F}} g_1 v_h \,\mathrm{d}s. \end{aligned} \tag{2.112}$$

Remark. From Definition 2.55 we obtain the global stiffness A and global mass matrix B in line with Definitions 2.40 and 2.41, which can be block-partitioned as

$$A = \begin{pmatrix} A_{\kappa_1} & 0 & \dots & 0 \\ 0 & A_{\kappa_2} & \ddots & \vdots \\ \vdots & \ddots & \ddots & 0 \\ 0 & \dots & 0 & A_{\kappa_N} \end{pmatrix} \tag{2.113}$$

and

$$B = \begin{pmatrix} B_{\kappa_1} & 0 & \dots & 0 \\ 0 & B_{\kappa_2} & \ddots & \vdots \\ \vdots & \ddots & \ddots & 0 \\ 0 & \dots & 0 & B_{\kappa_N} \end{pmatrix} \tag{2.114}$$

where we have $N = |\mathcal{T}_h|$ local stiffness and mass matrices of size $N_{sh} \times N_{sh}$.

DG for Hyperbolic First-Order Nonlinear Conservation Systems

We will now return to first-order nonlinear conservation systems that were described in Definition 2.6. For broken Sobolev space we obtain for stationary equations after component-wise multiplication with test-functions $V \in \left[\mathcal{H}^1(\mathcal{T}_h)\right]^m$ such as summation and integration over single elements $\kappa \in \mathcal{T}_h$ [94, p. 76]

$$\sum_{\kappa\in\mathcal{T}_h}\left(-\int_\kappa F(U) : \nabla_h V \,\mathrm{d}x + \int_{\partial\kappa}(F(U)\cdot n)\cdot V \,\mathrm{d}s\right) = 0. \tag{2.115}$$

Since the solution is by definition discontinuous at cell transitions we must replace the nonlinear flux by a numerical flux function $\mathcal{F} : [T(\mathcal{T}_h)]^m \times [T(\mathcal{T}_h)]^m \times [T(\mathcal{T}_h)]^d \to [T(\mathcal{T}_h)]^m$, that is described in detail in the next subsection. The discretized equation reads as

$$\sum_{\kappa\in\mathcal{T}_h}\left(-\int_\kappa F(U_h) : \nabla_h V_h \,\mathrm{d}x + \int_{\partial\kappa}\mathcal{F}(U_h^+, U_h^-, n^+)\cdot V_h^+ \,\mathrm{d}s\right) = 0. \tag{2.116}$$

Remark. The last integral above is defined on elemental boundaries. However, most available finite element solver deal with face-based integrals. In order to transfer equations, we use (2.100) or the following identity for $U^+ \in [T(\mathcal{T}_h)]^d$ and $v^+ \in T(\mathcal{T}_h)$ [94, Lemma 9.3]

$$\sum_{\kappa\in\mathcal{T}_h\setminus\Gamma}\left(\int_{\partial\kappa} U^+\cdot n^+ v^+ \,\mathrm{d}s\right) = \sum_{\hat{F}\in\mathcal{F}_h^i}\int_{\hat{F}}\{\{U\}\}\cdot[\![v]\!]\,\mathrm{d}s + \sum_{\hat{F}\in\mathcal{F}_h^i}\int_{\hat{F}}[\![v]\!]\{\{U\}\}\,\mathrm{d}s, \tag{2.117}$$

$$\sum_{\kappa\in\mathcal{T}_h}\left(\int_{\partial\kappa} U^+\cdot n^+ v^+ \,\mathrm{d}s\right) = \sum_{\hat{F}\in\mathcal{F}_h^i\cup\mathcal{F}_h^e}\int_{\hat{F}}\{\{U\}\}\cdot[\![v]\!]\,\mathrm{d}s + \sum_{\hat{F}\in\mathcal{F}_h^i}\int_{\hat{F}}[\![v]\!]\{\{U\}\}\,\mathrm{d}s. \tag{2.118}$$

Numerical Flux Functions

In (2.116) we need to specify the numerical flux function, which can be interpreted as weak imposition of boundary data for inner and outer cell transitions. The numerical flux function needs to be locally Lipschitz w.r.t. to each component such as consistent and conservative (cf. to Definitions 2.48 and 2.49) [94, p. 78].

Definition 2.56. *(Numerical Flux Consistency) On each element $\kappa \in \mathcal{T}_h$ a numerical flux is called consistent with the original flux if*

$$\mathcal{F}(U^+, U^+, n) = F(U^+)\cdot n. \tag{2.119}$$

Definition 2.57. *(Numerical Flux Conservativeness) Given two adjacent elements $\kappa, \kappa' \in \mathcal{T}_h$, where we denote $n_{\kappa'} = -n$, we define a flux to be conservative if on $\hat{F} := \partial\kappa\cap\partial\kappa' \neq \emptyset$ it holds that*

$$\mathcal{F}(U^+, U^-, n) = -\mathcal{F}(U^+, U^-, -n). \tag{2.120}$$

Frequently used numerical flux functions that incorporate properties of aforementioned definitions are [94]:

Definition 2.58. *(Flux Variants)*

i) Upwind Flux

$$\mathcal{F}_1(U^+, U^-, n)\Big|_{\partial\kappa} = \frac{1}{2}\left(F(U^+)\cdot n + F(U^-)\cdot n\right). \tag{2.121}$$

ii) Local Lax Friedrichs Flux

$$\mathcal{F}_2(U^+, U^-, n)\Big|_{\partial\kappa} = \frac{1}{2}\left(F(U^+)\cdot n + F(U^-)\cdot n + \alpha_{\max}(U^+ - U^-)\right), \tag{2.122}$$

where $\alpha_{\max} = \max_{V=U^+,U^-}\{|\lambda(B(V, n_\kappa))|\}$ *with* $\lambda(B(V, n_\kappa))$ *as in Definition 2.7.*

iii) HLLE Flux

$$\mathcal{F}_3(U^+, U^-, n)\Big|_{\partial\kappa} = \frac{1}{\lambda^+ - \lambda^-}\left(\lambda^+ F(U^+)\cdot n - \lambda^- F(U^-)\cdot n - \lambda^+\lambda^-(U^+ - U^-)\right), \tag{2.123}$$

where $\lambda^+ = \max(\lambda_{\max}, 0)$ *and* $\lambda^- = \min(\lambda_{\min}, 0)$*, for* $\lambda_{\max}$ *and* $\lambda_{\min}$ *defined in accordance with* $\alpha_{\max}$ *without reduction to absolute values.*

Temporal Discretization

The strategy of spatial discretizations, that are subsequently followed by time integration is referred to as the method of lines [69, Section 6.1.4]. We will restrict in the following to this technique. However, we will not conceal the fact that space-time models for simultaneous discretizations have become a rapidly growing field, offering promising advantages such as space-time adaptivity and parallel solution strategies [69, Section 6.3.2].
Upstream techniques of Section 2.3.2 and 2.3.3 generally provide with systems of ordinary differential equations, i.e.

$$\frac{\mathrm{d}U_h}{\mathrm{d}t} = L(U_h). \tag{2.124}$$

Classically this can be solved via one-step methods, i.e. we can compute the solution at time $k+1$ with the help of the solution at time k for global stiffness A and mass matrix B as well as for some force vector b by relying on broadly known methods that can be classified within the θ-method [30].

Definition 2.59. *(θ − method) For $\theta \in [0, 1]$ a numerical one step method is classified in the θ-method if it is of the form*

$$B\frac{U_h^{k+1} - U_h^k}{\Delta t} + A\left[\theta U_h^{k+1} + (1-\theta)U_h^k\right] = \theta b^{k+1} + (1-\theta)b^k. \tag{2.125}$$

Remark. The forward Euler is hereby obtained for $\theta = 0$

$$B\frac{U_h^{k+1} - U_h^k}{\Delta t} + AU^k = b^k, \tag{2.126}$$

the backward Euler for $\theta = 1$

$$B\frac{U_h^{k+1} - U_h^k}{\Delta t} + AU_h^{k+1} = b^{k+1} \tag{2.127}$$

and the Crank-Nicolson scheme as the arithmetic mean for $\theta = 1/2$

$$B\frac{U_h^{k+1} - U_h^k}{\Delta t} + A\left[\frac{1}{2}U_h^{k+1} + \frac{1}{2}U_h^k\right] = \frac{1}{2}b^{k+1} + \frac{1}{2}b^k. \tag{2.128}$$

Since providing higher accuracy and stability Runge-Kutta schemes, in combination with DG denoted as RKDG-schemes, are frequently used [57].

Definition 2.60. *(Runge-Kutta Schemes) The K-step Runge Kutta follows the procedure of*

i) initialize $U_h^{(0)} := U_h^k$,

ii) for $l \in \{1, ..., K\}$ *intermediate steps*

$$U_h^{(l)} = \sum_{m=1}^{l-1} \left(\alpha_{ml} U_h^{(m)} + \Delta t \beta_{ml} L(U_h^{(m)})\right) \tag{2.129}$$

for characteristic coefficients $\beta_{ml}, \alpha_{ml} \in \mathbb{R}$,

iii) set $U_h^{k+1} = U_h^l$.

Shocks

The common shock phenomenon of hyperbolic PDEs describes the development of discontinuities even when starting from a continuous setting [58]. Occurrences cause not only challenges in the theoretical, e.g. the non-uniqueness of a weak form solution, but also in the numerical treatment of solutions, e.g. oscillations in shock locations for high-order discretizations. These so-called Gibbs oscillations [95] lead in the worst way to a breakdown of the solution scheme. Therefore it is of high importance to us to find algorithmic handles, with regards to Chapters 5-7, where we will meet equations of described nature. For DG-approaches, two techniques are frequently used for dealing with non-physical oscillations. The first stands in line with applying vanishing viscosity to ensure the existence of entropy solutions [62]. More precisely, it builds up on the continuous formulation of the equation, i.e. the equation itself is slightly perturbed from its native form by adding stabilizing artificial viscosity to the equation under investigation [134]. The second technique accumulates in the terminology of limiters, and builds up on the discretized solution [58]. In this sense, limiters are used as a post-processing tool for reconstructions in high-order discretization methods.

Slope Limiters

The usage of slope limiters relies on the calculation of the discretized solutions and secondly a nonlinear projection operator to prevent oscillations [56, Section 3.13].

Definition 2.61. *(Slope Limiter) We define an operator to be a valid slope limiter* $\Lambda\Pi : W_h \to W_h$ *for discretized solution* $v_h \in W_h$ *and* $u_h := \Lambda\Pi(v_h)$ *if it guarantees*

i) mass conservation, i.e.

$$u_c = v_c \tag{2.130}$$

on each element $\kappa \in \mathcal{T}_h$ *for associated mean values* $u_c, v_c \in \mathbb{R}$,

ii) nonincreasing total variation for $w_h \in W_h$, *i.e.*

$$|w_h|_{TV(a,b)} \leq |u_h|_{TV(a,b)} \tag{2.131}$$

for solution to a propagation scheme of Definition 2.59, e.g. $w_h = u_h + \Delta t L_h(u_h)$ *for sufficiently small step-size* Δt *and total variation*

$$|u_h|_{TV(a,b)} = \sum_{j=1}^{N_{sh}} |u_{h,j+1} - u_{h,j}|, \tag{2.132}$$

iii) no deterioration in the accuracy of the finite element solution $||u_h - u|| \leq ||v_h - u||$ *compared to the physical solution.*

In the literature many of such projection operators are applied [25, 58, 86, 110]. In this section we restrict ourselves to the so-called vertex-based slope limiter [110]. The idea can simply be summarized as using Taylor basis functions to adjust derivatives without changing the mean. For polynomial space $\mathbb{P}_1$ the steepest possible slope limiter $0 \leq \alpha_\kappa \leq 1$ is defined for mean $u_c \in \mathbb{R}$ of element $\kappa \in \mathcal{T}_h$, where the bounds are dependent on vertices x_i of the element and of all element neighbours $\kappa' \in \mathcal{T}_h$ sharing a common face $\hat{F} \in \mathcal{F}_h$

$$u_h(x) = u_c + \alpha_\kappa (\nabla u)_c \cdot (x - x_c) \quad \text{for } x \in \kappa \tag{2.133}$$

with

$$\alpha_\kappa = \min_i \begin{cases} \min\left\{1, \frac{u_\kappa^{max} - u_c}{u_{x_i} - u_c}\right\} & \text{if } u_{x_i} - u_c > 0 \\ 1 & \text{if } u_{x_i} - u_c = 0 \\ \min\left\{1, \frac{u_\kappa^{min} - u_c}{u_{x_i} - u_c}\right\} & \text{if } u_{x_i} - u_c < 0 \end{cases} \tag{2.134}$$

for $u_\kappa^{max} := \max\{u_c, u_{x_i'}^{max}\}$ and $u_\kappa^{min} := \min\{u_c, u_{x_i'}^{min}\}$ for $x_i \in \kappa'$ this ensures at vertices $x_i \in \kappa$ that

$$u_\kappa^{min} \leq u(x_i) \leq u_\kappa^{max} \quad \forall x_i \in \kappa. \tag{2.135}$$

The procedure is extendable to polynomials of arbitrary order limiting all derivatives of order k that arise from Taylor series expansions by a common factor $0 \leq \alpha_\kappa^k \leq 1$ [110].

Remark. Exemplifying applications for constructed situations for polyonimals of order $k = 1$ are shown in one dimension in Figure 2.1 and in two dimensions in Figure 2.2.

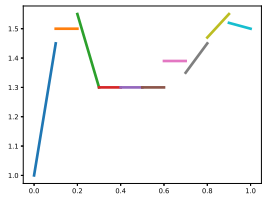

(a) Before Slope Limiting

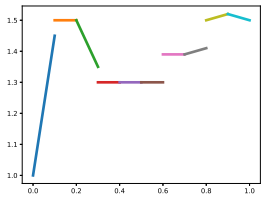

(b) After Slope Limiting

Figure 2.1: 1D Slope Limiter

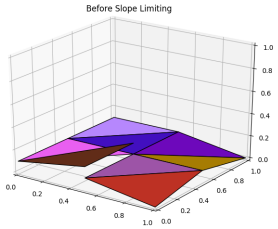

(a) Before Slope Limiting

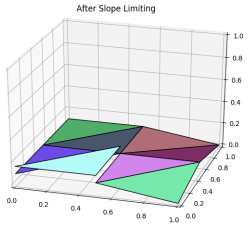

(b) After Slope Limiting

Figure 2.2: 2D Slope Limiter

Remark. Slope limiters provide robust solutions, while preserving conservation properties. However, as a post-discretization tool, a capture in an optimization setting based on the continuous form of a constraining PDE appears not straightforward. Even in discrete solution-based approaches one would still need to rely on differentiable alternatives for the slope limiter [180].

Artificial Viscosity

For first-order hyperbolic systems as of Definition (2.6) artificial viscosity defines the equation-wise addition of μ-weighted second-order derivatives as in Definition 2.38. A simple predefinition of the weights can lead to a prevention of developing discontinuities. However, more sophisticated approaches tackle this problem by a variable solution-dependent weight. Most commonly viscosity is controlled by shock detectors, e.g. [147] adds piecewise constant viscosity, [24] smooths out discontinuous cell transitions and [106] uses continuous piecewise linear polynomials. We will restrict ourselves here and in Chapters 5-7 on the shock-detector by Persson-Perraire [147], which is presented in the following.

We investigate finite element representations $u_h \in W_h$ and $\tilde{u}_h \in \tilde{W}_h$ of a solution, i.e.

$$u_h = \sum_{i=1}^{k} u_i \theta_i \quad \tilde{u}_h = \sum_{i=1}^{k-1} u_i \theta_i, \tag{2.136}$$

where $P := \mathbb{P}_k$ and $\tilde{u}_h$ is the solution where the polynomial of highest degree k is left out, which is obtained from the solution u_h by interpolation. Based on this, an element-wise smoothness indicator factor is calculated on $\kappa \in \mathcal{T}_h$

$$S_\kappa = \frac{(u_h - \tilde{u}_h, u_h - \tilde{u}_h)_{L^2(\kappa)}}{(u_h, u_h)_{L^2(\kappa)}}. \tag{2.137}$$

Subsequently, it zeroes whenever finite element solutions are smooth and increases in the presence of large oscillations and sharp gradients. Based on the above, the elemented μ-weight is determined for $\kappa \in \mathcal{T}_h$ as

$$\mu_\kappa = \begin{cases} 0 & \text{if } s_\kappa < s_0 - \alpha \\ \frac{\mu_0}{2}\left(1 + \sin\frac{\pi(s_\kappa - s_0)}{2\kappa}\right) & \text{if } s_0 - \alpha \leq s_\kappa \leq s_0 + \alpha \\ \mu_0 & \text{if } s_\kappa > s_0 - \alpha. \end{cases} \tag{2.138}$$

From this, we obtain $\mu_\kappa \in [0, \mu_0]$, hence the scheme requires the definition of constant $\mu_0, s_0, \alpha > 0$ such as defining e.g. $s_\kappa = \log_{10} S_\kappa$.

Remark. The presented technique can be exemplifying demonstrated on the one-dimensional, inviscid Burgers' equation [27], that can be stated under addition of artificial viscosity on $[0,1] \times (0,T)$ as

$$\partial_t u + u\partial_x u - \mu\partial^2_{xx} u = 0. \tag{2.139}$$

We hereby investigate initial and boundary conditions as

$$\begin{aligned} u_0(x) &= \max(\sin(2\pi x), 0) && \text{on } [0,1] \times \{0\}, \\ u|_{\{0\}} &= u|_{\{1\}} && \text{on } \{0,1\} \times (0,T). \end{aligned}$$

Results can be taken for $\mathbb{P}_5$ from Figure 2.3, where we observe oscillations around the shock location in the left subfigure, which is smeared out after introducing the non-zero viscosity-weight of the central one in the right subfigure.

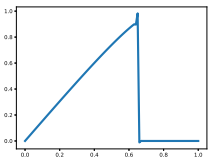

(a) Solution to Inviscid Burgers' Equation for $t = 0.5$

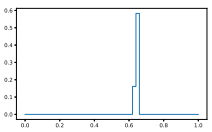

(b) Viscosity Weight via Shock Detection

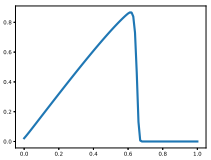

(c) Solution to Inviscid Burgers' Equation with Artificial Viscosity for $t = 0.5$

Figure 2.3: Artificial Viscosity for Burgers' Equation

Remark. The general drawback of the artificial viscosity approach lies in the non-preserving of the local maximum principle. Whereas from a numerical point of view, the aforementioned scheme has the disadvantage of causing restrictions on the time-steps due to possible discontinuities of the μ-weights [147].
However, artificial viscosity stays meaningful in an optimization setting based on the continuous description of the constraining PDE. Due to this argumentation, we rely on the latter approach in the upcoming chapters.

Chapter 3

Shape & Topology Optimization

This chapter introduces the basic definitions and theorems in the optimization of shapes in Section 3.1 and topologies in Section 3.2. Based on this, we will introduce in Section 3.3 algorithmic techniques to deal with these problems in a numerical setting.

3.1 Basics of Shape Optimization

The idea of shape optimization is to deform an object ideally to minimize some target functional. Hence, to find a suitable matter of deforming, we are interested in some shape analogy of a classical derivative. Here we use a methodology that is commonly used in shape optimization, extensively elaborated in various works [52, 172, 65]. In this section we fix required definitions and amend whenever it appears necessary. During this chapter we start out with the continuous setting and set remarks on the validity of the discrete counterpart.
The centre of interests builds a generic shape functional [65, Chapter 9, Section 3.1].

Definition 3.1. *(Shape Functional) For nonempty superset $D \subset \mathbb{R}^d$, where $\mathcal{A} \subset \{\Omega : \Omega \subset D\}$ is a set of subsets, the functional*

$$J : \mathcal{A} \to \mathbb{R}, \quad \Omega \mapsto J(\Omega) \tag{3.1}$$

is called a shape functional.

The ultimate goal in this work is to use these functionals in optimization. Due to this reason, the so-called perturbation of identity is introduced [65, Chapter 4, Section 3.2].

Definition 3.2. *(Perturbation of Identity) The perturbation of identity maps, via family of mappings $\{\tau_\epsilon\}_{\epsilon\in[0,\beta]}$ for $\beta > 0$, each current position $x \in \Omega$ to another by $\tau_\epsilon(x)$ for direction $V \in C_c^k(D, \mathbb{R}^d)$ for $k \in \bar{\mathbb{N}}_0$ by*

$$x_\epsilon = \tau_\epsilon(x) = x + \epsilon V(x). \tag{3.2}$$

According to this methodology, we can map the whole domain Ω to another Ω_ϵ such that

$$\Omega_\epsilon = \{x + \epsilon V(x) | x \in \Omega\}. \tag{3.3}$$

Definitions 3.1-3.2 are the ingredients to define a derivative w.r.t. the domain [65, Chapter 9, Section 3.1].

Definition 3.3. *(Eulerian Semi/Shape Derivative) The Eulerian Semi-Derivative*

$$DJ(\Omega)[V] = lim_{\epsilon \to 0^+} \frac{J(\Omega_\epsilon) - J(\Omega)}{\epsilon} \tag{3.4}$$

is the directional derivative of shape functional J at Ω in direction V and in this sense is J called shape differentiable at Ω if for all directions $V \in C_c^k(D, \mathbb{R}^d)$ the Eulerian derivative exists and it holds

$$\left(\mathcal{C}_c^k(D, \mathbb{R}^d)\right)^* \ni G(\Omega) := (V \mapsto DJ(\Omega)[V]), \tag{3.5}$$

i.e. the mapping is an element of the associated dual space.

Remark. Domain D of Definition 3.1 is commonly referred to as hold-all and any set $\Omega \in \mathcal{A}$ as admissible.

Remark. Commonly is the order of regularity explicitly mentioned in the notion of shape differentiability. In this sense, J is called shape differentiable of class C^k. In [65, Chapter 9, Definition 3.4] the vector distribution $G(\Omega)$ in the setting of Definition 3.3 is referred to as the shape gradient, however, we reserve this terminology for the Riesz representative w.r.t. an inner product, for $G(\Omega) \in H^*$ for some Hilbert space H.

The following theorem states that under some regularity assumptions on the boundary of Ω only normal boundary forces have an impact on shape functional $J(\Omega)$, i.e. the support of vector distribution $G(\Omega)$ is contained in Γ.

Theorem 3.4. *(Hadamard-Zolésio Structure Theorem) For a shape differentiable functional J of class C^k with C^{k+1}-boundary Γ, there exists a scalar distribution $g \in \left(C_c^k(\Gamma)\right)^*$ with $\Gamma := \partial\Omega$ such that $G(\Omega) \in C_c^k(D, \mathbb{R}^d)^*$ is given by*

$$G(\Omega) = g(V|_\Gamma \cdot n), \tag{3.6}$$

where we refer to the image of the trace-operator

$$T : C_c^k(\overline{D}, \mathbb{R}^d) \to C_c^k(\Gamma, \mathbb{R}^d), \quad V \mapsto V|_\Gamma. \tag{3.7}$$

Proof. See [172, Theorem 2.27]. □

Remark. The shape derivative still exists for piecewise, smooth domains, however the Hadamard-Zolésio structure theorem does not hold any more. Due to this reason, the shape derivative can also feature tangential forces, e.g. as it can be seen in the discrete setting.

Definition 3.5. *(Boundary Form of Shape Derivative) In the setting of Definition 3.3 the shape derivative can be written in boundary form as*

$$DJ_\Gamma[V] := \int_\Gamma g(V \cdot n)\,\mathrm{d}s \tag{3.8}$$

for $g \in L^1(\Gamma)$.

In the continuous setting we can find an equivalent form [166].

Definition 3.6. *(Volume Form of Shape Derivative) In the setting of Definition 3.3 the shape derivative can be written in volume form as*

$$DJ_\Omega[V] := \int_\Omega \tilde{g}(V)\,\mathrm{d}x. \tag{3.9}$$

for some differential operator $\tilde{g}$ *acting linearly on* V.

Remark. In accordance with the remark to Theorem 3.4 it was observed in [112] that the volume formulation comes with advantage of requiring less regularity on the domain, which is beneficial from the numerical point of view [96]. In the following chapters, we will hence mostly restrict ourselves to the volume formulation of the shape derivative.

Before all, optimizing shapes requires the appropriate definition of spaces in which the deformed domains move, we hereby follow [123].

Definition 3.7. *(Shape Space) For a compact manifold* M *and Riemannian manifold* N *with* $\dim(M) < \dim(N)$ *the shape space is defined to be the space of all submanifolds as*

$$B_e(M,N) := \mathrm{Emb}(M,N) \setminus \mathrm{Diff}(M) \tag{3.10}$$

which represent all embeddings $\mathrm{Emb}(M,N) \subset C^\infty(M,N)$ *of* M *into* N *modulo the group of smooth diffeomorphisms of* M *into itself.*

Remark. In this work we will deal with two-dimensional shapes only, for which the set of all admissible shapes is defined by [122]

$$B_e = B_e(S^1,\mathbb{R}^2) := \mathrm{Emb}(S^1,\mathbb{R}^2) \setminus \mathrm{Diff}(S^1). \tag{3.11}$$

Hence, this space holds all embeddings of the unit sphere in the plane modulo re-parametrizations. A point in B_e is then explicitly characterised by

$$c : S^1 \to \mathbb{R}^2, \theta \mapsto c(\theta), \tag{3.12}$$

where all smooth normal vector fields along c are isomorphic to the tangent space, which forms the two-dimensional counterpart for the general case defined in [28], i.e.

$$T_c B_e = \left\{ h : h = \alpha n, \alpha \in C^\infty(S^1) \right\} \tag{3.13}$$

Remark. In the literature the first Sobolev-metric has proven to be useful in domain perturbations [164], i.e. in the two-dimensional setting we have

$$\begin{aligned} g^1 : T_cB_e \times T_cB_e &\to \mathbb{R} \\ (h,k) &\mapsto \int_{S^1} \langle (\mathbf{I}_2 - A\triangle_c)h, k\rangle \,\mathrm{d}s = \langle (\mathbf{I}_2 - A\triangle_c)h, k\rangle_{L^2(S^1)} \end{aligned} \tag{3.14}$$

for Laplace-Beltrami operator $\triangle_c$ on the surface.
In this setting is the Riemannian shape gradient of a shape functional $J(\Omega)$ w.r.t. the first Sobolev metric g^1 given as [164]

$$\nabla^{g^1} J(\Omega) = qn \qquad (\mathbf{I}_2 - AD_s^2)q = g. \tag{3.15}$$

for g in line with Definition 3.5.

In the next definition we follow [166].

Definition 3.8. *(Steklov-Poincaré Type Metric) For compact, Lipschitz-domain $\Omega \subset D \subset \mathbb{R}^d$ with $\Omega \neq \emptyset$ is the Steklov-Poincaré type metric defined as*

$$\begin{aligned} g^S : H^{1/2}(\Gamma) \times H^{1/2}(\Gamma) &\to \mathbb{R} \\ (h,k) &\mapsto \int_\Gamma h\left[(S^p)^{-1}k\right] \mathrm{d}s \end{aligned} \tag{3.16}$$

for projected Poincaré-Steklov operator

$$S^p : \left(H^{1/2}(\Gamma)\right)^* \to H^{1/2}(\Gamma), \quad h \mapsto T(U)\cdot n \tag{3.17}$$

for $U \in H_0^1(D,\mathbb{R}^d)$ that is solution to

$$a(U,V) = \int_\Gamma h\,[T(V)\cdot n]\,\mathrm{d}s, \quad \forall V \in H_0^1(D,\mathbb{R}^d) \tag{3.18}$$

for symmetric and bilinear form $a : H_0^1(D,\mathbb{R}^d)\times H_0^1(D,\mathbb{R}^d) \to \mathbb{R}$, where $T : H_0^1(D,\mathbb{R}^d) \to H^{1/2}(\Gamma)$ is referred to as the trace-operator of Theorem 2.24.

This metric can be used for gradient calculations.

Definition 3.9. *(Shape Gradient w.r.t. the Steklov-Poincaré metric) For $g \in C^\infty(\Gamma)$ a representation of the shape derivative w.r.t. the Steklov-Poincaré type metric g^S is characterized by*

$$g^S(\phi,h) = (g,\phi)_{L^2(\Gamma)}, \quad \forall \phi \in C^\infty(\Gamma). \tag{3.19}$$

Remark. From equality (3.19) we can see that $h = S^p g = T(U)\cdot n$, where $U \in H_0^1(D,\mathbb{R}^d)$ is a solution to

$$a(U,V) = \int_\Gamma g\,[T(V)\cdot n]\,\mathrm{d}s = DJ_\Gamma[V] = DJ_\Omega[V], \quad \forall V \in H_0^1(D,\mathbb{R}^d). \tag{3.20}$$

The equation above allows the development of a shape optimization algorithm which utilizes the shape derivative in volume form. We will use the weak form of the linear elasticity as symmetric, bilinear form throughout Chapters 4-7. However, we would like to highlight that this not an exclusive option as it can be seen in Section 3.3.

As pointed out in [176] there exist various ways to prove the existence and to derive the shape derivative of (3.4), e.g. the min-max [65] and the chain rule [172] approach such as the methods of rearrangement [100] and of Céa [49] . We orient on [181, Chapter 4] and obtain the shape derivative and its existence for a PDE-constrained shape optimization problem by an application of the theorem in reference [61] in correspondence to the min-max formulation of the Lagrangian in Chapters 4-7. In this setting, we implicitly assume the existence of arising material derivatives, that are introduced shortly [35]. For a material derivative-free approach we once more refer to [176].

Definition 3.10. *(Material Derivative) The material derivative of some scalar function* $p : \Omega \to \mathbb{R}$ *at* $x \in \Omega$ *is defined by the derivative of a composed function* $p_\epsilon \circ \tau_\epsilon : \Omega \to \Omega_\epsilon \to \mathbb{R}$ *for* $p_\epsilon : \Omega_\epsilon \to \mathbb{R}$ *as*

$$D_m p(x) := \lim_{\epsilon \to 0^+} \frac{p_\epsilon \circ \tau_\epsilon(x) - p(x)}{\epsilon} = \frac{d}{d\epsilon}(p_\epsilon \circ \tau_\epsilon)(x)\big|_{\epsilon=0^+}. \tag{3.21}$$

By using this definition, the shape derivative, for a scalar p and a vector-valued P, for which the material derivative, is applied component-wise, can be stated as

Definition 3.11. *The shape derivative of a generic and differentiable scalar function* $p : \Omega \to \mathbb{R}$ *and vector-valued* $P : \Omega \to \mathbb{R}^d$ *is defined as*

$$Dp[V] := D_m p - V^T \nabla p, \tag{3.22}$$

$$DP[V] := D_m P - V^T \nabla P. \tag{3.23}$$

Remark. The distinction in the definition above is that ∇p is the gradient of a scalar and ∇P is the tensor derivative of a vector. In the following, we will interchangeably use the abbreviation $\dot{p}$ and $\dot{P}$ to mark the material derivative of p and P.

In Chapters 4-8 we will need to have the following calculation rules on board [35].

Lemma 3.12. *(Calculation Rules Material Derivative) For a generic scalar function* $p : \Omega \to \mathbb{R}$ *and vector-valued* $P : \Omega \to \mathbb{R}^d$ *the following rules hold*

$$D_m(pq) = D_m pq + pD_m q \tag{3.24}$$

$$D_m \nabla p = \nabla D_m p - \nabla V^T \nabla p \tag{3.25}$$

$$D_m \nabla P = \nabla D_m P - \nabla V^T \nabla P \tag{3.26}$$

$$D_m(\nabla q^T \nabla p) = \nabla D_m p^T \nabla q - \nabla q^T (\nabla V + \nabla V^T) \nabla p + \nabla p^T \nabla D_m q. \tag{3.27}$$

Proof. The proof can be extracted from [35]. □

In addition, the basic idea in the proof of the shape derivative in the next section will be to pull back each integral defined on the on the transformed field back to the original configuration. We therefore need to state a rule for differentiating domain integrals.

Lemma 3.13. *(Differentiating Domain Integrals) In the setting of Definition 3.10 the rule for differentiating domain integrals states as*

$$\frac{d}{d\epsilon}\left(\int_{\Omega_\epsilon} p_\epsilon \,\mathrm{d}x_\epsilon\right)\Big|_{\epsilon=0^+} = \int_\Omega (D_m p + \nabla \cdot Vp)\,\mathrm{d}x. \tag{3.28}$$

Proof. For the proof we refer to [35]. □

For boundary integrals the following useful formula is needed [65, Chapter 9, Section 5.5].

Lemma 3.14. *(Tangential Green Formula) In the setting of Definition 3.10 the tangential Green formula can be stated for $d > 1$ as*

$$\int_\Gamma \kappa_m p(V \cdot n)\,\mathrm{d}s = \int_\Gamma (p\,\mathrm{div}_\Gamma(V) + \nabla_\Gamma p \cdot V)\,\mathrm{d}s \tag{3.29}$$

for additive curvature obtained from the mean curvature

$$\kappa_m := \mathrm{div}_\Gamma(n), \tag{3.30}$$

where

$$\mathrm{div}_\Gamma(V) := \mathrm{div}(V) - \left(\frac{\partial V}{\partial n}, n\right) \tag{3.31}$$

and

$$\nabla_\Gamma p := \nabla p - (\nabla p, n)n. \tag{3.32}$$

Proof. The result is obtained in [65, Chapter 9, Section 5.5]. □

So far, all presented techniques for optimization were stated in a continuous, infinite-dimensional setting, i.e. derivative calculations are preceding the actual implementation. However, reversing the order requires the investigation of a finite-dimensional setting under limited regularity depending on the chosen discretization. In general, one refers to the respective case via its sequence of events and hence to either the differentiate-then-discretize or alternatively the discretize-then-differentiate or simply the continuous and discrete approach. For shape optimization many results from the continuous carry over canonically to the discretized setting, starting from a discrete counterpart of the perturbation of identity of Definition 3.2 for a mesh as in Definition 2.33 [35].

Definition 3.15. *(Discretized Perturbation of Identity) The perturbation of identity w.r.t. a single vertex perturbation $\delta x_l \in \mathbb{R}^d$ for vertices $l \in \{1, ..., L\}$ is defined for points on $x \in \Omega$ and $x_\epsilon \in \Omega_\epsilon$ as*

$$\begin{aligned} x_\epsilon &= \tau_\epsilon(x) \\ &= x + \epsilon \delta x_l N_l^1(x) \\ &= x + \epsilon V_l(x), \end{aligned} \tag{3.33}$$

where N_l^1 are Lagrange ansatz functions of first-order for continuous piecewise-linear polynomials in accordance with the remark to Definition 2.31.

Remark. The ultimate position $x_\epsilon \in \Omega_\epsilon$ can be calculated using summed vertex contributions, i.e.

$$x_\epsilon = x + \epsilon \sum_{l=1}^{L} \delta x_l N_l^1(x). \tag{3.34}$$

The discretized perturbation of identity interpolates the deformation $\epsilon \delta x_l$ of vertex $l \in \{1, ..., L\}$ on the support of N_l^1.

Remark. The central role of the Hadamard-Zolésio structure theorem 3.4 is mitigated in the discrete setting, since a pass from volume forms of the shape derivative (3.9) to the needed boundary form (3.8) is not available due to the limited regularity of domain and discrete solution variables [65, p. 562].

As pictured before, mesh-based approaches naturally offer themselves for practical computations. However, it should also not be concealed, that Definition 3.10 applied to PDEs of Definition 2.6, opens the door to a whole range of fundamentally different numerical techniques, as it builds the bridge between mesh-based discretizations in the so-called Eulerian framework, confer Section 2.3.1 for representatives, and meshfree discretizations in the so-called Lagrangian framework [111, Chapter 1]. We will investigate continuous shape derivatives arising from an Eulerian flow field formulation in Chapters 4-7 and turn towards discrete shape derivatives for a Lagrangian flow field formulation in Chapter 8. In Figure 3.1 the distinct paths, that are taken throughout this thesis, are visualized.

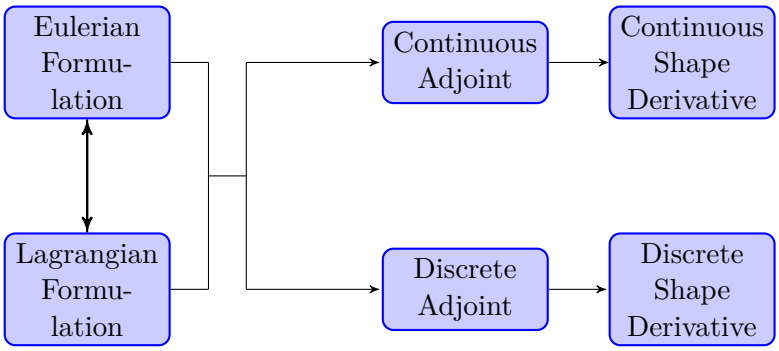

Figure 3.1: Optimization Strategies

3.2 Basics of Topology Optimization

In this section we briefly describe the basics of topology optimization following the monograph [136], which builds up on [171, 83] that firstly introduced a mathematical framework for topological perturbations.

Definition 3.16. *(Topological Perturbation) For an arbitrary point $x \in \Omega \subset D \subset \mathbb{R}^d$ we define a topological perturbation as the region of size $\epsilon > 0$ for open, bounded and*

connected $w \subset \mathbb{R}^d$ *with* $0 \in w$ *, i.e.*

$$w_\epsilon(x) = x + \epsilon w \subset \Omega. \tag{3.35}$$

In this sense we obtain a perturbed domain $\Omega_\epsilon = \Omega \setminus \overline{w_\epsilon}$ with boundary $\partial\Omega_\epsilon = \partial\Omega \cup \partial w_\epsilon$.

Definition 3.17. *(Topological Derivative) Consider a shape functional as in Definition 3.1, then for asymptotic expansion*

$$J(\Omega_\epsilon) = J(\Omega) + f(\epsilon) D_T J(\Omega)(x) + o(f(\epsilon)), \tag{3.36}$$

with $f : \mathbb{R}^+ \to \mathbb{R}^+$ *and* $\lim_{\epsilon \to 0} f(\epsilon) = 0$ *we call the mapping*

$$x \mapsto D_T J(\Omega)(x) \tag{3.37}$$

the topological derivative of shape functional $J(\Omega)$ *at* $x \in \Omega$.

Remark. As an alternative to Definition 3.17, we can define the topological derivative by

$$D_T J(\Omega)(x) = \lim_{\epsilon \to 0^+} \frac{J(\Omega_\epsilon) - J(\Omega)}{f(\epsilon)}, \tag{3.38}$$

which follows immediately from a rearrangement in Definition 3.17.

Remark. Commonly in the literature and in computations of Chapter 4, the topological perturbation is defined as a ball $B_\epsilon(x)$ with centre point $x \in \Omega$ for radius $\epsilon > 0$.

Topological sensitivity analyses have been performed via various method, e.g. in [83, 137] the domain truncation method, while in [11] the generalized Lagrangian method is used. Frequently derivatives rely on computations that exploit the relation between shape and topological derivative [136, Proposition 1.1].

Theorem 3.18. *In the setting of Definition 3.17 the topological derivative can be obtained via the topological shape sensitivity method as*

$$D_T J(\Omega)(x) = \lim_{\epsilon \to 0} \left[\frac{1}{f'(\epsilon)} \frac{d}{d\epsilon} J(\Omega_\epsilon) \right]. \tag{3.39}$$

Proof. We refer to [136, Proposition 1.1], where it is observed, that differentiating (3.36) for ϵ leads to

$$\frac{d}{d\epsilon} J(\Omega_\epsilon) = f'(\epsilon) D_T J(\Omega)(x) + \mathcal{R}'(f(\Omega_\epsilon)) f'(\epsilon) \tag{3.40}$$

for $\mathcal{R}(f(\epsilon)) := o(f(\epsilon))$ such that (3.39) follows from rearrangements for chosen $f'(\epsilon)$ such that $0 < D_T J(\Omega)(x) < \infty$ and $\mathcal{R}'(f(\epsilon)) \to 0$, if $\epsilon \to 0$. □

Most practical applications and all treated examples in this work rely on PDE-constrained shape functionals. Obviously, this reinforces the significance of boundary conditions. We refer to [9], which provides a nice overview of Dirichlet, Neumann and transmissive conditions elaborated for elliptic PDEs. In Chapter 4 we examine the latter for a Helmholtz scattering problem for the inclusion and exclusion of holes via perturbed domain

$$\Omega_\epsilon(x) = \begin{cases} \Omega \setminus \overline{w_\epsilon}(x) & \text{if } x \in \Omega \\ \Omega \cup w_\epsilon(x) & \text{if } x \in D \setminus \Omega. \end{cases} \tag{3.41}$$

3.3 Numerical Methods for Domain Perturbations

In this section we will investigate numerical methods for shape and topology optimization, that have proven to be useful within the last decades. Introduced approaches form the basis for numerical investigations of shape optimization for different wave specifications in Chapters 4-8.

3.3.1 Shape Optimization Based on the Volume Form

In the following we present, without the claim for completeness, a brief overview on numerical methods, that utilize the volume form of the shape derivative (3.9). In this light, we have stated in the remark to Definition 3.9 that Steklov-Poincaré type metrics allow us to make use of the shape derivative in volume form for gradient computations in the form of (3.20). Furthermore, we mention here the recent work regarding the p-Laplacian for $p > 2$, that comes with the advantage of the ability to resolve optimal shapes with sharp corners [131]. However, in the following we present two competing approaches for discrete mesh deformations, that consider the weak form of the linear elasticity equation as the symmetric bilinear form [71, 166]. A numerical comparison of both techniques w.r.t. run times can be taken from the end of this section. We will decide in favour of one method based on this analysis for the rest of the thesis.

Deformations Based on Steklov-Poincaré Type Metrics

Following [71] we denote the elasticity operator, which is to be specified in Chapter 4, as $E : H^1(\Omega)^d \to (H^1(\Omega)^d)^*$. According to update formula (3.20) the negative shape gradient is obtained as Riesz-representative and alternatively via the following optimization problem

$$\min_{V \in H^1(\Omega)^d} DJ(\Omega)[V] + \frac{1}{2}\langle EV, V\rangle. \tag{3.42}$$

In the continuous setting the shape derivative, due Theorem 3.4, consists of normal boundary forces only. However, in the discretized setting, this reasoning is not available

due to the lack of regularity of domain and finite element solutions. In reference [166] the projection $p : W_h \to W_h$ is proposed

$$p(V_h(x)) = \begin{cases} V_h(x) & \text{if } x \in \text{supp}(\Gamma_h) \\ 0 & \text{else,} \end{cases} \tag{3.43}$$

where we for clarity denote an H^1-conformal finite element space by W_h with $m = d$ in (2.78). Instead of solving (3.42), the task is then to find $V_h \in W_h$ for canonically discretized operators

$$E_h V_h = -DJ_h(\Omega, p(\tilde{V}_h)) \quad \forall \tilde{V}_h \in W_h. \tag{3.44}$$

The straightforward discrete counterpart to the property of Theorem 3.4 is to enforce it explicitly for solution of optimization problem (3.42) [71]. In this sense, the normal force operator $N : L^2(\Gamma) \to (H^1(\Omega)^d)^*$ can be used to restrict the solution of (3.42) to be on the boundary by

$$\langle Nf, V \rangle = \int_\Gamma f(V \cdot n) \, \mathrm{d}s \tag{3.45}$$

for all $f \in L^2(\Gamma)$ such that

$$\begin{aligned} \min_{V \in H^1(\Omega)^d, f \in L^2(\Gamma)} & DJ(\Omega)[V] + \frac{1}{2}\langle EV, V \rangle \\ \text{s.t. } & EV - Nf = 0. \end{aligned} \tag{3.46}$$

For this problem necessary and sufficient optimality conditions are obtained for (3.46), introducing Lagrange-multiplier $\Pi \in H^1(\Omega)^d$ as [71]

$$\begin{pmatrix} E & 0 & E \\ 0 & 0 & -N^{ad} \\ E & -N & 0 \end{pmatrix} \begin{pmatrix} V \\ f \\ \Pi \end{pmatrix} = \begin{pmatrix} -DJ(\Omega)[\cdot] \\ 0 \\ 0 \end{pmatrix} \tag{3.47}$$

for adjoint $N^{ad} : H^1(\Omega)^d \to L^2(\Gamma)$, which is canonically discretized in appropriate finite element approximation spaces.

Remark. In [71] it was stated that (3.44) may in contrast to the solution of (3.47) not lead to a descent direction due to spurious tangential movements. In addition, it was stated that (3.44) can be computed faster than (3.47), since it results in a smaller linear system. We will analyze this aspect in the following numerically.

Numerical Comparison

We compare both approaches on a uniform circle for an increasing number of vertices and elements for the minimization of a domain-dependent shape functional, constrained to the solution of a reaction-diffusion PDE from Definition 2.38 with Dirichlet boundaries.

The comparison is done based on the GitHub source[1] provided by [71]. The discs are constructed using the build-in FEniCS class UnitDiscMesh, which returns unit circles with $1 + 3n(n + 1)$ vertices and $6n^2$ elements. In Figure 3.2 exemplifying meshes are displayed for $n \in \{2, 4, 8, 20\}$.

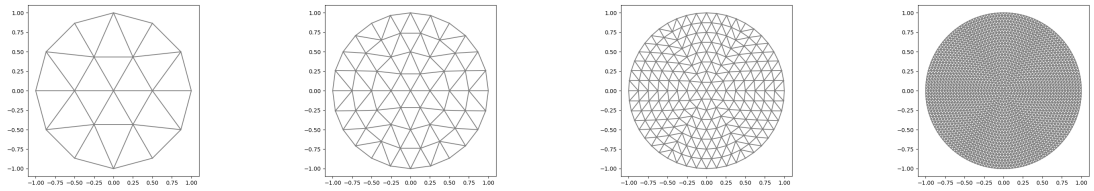

(a) $n = 2$ (b) $n = 4$ (c) $n = 8$ (d) $n = 20$

Figure 3.2: Uniform Circles

(a) Size of Linear System (b) Solution Time for $n \in \{1, ..., 22\}$

Figure 3.3: Numerical Comparison

The difference between the two graphs on the left figure in Figure 3.3 comes from the additional normal force projection in (3.47). Hence, the system is increasing by the number of exterior nodes. In addition, it is observed in the right part of Figure 3.3 that the required time for solving the block system in (3.47) is nearly doubled for this specific problem for 2000 vertices compared to the system (3.44).

Remark. In practice is the number of exterior nodes frequently increased in order to obtain a higher resolution at the variable boundary or interface, we underline that this only increases effects in Figure 3.3, where uniform meshes as in Figure 3.2 have been investigated.
An algorithm for shape optimization based e.g. on a gradient descent scheme, as we will see in the following, requires multiple solutions to either (3.44) or (3.47), such that observations intensify. Since we will work with meshes of an increased amount of vertices, we advocate for the use of (3.44) in this work.

[1] https://github.com/gerw/restricted_mesh_deformations

3.3.2 Shape & Topology Optimization Based on the Boundary Form

This section will investigate shape and topology perturbations that rely on the boundary form of the shape derivative (3.8). As we have already seen in Section 3.1, the first Sobolev metric in conjunction with the Laplace-Beltrami operator can be used for mesh deformations [164]. In this section we introduce an alternative technique, based on the level-set method (LSM) [142], which was firstly remodelled for shape optimization in [141, 5] and is advantageous in resolving and merging complex structures. The technique offers itself for the exploitation of the topological derivative of Definition 3.17 for the additional creation of holes in the calculation domain as firstly demonstrated in [41]. As this approach leads to unstable results [41], we introduce an alternative developed in [12] to overcome some of the weaknesses. The latter approach is also used in the numerical section of Chapter 4.

Basics of LSM

This section forms the basis for the LSM, which is refactored for the application to shape and topology optimization and builds up on the domain description that was introduced in Theorem 2.13. In this setting, the classical update scheme for the level-set is obtained introducing and differentiating w.r.t a pseudo-time $t \in (0,T)$ such as using the definition of the exterior normal, which yields a form of the general Hamilton-Jacobi equation [72, Chapter 10].

Definition 3.19. *(Hamilton-Jacobi) The evolution of the level-set function is given by the solution to the so-called Hamilton-Jacobi equation as*

$$\frac{\partial \xi}{\partial t} + H(\nabla \xi, x) = 0 \quad \text{in } \Omega \times (0,T) \tag{3.48}$$

for Hamiltonian $H : \mathbb{R}^d \times \Omega \to \mathbb{R}$ *given as* $H(\nabla\xi, x) = s|\nabla\xi|$ *for* $s : \Omega \times (0,T) \to \mathbb{R}$.

Remark. Using Definition 3.19 for the propagation may lead to numerical instabilities [5]. Commonly, this is countered by the addition of artificial viscosity as introduced in Section 2.3.3 for $\mu > 0$, i.e.

$$\frac{\partial \xi}{\partial t} + s|\nabla\xi| - \mu\Delta\xi = 0 \quad \text{in } \Omega \times (0,T) \tag{3.49}$$

and more frequently by reinitialization

$$\frac{\partial \xi}{\partial t} + \operatorname{sgn}(\xi)\left(|\nabla\xi| - 1\right) = 0 \quad \text{in } \Omega \times (0,T). \tag{3.50}$$

LSM in Shape & Topology Optimization

As a consequence of the Hadamard-Zolésio theorem the shape derivative consists of normal boundary forces only, which provides us with a valid descent direction of first order, if $V = -gn$. Since we have by Taylor-expansion

$$J(\Omega_\epsilon) = J(\Omega) + \epsilon DJ(\Omega)[V] + o(\epsilon) = J(\Omega) - \epsilon \int_\Gamma g^2 \,\mathrm{d}s + o(\epsilon). \tag{3.51}$$

Hence, the Hamilton-Jacobi equation from Definition 3.19 is redefined for shape optimization as in [5] via the boundary form of the shape derivative.

Definition 3.20. *(Hamilton-Jacobi Propagation for Shape Optimization) The Hamilton-Jacobi equation in shape optimization is defined as*

$$\frac{\partial \xi}{\partial t} - g|\nabla \xi| = 0 \quad \text{in } \Omega \times (0,T) \tag{3.52}$$

for extension of g in terms of (3.8) on the space-time cylinder $\Omega \times (0,T)$.

In [41] Definition 3.20 is extended for the insertion of holes utilizing the topological derivative from Definition 3.17.

Definition 3.21. *(Hamilton-Jacobi Propagation for Shape & Topology Optimization) The Hamilton-Jacobi equation in shape and topology optimization defines as*

$$\frac{\partial \xi}{\partial t} - g|\nabla \xi| - wD_T J(\Omega) = 0 \quad \text{in } \Omega \times (0,T) \tag{3.53}$$

for given weight $w \geq 0$.

Remark. The convergence in using Definition 3.21 is strongly weight-dependent. In [41] it was shown that large choices may lead to steep level sets, while small choices may lead to small oscillations and the creation of new holes.

LSM for the Generalized Topological Derivative In the following we present an algorithm that circumvents the drawbacks above, following [12]. It is used in Chapter 4 to perform topology optimization for the mitigation of coastal erosion and is based on resigning the topological derivative on different parts of the domain.

Definition 3.22. *(Generalized Toplogical Derivative) We define the generalized topological derivative as*

$$\tilde{g}(x) := \begin{cases} -D_T J(\Omega)(x) & \text{if } x \in \Omega \\ D_T J(\Omega)(x) & \text{if } x \in D \setminus \Omega. \end{cases} \tag{3.54}$$

Definition 3.23. *(Local Minimality Conditions) Necessary local minimality conditions are given by*

$$\begin{cases} \tilde{g}(x) \leq 0 & \text{if } x \in \Omega \\ \tilde{g}(x) \geq 0 & \text{if } x \in D \setminus \Omega \end{cases} \tag{3.55}$$

and sufficient local minimality conditions as

$$\begin{cases} \tilde{g}(x) < 0 & \text{if } x \in \Omega \\ \tilde{g}(x) > 0 & \text{if } x \in D \setminus \Omega. \end{cases} \tag{3.56}$$

From these optimality conditions in accordance with Definition 2.13, we can conclude the existence of $\tau > 0$ such that $\tilde{g} = \tau\xi$, which provides us with the following level-set update scheme [12].

Definition 3.24. *(Orthogonal Projection Propagation in Topology Optimization) The orthogonal projection propagation equation in topology optimization is defined as*

$$\frac{\partial \xi}{\partial t} - p_{\xi^\perp}(\tilde{g}) = 0 \qquad in\ \Omega \times (0,T) \tag{3.57}$$

for orthogonal projection operator on the orthogonal complement of ξ, i.e.

$$p_{\xi^\perp}(\tilde{g}) = \tilde{g} - \frac{(\tilde{g},\xi)_{L^2(D)}}{||\xi||^2_{L^2(D)}}\xi. \tag{3.58}$$

Remark. Discretizations are based on the solution to evolution equation (3.57) for an Euler scheme on the sphere, which is given for angle $\psi_i \in [0,\theta_i]$ with

$$\theta_i = \arccos\left[\frac{(\tilde{g}_i,\xi_i)_{L^2(D)}}{||\tilde{g}_i||_{L^2(D)}}\right] \tag{3.59}$$

as [12]

$$\xi_{i+1} = \cos\psi_i\xi_i + \sin\xi_i\frac{p_{\xi_i^\perp}(\tilde{g}_i)}{||p_{\xi_i^\perp}(\tilde{g}_i)||_{L^2(D)}} \tag{3.60}$$

such that a change of variables $\psi_i = \rho_i\theta_i$ gives the update formula

$$\xi_{i+1} = \frac{1}{\sin\theta_i}\left[\sin((1-\rho_{step,i})\theta_i)\xi_i + \sin(\kappa_i\theta_i)\frac{\tilde{g}_i}{||\tilde{g}_i||_{L^2(D)}}\right], \tag{3.61}$$

where $\rho_{step,i}$ is a line-search parameter for the respective iteration.

Chapter 4

Shape & Topology Optimization for Helmholtz Scattering

This chapter serves as a simple entrance into the application of shape and topology optimization for the mitigation of coastal erosion. We hereby obtain a PDE-constrained optimization problem by constraining an objective of tracking type [63, Section 1.1] to the solution of a time-harmonic, elliptic PDE - the Helmholtz equation in the form of a scattering problem. We would like to highlight that this builds an extension to [127], who relied on a fixed parametrization during optimization and to [105], where a level-set method for shape optimization is used as described in Section 3.3.2.
The chapter is structured as follows: In Section 4.1 we formulate the Helmholtz PDE in a wave propagation setting, which is subsequently put as a constraint to an appropriate objective in Section 4.2 to obtain a PDE-constrained optimization problem. In Section 4.3 we will derive the necessary tools to solve this problem, by deriving the adjoint equation, the shape derivative in volume form and boundary form such as the topological derivative. The final part, Section 4.4, will then use the obtained shape derivative for firstly a simplified mesh and secondly a realistic mesh, picturing the Langue de Barbarie, that was part of the introductory example in Section 1.1. These investigations will be followed by applications for topology optimization that are based on the algorithm that was presented in Section 3.3.2 following [12].

4.1 PDE Derivation

In [36] Juri Berkhoff derived the mild-slope equation, that serves as a simplistic time-harmonic wave propagation model, starting from a refraction-diffraction equation and the subsequent application of depth-integration.

Definition 4.1. *(Mild-Slope Equation) The mild-slope equation is defined as*

$$\nabla \left(C C_g \nabla \hat{u} \right) + \omega^2 \frac{C_g}{C} \hat{u} = 0 \quad \text{on } \Omega, \tag{4.1}$$

for complex potential function $\hat{u} : \Omega \to \mathbb{C}$*, angular frequency* $\omega \in \mathbb{R}$*, local phase* $C \in \mathbb{R}$ *and group velocities* $C_g \in \mathbb{R}$ *of the wave field.*

To equation (4.1) the Radder-transformation [149] as $u = \hat{u}\sqrt{CC_g}$ can be applied, which leads us to

$$\nabla^2 u + k_C^2 u = 0, \tag{4.2}$$

where the effective wave number is defined by

$$k_C^2 = k^2 - \frac{\nabla^2 \left(\sqrt{CC_g}\right)}{\sqrt{CC_g}} \tag{4.3}$$

for wave number $k \in \mathbb{R}$ which is the root of the dispersion relation

$$\omega^2 = gk \tanh(kH) \tag{4.4}$$

for local water height H and gravitational acceleration g. The phase and group velocities are defined as $C = \frac{\omega}{k}$ and $C_g = \frac{\partial \omega}{\partial k}$. In harbors and in general shallow water we assume

$$k^2 := \frac{\omega^2}{gH}, \qquad C = C_g := \sqrt{gH}, \qquad k_C^2 := \frac{\omega^2}{gH} - \frac{\nabla^2 H}{2H} + \frac{|\nabla H|^2}{4H^2} \tag{4.5}$$

and we can approximate k_c by k if

$$|\nabla^2 H| \ll \frac{2\omega^2}{g}, \qquad |\nabla H|^2 \ll \frac{4\omega^2 H}{g} \tag{4.6}$$

implying a slowly varying depth or high frequencies, which provides us with the elliptic Helmholtz equation in known form.

Definition 4.2. *(Helmholtz Equation) The Helmholtz equation is defined as*

$$\nabla^2 u + k^2 u = 0 \quad \text{on } \Omega, \tag{4.7}$$

for complex solution variable $u : \Omega \to \mathbb{C}$ *and wave number* $k \in \mathbb{R}$*.*

4.2 Model Formulation

Suppose we are given an open domain $\tilde{\Omega} \subset \mathbb{R}^2$, which is split into the disjoint sets $\Omega, D \subset \tilde{\Omega}$ such that $\Omega \cup D \cup \Gamma_5 = \tilde{\Omega}$, $\Gamma_1 \cup \Gamma_2 \cup \Gamma_3 \cup \Gamma_4 = \partial\tilde{\Omega}$ and $\Gamma_1 \cup \Gamma_2 \cup \Gamma_3 \cup \Gamma_4 \cup \Gamma_5 := \Gamma$. In this setting we assume the variable, interior Γ_5 and the fixed outer boundary $\partial\tilde{\Omega}$ to be at least Lipschitz, i.e. with $C^{0,1}$-boundary. One simple example of such kind is visualized below in Figure 4.1. We interpret Γ_1 as coastline, Γ_2 and Γ_3 as lateral sea, Γ_4 as open sea and Γ_5 as obstacle boundary. On the illustrative domain we model water waves by the complex solution field to the stationary, elliptic Helmholtz equation from Definition

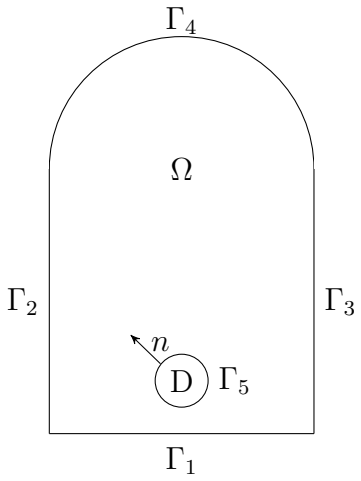

Figure 4.1: Illustrative Domain with Initial Circled Obstacle

4.2, alongside suitable boundary conditions that are detailed below. The complexity is introduced for a total field $u := u_{\text{inc}} + u_{\text{sc}}$, consisting of a given incoming wave, i.e.

$$u_{\text{inc}} : \Omega \to \mathbb{C}, \quad x \mapsto A \exp(ikx \cdot d_\delta) \tag{4.8}$$

for amplitude or maximal surface elevation $A > 0$ and wave direction $d_\delta = (\cos\delta, \sin\delta)$ for $\delta \in \mathbb{R}$ such as a scattered wave $u_{\text{sc}} : \Omega \to \mathbb{C}$.
In the course of this chapter we will also deal with a second problem, placing a transmissive obstacle D in $\tilde{\Omega}$ for porosity coefficient $\phi \in (0, 1]$, e.g. interpreted as geotextile tube [128]. Due to this reason, we firstly modify the problem such that we are solving for two distinct wave fields on Ω and D (cf. to [144]), i.e.

$$-\nabla^2 u - k^2 u = 0 \qquad \text{on } \Omega \tag{4.9}$$

$$-\nabla^2 s - k^2 s = 0 \qquad \text{on } D \tag{4.10}$$

for transmission boundaries

$$\begin{aligned} u &= s && \text{on } \Gamma_5 \\ \frac{\partial u}{\partial n} &= \phi \frac{\partial s}{\partial n} && \text{on } \Gamma_5. \end{aligned} \tag{4.11}$$

The two wave descriptions can be rewritten as a single equation by the usage of a discontinuous transmission coefficient

$$\phi := \begin{cases} \phi_1, & \text{if } x \in \Omega \\ \phi_2, & \text{if } x \in D \end{cases} \tag{4.12}$$

with interface boundary conditions in the sense of (4.11) as

$$\begin{aligned} [\![u]\!] &= 0 \\ [\![\phi \frac{\partial u}{\partial n}]\!] &= 0. \end{aligned} \tag{4.13}$$

Remark. The latter approach requires calculations on $\tilde{\Omega}$, such that we can write integrals as

$$\int_{\tilde{\Omega}} := \int_{\Omega} + \int_{D} \tag{4.14}$$

In what follows, we assume this decomposition, whenever dealing with the transmissive case.

Remark. The PDE-constrained optimization problem, especially proposed boundary conditions, are mainly taken from [127]. However, we will investigate the problem in a shape and topology optimization setting not relying on a finite design space but on shape calculus. In the following, we elaborate on the individual components.

Remark. For clarity, in Chapter 3 and in most literature [172, 65] the letter $D \subset \mathbb{R}^d$ is reserved for the hold-all domain which accommodates admissible shapes $\Omega \in \mathcal{A}$. In this chapter and in the following it represents the deformable obstacle, which moves within $\tilde{\Omega} \subset \mathbb{R}^2$. In this light, shape space considerations of Section 3.1 apply to the boundary or interface of obstacle D.

Sommerfeld Radiation Condition

The model is equipped with an open or non-reflecting boundary at sea level in form of a Sommerfeld radiation condition, ensuring the well-posedness of the problem in the sense of Hadamard [72, Section 1.3.1.] by demanding that scattered waves are not reflected at an infinite boundary [162], i.e.

$$\begin{aligned} \lim_{r\to\infty} r^{1/2}\left(\frac{\partial u_{\text{sc}}}{\partial r} - iku_{\text{sc}}\right) = 0 \\ r = |x|. \end{aligned} \tag{4.15}$$

Since being restricted to a finite domain, the condition is first-order approximated on Γ_4 as [127]

$$\frac{\partial u - u_{\text{inc}}}{\partial n} - ik(u - u_{\text{inc}}) = 0, \tag{4.16}$$

where due to the half circle boundary it holds that $\frac{\partial}{\partial r} = \frac{\partial}{\partial n}$ for radial distance r.

Remark. For a more comprehensive view on non-reflecting wave propagation a second order approximation [168] or a "perfectly matched layer" [31] could be used. However, effects of latter are hard to capture in a differentiate-then-discretize setting.

Partially Absorbing Boundary Condition

We assume partial reflection of the waves at the coast Γ_1 and at the obstacle Γ_5, i.e. [37, Section 3.2]

$$\frac{\partial u}{\partial n} + k\alpha u = 0, \tag{4.17}$$

where $\alpha = \alpha_0 + i\alpha_1 \in \mathbb{C}$ represents a complex transmission coefficient.

Remark. The general solution was derived as [37, Section 3.2]

$$\begin{aligned} \alpha_0 &= \frac{2K \sin\beta \cos\gamma}{1 + K^2 + 2K\cos\beta} \\ \alpha_1 &= \frac{(1 - K^2)\cos\gamma}{1 + K^2 + 2K\cos\beta} \end{aligned} \tag{4.18}$$

with reflection coefficient $K \in \mathbb{R}$, that is the ratio between reflected and incident wave height, reflection phase angle β and the incident wave angle with the boundary normal γ.
The choice of α is a priori a rocky question as it needs to incorporate the angles of the incoming such as already scattered waves. Since the preceding formulation is based on the assumption that the transmission coefficient is known for all parts of the boundary, we follow [99] for simplification and set $\gamma = 0$ and $\beta = 0$, which leads for (4.18) to

$$\begin{aligned} \alpha_0 &= 0 \\ \alpha_1 &= \frac{1 - K}{1 + K}. \end{aligned} \tag{4.19}$$

In [127, 105] the simple case for full reflection, i.e. $K = 1, \beta = \gamma = 0$ and hence $\alpha = 0$ is considered such that (4.17) reduces to $\frac{\partial u}{\partial n} = 0$. This is commonly referred to as sound-hard scattering [59, Section 1.1], implying

$$\frac{\partial u_{\text{inc}}}{\partial n} = -\frac{\partial u_{\text{sc}}}{\partial n}. \tag{4.20}$$

This assumption simplifies not only the calculation for the field but also for the shape derivative, as we will see in Section 4.3, at the cost of potentially inaccurate reflections at respective boundaries.
Frequently, obstacle problems with Dirichlet boundary conditions are investigated, which are referred to as sound-soft scattering [59, Section 3.2]. We will restrict ourselves to the sound-hard case and otherwise refer to [75].

Periodic Boundary Condition

Periodic boundary conditions are placed on lateral boundaries Γ_2 and Γ_3 as

$$u_{|\Gamma_2} = u_{|\Gamma_3}. \tag{4.21}$$

Remark. These conditions allow to significantly reduce the computational domain size, e.g. instead of modeling the whole coastline, it allows the field calculation for a reduced domain assuming periodic reproducibility along the shore.

Objective Function

We primarily aim for minimization of a tracking-type objective [63, Section 1.1]. Hence, we define the objective $J_{1|2} : \Omega \to \mathbb{R}$ to be

i) for single direction and frequency as:

$$J_1(\Omega) = \nu_1 ||u - \bar{u}||^2_{L^2_{\mathbb{R}}(\Gamma_1)} \tag{4.22}$$

for target height $\bar{u} \in L^2_{\mathbb{R}}(\Gamma_1)$.

ii) for multiple directions $\{d_{\delta_j}\}_{1\leq j\leq N}$ with different weights $\{w_j\}_{1\leq j\leq N}$ each for different wave numbers $\{k_i\}_{1\leq i\leq M}$ as:

$$J_2(\Omega) = \sum_{i,j=1}^{M,N} w_j J_{k_i,\delta_j}(\Omega). \tag{4.23}$$

In either case, to ensure that the obstacle is not becoming arbitrarily large we add a volume penalty controlled by $\nu_3 \geq 0$, i.e.

$$J_3(\Omega) = -\nu_3 \int_\Omega 1 \, \mathrm{d}x \tag{4.24}$$

or alternatively in the transmissive setting as

$$J_3(\Omega) = \nu_3 \int_D 1 \, \mathrm{d}x \tag{4.25}$$

such as a perimeter regularization

$$J_4(\Omega) = \nu_4 \int_{\Gamma_5} 1 \, \mathrm{d}s. \tag{4.26}$$

The total objective then reads as

$$J(\Omega) = J_{1|2}(\Omega) + J_3(\Omega) + J_4(\Omega). \tag{4.27}$$

Remark. In (4.22) and in what follows, we follow [105] and define in terms of the real part

$$(f,g)_{L^2_{\mathbb{R}}(\Omega)} := \Re(f,g)_{L^2_{\mathbb{C}(\Omega)}} := \Re(f,\bar{g})_{L^2(\Omega)}. \tag{4.28}$$

Defining the inner product as in (4.28) is beneficial for numerical implementations, as described in Section 4.4, since relying on the plain $L^2(\Omega)$-product would lead to mixed spaces that are cumbersome to model.

Remark. The volume penalization could also be replaced by geometrical constraint to meet a certain voluminous value, e.g. the initial size of the obstacle

$$\int_\Omega 1 \, \mathrm{d}x = \mathrm{vol}(\Omega) = \mathrm{vol}(\Omega_0) = \int_{\Omega_0} 1 \, \mathrm{d}x.$$

In Section 4.5 we refer to this alternative.

4.3 Adjoint-Based Shape & Topology Optimization

We reformulate the constrained optimization problem of the preceding section with the help of the Lagrangian

$$\mathcal{L}(\Omega, u, v, v_1, v_2, v_3) = J_1(\Omega) + a(\Omega; u, v, v_1, v_2, v_3) - l(\Omega; v_3), \tag{4.29}$$

where $J_1(\Omega)$ is the objective (4.22) and the boundary value problem (4.7) with (4.21)-(4.17) is written in weak form, i.e.

$$a(\Omega; u, v, v_1, v_2, v_3) = l(\Omega, v_3), \quad \forall v \in H^1(\Omega) \tag{4.30}$$

and for all $v_1, v_2, v_3 \in H^{1/2}(\Gamma)$. In this equation $a(\Omega; u, v, v_1, v_2, v_3)$ defines the bilinear form

$$\begin{aligned} a(\Omega; u, v, v_1, v_2, v_3) =& (\nabla u, \nabla v)_{L^2_{\mathbb{R}}(\Omega)} - k^2 (u, v)_{L^2_{\mathbb{R}}(\Omega)} - \Big(\frac{\partial u}{\partial n}, v\Big)_{L^2_{\mathbb{R}}(\Gamma \setminus (\Gamma_2 \cup \Gamma_3))} \\ & - \Big(\frac{\partial u}{\partial n} + k\alpha u, v_1\Big)_{L^2_{\mathbb{R}}(\Gamma_1, \Gamma_5)} + \Big(u - u\big|_{\Gamma_3}, v_2\Big)_{L^2_{\mathbb{R}}(\Gamma_2)} \\ & + (u - u\big|_{\Gamma_2}, v_2)_{L^2_{\mathbb{R}}(\Gamma_3)} - \Big(\frac{\partial u}{\partial n} - ik(u), v_3\Big)_{L^2_{\mathbb{R}}(\Gamma_4)} \end{aligned} \tag{4.31}$$

and $b(\Omega; v_3)$ the linear form

$$b(\Omega, v_3) = \Big(\frac{\partial u_{\text{inc}}}{\partial n} - ik(u_{\text{inc}}), v_3\Big)_{L^2_{\mathbb{R}}(\Gamma_4)}. \tag{4.32}$$

Remark. The transmissive case leads us to a bilinear form as

$$\begin{aligned} a(\Omega; u, v, v_1, v_2, v_3) =& \Big(\phi \nabla u, \nabla v\Big)_{L^2_{\mathbb{R}}(\Omega)} - k^2 \Big(\phi u, v\Big)_{L^2_{\mathbb{R}}(\Omega)} - \Big(\phi \frac{\partial u}{\partial n}, v\Big)_{L^2_{\mathbb{R}}(\partial\tilde{\Omega} \setminus (\Gamma_2 \cup \Gamma_3))} \\ & - \Big(\phi \frac{\partial u}{\partial n}, v\Big)_{L^2_{\mathbb{R},[\![]\!]}(\Gamma_5)} - \Big(\phi \frac{\partial u}{\partial n} - k\alpha u, v_2\Big)_{L^2_{\mathbb{R}}(\Gamma_1)} - \Big(u - u\big|_{\Gamma_3}, v_2\Big)_{L^2_{\mathbb{R}}(\Gamma_2)} \\ & - (u - u\big|_{\Gamma_2}, v_2)_{L^2_{\mathbb{R}}(\Gamma_3)} - \Big(\frac{\partial u}{\partial n} - ik(u), v_3\Big)_{L^2_{\mathbb{R}}(\Gamma_4)}, \end{aligned} \tag{4.33}$$

where $L^2_{\mathbb{R},[\![]\!]}(\Gamma_5)$ denotes the usage of jumps in the associated integrals.

Remark. To continue with adjoint calculations we are required to integrate by parts twice on the derivative-containing terms such that we exemplifying obtain for non-transmissive obstacle

$$\begin{aligned} a(\Omega; v, u) =& - \Big(u, \nabla^2 v\Big)_{L^2_{\mathbb{R}}(\Omega)} - \Big(v, \frac{\partial u}{\partial n}\Big)_{L^2_{\mathbb{R}}(\Gamma)} + \Big(u, \frac{\partial v}{\partial n}\Big)_{L^2_{\mathbb{R}}(\Gamma \setminus (\Gamma_2 \cup \Gamma_3))} - k^2 \Big(u, v\Big)_{L^2_{\mathbb{R}}(\Omega)} \\ & - \Big(\frac{\partial u}{\partial n} + k\alpha u, v_1\Big)_{L^2_{\mathbb{R}}(\Gamma_1, \Gamma_5)} - \Big(u - u\big|_{\Gamma_3}, v_2\Big)_{L^2_{\mathbb{R}}(\Gamma_2)} - \Big(u - u\big|_{\Gamma_2}, v_2\Big)_{L^2_{\mathbb{R}}(\Gamma_3)} \\ & - \Big(\frac{\partial u}{\partial n} - ik(u), v_3\Big)_{L^2_{\mathbb{R}}(\Gamma_4)}. \end{aligned} \tag{4.34}$$

Remark. Instead of multipliers it is also possible to derive adjoint and shape derivative based on an insertion of boundary conditions, whenever it can be reflected in the associated weak form.

Remark. We can regard the Lagrangian (4.29) w.r.t. $J_2(\Omega)$ in the same manner. In the following we restrict to $J_1(\Omega)$ for simplicity.

We obtain the state equation from differentiating the Lagrangian for the test-functions and the adjoint equation from differentiating w.r.t. state variable. The adjoint is formulated in the following theorem:

Theorem 4.3. *(Adjoint) Assume that the elliptic PDE problem (4.7) as of Section 4.2 is H^1-regular, so that its solution u is at least in $H^1(\Omega)$. Then the adjoint in strong form is given by*

$$\begin{aligned}
-\nabla^2 v - k^2 v &= 0 && \text{on} \quad \Omega \\
s.t. \quad \frac{\partial v}{\partial n} &= -(u - u_0) + k\alpha v && \text{on} \quad \Gamma_1 \\
v\big|_{\Gamma_2} &= v\big|_{\Gamma_3} && \text{on} \quad \Gamma_2, \Gamma_3 \\
\frac{\partial v}{\partial n} &= -ikv && \text{on} \quad \Gamma_4 \\
\frac{\partial v}{\partial n} &= k\alpha v && \text{on} \quad \Gamma_5.
\end{aligned} \tag{4.35}$$

Proof. Any directional derivative of $\mathcal{L}$ w.r.t. $\tilde{u}$ must be zero at the solution u, hence

$$0 = \frac{d}{d\epsilon}\mathcal{L}(u + \epsilon\tilde{u}, v, v_1, v_2, v_2, v_3)\big|_{\epsilon=0}. \tag{4.36}$$

Using the definition of the Lagrangian (4.29) gives

$$\begin{aligned}
&= \frac{d}{d\epsilon}\Bigg[\frac{1}{2}(u + \epsilon\tilde{u} - u_0, u + \epsilon\tilde{u} - u_0)_{L^2_{\mathbb{R}}(\Gamma_1)} - \Big(u + \epsilon\tilde{u}, \nabla^2 v\Big)_{L^2_{\mathbb{R}}(\Omega)} \\
&- \Big(v, \frac{\partial u + \epsilon\tilde{u}}{\partial n}\Big)_{L^2_{\mathbb{R}}(\Gamma\setminus(\Gamma_2\cup\Gamma_3))} + \Big(u + \epsilon\tilde{u}, \frac{\partial v}{\partial n}\Big)_{L^2_{\mathbb{R}}(\Gamma\setminus(\Gamma_2\cup\Gamma_3))} - k^2\Big(u + \epsilon\tilde{u}, v\Big)_{L^2_{\mathbb{R}}(\Omega)} \\
&- \Big(\frac{\partial\Big(u + \epsilon\tilde{u}) - u_{\text{inc}}}{\partial n} - ik(u + \epsilon\tilde{u} - u_{inc}), v_3\Big)_{L^2_{\mathbb{R}}(\Gamma_4)} \\
&- \Big(\frac{\partial(u + \epsilon\tilde{u})}{\partial n} + k\alpha(u + \epsilon\tilde{u}), v_1\Big)_{L^2_{\mathbb{R}}(\Gamma_1,\Gamma_5)} \\
&+ \Big(u + \epsilon\tilde{u} - u\big|_{\Gamma_3} + \epsilon\tilde{u}\big|_{\Gamma_3}, v_2\Big)_{L^2_{\mathbb{R}}(\Gamma_2)} + \Big(u + \epsilon\tilde{u} - u\big|_{\Gamma_2} + \epsilon\tilde{u}\big|_{\Gamma_2}, v_2\Big)_{L^2_{\mathbb{R}}(\Gamma_3)}\Bigg]\Bigg|_{\epsilon=0}.
\end{aligned} \tag{4.37}$$

This yields

$$\begin{aligned}
=&(u-u_0,\tilde{u})_{L^2_{\mathbb{R}}(\Gamma_1)} - \Big(\tilde{u},\nabla^2 v\Big)_{L^2_{\mathbb{R}}(\Omega)} \\
&-\Big(v,\frac{\partial\tilde{u}}{\partial n}\Big)_{L^2_{\mathbb{R}}(\Gamma\setminus(\Gamma_2\cup\Gamma_3))} + \Big(\tilde{u},\frac{\partial v}{\partial n}\Big)_{L^2_{\mathbb{R}}(\Gamma\setminus(\Gamma_2\cup\Gamma_3))} - k^2\Big(\tilde{u},v\Big)_{L^2_{\mathbb{R}}(\Omega)} \\
&-\Big(\frac{\partial\tilde{u}}{\partial n} - ik\tilde{u},v_3\Big)_{L^2_{\mathbb{R}}(\Gamma_4)} - \Big(\frac{\partial\tilde{u}}{\partial n} + k\alpha\tilde{u},v_1\Big)_{L^2_{\mathbb{R}}(\Gamma_1,\Gamma_5)} \\
&-\Big(\tilde{u}-\tilde{u}|_{\Gamma_3},v_2\Big)_{L^2_{\mathbb{R}}(\Gamma_2)} - \Big(\tilde{u}-\tilde{u}|_{\Gamma_2},v_2\Big)_{L^2_{\mathbb{R}}(\Gamma_3)}.
\end{aligned} \tag{4.38}$$

We obtain the adjoint equation on Ω in strong form by taking the variation as $\tilde{u}\in C_0^\infty$, i.e.

$$-\nabla^2 v - k^2 v = 0 \quad \text{ on } \Omega. \tag{4.39}$$

In addition, $\tilde{u}\in H_0^1(\Omega)$ on Γ_1,Γ_4 and Γ_5 leads to

$$-\Big(v,\frac{\partial\tilde{u}}{\partial n}\Big)_{L^2_{\mathbb{R}}(\Gamma\setminus(\Gamma_2\cup\Gamma_3))} - \Big(v_3,\frac{\partial\tilde{u}}{\partial n}\Big)_{L^2_{\mathbb{R}}(\Gamma_4)} - \Big(v_1,\frac{\partial\tilde{u}}{\partial n}\Big)_{L^2_{\mathbb{R}}(\Gamma_1,\Gamma_5)} = 0. \tag{4.40}$$

From this we know that $v=-v_3$ on Γ_4 and $v=-v_1$ on Γ_1 and Γ_5. Finally, $\tilde{u}\in H^1(\Omega)$ leads to

$$\begin{aligned}
&\Big(u-u_0,\tilde{u}\Big)_{L^2_{\mathbb{R}}(\Gamma_1)} + \Big(\tilde{u},\frac{\partial v}{\partial n}\Big)_{L^2_{\mathbb{R}}(\Gamma\setminus(\Gamma_2\cup\Gamma_3))} \\
&+\Big(ik(\tilde{u}),v_3\Big)_{L^2_{\mathbb{R}}(\Gamma_4)} - \Big(k\alpha(\tilde{u}),v_1\Big)_{L^2_{\mathbb{R}}(\Gamma_1,\Gamma_5)} \\
&+\Big(\tilde{u}-\tilde{u}|_{\Gamma_3},v_2\Big)_{L^2_{\mathbb{R}}(\Gamma_2)} + \Big(\tilde{u}-\tilde{u}|_{\Gamma_2},v_2\Big)_{L^2_{\mathbb{R}}(\Gamma_3)} = 0.
\end{aligned} \tag{4.41}$$

This provides us with boundary conditions for normal n as claimed, due to the conjugate symmetry of the complex inner product. □

With solution to state and adjoint equation the shape derivative of Definition 3.3 can be derived.

Remark. As described in Chapter 3 shape derivatives can for a sufficiently smooth domain be described via boundary formulations using the Hadamard-Zolésio structure theorem 3.4. The integral over Ω is then replaced by an integral over Γ_5 that acts on the associated normal vector. In this chapter, we calculate the deformation field based on the domain formulation and use the boundary formulation for the derivation of the topological derivative.

Theorem 4.4. *(Shape Derivative Volume Form) Assume that the elliptic PDE problem (4.7) as of Section 4.2 (for full reflection) is H^1-regular, so that its solution u is at least in $H^1(\Omega)$. Moreover, assume that the adjoint equation (4.35) admits a solution $v\in H^1(\Omega)$. Then the shape derivative of the objective $J_1(\Omega)$ in the direction V is given by*

$$\begin{aligned} DJ_1(\Omega)[V] = &(\operatorname{div}(V)\nabla v, \nabla u)_{L^2_{\mathbb{R}}(\Omega)} - k^2 (\operatorname{div}(V) v, u)_{L^2_{\mathbb{R}}(\Omega)} \\ &- \left((\nabla V + \nabla V^T)\nabla v, \nabla u\right)_{L^2_{\mathbb{R}}(\Omega)}. \end{aligned} \tag{4.42}$$

Proof. As in [165], the theorem of Correa and Seger [61] is applied on the right hand side of (4.43). The assumptions of this theorem can be verified as in [65, Chapter 10 Section 6.4]. Then the following equality holds

$$J_1(\Omega) = \min_u \max_v \mathcal{L}(\Omega, u, v) \tag{4.43}$$

The definition of the shape derivative (3.4) in terms of the Lagrangian gives

$$\begin{aligned} &D\mathcal{L}(\Omega, u, v, v_1, v_2, v_3)[V] \\ &= \lim_{\epsilon \to 0^+} \frac{\mathcal{L}(\Omega_\epsilon; u, v, v_1, v_2, v_3) - \mathcal{L}(\Omega; u, v, v_1, v_2, v_3)}{\epsilon} \\ &= \frac{d}{d\epsilon} \mathcal{L}(\Omega_\epsilon, u, v, v_1, v_2, v_3)\big|_{\epsilon=0^+}. \end{aligned}$$

We start by investigation of terms of leading order, where we first use (3.28), e.g.

$$\frac{d^+}{d\epsilon}\left((\nabla u, \nabla v)_{L^2_{\mathbb{R}}(\Omega_\epsilon)}\right)\Big|_{\epsilon=0} = D_m(\nabla u, \nabla v)_{L^2_{\mathbb{R}}(\Omega)} + \operatorname{div}(V)(\nabla u, \nabla v)_{L^2_{\mathbb{R}}(\Omega)}. \tag{4.44}$$

Then the first term is rewritten using (3.27)

$$\begin{aligned} =&(\nabla D_m u, \nabla v)_{L^2_{\mathbb{R}}(\Omega)} - (\nabla u, (\nabla V + \nabla V^T)\nabla v)_{L^2_{\mathbb{R}}(\Omega)} \\ &+(\nabla u, \nabla D_m v)_{L^2_{\mathbb{R}}(\Omega)} + \operatorname{div}(V)(\nabla u, \nabla v)_{L^2_{\mathbb{R}}(\Omega)}. \end{aligned} \tag{4.45}$$

For the second integral we obtain again using (3.28)

$$\frac{d^+}{d\epsilon}\left((-k^2 u, v)_{L^2_{\mathbb{R}}(\Omega_\epsilon)}\right)\Big|_{\epsilon=0} = -D_m(k^2 u, v)_{L^2_{\mathbb{R}}(\Omega)} - \operatorname{div}(V)(k^2 u, v)_{L^2_{\mathbb{R}}(\Omega)}. \tag{4.46}$$

Similar to before the first integral is rewritten using (3.24), such that we get

$$= -(k^2 D_m u, v)_{L^2_{\mathbb{R}}(\Omega)} - (k^2 u, D_m v)_{L^2_{\mathbb{R}}(\Omega)} - \operatorname{div}(V)(k^2 (u, v)_{L^2_{\mathbb{R}}(\Omega)}. \tag{4.47}$$

If we finally rearrange the terms with $D_m(u)$ and $D_m(v)$, let them act as test functions, apply the saddle point conditions, which means that the state equation (4.7) with (4.17)-(4.21) and adjoint equation (4.35) are fulfilled, the terms consisting of $D_m(u)$ and $D_m(v)$ cancel. By adding all terms above up the shape derivative $DJ_1(\Omega)[V]$ is established. □

Remark. In case of partial reflection the boundary terms are obtained by observing

$$\frac{d^+}{d\epsilon}\left((\alpha u, v)_{L^2_{\mathbb{R}}(\Gamma_{5_\epsilon})}\right)\Big|_{\epsilon=0} = D_m(\alpha u, v)_{L^2_{\mathbb{R}}(\Gamma_5)} + \operatorname{div}_{\Gamma_5}(V)(\alpha u, v)_{L^2_{\mathbb{R}}(\Gamma_5)} \tag{4.48}$$

with the convention of Lemma 3.14

$$\operatorname{div}_\Gamma(V) = \operatorname{div}(V) - n \cdot (\nabla V) n \tag{4.49}$$

and application of saddle point conditions.

Remark. Having obtained the sound-hard Helmholtz shape derivative in volume form, the shape derivate in boundary form can be deduced, i.e.

$$DJ_{1,\Gamma}(\Omega)[V] = \left[(\nabla v, \nabla u)_{L^2_{\mathbb{R}}(\Gamma_5)} - k^2\,(v,u)_{L^2_{\mathbb{R}}(\Gamma_5)}\right](V,n)_{L^2(\Gamma_5)}, \tag{4.50}$$

which is obtained by integration by parts on (4.42) and vector calculus identities. We refer to [75] for a more detailed derivation.

Remark. For a sound-soft scatterer [75] or partially absorbing boundary conditions (4.17), we would obtain additional terms depending on partial derivatives in normal direction.

We are now in the position to derive the topological derivative in the transmissive case as described in the following theorem.

Theorem 4.5. *(Topological Derivative) Under the assumptions of Theorem 4.4 the topological derivative D_T of the objective $J_1(\Omega)$ (without perimeter regularization) is given as*

$$D_T J_1(\Omega)(x) = \begin{cases} \Re\left[\frac{2(\phi_2-\phi_1)}{1+\frac{\phi_2}{\phi_1}}\nabla u\cdot\nabla\bar{v} + (\phi_1 k^2 - \phi_2 k^2)u\bar{v}\right] & \text{on } \Omega \\ \Re\left[\frac{2(\phi_1-\phi_2)}{1+\frac{\phi_1}{\phi_2}}\nabla u\cdot\nabla\bar{v} + (\phi_2 k^2 - \phi_1 k^2)u\bar{v}\right] & \text{on } D. \end{cases} \tag{4.51}$$

Proof. The proof can either follow [45], using the topological shape sensitivity method of Theorem 3.18, where the extension for objective and boundary conditions are obtained trivially.
Alternatively, in [82] the method developed in [64] was generalized to a class of PDEs, which contains among others linear and elliptic PDEs. Following [82, Example 3.1], while reducing to diffusive and reactive terms such as extending for the inner product (4.28), the topological derivative can be derived for suitable choice of parameters. □

For completeness, we finally require the shape derivative of the volume penalty and the perimeter regularization as [172, Section 2.11, 2.18]

$$DJ_3(\Omega)[V] = \nu_3 \int_\Omega -\operatorname{div}(V)\,\mathrm{d}x \tag{4.52}$$

$$DJ_4(\Omega)[V] = \nu_4 \int_{\Gamma_5} \kappa_m \langle V, n\rangle\,\mathrm{d}s \tag{4.53}$$

for additive curvature κ_m of Lemma 3.14.

4.4 Numerical Results for Shape Optimization

In this section we describe the numerical algorithm to solve the PDE-constrained optimization problem via shape optimization and present applications to a simplistic domain for non-transmissive obstacle such as a domain representing the Langue de Barbarie.

4.4.1 Implementation Details

We are relying on the classical structure of adjoint-based shape optimization gradient-descent algorithms. However, we motivate the location and shape of the initial obstacle by the usage of the topological derivative $D_T J_{1|2}(\Omega)(x)$ of Theorem 4.5 for sound-hard scattering, i.e. $\phi_2 = 0$. In this light, we exploit the obtained scalar field to initialize an obstacle with the help of a density-based spatial clustering algorithm (DBSCAN) [70]. The obstacle is then deformed in a second step by usage of shape optimization. The procedure is shortly sketched in the following algorithm.

Algorithm 1 Shape Optimization Algorithm

Initialization, Evaluation of Sound-Hard Topological Derivative $D_T J_{1|2}(\Omega)(x)$ & Initialization Obstacle via DBSCAN

while $||DJ_{1|2}(\Omega_k)[V]|| > \epsilon_{TOL}$ **do**

1. Calculate State u_k
2. Calculate Adjoint v_k
3. Calculate Gradient W_k [via $DJ_{1|2,3,4}(\Omega)[V]$ & Linear Elasticity (4.54)]
4. Perform Linesearch for $\tilde{W}_k$
5. Calculate Ω_{k+1} [via $\tilde{W}_k$ and (3.33)]

end while

To compute the solution to boundary value problem (4.7), the adjoint problem (4.35) and to finally deform the domain, we are relying on the finite element solver FEniCS [6]. As described in Section 2.3.2 the CG-method offers itself to discretize the elliptic equation via conformal finite element approximation space. Updating the finite element mesh in each iteration is done via the solution $W : \Omega \to \mathbb{R}^2$ of the linear elasticity equation, that serves as bilinear form in Definition 3.9 [166]

$$\begin{aligned} \int_\Omega \sigma(W) : \epsilon(V)\,\mathrm{d}x &= DJ(\Omega)[V] \qquad && \forall V \in H_0^1(\tilde{\Omega}, \mathbb{R}^2) \\ \sigma &:= \lambda_{elas} T(\epsilon(W))\mathbf{I}_2 + 2\mu_{elas}\epsilon(W) \\ \epsilon(W) &:= \frac{1}{2}\left(\nabla W + \nabla W^T\right) \\ \epsilon(V) &:= \frac{1}{2}\left(\nabla V + \nabla V^T\right), \end{aligned} \tag{4.54}$$

for identity matrix $\mathbf{I}_2 \in \mathbb{R}^{2\times 2}$, where σ and ϵ are called strain and stress tensor and λ_{elas} and μ_{elas} are called Lamé parameters. In our calculations we have chosen $\lambda_{elas} = 0$ and μ_{elas} as the solution of the following Poisson problem [166]

$$\begin{aligned} -\triangle \mu &= 0 && \text{in} && \Omega \\ \mu &= \mu_{max} && \text{on} && \Gamma_5 \\ \mu &= \mu_{min} && \text{on} && \Gamma_1, \Gamma_2, \Gamma_3, \Gamma_4. \end{aligned} \tag{4.55}$$

The source term $DJ(\Omega)[V]$ in (4.54) consists of a volume and surface part, i.e. $DJ(\Omega)[V] = DJ_\Omega[V] + DJ_{\Gamma_5}[V]$. Here the volumetric share comes from our Helmholtz shape deriva-

tive $DJ_{1|2}(\Omega)[V]$ and the shape derivative of the volume penalty $DJ_3(\Omega)[V]$, where we use the projection of (3.43) and only assemble for test vector fields whose support intersects with the interface Γ_5 and is set to zero for all other basis vector fields. The surface part comes from the shape derivative of the perimeter regularization $DJ_4(\Omega)[V]$.

Remark. In order to guarantee the attainment of useful shapes, which minimize the objective, a backtracking line search is used, which limits the step size in case the shape space of Definition 3.7 is left, i.e. having intersecting line segments. In addition, a simple check for a decrease of the objective is added.

Remark. Computational solutions to state, adjoint and shape derivative, require the manual calculation of the complex inner products' real part by splitting all occurring trial and test functions in real and imaginary part, e.g.

$$\begin{aligned}(u,v)_{L^2_{\mathbb{R}}(\Omega)} &= (u_{\Re}+iu_{\mathbb{I}}, v_{\Re}+iv_{\mathbb{I}})_{L^2_{\mathbb{R}}(\Omega)} = (u_{\Re},v_{\Re})_{L^2(\Omega)} + (u_{\mathbb{I}},v_{\mathbb{I}})_{L^2(\Omega)} \\ (iu,v)_{L^2_{\mathbb{R}}(\Gamma)} &= (iu_{\Re}-u_{\mathbb{I}}, v_{\Re}+iv_{\mathbb{I}})_{L^2_{\mathbb{R}}(\Gamma)} = (u_{\Re},v_{\mathbb{I}})_{L^2(\Gamma)} - (u_{\mathbb{I}},v_{\Re})_{L^2(\Gamma)},\end{aligned} \tag{4.56}$$

such as analogous computations for derivative containing products.

4.4.2 Ex.1: The Simplistic Mesh

In the first example, we will look at the model problem, that was described in Section 4.2. We interpret Γ_1 and Γ_5 as the reflective coastline and obstacle, Γ_2 and Γ_3 as the lateral, such as Γ_4 as the open sea boundary. As it is described before in Section 4.4, the topological derivative can be used to determine the location of an initial obstacle. Exemplifying, we show in Figure 4.2 an initial field on the simplistic mesh (subfigure (a)) for which we target a zero amplitude along the shoreline, such that the topological derivative is evaluated accordingly (subfigure (b)). A filter e.g. in form of a DBSCAN-algorithm is then used to initialize an obstacle. Here results are shown for a minimum number of points in a cluster $m = 10$ and threshold $\epsilon = 7$, where colors apart from blue build useful clusters (subfigure (c)).

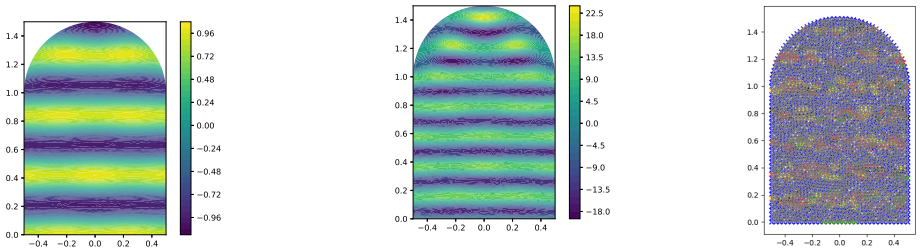

(a) Field for Absent Obstacle

(b) Topological Derivative for Sound-Hard Obstacle

(c) Solution to DBSCAN

Figure 4.2: Ex.1 Initialization of Obstacle

We have used this information to generate the meshes in Figure 4.3 with help of the mesh generator GMSH [85]. We have discretized finer around the obstacle to ensure a

high resolution for the shape optimization routine. A reducing effect on the wave height along the shore Γ_1 of the created meshes for single and multi-wave case can already be observed for the pure placement of the obstacles in Figure 4.4. The forthcoming analysis is based on time-harmonic wave propagations as in (4.7) with associated boundary conditions. We first model a single incident wave such that the angle of the obstacle's lower boundary normal and incoming direction is zero by choosing $\delta = 1.5\pi$ and a suitable wave number e.g. $k = 15$ in the first two subfigures of Figures 4.4-4.6. In the multi-wave case (4.23) we model the sum of $N = 3$ waves with $\delta_j \in \{1.25\pi, 1.5\pi, 1.75\pi\}$ for weights $w_j \in \{0.6, 0.3, 0.1\}$ such as $M = 2$ frequencies with $k_i \in \{11, 15\}$, which can be taken from the third subfigures in Figures 4.4-4.6 and can be interpreted as strong waves from north-west. In all the test cases we model full reflection, i.e. $\alpha = 0$. In the objective we enforce regularization of the perimeter by a weight of $\nu_2 = 0.1$. The solution to the state and adjoint equation is of linear nature, hence we use the FEniCS solver for linear PDEs. Having solved state and adjoint equations the mesh deformation is performed as described before, where we specify $\mu_{min} = 10$ and $\mu_{max} = 100$ in (4.54). The step size is at $\rho_{step} = 0.04$ and shrinks whenever criteria for line searches are not met. We can extract results of shape optimization from Figure 4.5, where we according to Figure 4.6 obtain decreases in the objectives of 27.72%, 53.01% and 6.14%.

(a) Rectangular Obstacle (b) Circled Obstacle

Figure 4.3: Ex.1 Initial Meshes

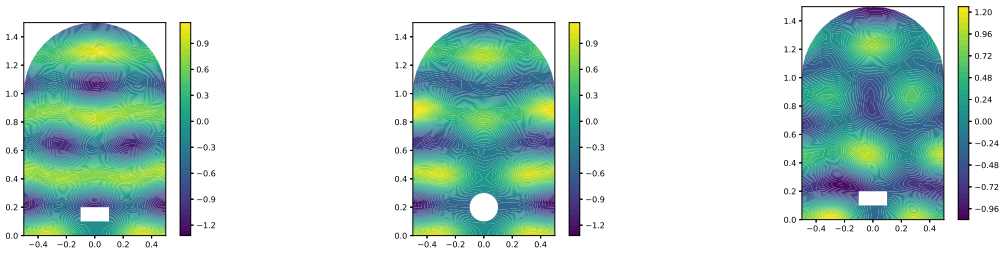

(a) Rectangular Obstacle (b) Circled Obstacle (c) Multiple Waves and Rectangle Obstacle

Figure 4.4: Ex.1 Initial Fields

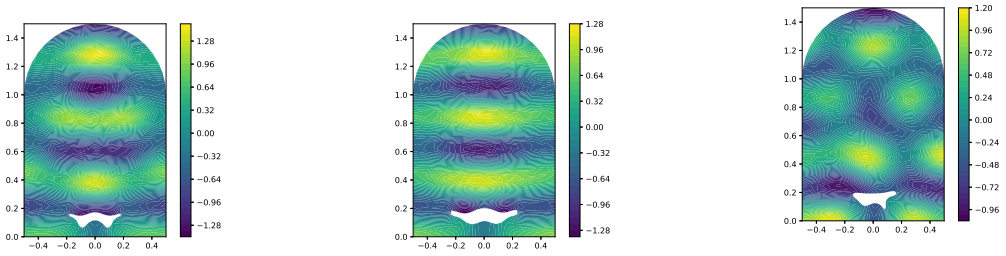

(a) Rectangular Obstacle (b) Circled Obstacle (c) Multiple Waves and Rectangular Obstacle

Figure 4.5: Ex.1 Final Fields

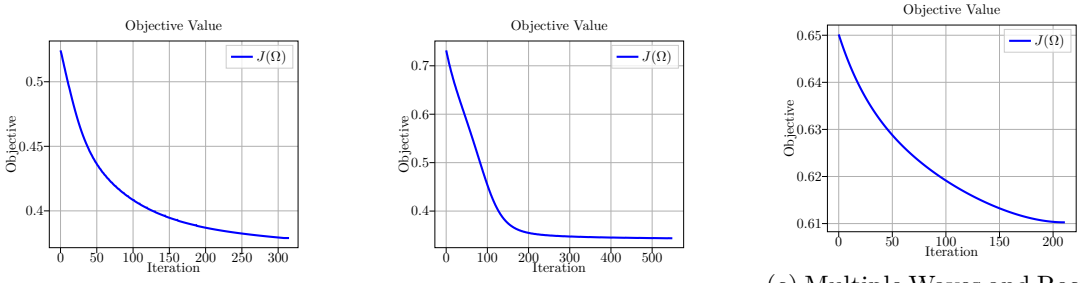

(a) Rectangular Obstacle (b) Circled Obstacle (c) Multiple Waves and Rectangular Obstacle

Figure 4.6: Ex.1 Objectives

4.4.3 Ex.2: The Langue de Barbarie Mesh

More realistic computations are performed in the second example. Here we look at the LdB, that served as a motivational example in Section 1.1 for the usage of shape and topology optimization for the prevention of coastal erosion. Adjusting our model to this specific coastal section starts on mesh level. Shorelines are taken from the free GSHHG databank[1] following [19]. We build an interface from a geographical information system (QGIS3[2]) for processing the data to the computer aided design software GMSH for the mesh generation. Similar to the preceding example, we interpret Γ_1 as the coastline of islands and mainlands and Γ_4 as the open sea boundary. We have inserted a smaller artificial island, which shape is to be optimized in front of the second and third with boundary denoted as Γ_5 (cf. to Figure 4.8). The wave's propagation is modeled monodirectionally to the shores with $\delta = 1.8\pi$ and wave-number $k = 35$. The initial mesh can be extracted from Figure 4.7.

[1] https://www.ngdc.noaa.gov/mgg/shorelines/
[2] http://www.qgis.org

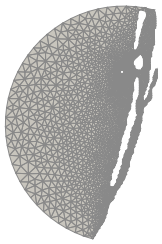

Figure 4.7: Initial LdB Mesh

Figure 4.8 pictures fields to the initial and optimized mesh after 361 iterations of optimization for partial reflection with $\alpha_1 = 0.5$ using the formula of (4.19) such as an initial step size $\rho_{step} = 0.01$.

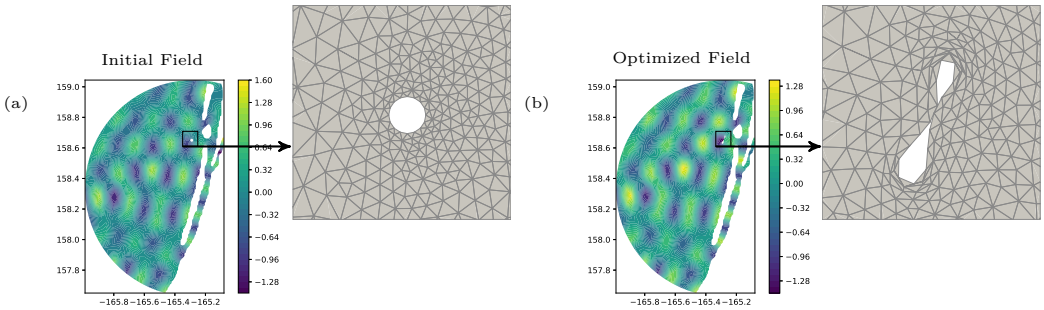

Figure 4.8: (a) Initial Field and Obstacle for Partial Reflection, (b) Optimized Field and Obstacle for Partial Reflection

One can observe a similar behavior as in Section 4.4.2, where the obstacle is stretched to protect an as large as possible area. The computation stopped after obtaining intersecting line segments at the obstacle's center in Figure 4.8. However, in Figure 4.9 we can still observe a significant decrease in the objective functional, taking into account that the area of the scatterer is comparably low to the area of the shorelines.

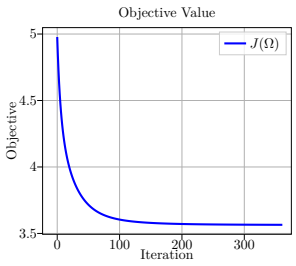

Figure 4.9: LdB Objective for Partial Reflection

Remark. From a practical, durability viewpoint are thin obstacles, as in Figures 4.8, which also lead to breakdown of the optimization algorithm due to intersecting line segments, not ideal. To circumvent this problem we use a thinness penalty dealing with shallow water equations in Chapters 5-7.

4.5 Numerical Results for Topology Optimization

In this section we investigate results for the derived topological derivative in the transmissive case, where we divide between strong ϕ_1 and weak ϕ_2 material introducing an associated coefficient (4.12). In accordance to Theorem 2.13, an implicit description of boundaries is hereby given. As it was among others observed in [169], topological optimization problems are often ill-posed, i.e. tend to develop more and more complex structures without achieving convergence to a final state. Typically geometrical constraints as perimeter regularization are used to encounter this [14, 13]. Ultimately, implicit domain descriptions alongside greyscale boundaries, that maybe appear throughout the usage of numerical techniques as presented in Section 3.3.2, demand a density-based counterpart to (4.26), which states as

$$\mathrm{P}(\tilde{\Omega}) := \int_{\tilde{\Omega}} |D\phi| \, \mathrm{d}x = |D\phi|(\tilde{\Omega}), \tag{4.57}$$

where $|D\phi|(\tilde{\Omega})$ is the total variation of a function of bounded variation $\phi \in BV(\tilde{\Omega})$ [65, Chapter 5, Section 6.1]. As it was elaborated in [13], although this description is based on a mathematical neat framework it is not beneficial in a numerical setting. In this light, approximative functionals possessing properties of so-called Γ-convergence [119] are most often used. Hence, we follow [14], which provided the required convergence to a variant of (4.57) and pose as an additional penalty

$$F^{\epsilon}_{PER}(\phi) = \frac{1}{\epsilon} \int_{\tilde{\Omega}} (1 - L_\epsilon(\phi)) \, \phi \, \mathrm{d}x, \tag{4.58}$$

where $L_\epsilon(\phi)$ is the unique solution $u_\epsilon \in H^1(\Omega)$ to the regularizing elliptic PDE

$$\begin{aligned} -\epsilon^2 \Delta u_\epsilon + u_\epsilon &= \phi \quad \text{in } \tilde{\Omega} \\ \frac{\partial u_\epsilon}{\partial n} &= 0 \quad \text{on } \partial\tilde{\Omega}. \end{aligned} \tag{4.59}$$

In contrast to Section 4.4, we will constrain objective $J_{1|2}(\Omega)$ by the additional constraint

$$|\tilde{\Omega}| \geq \mathrm{Vol}^*, \tag{4.60}$$

where $0 < \mathrm{Vol}^* \leq |\tilde{\Omega}_0|$ is a to be specified target volume. This constraint can e.g. be incorporated via usage of a linear and quadratic penalty [44] in line with the approximated perimeter as

$$\tilde{J}(\Omega) = J_{1|2}(\Omega) + \lambda h^+_\Omega + \frac{\alpha}{2}(h^+_\Omega)^2 + \nu_5 F^{\epsilon}_{PER}(\phi) \tag{4.61}$$

for $h_\Omega^+ = \max\{h_\Omega, -\frac{\lambda}{\alpha}\}$ and $h_\Omega = \mathrm{Vol}^* - |\tilde{\Omega}|$ with possibly to be determined Lagrange multipliers $\lambda, \alpha > 0$. In this case topological derivatives are obtained immediately by

$$\begin{aligned} h_\Omega^+ &= \begin{cases} h_\Omega & \text{if } \frac{\lambda}{\alpha} + h_\Omega > 0 \\ -\frac{\lambda}{\alpha} & \text{else} \end{cases} \quad \Rightarrow \quad D_T h_\Omega^+ = \begin{cases} 1 & \text{if } \frac{\lambda}{\alpha} + h_\Omega > 0 \\ 0 & \text{else} \end{cases} \\ (h_\Omega^+)^2 &= \begin{cases} h_\Omega^2 & \text{if } \frac{\lambda}{\alpha} + h_\Omega > 0 \\ \frac{\lambda^2}{\alpha^2} & \text{else} \end{cases} \quad \Rightarrow \quad D_T (h_\Omega^+)^2 = \begin{cases} 2h_\Omega & \text{if } \frac{\lambda}{\alpha} + h_\Omega > 0 \\ 0 & \text{else} \end{cases} \end{aligned} \tag{4.62}$$

such that the topological derivative of the total volume penalty states as

$$D_T(\lambda h_\Omega^+ + \frac{\alpha}{2}(h_\Omega^+)^2) = \max(0, \lambda + \alpha h_\Omega). \tag{4.63}$$

The required topological derivative of the approximated penalty is in turn given as [10]

$$D_T F_{PER}^\epsilon(\phi) = \frac{1}{\epsilon}(1 - 2u_\epsilon). \tag{4.64}$$

In this setting, we utilize the numerical algorithm that is based on level-sets introduced in Section 3.3.2, derived in [12] and extended for additional augmented Lagrangian steps. Here we highlight that we calculate the perimeter for a fixed value of $\epsilon > 0$, whereas in [13] it is proposed to add an additional loop to truly approximate the perimeter functional. The pseudocode is sketched in Algorithm 2.

Algorithm 2 Topology Optimization via Level-Sets Augmented Lagrangian and Perimeter Regularization

Initialization i.a. Level Set ξ_0, Step Size ρ_{step}, $\gamma > 1$, $c \in (0, 1)$
while $(h_\Omega^+)^i > \epsilon_{TOL}$ **do**
  while $\theta_{i,k} > \epsilon_{TOL}$ **do**
    1.1. Construct Domain $\tilde{\Omega}_{i,k}$ via $\xi_{i,k}$
    1.2. Solve State Equations $u_{i,k}, u_{\epsilon,i,k}$
    1.3. Solve Adjoint Equation $p_{i,k}$
    1.4. Compute Generalized Topological Derivative $\tilde{g}_{i,k}$ via Definition 3.22
    1.5. Calculate Update Formula for $\xi_{i,k+1}$ (3.61), with Line Search for $\rho_{step,i,k}$
    1.6. Compute Angle $\theta_{i,k+1}$ via (3.59)
  end while
  2.1 Update Lagrange Multiplier $\lambda^{i+1} = \max\{0, \lambda^i + \alpha^i (h_\Omega^+)^{i+1}\}$
  2.2 Update Step Size $\alpha^{i+1} = \gamma\alpha^i$ if $|(h_\Omega^+)^{i+1}| \geq c|(h_\Omega^+)^i|$ else $\alpha^{i+1} = \alpha^i$
end while

4.5.1 Ex.1: The Simplistic Mesh

We start with the mesh and field properties for the Helmholtz scatterer as described in Section 4.5.1 and visualized in Figure 4.2. Strong and weak material are represented by

$\phi_1 = 1$ and $\phi_2 = 0.1$. To take into account practical in-feasibilities of deep-water obstacles we weight the generalized topological gradient of Definition 3.22 using an activation function as follows

$$\tilde{g}_w(x) := z(x)\tilde{g}(x) \tag{4.65}$$

for suitable $z : \Omega \to \mathbb{R}$. The resulting topological derivatives for constant and Gaussian activation e.g. with $z_1(x) = \exp\left[-10x^2 - 50(y - 0.1)^2\right]$, can be taken from Figure 4.10. For the level-set algorithm of Section 3.3.2 we choose an initial step size of $\rho_{step} = 0.05$ and work with fixed $\nu_5 = 0.1$ and $\epsilon = 0.1$ for the perimeter regularization. The volume penalization starts with initial weights $\lambda = 0$, $\alpha = 0.1$ and chooses $\gamma = 1.5$ as well as $c = 0.5$ in the update step of the Lagrange multipliers. After performing multiple augmented Lagrangian steps we obtain a minimizing material distribution for $\text{Vol}^* = 0.95|\tilde{\Omega}_0|$ with the solution's real part visualized in Figure 4.11. However, we highlight here, that minimizing materials are strongly dependent on various input-parameters as the initial level-set, the elements' diameters such as the Lagrange multiplier or control and regularization parameters. For all further subtleties and heuristics we refer to [12] and [175].

(a) $z(x) := c$ (b) $z(x) := z_1(x)$

Figure 4.10: Iteration $i = 0$: Generalized Topological Derivative

(a) Material Distribution ϕ (b) Real Part of Solution $\mathcal{R}[u]$

Figure 4.11: Final Augmented Lagrangian Iteration $i = 11$

Chapter 5

Shape Optimization for Shallow Water Equations

In this chapter we select one of the most widely applied system of wave equations. We describe the hydrodynamics by the set of Saint-Venant or better known as shallow water equations (SWE), that originate from the famous Navier-Stokes equations by depth-integration, based on the assumption that horizontal length-scales are much larger than vertical ones [23].
The calculation of the SWE continuous adjoint and shape derivative such as its use in free-form shape optimization for the mitigation of coastal erosion appears novel. However, we emphasize, that the SWE have been used before in the optimization of practical applications, e.g. using discrete adjoints via automatic differentiation in the optimization of the location of tidal turbines [80], to optimize the shape of fish passages in finite design spaces [8, 102] and to encounter coastal erosion via an optimal sand transport problem [125].
The chapter is structured as follows: In Section 5.1 we derive viscous SWE following the original idea in reference [23]. In Section 5.2 we then constrain an objective to the associated solution to obtain a PDE-constrained optimization problem. This is followed by the derivation of the adjoint equations and the shape derivative in volume form in Section 5.3. The final part, Section 5.4, will then apply the results to firstly a simplified mesh and secondly to more realistic meshes, picturing the LdB and extending results to spherical world meshes calculated on immersed manifolds.

5.1 PDE Derivation

The SWE can be derived by depth-integrating the three-dimensional Navier-Stokes equations [23, 155]. We will follow this idea in Appendix A and derive

Theorem 5.1. *(Viscous SWE) The viscous shallow water equations are identified as a*

system ensuring conservation of mass and $x-, y-$momentum on $\Omega \times (0,T)$, i.e.

$$\begin{aligned}
\frac{\partial H}{\partial t} + \frac{\partial (H\bar{u})}{\partial x} + \frac{\partial (H\bar{v})}{\partial y} &= 0 \\
\frac{\partial H\bar{u}}{\partial t} + \frac{\partial (H\bar{u}^2)}{\partial x} + \frac{\partial (H\bar{u}\bar{v})}{\partial y} &= -gH\frac{\partial z_0}{\partial x} - gH\frac{\partial H}{\partial x} + \frac{\partial}{\partial x}\left(H\mu\frac{\partial \bar{u}}{\partial x}\right) + \frac{\partial}{\partial y}\left(H\mu\frac{\partial \bar{u}}{\partial y}\right) - \frac{\tau_x^b}{\rho} + \frac{\tau_x^s}{\rho} \\
\frac{\partial H\bar{v}}{\partial t} + \frac{\partial (H\bar{v}\bar{u})}{\partial x} + \frac{\partial (H\bar{v}^2)}{\partial y} &= -gH\frac{\partial z_0}{\partial y} - gH\frac{\partial H}{\partial y} + \frac{\partial}{\partial x}\left(H\mu\frac{\partial \bar{v}}{\partial x}\right) + \frac{\partial}{\partial y}\left(H\mu\frac{\partial \bar{v}}{\partial y}\right) - \frac{\tau_y^b}{\rho} + \frac{\tau_y^s}{\rho}
\end{aligned} \tag{5.1}$$

for viscosity weight and density $\mu, \rho > 0$, for bottom and surface shear stress $\tau^b, \tau^s : \Omega \times (0,T) \to \mathbb{R}^2$ and for scalar solutions $H, \bar{u}, \bar{v} : \Omega \times (0,T) \to \mathbb{R}$ with depth-averaged variables

$$\bar{u} = \frac{1}{H}\int_{z_0}^{z_0+H} u \,\mathrm{d}z \quad \text{and} \quad \bar{v} = \frac{1}{H}\int_{z_0}^{z_0+H} v \,\mathrm{d}z, \tag{5.2}$$

for sediment level $z_0 : \Omega \to \mathbb{R}$ under shallow assumptions.

Proof. See Appendix A. □

Remark. SWE are often derived for the more general case of an arbitrary reference datum. In our setting we refer to the case of a zero reference height for positive sediment and water heights as in Figure 5.2.

Remark. Commonly, friction formulae for SWE are determined empirically, by the observation that friction terms depend on water depth, bottom topography and the square of the velocity. Hence, friction is introduced as a source term in the x- and y-momentum equation, i.e. in vector notation

$$\frac{\tau^b}{\rho} = \begin{pmatrix} gHS_x \\ gHS_y \end{pmatrix}. \tag{5.3}$$

Surface shear stresses can be interpreted as wind effects on the water [155]. However, in this thesis we neglect such forces.

5.2 Model Formulation

Suppose we are given an open domain $\tilde{\Omega} \subset \mathbb{R}^2$, which is split into the disjoint sets $\Omega, D \subset \tilde{\Omega}$ such that $\Omega \cup D \cup \Gamma_3 = \tilde{\Omega}$, $\Gamma_1 \cup \Gamma_2 = \partial\tilde{\Omega}$. We assume the variable, interior boundary Γ_3 and the fixed outer $\partial\tilde{\Omega}$ to be at least Lipschitz. One simple example of such kind is visualized below in Figure 5.1.

On this domain we model water wave and velocity fields as solution to SWE, as introduced in Section 5.1, with artificial viscosity, as introduced in Section 2.3.3, i.e.

$$\partial_t U + \nabla \cdot F(U) - \nabla \cdot (G(\mu)\nabla \hat{U}) = S(U) \quad \text{in } \Omega \times (0,T), \tag{5.4}$$

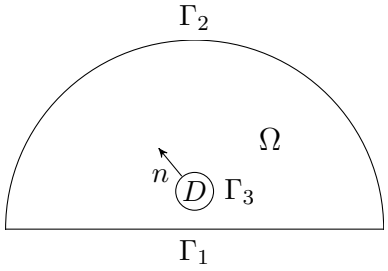

Figure 5.1: Illustrative Domain Ω with Initial Circled Obstacle D and Boundaries Γ_1, Γ_2 and Γ_3

where we are given the SWE in vector notation with flux matrix

$$F(U) = \begin{pmatrix} Q \\ \frac{Q}{H} \otimes Q + \frac{1}{2} g H^2 \mathbf{I}_2 \end{pmatrix} = \begin{pmatrix} Hu & vH \\ Hu^2 + \frac{1}{2} g H^2 & Huv \\ Huv & Hv^2 + \frac{1}{2} g H^2 \end{pmatrix} \tag{5.5}$$

for identity matrix $\mathbf{I}_2 \in \mathbb{R}^{2\times 2}$, gravitational acceleration g and solution $U : \Omega \times (0, T) \to \mathbb{R} \times \mathbb{R}^2$, where for simplicity the domain and time-dependent components are denoted by $U = (H, Q) = (H, Hu, Hv)$, with H being the water height and Hu, Hv the weighted horizontal and vertical discharge or velocity. For notational ease, we disregard diacritics for depth-averaged quantities in (5.1) and in addition set $\hat{U} = (H + z, Q)$ for scalar sediment height $z : \Omega \to \mathbb{R}$. The setting can be taken from Figure 5.2.

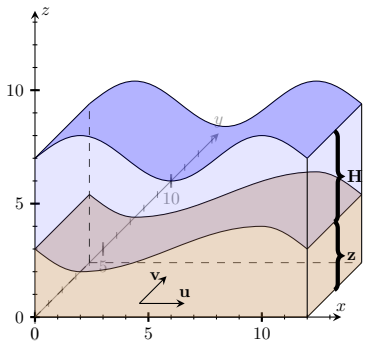

Figure 5.2: Cross-Section for Identification of Wave Height H, Sediment Height z and Velocities u and v

The source term in (5.4) is defined as

$$S(U) = \begin{pmatrix} 0 \\ -gH\frac{\partial z}{\partial x} - gHu\frac{\sqrt{u^2+v^2}}{KH^{4/3}} \\ -gH\frac{\partial z}{\partial y} - gHv\frac{\sqrt{u^2+v^2}}{KH^{4/3}} \end{pmatrix}, \tag{5.6}$$

where the first term responds to variations in the bed slope and the second term originates from (5.3) resembling the Manning formula to respond to bottom friction, where $K > 0$ is Manning's roughness coefficient [53, Section 3.3.2]. For the boundaries we use rigid-wall and outflow conditions for Γ_1, Γ_3 and Γ_2 by setting the velocity in normal direction to zero and prescribing a water height H_1 at the boundary, such that

$$\begin{aligned} &Q \cdot n = 0, \nabla(H+z) \cdot n = 0, \nabla Q_1 \cdot n = 0, \nabla Q_2 \cdot n = 0 \quad \text{on} \quad \Gamma_1, \Gamma_3 \times (0,T) \\ &H = H_1, \nabla Q_1 \cdot n = 0, \nabla Q_2 \cdot n = 0 \quad \text{on} \quad \Gamma_2 \times (0,T). \end{aligned} \tag{5.7}$$

Initial conditions for U are implemented by prescribing a fixed starting point U_0, i.e.

$$U = U_0 \quad \text{in} \quad \Omega \times \{0\}. \tag{5.8}$$

Remark. As it can be observed in Theorem 5.1, original viscous SWE are an incomplete parabolic system, where viscosity is only placed on the momentum equation. To prevent shocks or discontinuities that can appear in the original formulation of the hyperbolic SWE even for continuous data in finite time, an additional artificial viscous term is added in the continuity equation such that we obtain a set of fully parabolic equations. We control the amount of added diffusion by the diagonal matrix $G(\mu) = \sum_{i=1}^{n} e_i^T \mu e_i e_i^T$ with entries $\mu = (\mu_v, \mu_f) \in \mathbb{R}_+ \times \mathbb{R}_+^2$ and basis vector $e_i \in \mathbb{R}^n$ with n being the number of dimensions in vector μ. In this setting μ_f is fixed, while we rely on shock detection in the determination of μ_v following [147] as introduced in Section 2.3.3. Ultimately, a physical interpretation can be obtained for the introduction of the viscous part in the conservation of momentum equations. However, μ_v is solely based on stabilization arguments, where we follow the justification as in [90]. The complete parabolic problem together with well-posed boundary conditions [140] provides us with a well-posed problem.

We obtain a PDE-constrained optimization problem for objective

$$J(\Omega) = J_1(\Omega) + J_2(\Omega) + J_3(\Omega) + J_4(\Omega) + J_5(\Omega), \tag{5.9}$$

where we are trying to minimize the mechanical wave energy of destructive waves at the shore Γ_1, that are waves above a critical threshold $H_{\text{cr}} > 0$ [128], over a time window $\tilde{T} \subset (0,T)$, i.e.

$$J_1(\Omega) = \int_{\tilde{T}} \int_{\Gamma_1} \nu_1 E \sigma_\alpha (H - H_{\text{cr}}) \, \mathrm{d}s \, \mathrm{d}t \tag{5.10}$$

for mechanical wave energy $E = \frac{1}{8}\rho g H^2$ and reduction to destructive sea waves enforced by usage of the sigmoid function $\sigma_\alpha : \mathbb{R} \to \mathbb{R}$ with slope parameter $\alpha > 0$. In addition, we aim for zeroed velocities

$$J_2(\Omega) = \int_0^T \int_{\Gamma_1} \frac{\nu_2}{2} ||Q||_2^2 \, \mathrm{d}s \, \mathrm{d}t. \tag{5.11}$$

These objectives are supplemented by a volume penalty and a perimeter regularization, which are known from Chapter 4, i.e.

$$J_3(\Omega) = -\nu_3 \int_\Omega 1 \, \mathrm{d}x, \tag{5.12}$$

and

$$J_4(\Omega) = \nu_4 \int_{\Gamma_3} 1 \, \mathrm{d}s. \tag{5.13}$$

Additionally, a minimal thinness penalty on obstacle level is added by following [4] as

$$J_5(\Omega) = \nu_5 \int_{\Gamma_3} \int_0^{d_{min}} \left[\left(d_\Omega \left(x - \xi \vec{n}(x) \right) \right)^+ \right]^2 \mathrm{d}\xi \, \mathrm{d}s. \tag{5.14}$$

Here d_Ω represents the signed distance function (SDF) with value

$$d_\Omega(x) = \begin{cases} d(x, \partial\Omega) & \text{if } x \in \Omega \\ 0 & \text{if } x \in \partial\Omega \\ -d(x, \partial\Omega) & \text{if } x \in \bar{\Omega}^c, \end{cases} \tag{5.15}$$

where the Euclidian distance of $x \in \mathbb{R}^d$ to a closed set $K \subset \mathbb{R}^d$ is defined as

$$d(x, K) = \min_{y \in K} ||x - y||_2 \tag{5.16}$$

for Euclidian distance $||.||_2$. The latter penalty can be justified by arguing, that an increased thinness would be undesirable with regards to the durability of the optimized shape. From a shape computational viewpoint, it ensures staying in the associated shape space. In numerics it prevents intersections of line segments, which we could observe in Section 4.4.3 and may cause a breakdown of the optimization algorithm. In this light, we only take into account the positive part of the SDF of the offset value. Hence, we define for a real-valued function $f : \Omega \to \mathbb{R}$ the positive part as

$$f^+ = \max(f(x), 0) = \begin{cases} f(x) & \text{if } f(x) > 0 \\ 0 & \text{otherwise} \end{cases}. \tag{5.17}$$

As before, the objective is controlled by parameters $\nu_1, \nu_2, \nu_3, \nu_4$ and ν_5 which need to be defined a priori (for further details cf. to Section 4.4).

Remark. In Chapters 6-8 we will replace objectives (5.10) and (5.11) with a general tracking-type objective, for justification we refer to Chapter 6.

5.3 Adjoint-Based Shape Optimization

We take care of the constraints (5.4) and formulate the Lagrangian

$$\mathcal{L}(\Omega, U, P) = J_{1,2}(\Omega) + a(U, P) - b(P), \tag{5.18}$$

where $J_{1,2}(\Omega) = J_1(\Omega) + J_2(\Omega)$ consists of the first two objectives (5.10)-(5.11), and $a(U, P)$ and $b(P)$ are obtained from the boundary value problem (5.4). As introduced in

Section 2.2 we rewrite the equations in weak form by multiplying with some arbitrary test function $P \in H^1(\Omega \times (0,T))^3$ obtaining the form $a(U,P) = a(H,Q,p,R)$

$$\begin{aligned} a(H,Q,p,R) := &\int_0^T \int_\Omega \left[\frac{\partial H}{\partial t} + \nabla \cdot Q\right] p \,\mathrm{d}x \,\mathrm{d}t \\ &+ \int_0^T \int_\Omega \left[\frac{\partial Q}{\partial t} + \nabla \cdot \left(\frac{Q}{H} \otimes Q + \frac{1}{2} g H^2 \mathbf{I}_2\right)\right] \cdot R \,\mathrm{d}x \,\mathrm{d}t \\ &+ \int_0^T \int_\Omega \mu_v \nabla(H+z) \cdot \nabla p \,\mathrm{d}x \,\mathrm{d}t - \int_0^T \int_{\Gamma_2} \mu_v \nabla(H_1+z) \cdot n p \,\mathrm{d}s \,\mathrm{d}t \\ &+ \int_0^T \int_\Omega G(\mu_f) \nabla Q : \nabla R \,\mathrm{d}x \,\mathrm{d}t + \int_0^T \int_\Omega g H \nabla z \cdot R \,\mathrm{d}x \,\mathrm{d}t \end{aligned} \tag{5.19}$$

and a zero perturbation term.

Remark. For readability we left out the friction term, however up to some repetitive use of chain and product rule the handling stays the same as for the variations in the bed slope.

Remark. Here and in what follows we assume the flow to be free of discontinuities, e.g. induced by a discontinuous bottom profile z or wave height H, which would prohibit us from performing adjoint-sensitivity analyses and ensuring the requirements in Theorem 5.2 and 5.3.

We obtain state equations from differentiating the Lagrangian with respect to P and the auxiliary problem, the adjoint equations, from differentiating the Lagrangian with respect to the states U. The adjoint is formulated in the following theorem:

Theorem 5.2. *(Adjoint) Assume that the parabolic PDE problem (5.4) is H^1-regular, so that its solution U is at least in $H^1(\Omega \times (0,T))^3$. Then the adjoint in strong form (without friction term) is given by*

$$\begin{aligned} -\frac{\partial p}{\partial t} + \frac{1}{H^2}(Q \cdot \nabla) R \cdot Q - gH(\nabla \cdot R) - \nabla \cdot (\mu_v \nabla p) + g \nabla z \cdot R &= -\nu_1 (E\sigma_\alpha)_{H,\Gamma_1,\tilde{T}} \\ -\frac{\partial R}{\partial t} - \nabla p - \frac{1}{H}(Q \cdot \nabla) R - \frac{1}{H}(\nabla R)^T Q - \nabla \cdot (G(\mu_f) \nabla R) &= -\nu_2 (Q)_{\Gamma_1} \end{aligned} \tag{5.20}$$

where we have on $\Gamma_1 \times \tilde{T}$

$$(E\sigma_\alpha)_{H,\Gamma_1,\tilde{T}} = 2\frac{E}{H}\sigma_\alpha(H - H_{cr}) + E\sigma_\alpha(H - H_{cr})(1 - \sigma_\alpha(H - H_{cr})) \tag{5.21}$$

such as final time conditions

$$\begin{aligned} p &= 0 \quad in \quad \Omega \times \{T\} \\ R &= 0 \quad in \quad \Omega \times \{T\} \end{aligned} \tag{5.22}$$

and boundary conditions

$$\begin{aligned} R \cdot n = 0, \nabla p \cdot n = 0, \nabla R_1 \cdot n = 0, \nabla R_2 \cdot n = 0 \quad &on \quad \Gamma_1, \Gamma_3 \times (0,T) \\ pn + \frac{1}{H_1}(Q \cdot n)R + \frac{1}{H_1}(QR) \cdot n = 0, \nabla R_1 \cdot n = 0, \nabla R_2 \cdot n = 0 \quad &on \quad \Gamma_2 \times (0,T). \end{aligned} \tag{5.23}$$

Proof. We need to rewrite the weak form (5.19) as

$$\begin{aligned} a(H,Q,p,R) = &\int_0^T \int_\Omega -\frac{\partial p}{\partial t} H \,\mathrm{d}x\,\mathrm{d}t + \int_\Omega [H(x,T)p(x,T) - H_0 p(x,0)]\,\mathrm{d}x \\ &+ \int_0^T \int_\Omega -Q \cdot \nabla p \,\mathrm{d}x\,\mathrm{d}t + \int_0^T \int_\Gamma pQ \cdot n \,\mathrm{d}s\,\mathrm{d}t \\ &+ \int_0^T \int_\Omega -(H+z)\nabla \cdot (\mu_v \nabla p)\,\mathrm{d}x\,\mathrm{d}t \\ &+ \int_0^T \int_\Gamma [\mu_v (H+z)\nabla p \cdot n - p\mu_v \nabla (H+z) \cdot n]\,\mathrm{d}s\,\mathrm{d}t \\ &+ \int_0^T \int_\Omega -\frac{\partial R}{\partial t} \cdot Q \,\mathrm{d}x\,\mathrm{d}t + \int_\Omega [Q(x,T) \cdot R(x,T) - Q_0 \cdot R(x,0)]\,\mathrm{d}x \\ &+ \int_0^T \int_\Omega -\frac{Q}{H} \cdot \nabla R \cdot Q \,\mathrm{d}x\,\mathrm{d}t + \int_0^T \int_\Gamma \frac{Q}{H} \cdot RQ \cdot n \,\mathrm{d}s\,\mathrm{d}t \\ &+ \int_0^T \int_\Omega -\frac{1}{2} g H^2 \nabla \cdot R \,\mathrm{d}x\,\mathrm{d}t + \int_0^T \int_\Gamma \frac{1}{2} g H^2 R \cdot n \,\mathrm{d}s\,\mathrm{d}t \\ &+ \int_0^T \int_\Omega -Q \cdot \nabla \cdot (G(\mu_f)\nabla R)\,\mathrm{d}x\,\mathrm{d}t + \int_0^T \int_\Omega gH \nabla z \cdot R \,\mathrm{d}x\,\mathrm{d}t \\ &+ \int_0^T \int_\Gamma [G(\mu_f)Q \cdot \nabla R \cdot n - R \cdot G(\mu_f)\nabla Q \cdot n]\,\mathrm{d}s\,\mathrm{d}t. \end{aligned}$$

Inserting Boundary Conditions leads to

$$\begin{aligned} a(H,Q,p,R) = &\int_0^T \int_\Omega -\frac{\partial p}{\partial t} H \,\mathrm{d}x\,\mathrm{d}t + \int_\Omega [H(x,T)p(x,T) - H_0 p(x,0)]\,\mathrm{d}x \\ &- \int_0^T \int_\Omega Q \cdot \nabla p \,\mathrm{d}x\,\mathrm{d}t + \int_0^T \int_{\Gamma_2} pQ \cdot n \,\mathrm{d}s\,\mathrm{d}t \\ &- \int_0^T \int_\Omega \frac{1}{2} g H^2 \nabla \cdot R \,\mathrm{d}x\,\mathrm{d}t - \int_0^T \int_\Omega (H+z)\nabla \cdot (\mu_v \nabla p)\,\mathrm{d}x\,\mathrm{d}t \\ &+ \int_0^T \int_{\Gamma_2} -p\mu_v \nabla (H_1 + z) \cdot n \,\mathrm{d}s\,\mathrm{d}t \\ &+ \int_0^T \int_{\Gamma_1, \Gamma_3} \mu_v (H+z)\nabla p \cdot n \,\mathrm{d}s\,\mathrm{d}t + \int_0^T \int_{\Gamma_2} \mu_v H_1 \nabla p \cdot n \,\mathrm{d}s\,\mathrm{d}t \\ &- \int_0^T \int_\Omega \frac{\partial R}{\partial t} \cdot Q \,\mathrm{d}x\,\mathrm{d}t + \int_\Omega [Q(x,T) \cdot R(x,T) - Q_0 \cdot R(x,0)]\,\mathrm{d}x \\ &- \int_0^T \int_\Omega \frac{Q}{H} \cdot \nabla R \cdot Q \,\mathrm{d}x\,\mathrm{d}t + \int_0^T \int_{\Gamma_2} \frac{Q}{H_1} \cdot RQ \cdot n \,\mathrm{d}s\,\mathrm{d}t \end{aligned}$$

$$
\begin{aligned}
&+\int_0^T\int_{\Gamma_1,\Gamma_3}\frac{1}{2}gH^2R\cdot n\,\mathrm{d}s\,\mathrm{d}t+\int_0^T\int_{\Gamma_2}\frac{1}{2}gH_1^2R\cdot n\,\mathrm{d}s\,\mathrm{d}t\\
&-\int_0^T\int_\Omega Q\cdot\nabla\cdot(G(\mu_f)\nabla R)\,\mathrm{d}x\,\mathrm{d}t+\int_0^T\int_{\Gamma_1,\Gamma_2,\Gamma_3}G(\mu_f)Q\nabla R\cdot n\,\mathrm{d}s\,\mathrm{d}t\\
&+\int_0^T\int_\Omega gH\nabla z\cdot R\,\mathrm{d}x\,\mathrm{d}t.
\end{aligned}
$$

Differentiating for the state variable H leads to

$$
\begin{aligned}
\frac{\partial a(H,Q,p,R)}{\partial H}=&\int_0^T\int_\Omega-\frac{\partial p}{\partial t}\,\mathrm{d}x\,\mathrm{d}t+\int_\Omega p(x,T)\,\mathrm{d}x\\
&+\int_0^T\int_\Omega-\nabla\cdot(\mu_v\nabla p)\,\mathrm{d}x\,\mathrm{d}t+\int_0^T\int_{\Gamma_1,\Gamma_3}[\mu_v\nabla p\cdot n]\,\mathrm{d}s\,\mathrm{d}t\\
&+\int_0^T\int_\Omega\frac{Q}{H^2}\cdot\nabla R\cdot Q\,\mathrm{d}x\,\mathrm{d}t\\
&+\int_0^T\int_\Omega-gH\nabla\cdot R\,\mathrm{d}x\,\mathrm{d}t+\int_0^T\int_{\Gamma_1,\Gamma_3}gHR\cdot n\,\mathrm{d}s\,\mathrm{d}t\\
&+\int_0^T\int_\Omega g\nabla z\cdot R\,\mathrm{d}x\,\mathrm{d}t
\end{aligned}
$$

and for Q to

$$
\begin{aligned}
\frac{\partial a(H,Q,p,R)}{\partial Q}=&\int_0^T\int_\Omega-\frac{\partial R}{\partial t}\,\mathrm{d}x\,\mathrm{d}t+\int_\Omega R(x,T)\,\mathrm{d}x\\
&-\int_0^T\int_\Omega\nabla p\,\mathrm{d}x\,\mathrm{d}t+\int_0^T\int_{\Gamma_2}pn\,\mathrm{d}s\,\mathrm{d}t\\
&-\int_0^T\int_\Omega\frac{1}{H}(\nabla R)^TQ-\frac{1}{H}(Q\cdot\nabla)RQ\,\mathrm{d}x\,\mathrm{d}t\\
&+\int_0^T\int_{\Gamma_2}\frac{1}{H_1}(Q\cdot n)R\,\mathrm{d}s\,\mathrm{d}t+\int_0^T\int_{\Gamma_2}\frac{1}{H_1}(QR)\cdot n\,\mathrm{d}s\,\mathrm{d}t\\
&+\int_0^T\int_\Omega-\nabla\cdot(G(\mu_f)\nabla R)\,\mathrm{d}x\,\mathrm{d}t+\int_0^T\int_{\Gamma_1,\Gamma_2,\Gamma_3}G(\mu_f)\nabla Rn\,\mathrm{d}s\,\mathrm{d}t.
\end{aligned}
$$

Now if $\frac{\partial a(H,Q,p,R)}{\partial U}=-\frac{\partial J_{1,2}}{\partial U}$ then $\frac{\partial\mathcal{L}}{\partial U}=0$ is fulfilled. From this we get the adjoint in strong form with boundary and terminal conditions (5.20)-(5.23). □

The obtained adjoint equations can be written in vector form as

$$
-\frac{\partial P}{\partial t}+AP_x+BP_y+CP-\nabla\cdot(G(\mu)\nabla P)=S, \tag{5.24}
$$

where

$$
A=\begin{pmatrix}0&\frac{Q_1}{H^2}-gH&\frac{Q_1Q_2}{H^2}\\-1&-2\frac{Q_1}{H}&-\frac{Q_2}{H}\\0&0&-\frac{Q_1}{H}\end{pmatrix},\quad B=\begin{pmatrix}0&\frac{Q_1Q_2}{H^2}&\frac{Q_2^2}{H^2}-gH\\0&-\frac{Q_2}{H}&0\\-1&-\frac{Q_1}{H}&-2\frac{Q_2}{H}\end{pmatrix} \tag{5.25}
$$

and C originates from variations in the sediment in (5.6) such that

$$C = \begin{pmatrix} 0 & g\frac{\partial z}{\partial x} & g\frac{\partial z}{\partial y} \\ 0 & 0 & 0 \\ 0 & 0 & 0 \end{pmatrix}. \tag{5.26}$$

Finally, S corresponds to the right hand-side of (5.20).

Remark. If one desires to include additional sources, e.g. accounting for sediment friction, C from (5.26) would need to be adjusted.

Theorem 5.3. *(Shape Derivative) Assume that the parabolic PDE problem (5.4) is H^1-regular, so that its solution U is at least in $H^1(\Omega \times (0,T))^3$. Moreover, assume that the adjoint equation (5.20) admits a solution $P \in H^1(\Omega \times (0,T))^3$. Then the shape derivative of the objectives $J_{1,2}(\Omega)$ (without friction term) in the direction V is given by*

$$\begin{aligned} DJ_{1,2}(\Omega)[V] = \int_0^T \int_\Omega \Big[& -(\nabla V)^T : \nabla Q p - (\nabla V)^T : \nabla Q \frac{Q}{H} \cdot R - (\nabla V Q \cdot \nabla)\frac{Q}{H} \cdot R \\ & -gH(\nabla V)^T \nabla H \cdot R - \mu_v \nabla (H+z)^T (\nabla V + \nabla V^T) \nabla p \\ & -G(\mu_f)\nabla Q \nabla V : \nabla R - G(\mu_f)\nabla Q \nabla V^T : \nabla R \\ & -gH\nabla V^T \nabla z \cdot R + \operatorname{div}(V)\Big\{ \frac{\partial H}{\partial t} p + \nabla \cdot Q p + \frac{\partial Q}{\partial t} \cdot R \\ & +(Q \cdot \nabla)\frac{Q}{H} \cdot R + \nabla \cdot Q \frac{Q}{H} \cdot R + \frac{1}{2} g \nabla H^2 \cdot R + gH \nabla z \cdot R \\ & +\mu_v \nabla (H+z) \cdot \nabla p + G(\mu_f)\nabla Q : \nabla R \Big\} \Big] \, \mathrm{d}x \, \mathrm{d}t. \end{aligned} \tag{5.27}$$

Proof. We regard the Lagrangian (5.18). Following the same arguments as in proof of Theorem 4.4, we now apply the rule (3.22) for differentiating domain integrals, alongside with boundary conditions

$$\begin{aligned} & d\mathcal{L}(\Omega, U, P) = \\ & = \lim_{\epsilon \to 0^+} \frac{\mathcal{L}(\Omega_\epsilon; U, P) - \mathcal{L}(\Omega; U, P)}{\epsilon} \\ & = \frac{d^+}{d\epsilon} \mathcal{L}(\Omega_\epsilon, U, P)\big|_{\epsilon=0} = \frac{d^+}{d\epsilon} \mathcal{L}(\Omega_\epsilon, H, Q, p, R)\big|_{\epsilon=0} \\ & = \int_\Omega \Big[\int_0^T -D_m \left(\frac{\partial p}{\partial t} H \right) \mathrm{d}t + D_m \left(H(x,T)p(x,T) - H_0 p(x,0) \right) \\ & - \int_0^T D_m \left(\frac{\partial R}{\partial t} \cdot Q \right) \mathrm{d}t + D_m \left(Q(x,T) \cdot R(x,T) - Q_0 \cdot R(x,0) \right) \\ & + \int_0^T D_m \left(\nabla \cdot Q p \right) \mathrm{d}t + \int_0^T D_m \left(\mu_v \nabla (H+z) \cdot \nabla p \right) \mathrm{d}t \\ & + \int_0^T D_m \left(\nabla \cdot \left(\frac{Q}{H} \otimes Q \right) \cdot R \right) \mathrm{d}t + \int_0^T + D_m \left(\frac{1}{2} g \nabla H^2 \cdot R \right) \mathrm{d}t \end{aligned}$$

$$
\begin{aligned}
&+ \int_0^T D_m\left(G(\mu_f)\nabla Q : \nabla R\right) \mathrm{d}t + \int_0^T D_m\left(gH\nabla z \cdot R\right) \mathrm{d}t \\
&+ \operatorname{div}(V)\Big(\int_0^T -\frac{\partial p}{\partial t} H \,\mathrm{d}t + H(x,T)p(x,T) - H_0 p(x,0) \\
&+ \int_0^T -\frac{\partial R}{\partial t} \cdot Q \,\mathrm{d}t + Q(x,T)\cdot R(x,T) - Q_0 \cdot R(x,0) + \int_0^T \nabla \cdot Qp \,\mathrm{d}t \\
&+ \int_0^T \mu_v \nabla(H+z)\cdot \nabla p \,\mathrm{d}t + \int_0^T \nabla \cdot \left(\frac{Q}{H}\otimes Q\right)\cdot R \,\mathrm{d}t \\
&+ \int_0^T \frac{1}{2} g \nabla H^2 \cdot R \,\mathrm{d}t + \int_0^T G(\mu_f)\nabla Q : \nabla R + \int_0^T gH\nabla z \cdot R \,\mathrm{d}t\Big)\Big] \,\mathrm{d}x \\
&+ \int_{\Gamma_1} \Big[\int_{\tilde{T}} D_m\left(\nu_1 E \sigma_\alpha(H - H_{\mathrm{cr}})\right) \mathrm{d}t + \int_0^T D_m\left(\frac{\nu_2}{2}||Q||_2^2\right) \mathrm{d}t \\
&+ \operatorname{div}_{\Gamma_1}(V)\left(\int_{\tilde{T}} \nu_1 E \sigma_\alpha(H - H_{\mathrm{cr}}) \,\mathrm{d}t + \int_0^T \frac{\nu_2}{2}||Q||_2^2 \,\mathrm{d}t\right)\Big] \,\mathrm{d}s \\
&+ \int_{\Gamma_2} \Big[\int_0^T -D_m\left(\mu_v \nabla(H_1 + z)\cdot np \,\mathrm{d}t\right) \\
&+ \operatorname{div}_{\Gamma_2}(V)\Big(\int_0^T -\mu_v \nabla(H_1+z)\cdot np \,\mathrm{d}t\Big)\Big] \,\mathrm{d}s,
\end{aligned}
$$

where $\operatorname{div}_\Gamma V = \operatorname{div} V - n\cdot(\nabla V)n$ is the tangential divergence of the vector field V as introduced in Lemma 3.14. Now the product rule (3.24) yields

$$
\begin{aligned}
&= \int_\Omega \Big[\int_0^T -D_m\left(\frac{\partial p}{\partial t}\right) H - \frac{\partial p}{\partial t}\dot{H} \,\mathrm{d}t \\
&+ \dot{H}(x,T)p(x,T) + H(x,T)\dot{p}(x,T) - H_0\dot{p}(x,0) \\
&+ \int_0^T D_m\left(\frac{\partial R}{\partial t}\right)\cdot Q - \frac{\partial R}{\partial t}\cdot \dot{Q} \,\mathrm{d}t + \dot{Q}(x,T)\cdot R(x,T) \\
&+ Q(x,T)\cdot \dot{R}(x,T) - Q_0 \cdot \dot{R}(x,0) + \int_0^T \dot{p}\cdot\nabla\cdot Q + pD_m(\nabla\cdot Q) \,\mathrm{d}t \\
&+ \int_0^T \left(\mu_v D_m(\nabla(H+z))\cdot\nabla p + \mu_v \nabla(H+z)\cdot D_m(\nabla p)\right) \mathrm{d}t \\
&- \int_0^T D_m\left(\nabla\cdot\left(\frac{Q}{H}\otimes Q\right)\right)\cdot R \,\mathrm{d}t + \int_0^T \nabla\cdot\left(\frac{Q}{H}\otimes Q\right)\cdot D_m\left(R\right) \mathrm{d}t \\
&+ \int_0^T \left(\frac{1}{2} g D_m(\nabla H^2)\cdot R + \frac{1}{2} g \nabla H^2 \cdot D_m(R)\right) \mathrm{d}t \\
&+ \int_0^T \left(D_m\left(G(\mu_f)\nabla Q\right) : \nabla R + G(\mu_f)\nabla Q : D_m\left(\nabla R\right)\right) \mathrm{d}t \\
&+ \int_0^T g\dot{H}\nabla z \cdot R \,\mathrm{d}t + \int_0^T gH D_m(\nabla z)\cdot R \,\mathrm{d}t + \int_0^T gH\nabla z\cdot \dot{R} \,\mathrm{d}t \\
&+ \quad \operatorname{div}(V)\Big(\int_0^T -\frac{\partial p}{\partial t} H \,\mathrm{d}t + H(x,T)p(x,T) - H_0 p(x,0)
\end{aligned}
$$

$$
\begin{aligned}
&+\int_0^T -\frac{\partial R}{\partial t}\cdot Q\,\mathrm{d}t + Q(x,T)\cdot R(x,T) - Q_0\cdot R(x,0) + \int_0^T p\nabla\cdot Q\,\mathrm{d}t\\
&+\int_0^T \mu_v\nabla(H+z)\cdot\nabla p\,\mathrm{d}t + \int_0^T \nabla\cdot\left(\frac{Q}{H}\otimes Q\right)\cdot R\,\mathrm{d}t\\
&+\int_0^T +\frac{1}{2}g\nabla H^2\cdot R\,\mathrm{d}t + \int_0^T G(\mu_f)\nabla Q:\nabla R + \int_0^T gH\nabla z\cdot R\,\mathrm{d}t\Big)\Big]\,\mathrm{d}x\\
&+\int_{\Gamma_1}\Big[\int_{\tilde{T}}\nu_1\left(\frac{1}{4}g\rho H\sigma_{\alpha,H_{\mathrm{cr}}}(H) + E\sigma_{\alpha,H_{\mathrm{cr}}}(H)(1-\sigma_{\alpha,H_{\mathrm{cr}}}(H))\right)\dot{H}\,\mathrm{d}t\\
&+\int_0^T \nu_2 Q\cdot\dot{Q}\,\mathrm{d}t\\
&+\quad \mathrm{div}_{\Gamma_1}(V)\left(\int_{\tilde{T}}\nu_1 E\sigma_{\alpha,H_{\mathrm{cr}}}(H)\,\mathrm{d}t + \int_0^T \frac{\nu_2}{2}||Q||_2^2\,\mathrm{d}t\right)\Big]\,\mathrm{d}s\\
&+\int_{\Gamma_2}\Big[\int_0^T -\mu_v\nabla(H_1+z)\cdot n\dot{p}\,\mathrm{d}t + \mathrm{div}_{\Gamma_2}(V)\Big(\int_0^T -\mu_v\nabla(H_1+z)\cdot np\,\mathrm{d}t\Big)\Big]\,\mathrm{d}s.
\end{aligned}
$$

The non-commuting of the material derivative (3.25), (3.26) and (3.27) such as integration by parts, regrouping and the fact that the sediment moves along with the deformation leads to

$$
\begin{aligned}
&=\int_{\Gamma_1}\Big[\int_{\tilde{T}}\left(\frac{1}{4}g\rho H\sigma_{\alpha,H_{\mathrm{cr}}}(H) + E\sigma_{\alpha,H_{\mathrm{cr}}}(H)(1-\sigma_{\alpha,H_{\mathrm{cr}}}(H))\right)\dot{H}\,\mathrm{d}t\\
&+\int_0^T \nu_2 Q\cdot\dot{Q}\,\mathrm{d}t\Big]\,\mathrm{d}s\\
&+\int_\Omega\Big[\int_0^T\Big(-\frac{\partial p}{\partial t} + \frac{1}{H^2}(Q\cdot\nabla)R\cdot Q - gH(\nabla\cdot R) - \nabla\cdot(\mu_v\nabla p) + g\nabla z\cdot R\Big)\dot{H}\\
&+\left(-\frac{\partial R}{\partial t} - \nabla p - \frac{1}{H}(Q\cdot\nabla)R - \frac{1}{H}(\nabla R)^T Q - (\nabla\cdot(G(\mu_f)\nabla R))\right)\cdot\dot{Q}\\
&+\left(\frac{\partial H}{\partial t} + \nabla\cdot(Q - \mu_v\nabla(H+z))\right)\dot{p}\\
&+\left(\frac{\partial Q}{\partial t} + \nabla\cdot\left(\frac{Q}{H}\otimes Q + \frac{1}{2}gH^2\mathbf{I}_2 - G(\mu_f)\nabla Q\right) + gH\nabla z\right)\cdot\dot{R}\,\mathrm{d}t\Big]\,\mathrm{d}x\\
&+\int_\Omega\int_0^T\Big[-(\nabla V)^T:\nabla Q p - (\nabla V)^T:\nabla Q\frac{Q}{H}\cdot R - (\nabla V Q\cdot\nabla)\frac{Q}{H}\cdot R\\
&-gH(\nabla V)^T\nabla H\cdot R - \mu_v\nabla(H+z)^T(\nabla V + \nabla V^T)\nabla p\\
&-G(\mu_f)\nabla Q\nabla V:\nabla R - G(\mu_f)\nabla Q\nabla V^T:\nabla R\\
&-gH\nabla V^T\nabla z\cdot R + \mathrm{div}(V)\Big\{\frac{\partial H}{\partial t}p + \nabla\cdot Qp + \frac{\partial Q}{\partial t}\cdot R\\
&+(Q\cdot\nabla)\frac{Q}{H}\cdot R + \nabla\cdot Q\frac{Q}{H}\cdot R + \frac{1}{2}g\nabla H^2\cdot R + gH\nabla z\cdot R\\
&+\mu_v\nabla(H+z)\cdot\nabla p + (G(\mu_f)\nabla Q):\nabla R\Big\}\Big]\,\mathrm{d}x\,\mathrm{d}t\\
&+\int_{\Gamma_1}\mathrm{div}_{\Gamma_1}(V)\Big[\int_{\tilde{T}}\nu_1 E\sigma_{\alpha,H_{\mathrm{cr}}}(H)\,\mathrm{d}t + \int_0^T\frac{\nu_2}{2}||Q||_2^2\,\mathrm{d}t\Big]\,\mathrm{d}s
\end{aligned}
$$

$$+\int_{\Gamma_2} \operatorname{div}_{\Gamma_2}(V)\Big[\int_0^T -\mu_v \nabla(H_1+z)\cdot np\,\mathrm{d}t\Big]\,\mathrm{d}s.$$

Since outer boundaries are not variable, in general the deformation field V vanishes in small neighborhoods around Γ_1, Γ_2 and the material derivative is zero, hence the boundary integrals vanish. In addition, evaluating the Lagrangian in its saddle point, the first integrals vanish such that we obtain the shape derivative in its final form. □

For the shape derivatives of the volume penalty and the perimeter regularization we refer to equations (4.52) and (4.53) of the previous chapter. In addition, we define the shape derivative of the thinness penalty (5.14) as [4]

$$\begin{aligned} DJ_5(\Omega)[V] \quad = \nu_5 \int_{\Gamma_3} \int_0^{d_{min}} \Big[V(x)\cdot\vec{n}(x)\Big\{ \kappa_m(x)(d_\Omega\,(x_m)^+)^2 \\ +2d_\Omega(x_m)^+ \nabla d_\Omega(x_m)\cdot\nabla d_\Omega(x)\Big\} \\ -V(p_{\partial\Omega}(x_m))\cdot\vec{n}(p_{\partial\Omega}(x_m))2(d_\Omega(x_m))^+\Big]\,\mathrm{d}\xi\,\mathrm{d}s \end{aligned} \tag{5.28}$$

for additive curvature κ_m of Lemma 3.14 and offset point $x_m = x - \xi n(x)$, where we require the shape derivative of the SDF [4]

$$Dd_\Omega(x)[V] = -V(p_{\partial\Omega}(x))\cdot\vec{n}(p_{\partial\Omega}(x)) \tag{5.29}$$

with operator $p_{\partial\Omega}$ that projects a point $x \in \Omega$ onto its closest boundary and holds for all $x \notin \Sigma$, where Σ is referred to as the ridge, where the minimum in (5.16) is obtained by two distinct points.

5.4 Numerical Results

We first discuss the implementation in detail, before applying these techniques to selected examples in the following subsections.

5.4.1 Implementation Details

We rely on the classical structure of adjoint-based shape optimization algorithms that was presented in Section 4.4 and is extended for the newly introduced objectives and penalty term in (5.9).

Algorithm 3 Shape Optimization Algorithm

Initialization
while $||DJ(\Omega_k)[V]|| > \epsilon_{TOL}$ **do**
1. Calculate SDF w_k [via AABBT]
2. Calculate State U_k [via (5.30)]
3. Calculate Adjoint P_k [via (5.30)]
4. Calculate Gradient W_k [via $DJ_{1,2,3,4,5}(\Omega)[V]$ & Linear Elasticity (4.54)]
5. Perform Linesearch for $\tilde{W}_k$
6. Calculate Ω_{k+1} [via $\tilde{W}_k$ and (3.33)]

end while

The solution to the SDF in (5.14) is mesh-dependent. For a mesh with undiscretized obstacle the SDF is approximated via axes-aligned-bounding-boxes trees (AABBT) [6] on a background mesh. We refer to Figure 5.3 for an exemplifying visualization. Note, we have highlighted the initial boundary mesh points in red, exemplifying offset points in blue such as mesh and background mesh in the left figure. In the right figure due to visibility, the distance of background nodes to all exterior boundaries of the original mesh is measured. Likewise based on AABBT the boundary projection, needed in (5.29) is

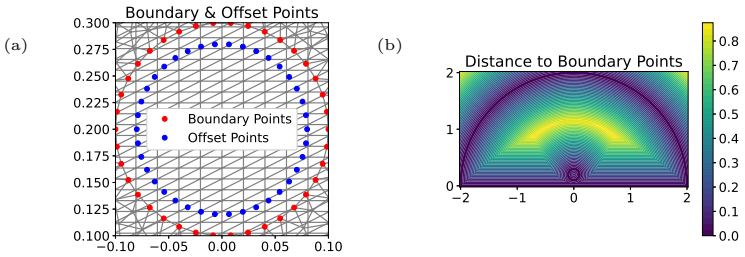

Figure 5.3: (a) Boundary and Offset Points on Mesh and Background Mesh, (b) Distance to Boundary Points via AABBT

computed using affine subspaces. Exemplary results for the closest distance of arbitrary points to the exterior of our basic mesh are visualized in Figure 5.4.

We solve the boundary value problem (5.4), the adjoint problem (5.20) and the deformation of the domain with the help of the finite element solver FEniCS [6], which is detailed in the following. For the time discretization we choose between implicit and explicit integration arising from theta-methods that are known from Definition 2.59. High accuracy for the spatial discretization is achieved using a symmetric interior penalty Galerkin (SIPG), that was introduced in Definition 2.55 for diffusive terms and utilizes (2.116) for advective terms. The discretization then reads for solution and test-function in conformal space to the associated broken Sobolev space $U_h, P_h \in W_h \subset \mathcal{H}^1(\mathcal{T}_h \times$

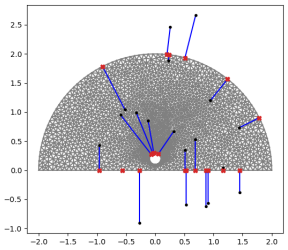

Figure 5.4: Closest Point Projection for Initial Point in Black and Projected Point in Red

$(0,T))^3$ with $\underline{[\![U]\!]} = U^+ \otimes n^+ + U^- \otimes n^-$ as

$$\begin{aligned} N_h(U_h,P_h) = \int_0^T \int_\Omega \Big[\frac{\partial U_h}{\partial t} \cdot P_h - F(U_h) : \nabla_h P_h + G(\mu)\nabla_h(\hat{U}_h) : \nabla_h P_h \\ - S(U_h)\cdot P_h \Big] \,\mathrm{d}x\,\mathrm{d}t + \int_0^T \sum_{\kappa\in\mathcal{T}_h} \int_{\partial\kappa\setminus\Gamma} \mathcal{F}(U_h^+, U_h^-, n)\cdot P_h^+ \,\mathrm{d}s\,\mathrm{d}t \\ + \int_0^T \int_{\mathcal{F}_h^i} \Big[\underline{\delta_h} : \underline{[\![P_h]\!]} - \{\{G(\mu)\nabla_h(P_h)\}\} : \underline{[\![\hat{U}_h]\!]} \\ - \{\{G(\mu)\nabla_h(\hat{U}_h)\}\} : \underline{[\![P_h]\!]} \Big] \,\mathrm{d}s\,\mathrm{d}t + N_{\Gamma,h}(U_h,P_h) = 0, \end{aligned} \tag{5.30}$$

where the numerical flux function $\mathcal{F} : [T(\mathcal{T}_h)]^3 \times [T(\mathcal{T}_h)]^3 \times [T(\mathcal{T}_h)]^2 \to [T(\mathcal{T}_h)]^3$ defines the fluxes at the discontinuous cell transitions, incorporating specific quantities at the respective boundaries and can be chosen as one of the fluxes that were listed in Definition 2.58. Hence, for the advective flux, the required SWE Jacobian is obtained for $\mathcal{J}_i(U) := \partial_U F_i(U)$ with

$$\mathcal{J}_1(U) = \begin{pmatrix} 0 & 1 & 0 \\ -\frac{Q_1^2}{H^2} + gH & 2\frac{Q_1}{H} & 0 \\ -\frac{Q_1Q_2}{H^2} & \frac{Q_2}{H} & \frac{Q_1}{H} \end{pmatrix} \quad \mathcal{J}_2(U) = \begin{pmatrix} 0 & 0 & 1 \\ -\frac{Q_1Q_2}{H^2} & \frac{Q_2}{H} & \frac{Q_1}{H} \\ -\frac{Q_2^2}{H^2} + gH & 0 & 2\frac{Q_2}{H} \end{pmatrix}, \tag{5.31}$$

where we obtain the following eigenvalues

$$\begin{aligned} \lambda(n_1\mathcal{J}_1 + n_2\mathcal{J}_2) &= \{\lambda_1,\lambda_2,\lambda_3\} \\ &= \{un_1 + vn_2 - c, un_1 + vn_2, un_1 + vn_2 + c\}, \end{aligned} \tag{5.32}$$

where $c = \sqrt{gH}$ denotes the wave celerity [3].

Remark. From (5.32) and Definition 2.7 also the hyperbolicity for the shallow water system is obtained, i.e. $\lambda_i \in \mathbb{R}$ for $i \in \{1,...,3\}$. In addition, if $c \neq 0$ or $H > 0$, we obtain distinct eigenvalues, which lead to strict hyperbolicity.

Remark. For a mesh with discretized obstacle and suitable transitional boundaries the SDF can be based on the solution of the diffusive Eikonal equation with $f(x) = 1$,

$q(x) = 0$

$$\begin{aligned} |\nabla w(x)| - \mu_{SDF}\Delta w(x) &= f(x) \qquad x \in \Omega \\ w(x) &= q(x) \qquad x \in \partial\Omega, \end{aligned} \tag{5.33}$$

written in weak form as

$$\int_\Omega \sqrt{\nabla w \cdot \nabla w} v \,\mathrm{d}x - \int_\Omega f v \,\mathrm{d}x + \int_\Omega \mu_{SDF} \nabla w \cdot \nabla v \,\mathrm{d}x = 0, \tag{5.34}$$

where $w \in H^1(\Omega)$ for all $v \in H^1(\Omega)$ and $\mu_{SDF} = \max\{h_e\}_{e\in\{1,\dots,N_{el}\}}$ is dependent on the maximum cell-diameter h_e of element $\kappa_e \in \mathcal{T}_h$. In this setting, the diffusive Eikonal equation can serve as an additional constraint to (5.10)-(5.14) and be considered in adjoint-based shape optimization.

Remark. In the presence of sources, especially for a discontinuous sediment z, a well-balanced numerical scheme is only obtained by methods of flux balancing. For this, the method presented in [183] is extended to two dimensions. In addition, diffusive terms introduced in (5.4) cancel naturally in still water conditions. Finally, numerical flux functions from Definition 2.58 are redefined. We refer to this in detail in Section 6.4.2, where we extend results to porous SWE.

In (5.30) we define the penalization term for the viscous fluxes as in Definition 2.55

$$\underline{\delta}_h(\hat{U}_h) = C_{IP}\frac{k^2}{h}\{\{G(\mu)\}\}\underline{[\![\hat{U}_h]\!]}, \tag{5.35}$$

where $C_{IP} > 0$ is a constant, $k > 0$ the polynomial order of the DG method and $h > 0$ the maximum mesh diameter. What is remaining in (5.30) is the specification of the boundary term, here we state that

$$\begin{aligned} N_{\Gamma,h}(U_h, P_h) = &\int_0^T \int_\Gamma \mathcal{F}(U_h^+, U_\Gamma(U_h^+), n) \cdot P_h^+ \,\mathrm{d}s\,\mathrm{d}t \\ &+ \int_0^T \int_{\Gamma_N} \Big[\underline{\delta}_\Gamma(\hat{U}_h^+) : P_h \otimes n + G(\mu^+)\nabla_h(\hat{U}_h^+) : P_h^+ \otimes n \\ &- G(\mu^+)\nabla_h V_h^+ : (\hat{U}_h^+ - U_\Gamma(\hat{U}_h^+)) \otimes n\Big] \,\mathrm{d}s\,\mathrm{d}t, \end{aligned} \tag{5.36}$$

where Γ_N are all boundaries of type Neumann. Additionally, we define

$$\underline{\delta}_\Gamma(U_h^+) = C_{IP} G(\mu^+)\frac{k^2}{h}(U_h^+ - U_\Gamma(U_h^+)) \otimes n \tag{5.37}$$

$$\mathcal{F}(U_h^+, U_\Gamma(U_h^+), n) = \frac{1}{2}[n \cdot F(U_h^+) + n \cdot F(U_\Gamma(U_h^+))]. \tag{5.38}$$

For the pure advective SWE open and rigid-wall boundary functions are defined as in [3]. Having obtained a discretized solution for the forward problem, we calculate the SWE-adjoint problem in the same manner using a DG discretization in space and a member of the theta-method for the time discretization. For this we rewrite the vector form of the SWE-adjoint (5.24) with the help of the product rule, i.e.

$$\frac{\partial P}{\partial t} - \nabla \cdot (AP, BP) - \tilde{C}P + \nabla \cdot (G(\mu)\nabla P) = -S, \tag{5.39}$$

where $\tilde{C}$ is defined to be

$$\tilde{C} = C - A_x - B_y. \tag{5.40}$$

The following theorem provides us then with the necessary eigenvalues of the adjoint flux Jacobian $\mathcal{J}_i^* := \partial_P F_i^*(P) = -\partial_P(AP, BP)$.

Theorem 5.4. *(Eigenvalues of the Adjoint Flux Jacobian) The eigenvalues of matrix $B^*(P,n)$ belonging to the adjoint flux Jacobian $\mathcal{J}_i^* := \partial_P F_i^*(P)$ equal the eigenvalues of matrix $B(U,n)$ belonging to the flux Jacobian $\mathcal{J}_i := \partial_U F_i(U)$ for $B(U,n) = \sum_{i=1}^2 n_i \mathcal{J}_i(U)$.*

Proof.

$$\lambda(B(U,n)) = \lambda(\sum_{i=1}^{2} n_i \partial_U F_i(U)) = \lambda(\sum_{i=1}^{2} n_i \partial_P F_i^*(P)) = \lambda(B^*(P,n)) \tag{5.41}$$

since $\sum_{i=1}^2 n_i \partial_U F_i(U) = \sum_{i=1}^2 n_i \partial_P F_i^*(P)^T$ which is due to the linearity of the adjoint system. The determinant-invariance of the transpose-operator then leads to the assertion. □

Remark. The theorem above also provides us with hyperbolicity for the adjoint system. However, the linearity would essentially enable us to solve the system with less expensive methods, which could result in less degrees of freedom. We furthermore highlight that Theorem 5.4 provides us with stability of the numerical scheme for the adjoint equations as well, e.g. if we have chosen the time steps in accordance with the CFL-condition [56, Chapter 3] for explicit time-integration in the forward problem.

The finite element mesh deformation is calculated via solution of the linear elasticity equation (4.54). The volumetric share of the shape derivative then comes from our SWE shape derivative w.r.t. the first two objectives (5.27) and the penalty on the volume (4.52). The surface part comes from the perimeter regularization (4.53) and the thinness constraint (5.28), where we have implemented the numerical attractive equivalent formulations using the definition of Green's tangential formula from Lemma 3.14, i.e.

$$DJ_4(\Omega)[V] = \nu_4 \int_{\Gamma_3} \Big[\nabla \cdot V - \langle \frac{\partial V}{\partial n}, n\rangle\Big] \,\mathrm{d}s \tag{5.42}$$

and

$$\begin{aligned} DJ_5(\Omega)[V] \quad = \nu_5 \int_{\Gamma_3} \int_0^{d_{min}} \Big[& V \cdot \Big\{\nabla((d_\Omega\,(x_m)^+)^2) - \langle \nabla((d_\Omega\,(x_m)^+)^2), n\rangle n\Big\} \\ & + (d_\Omega\,(x_m)^+)^2 \Big\{\nabla \cdot V - \langle \frac{\partial V}{\partial n}, n\rangle\Big\} \\ & + V \cdot \vec{n}\Big\{2 d_\Omega(x_m)^+ \nabla d_\Omega(x_m) \cdot n\Big\} \\ & - V(p_{\partial\Omega}(x_m)) \cdot \vec{n}(p_{\partial\Omega}(x_m)) 2 (d_\Omega(x_m))^+\Big] \,\mathrm{d}\xi \,\mathrm{d}s. \end{aligned} \tag{5.43}$$

Finally, a line search is implemented in accordance with Chapter 4.

5.4.2 Ex.1: The Half-Circled Mesh

In the first example, we will look at the model problem - the half circle that was described in Section 5.2. The associated mesh is displayed in Figure 5.5 and was created using the finite element mesh generator GMSH [85], we have meshed finer around the obstacle to ensure a high resolution. We set Gaussian initial conditions as $\hat{U}_0 = (1 + \exp(-15x^2 - 15(y-1)^2), 0, 0)$, which result in a wave traveling in time towards the boundaries. As before, we interpret $\Gamma_1, \Gamma_2, \Gamma_3$ as coastline, open sea and obstacle boundary. Accordingly, we prescribe the boundary conditions using rigid-wall conditions on Γ_1, Γ_3 and outflow boundaries on Γ_2. The parameters in the shallow water system are set as follows: For the weight of the diffusion terms in the momentum equation we set $\mu_f = (0.01, 0.01)$ and determine μ_v by the usage of the mentioned shock detector from Section 2.3.3. The gravitational acceleration is fixed at roughly 9.81 and the parameter K in Manning's formula is at 0.049 for a sandy beach. Our calculations are performed for two test cases - a linear decreasing bottom $z = 0.5 - 0.25y$ and a non-flat bottom determined by a Gaussian peak $z = \exp(-6(x-0.5)^2 - 6(y-0.2)^2)$, as displayed in Figure 5.5. We are targeting a minimal mechanical wave energy for waves above the water's rest height, such that the energy and sigmoid function are defined in terms of $H + z$ for threshold $H_{\text{cr}} = 1$ and slope parameter $\alpha = 10$ such as zeroed velocities by setting $\nu_1 = \nu_2 = 1$. In addition, we penalize volume and thinness by setting $\nu_3 = 1\text{e}{-4}, \nu_5 = 1\text{e}{-2}$ such as enforcing a stronger regularization by $\nu_4 = 1\text{e}{-4}$. In this example we have used an implicit backward

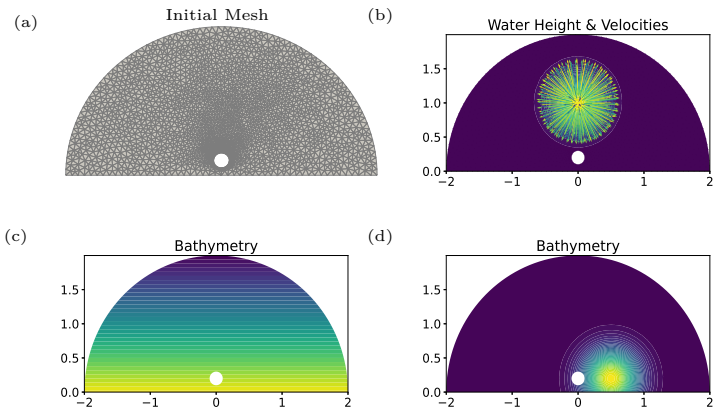

Figure 5.5: (a) Initial Mesh and Obstacle, (b) Field State at $t = 0.1$, (c) Linear Bathymetry, (d) Gaussian Peak Bathymetry

Euler time-scheme and a DG-method of first order that was described before. For the spatial discretization, we have used the HLLE-flux function for the advective terms and $C_{IP} = 20$ in the SIP-DG method. Solving the state equations requires the definition of the time-horizon, e.g. as $\tilde{T} = (0, T) = (0, 2.5)$, which is chosen to include one full wave

period, i.e. the travel of a wave to and from the shore. The discretization in time is based on a step size of $\Delta t = 5\text{e}{-3}$. Due to the nonlinear nature of the SWE we have used a Newton solver, where we set the absolute and relative tolerance as $\epsilon_{abs} = \epsilon_{rel} = 1\text{e}{-6}$. The solution of the adjoint problem follows likewise, but stepping backwards in time. Since the problem is linear, a Newton solver is no longer needed. Having solved state and adjoint equations the mesh deformation is performed as described, where we specify $\mu_{min} = 10$ and $\mu_{max} = 100$ in (4.54). The step size is at $\rho_{step} = 1$ and shrinks whenever criteria for line searches are not met. In Figure 5.6 results of the shape optimization are displayed, firstly for a linear and secondly a Gaussian bottom after 44 and 33 steps of optimization.

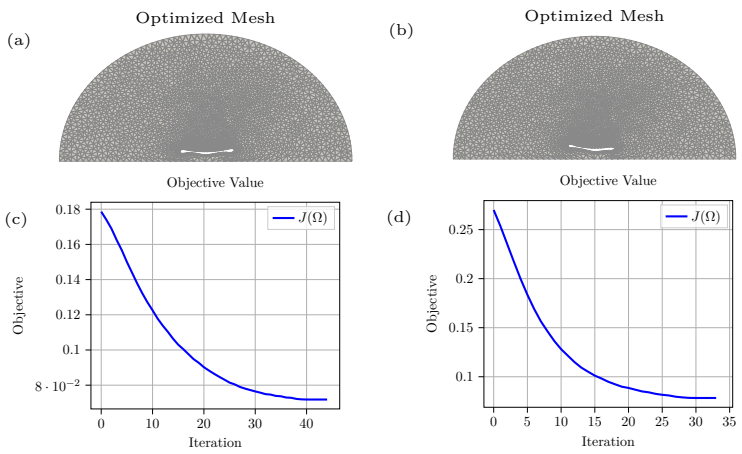

Figure 5.6: (a) Optimized Obstacle for Linear Seabed, (b) Optimized Obstacle for Gaussian Seabed, (c) Objective for Linear Seabed, (d) Objective for Gaussian Seabed

The deformations are symmetric in the first and in the opposing direction of the sediment hill in the second case. As we observe in the lower part of Figure 5.6, we reduce objectives by more than 60% in the first and more than 70% in the second example.

Remark. Interesting investigations could also include periodic lateral boundaries as in Chapter 5. However, as of FEniCS version 2019.1 periodic boundary conditions are not yet supported for *DG*-elements and would need to be manually implemented. We circumvent this by the usage of an half-circled open-sea boundary.

5.4.3 Ex.2: The Langue de Barbarie Mesh

We now regard the LdB coastal section, as described in Section 4.4.3, and interpret Γ_1 as coastline of the mainland and Γ_2 as the open sea boundary. However, this time is the variable boundary Γ_3 placed at the three offshore islands (cf. to Figure 5.8,5.9),

instead at one single artificial offshore island. The handling carries over analogously to the one-obstacle case and we remark that associated extensions for shape spaces are presented in [84]. As before in Section 5.4.2, we start with Gaussian initial conditions for the height of the water. Sediment data is taken from the GEBCO[2] databank, where bathymetric elevation is mapped to a mesh point using a nearest neighbors algorithm. The sediment elevation can be taken from Figure 5.7, while the wave propagation can be extracted from Figure 5.8.

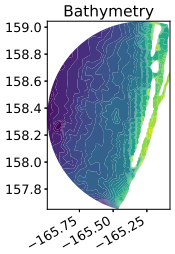

Figure 5.7: LdB Sediment Elevation

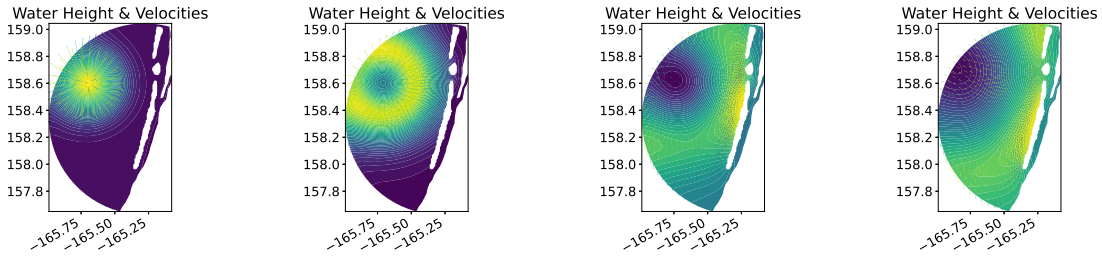

(a) $t = 0$ (b) $t = 0.5$ (c) $t = 1$ (d) $t = 1.5$

Figure 5.8: Visualization of a Wave Described by Height and Velocities, Traveling Towards the Shore for Initial Obstacle.

The remaining model-settings are similar to Subsection 5.4.2. Figure 5.9 pictures initial, such as deformed mesh and obstacle after 30 steps of optimization.

[2]https://www.gebco.net/

(a) Initial Mesh (b) Optimized Mesh

Figure 5.9: Initial and Optimized Mesh and Obstacle

One can observe a similar behavior as in Subsection 5.4.2, where the obstacle is stretched to protect an as large as possible area. In this setting, the optimizer suggests to reconnect the three islands. However, rebuilding the complete island would either call for a re-meshing procedure or an alternative algorithm for shape optimization, e.g. level-sets as described in Section 3.3.2 are capable of similar. We highlight that obtained results must be treated with caution, since rebuilding would require an excessive amount of landmass. In Figure 5.10 the convergence of the objective can be observed.

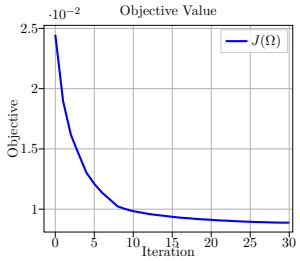

Figure 5.10: Objective for LdB Mesh

5.4.4 Ex.3: The World Mesh

In the third and last example, we extend presented techniques to immersed manifolds, in order to perform global shore protection. For this, we define Ω to be a smooth m-dimensional manifold immersed in R^n, where $m = 2$ denotes the topological dimension and $n = 3$ the geometric dimension. We refer to monograph [1, Chapter 3] for a comprehensive introduction in the field of differential geometry. Assuming a similar setting as before, Γ_1 represents the continent of Africa and Γ_2 the remaining coastal points. In addition, we have placed three initial circled obstacles with boundary Γ_3 in before the shore of West-Africa that serve as obstacle.

From the implementation side we have again used the GSHHG databank to obtain coastal data and mapped the points to a PolarSphere in GMSH (cf. to Figure 5.11). For the discretization we follow [154], from which an extension of the FEniCS software to the scenario above stems from. We aim for a solution in the geometric space i.e. $U_h = (H_h, u_h H_h, v_h H_h, w_h H_h)$ relying on DG-elements, i.e. $DG_1 \times DG_3$, where we weakly

Figure 5.11: High Resolution World Mesh

enforce the vector-valued velocity to be in the spherical tangent space. Alternatively, we could solve in the mixed discrete function space $DG_1 \times RT_1$, where RT_1 denotes Raviar-Thomas finite elements, which lie in the tangent space simple from its construction. We define initial conditions in the geometric space as $U_0 = (2 + \exp(-c(x - x_0)^2 - c(y - y_0)^2 - c(z - z_0)^2), 0, 0, 0)$ for suitable coordinates (x_0, y_0, z_0) and constant c. In contrast to the examples before, open sea boundaries are not required any more, such that all boundaries are subject to rigid boundary conditions. The seabed is for simplicity assumed to be flat. The remaining model-settings are similar to Subsection 5.4.2. The wave propagation is visualized in Figure 5.12.

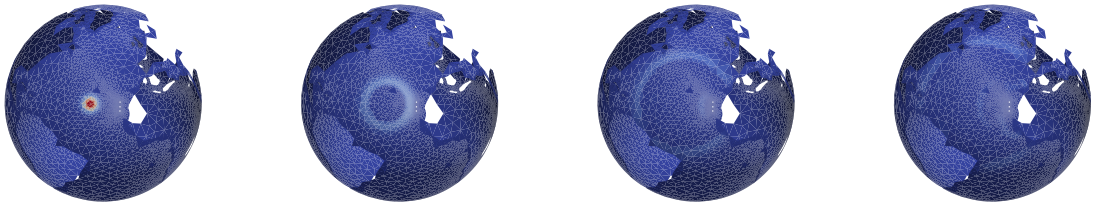

(a) $t = 0$ (b) $t = 0.5$ (c) $t = 1$ (d) $t = 1.5$

Figure 5.12: Visualization of a Wave Described by Height, Traveling Towards the Continents for Initial Obstacle.

For performing shape optimization we remark for completeness that updating the finite element mesh in each iteration is done via the solution $W : \Omega \to \mathbb{R}^3$ of the linear elasticity equation, where we again enforce a tangential solution and hence solve

$$\begin{aligned} \int_\Omega [\sigma(W) : \epsilon(V) - lK \cdot V + W \cdot K\gamma] \, \mathrm{d}x &= DJ(\Omega)[V] \\ \frac{\partial W}{\partial n} &= 0 \qquad \text{on} \qquad \Gamma_3 \\ W &= 0 \qquad \text{on} \qquad \Gamma_1, \Gamma_2 \end{aligned} \tag{5.44}$$

for unit outward normal K to the surface of the manifold, Lagrange multiplier $l \in DG_1$ for all (V, γ) such as σ and ϵ as in (4.54). We would like to highlight that (5.44) represents an elliptic PDE, that can without further ado being solved directly. However,

movements on a manifold would typically call for retractions, e.g. via usage of an exponential mapping [1, Chapter 4]. The resulting deformed obstacles can be seen in Figure 5.13.

(a) Initial Mesh (b) Optimized Mesh

Figure 5.13: Initial and Optimized Mesh and Obstacle

In Figure 5.14 we once more observe convergence of the objective function.

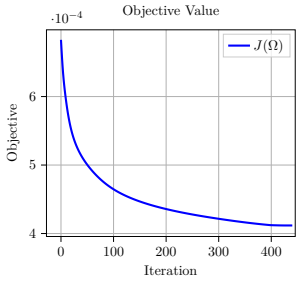

Figure 5.14: Objective for World Mesh

Lastly, we would like to point out that the obtained results are only offering a simplistic analysis to protect the shore of Africa Γ_1, that can be used as a first feasibility study. For a more comprehensive discussion one would need to adapt the model to non-shallow flows, simulate a non-flat seabed and take care on the wetting-drying phenomenon (cf. to Section 9.1). On coastal boundaries Γ_1, Γ_2 and Γ_3 more accurate solutions would be obtained by replacing rigid boundary conditions by partially absorbing boundary conditions. Finally, an extension of Γ_1 to all shores where various waves are produced with multiple obstacles placed before several shorelines, that are all restricted in volume, could lead to more sophisticated conclusions.

Chapter 6

Shape Optimization for Porous Shallow Water Equations

In this chapter we look at porous SWE, which arise from the desire to model regions of mitigated flow velocity. Areas of differing porosity coefficient can be exemplifying interpreted as a permeable obstacle such as a geotextile tube. This extension stands in line with computations performed for the time-independent Helmholtz scatterer for transmissive obstacles in Chapter 4. Porous SWE are being paid increasing attention throughout the last decade, mostly because its ability to perform large-scale urban flood modeling [67]. Over the years a variety of descriptions have been introduced differing in terms of conceptual, mathematical and numerical aspects [91, 156, 143]. Our model mainly builds up on [91], as it can be seen in Section 6.1, such that we are dealing with a single, depth-independent porosity parameter in the definition of the SWE. In addition, we restrict ourselves to isotropic porosity effects, such that the parameter cannot account for directional effects, which forms a legitimate assumption for a geotextile obstacle.
We hereby shortly sketch the novelties of this chapter: We would like to highlight that porous SWE have been modeled mainly by techniques relying on constant cell approximations via finite volume schemes. In this chapter we calculate and derive numerical solutions to porous SWE by high-order DG methods. In this setting once more artificial viscosity is introduced to counter possible oscillations that can appear around a shock location, where the viscosity is physically motivated by extending the viscous SWE to viscous, porous SWE in Section 6.1. To deal with numerical difficulties, that arise due to the discontinuous material coefficient, we extend the notion of a well-balanced DG scheme for classical SWE with discontinuous sediment [183] to porous, diffusive and two-dimensional variants in Section 6.4.2. We show that associated discretizations form the limit of a smoothed approach in Section 6.4.3. In addition, we would like to highlight, that porous SWE have not been investigated in any kind of optimization yet, such that we firstly formulate adjoint and shape derivative for this set of equations and provide an algorithmic handle to this.
The chapter is structured as follows: The derived porous SWE of Section 6.1 serve as a

constraint to obtain a PDE-constrained optimization problem in Section 6.2. To solve this problem the necessary tools are introduced in Section 6.3, by deriving adjoint equations and the shape derivative in volume form. In the final part, we present numerical techniques in Section 6.4 and applications in Section 6.5 for a sample mesh such as a representative mesh for the Mentawai islands in the south-west of Sumatra, Indonesia, that were part of the motivation in Section 1.1.

6.1 PDE Derivation

So far only porous SWE, without additional viscous terms, have been introduced in the literature. Due to this reason, we derive porous SWE, as it has been in done in [91], and extend the derivation for diffusive terms, relying on viscous SWE.

Theorem 6.1. *(Viscous Porous SWE) In the notion of Theorem 5.1 under disregard of diacritics viscous and porous SWE are identified as a system ensuring on* $\Omega \times (0,T)$ *conservation of mass*

$$\frac{\partial(\phi H)}{\partial t} + \frac{\partial(\phi H u)}{\partial x} + \frac{\partial(\phi H v)}{\partial y} = 0, \tag{6.1}$$

x-momentum

$$\begin{aligned} &\frac{\partial(\phi H u)}{\partial t} + \frac{\partial(\phi H u^2)}{\partial x} + \frac{\partial(\phi H uv)}{\partial y} \\ =& -g\phi H \frac{\partial z_0}{\partial x} - g\phi H \frac{\partial H}{\partial x} + g\frac{H^2}{2}\frac{\partial \phi}{\partial x} \\ &+ \frac{\partial}{\partial x}\left(\phi H \mu \frac{\partial u}{\partial x}\right) + \frac{\partial}{\partial y}\left(\phi H \mu \frac{\partial u}{\partial y}\right) - \phi \tau_x^b + \phi \tau_x^s \end{aligned} \tag{6.2}$$

and y-momentum

$$\begin{aligned} &\frac{\partial(\phi H v)}{\partial t} + \frac{\partial(\phi H vu)}{\partial x} + \frac{\partial(\phi H v^2)}{\partial y} \\ =& -g\phi H \frac{\partial z_0}{\partial y} - g\phi H \frac{\partial H}{\partial y} + g\frac{H^2}{2}\frac{\partial \phi}{\partial y} \\ &+ \frac{\partial}{\partial x}\left(\phi H \mu \frac{\partial v}{\partial x}\right) + \frac{\partial}{\partial y}\left(\phi H \mu \frac{\partial v}{\partial y}\right) - \phi \tau_y^b + \phi \tau_y^s. \end{aligned} \tag{6.3}$$

Proof. Assuming a constant water density $\rho = 1$ for porous SWE, the volume of water in a control volume is given by

$$V = \int_{y_0}^{y_0+\delta y} \int_{x_0}^{x_0+\delta x} \phi(x,y) H \,\mathrm{d}x \,\mathrm{d}y \tag{6.4}$$

with x_0, y_0 being the coordinates of the lower left corner of the control volume. Following [91] the continuity equation can be written as

$$\frac{\partial V}{\partial t} - F_{V,W} + F_{V,E} - F_{V,S} + F_{V,N} = 0 \tag{6.5}$$

where $F_{V,W}$ and $F_{V,E}$ denote volume fluxes through western and eastern side, i.e.

$$\begin{aligned} F_{V,W} &= \int_{y_0}^{y_0+\delta y} \phi H u(x_0, y)\,\mathrm{d}y \\ F_{V,E} &= \int_{y_0}^{y_0+\delta y} \phi H u(x_0+\delta x, y)\,\mathrm{d}y \end{aligned} \tag{6.6}$$

such as southern and northern sides

$$\begin{aligned} F_{V,S} &= \int_{x_0}^{x_0+\delta x} \phi H v(x, y_0)\,\mathrm{d}x \\ F_{V,N} &= \int_{x_0}^{x_0+\delta x} \phi H v(x, y_0+\delta y)\,\mathrm{d}x \end{aligned} \tag{6.7}$$

Substituting terms in (6.5) gives

$$\begin{aligned} &\int_{y_0}^{y_0+\delta y}\int_{x_0}^{x_0+\delta x} \frac{\partial(\phi(x,y)H)}{\partial t}\,\mathrm{d}x\,\mathrm{d}y \\ &- \int_{y_0}^{y_0+\delta y} \phi H u(x_0, y)\,\mathrm{d}y + \int_{y_0}^{y_0+\delta y} \phi H u(x_0+\delta x, y)\,\mathrm{d}y \\ &- \int_{x_0}^{x_0+\delta x} \phi H v(x, y_0)\,\mathrm{d}x + \int_{x_0}^{x_0+\delta x} \phi H v(x, y_0+\delta y)\,\mathrm{d}x = 0. \end{aligned} \tag{6.8}$$

When δx and δy tend to 0 it holds that

$$\begin{aligned} \lim_{\delta x\to 0} (\phi H u)(x_0+\delta x, y) - (\phi H u)(x_0, y) &= \delta x \frac{\partial}{\partial x}(\phi H u) \\ \lim_{\delta y\to 0} (\phi H v)(x, y_0+\delta y) - (\phi H v)(x, y_0) &= \delta y \frac{\partial}{\partial y}(\phi H v). \end{aligned} \tag{6.9}$$

The evaluation of the integrals in (6.8) leads to

$$\delta x\delta y \frac{\partial \phi H}{\partial t} + \delta x\delta y \frac{\partial}{\partial x}(\phi H u) + \delta x\delta y \frac{\partial}{\partial y}(\phi H v) = 0, \tag{6.10}$$

which in turn leads to the continuity balance as

$$\frac{\partial \phi H}{\partial t} + \frac{\partial}{\partial x}(\phi H u) + \frac{\partial}{\partial y}(\phi H v) = 0. \tag{6.11}$$

The derivation of the momentum balance is obtained similarly to the continuity equation. We hence will only investigate the inclusion of diffusion in the following. For the rest we refer to reference [91] such that the momentum balance in x-direction can be written as

$$M = \frac{\partial M_x}{\partial t} - F_{M,W} + F_{M,E} - F_{M,S} + F_{M,N} - P_W + P_E - W_x - B_x - R_x = 0 \tag{6.12}$$

where F-terms account for x-momentum fluxes, P-terms for pressure forces, such as W, B and R-terms for porosity influence such as bottom pressure and friction terms

with indices representing the western W, eastern E northern N and southern S sides of the control volume. As mentioned before, limiting values of all quantities are obtained from [91]. For viscous SWE as in [2] this momentum balance is extended by the volume diffusion through the western and eastern side as

$$\begin{aligned} D_W &= -\int_{y_0}^{y_0+\delta y} \mu\phi H u_x(x_0, y)\,\mathrm{d}y \\ D_E &= -\int_{y_0}^{y_0+\delta y} \mu\phi H u_x(x_0+\delta x, y)\,\mathrm{d}y \end{aligned} \tag{6.13}$$

such as southern and northern sides

$$\begin{aligned} D_S &= -\int_{x_0}^{x_0+\delta x} \mu\phi H u_y(x, y_0)\,\mathrm{d}x \\ D_N &= -\int_{x_0}^{x_0+\delta x} \mu\phi H u_y(x, y_0+\delta y)\,\mathrm{d}x, \end{aligned} \tag{6.14}$$

where u_x and u_y denote the first-order spatial partial derivatives with respect to x and y and μ the diffusion coefficient. Momentum balancing these terms then leads to

$$M - D_W + D_E - D_S + D_N = 0. \tag{6.15}$$

Substituting terms in (6.15) gives

$$\begin{aligned} M &+ \int_{y_0}^{y_0+\delta y} \mu\phi H u_x(x_0, y)\,\mathrm{d}y - \int_{y_0}^{y_0+\delta y} \mu\phi H u_x(x_0+\delta x, y)\,\mathrm{d}y \\ &+ \int_{x_0}^{x_0+\delta x} \mu\phi H u_y(x, y_0)\,\mathrm{d}x - \int_{x_0}^{x_0+\delta x} \mu\phi H u_y(x, y_0+\delta y)\,\mathrm{d}x = 0. \end{aligned} \tag{6.16}$$

When δx and δy tend to 0 it holds

$$\begin{aligned} \lim_{\delta x\to 0} (\mu\phi H u_x)(x_0+\delta x, y) - (\mu\phi H u_x)(x_0, y) &= \delta x \frac{\partial}{\partial x}(\mu\phi H u_x) \\ \lim_{\delta y\to 0} (\mu\phi H u_y)(x, y_0+\delta y) - (\mu\phi H u_y)(x, y_0) &= \delta y \frac{\partial}{\partial y}(\mu\phi H u_y). \end{aligned} \tag{6.17}$$

Evaluating integrals leads to

$$\delta x\delta y M - \delta x\delta y \frac{\partial}{\partial x}(\mu\phi H u_x) - \delta x\delta y \frac{\partial}{\partial y}(\mu\phi H u_y) = 0, \tag{6.18}$$

which yields the momentum balance as

$$M - \frac{\partial}{\partial x}(\mu\phi H u_x) - \frac{\partial}{\partial y}(\mu\phi H u_y) = 0 \tag{6.19}$$

The y-momentum is derived in accordance. □

6.2 Model Formulation

Suppose we are given an open domain $\Omega \subset \mathbb{R}^2$, which is split into the disjoint sets $\tilde{\Omega}, D \subset \Omega$ such that $\tilde{\Omega} \cup D \cup \Gamma_3 = \Omega$ and $\Gamma_1 \cup \Gamma_2 = \partial\Omega (=: \Gamma_{out})$. We assume the variable, interior boundary and the fixed outer $\partial\Omega$ to be at least Lipschitz. One simple example was visualized before in Figure 5.1.

On this domain we model water wave and velocity fields as the solution to porous SWE with artificial viscosity. We interpret $\Gamma_1, \Gamma_2, \Gamma_3$ as coastline, open sea and obstacle boundary and solve on $\Omega \times (0, T)$

$$\partial_t(\phi U) + \nabla \cdot (\phi F(U)) - \nabla \cdot (G(f(\phi, \mu))\nabla \hat{U}) = \phi S(U) + S_\phi(U), \tag{6.20}$$

where we are given the porous SWE in vector notation with flux matrix as in (5.4)

$$F(U) = \begin{pmatrix} Q \\ \frac{Q}{H} \otimes Q + \frac{1}{2} g H^2 \mathbf{I}_2 \end{pmatrix} = \begin{pmatrix} Hu & vH \\ Hu^2 + \frac{1}{2} g H^2 & Huv \\ Huv & Hv^2 + \frac{1}{2} g H^2 \end{pmatrix} \tag{6.21}$$

The difference to (5.4) is the inclusion of a possible discontinuous scalar function $\phi : \Omega \times (0, T) \to (0, 1]$ representing the respective portion of space that is available to the flow. We define

$$\phi := \begin{cases} \phi_1 = \text{const. in } \tilde{\Omega} \times (0, T) \\ \phi_2 = \text{const. in } D \times (0, T). \end{cases} \tag{6.22}$$

The setting can be taken from Figure 6.1, where the region with varying porosity factor on D is exemplifying highlighted in gray.

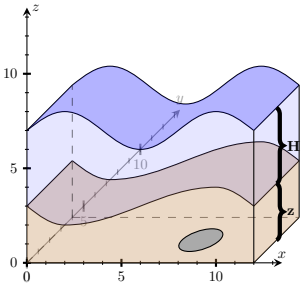

Figure 6.1: Cross-Section for Identification of Wave Height H, Sediment Height z and Obstacle

We define the first source term in (6.20), where we for simplicity disregard bottom frictions opposed to (5.6), as

$$S(U) = \begin{pmatrix} 0 \\ -gH\frac{\partial z}{\partial x} \\ -gH\frac{\partial z}{\partial y} \end{pmatrix}, \tag{6.23}$$

responding to variations in the bed slope. The second source term in (6.20) corresponds to variations in the porosity coefficient and is chosen as [91]

$$S_\phi(U) = \begin{pmatrix} 0 \\ g\frac{H^2}{2}\frac{\partial \phi}{\partial x} \\ g\frac{H^2}{2}\frac{\partial \phi}{\partial y} \end{pmatrix}. \tag{6.24}$$

For the SWE we employ outer boundary conditions as rigid-wall and open sea boundary conditions for Γ_1 and Γ_2 and transmissive interface conditions on $\Gamma_3 \times (0,T)$ for the continuity of the state

$$\begin{aligned} [\![H+z]\!] &= 0 \\ [\![Q_1]\!] &= 0 \\ [\![Q_2]\!] &= 0 \end{aligned} \tag{6.25}$$

the diffusive flux

$$\begin{aligned} [\![\nabla(H+z)\cdot n]\!] &= 0 \\ [\![\phi\nabla(Q_1)\cdot n]\!] &= 0 \\ [\![\phi\nabla(Q_2)\cdot n]\!] &= 0 \end{aligned} \tag{6.26}$$

and the advective flux

$$[\![\phi F(U)\cdot n]\!] = 0 \tag{6.27}$$

i.e.

$$\begin{aligned} [\![\phi Q\cdot n]\!] &= 0 \\ [\![\{\phi Q_1^2/H + 1/2 g\phi H^2; \phi Q_1 Q_2/H\}\cdot n]\!] &= 0 \\ [\![\{\phi Q_1 Q_2/H; \phi Q_2^2/H + 1/2 g\phi H^2\}\cdot n]\!] &= 0 \end{aligned} \tag{6.28}$$

for jump symbol on the interface Γ_3 defined by $[\![H]\!] := H|_{\tilde{\Omega}} - H|_{\tilde{D}}$. In addition, we prescribe to be determined initial conditions on $\Omega \times \{0\}$ as

$$U = U_0. \tag{6.29}$$

Remark. We control the amount of added diffusion by diagonal matrix $G(f(\phi,\mu))$ as defined in Section 5.2 with entries $f(\phi,\mu) = (\mu_v, \phi\mu_f, \phi\mu_f) \in \mathbb{R}^3_+$. In this setting μ_f is fixed to a small value, while we rely on shock detection in the determination of μ_v following [147] introduced in Section 2.3.3. We refer to Section 6.5.1 and 6.5.2 for more detailed information.

Remark. Instead of the derived non-linear formulation in Section 6.1, we will work with linear diffusion in the sense of artificial viscosity, that is for stability also placed on the continuity equation. We would like to highlight that adjoint-based shape optimization for non-linear diffusion can be handled in the same way, leading to additional terms in the adjoint equations and the shape derivative.

Remark. A constant porosity coefficient $\phi_1 = \phi_2$ in (6.20) leads to SWE in the classical form, that are subject for adjoint-based shape optimization in Chapter 5.

In this chapter we replace the minimization of wave energies along the shoreline, but are instead relying on an objective of tracking-type as in Chapter 4. In this setting we aim for rest-conditions of the water. Regions with comparable properties are known to mitigate sediment transport, e.g. as it can be seen in a coupling with equations of Exner-type in Chapter 7. Here we try to meet certain predefined wave height and velocities $\bar{U}$ at the shore Γ_1 weighted by diagonal matrix $N \in \mathbb{R}^{3\times 3}$, such that we minimize objective $J_1 : \Omega \to \mathbb{R}$, where

$$J_1(\Omega) = \int_0^T \int_{\Gamma_1} \frac{1}{2} ||N(\hat{U}(x,t) - \bar{U}(x,t))||_2^2 \,\mathrm{d}s\,\mathrm{d}t. \tag{6.30}$$

This objective is once more supplemented by volume and thinness penalty such as perimeter regularization as described in Section 5.2.

6.3 Derivation of Adjoint & Shape Derivative

We compute the adjoint equations and the shape derivative of the PDE-constrained optimization problem by formulating the Lagrangian

$$\mathcal{L}(\Omega, U, P) = J_1(\Omega) + a(U,P) - b(P), \tag{6.31}$$

where J_1 is objective (6.30), and $a(U,P)$ and $b(P)$ are obtained from boundary value problem (6.20). Here, we rewrite the equations in weak form by multiplying with some arbitrary test function $P \in H^1(\Omega \times (0,T))^3$ obtaining the form $a(U,P) = a(H,Q,p,R)$, which is defined as

$$\begin{aligned}
a(H,Q,p,R) := &\int_0^T \int_\Omega \left[\frac{\partial \phi H}{\partial t} + \nabla \cdot (\phi Q)\right] p \,\mathrm{d}x\,\mathrm{d}t \\
&+ \int_0^T \int_\Omega \mu_v \nabla(H+z)\cdot \nabla p \,\mathrm{d}x\,\mathrm{d}t - \int_0^T \int_{\Gamma_3} [\![\mu_v \nabla(H+z)\cdot np]\!] \,\mathrm{d}s\,\mathrm{d}t \\
&- \int_0^T \int_{\Gamma_2} \mu_v \nabla(H_1+z)\cdot np \,\mathrm{d}s\,\mathrm{d}t \\
&+ \int_0^T \int_\Omega \left[\frac{\partial \phi Q}{\partial t} + \nabla \cdot \left(\phi \frac{Q}{H} \otimes Q + \frac{1}{2} g \phi H^2 \mathbf{I}_2\right)\right] \cdot R \,\mathrm{d}x\,\mathrm{d}t \\
&+ \int_0^T \int_\Omega \mu_f \phi \nabla Q : \nabla R \,\mathrm{d}x\,\mathrm{d}t - \int_0^T \int_{\Gamma_3} [\![\phi \mu_f \nabla Q \cdot n \cdot R]\!] \,\mathrm{d}s\,\mathrm{d}t \\
&+ \int_0^T \int_\Omega g\phi H \nabla z \cdot R \,\mathrm{d}x\,\mathrm{d}t - \int_0^T \int_\Omega g \frac{H^2}{2} \nabla \phi \cdot R \,\mathrm{d}x\,\mathrm{d}t
\end{aligned} \tag{6.32}$$

and a zero perturbation term.

Remark. To deal with well-defined weak forms and to allow us to perform adjoint-based sensitivity analyses we once more assume the flow to be free of discontinuities, e.g. induced by a discontinuous bottom profile z or wave height H. In addition, we need to employ a specific handle to the discontinuous porosity coefficient. As in chapter 4 we follow the convention $\int_\Omega := \int_{\tilde{\Omega}} + \int_D$. In (6.32) and in what follows this decomposition is assumed.

Remark. For the discontinuous coefficient we could rely on a smoothed porosity controlled by $\alpha > 0$, i.e. $\phi = \lim_{\alpha \to 0} \phi_\alpha$, e.g. by using smoothed cell transitions or mollifiers [72, p. 629-630]. In this setting we could integrate over the whole domain Ω. Such a handle would call for the necessity to show convergence results for state, adjoint and shape derivative. Furthermore, we remark that a smoothing approach is presented in one dimension in Section 6.4.3, where we have used a smoothed step-function. Here interface conditions would not be required in the continuous form.

We obtain state equations from differentiating the Lagrangian w.r.t. P and the auxiliary problem, the adjoint equations, from differentiating the Lagrangian with respect to the states U. The adjoint is formulated in the following theorem:

Theorem 6.2. *(Adjoint) Assume that the parabolic PDE problem (6.20) is H^1-regular, so that its solution U is at least in $H^1(\Omega \times (0,T))^3$. Then the adjoint in strong form with solution $P = (p, R) \in H^1(\Omega \times (0,T))^3$ is given by*

$$\begin{aligned} \phi\Big[-\frac{\partial p}{\partial t} + \frac{1}{H^2}(Q \cdot \nabla)R \cdot Q - gH(\nabla \cdot R) + g\nabla z \cdot R\Big] \\ -\nabla \cdot (\mu_v \nabla p) - gH\nabla\phi \cdot R = -N_{11}((H+z) - \bar{H})_{\Gamma_1} \end{aligned} \tag{6.33}$$

and

$$\begin{aligned} \phi\Big[-\frac{\partial R}{\partial t} - \nabla p - \frac{1}{H}(Q \cdot \nabla)R - \frac{1}{H}(\nabla R)^T Q\Big] \\ -\nabla \cdot (\mu_f \phi \nabla R) = -G(N_{22,33})(Q - \bar{Q})_{\Gamma_1} \end{aligned} \tag{6.34}$$

with terminal

$$\begin{aligned} p &= 0 \qquad \text{in} \quad \Omega \times \{T\} \\ R &= 0 \qquad \text{in} \quad \Omega \times \{T\}, \end{aligned} \tag{6.35}$$

and outer boundary conditions

$$\begin{aligned} R \cdot n = 0, \nabla p \cdot n = 0, \nabla R_1 \cdot n = 0, \nabla R_2 \cdot n = 0 \qquad &\text{on} \quad \Gamma_1 \times (0,T) \\ \phi p n + \frac{\phi}{H_1}(Q \cdot n)R + \frac{\phi}{H_1}(QR) \cdot n = 0, \nabla R_1 \cdot n = 0, \nabla R_2 \cdot n = 0 \qquad &\text{on} \quad \Gamma_2 \times (0,T), \end{aligned} \tag{6.36}$$

as well as interface boundaries on Γ_3 as

$$\begin{aligned} [\![p]\!] = 0 \\ [\![R]\!] = 0 \end{aligned} \tag{6.37}$$

such as

$$\begin{aligned} [\![\nabla p \cdot n]\!] = 0 \\ [\![\phi \nabla R_1 \cdot n]\!] = 0 \\ [\![\phi \nabla R_2 \cdot n]\!] = 0 \end{aligned} \tag{6.38}$$

and

$$[\![\phi F_U(P) \cdot n]\!] = 0 \tag{6.39}$$

i.e.

$$\begin{aligned}\llbracket \phi(\frac{Q}{H^2}\cdot RQ + gHR)\cdot n\rrbracket &= 0\\ \llbracket \phi(p + 2Q_1/HR_1 + Q_2/HR_2; Q_2/HR_1)\cdot n\rrbracket &= 0\\ \llbracket \phi(Q_1/HR_1; p + 2Q_2/HR_2 + Q_1/HR_2)\cdot n\rrbracket &= 0.\end{aligned} \tag{6.40}$$

Proof. We perform integration by parts once more on time and spatial derivatives of the weak form (6.32), where boundaries are denoted as in Section 6.2, to obtain

$$\begin{aligned}a(H,Q,p,R) = &\int_0^T\int_\Omega -\frac{\partial p}{\partial t}\phi H\,\mathrm{d}x\,\mathrm{d}t + \int_\Omega \phi\left[H(x,T)p(x,T) - H_0p(x,0)\right]\mathrm{d}x\\
&+\int_0^T\int_\Omega -\phi Q\cdot\nabla p\,\mathrm{d}x\,\mathrm{d}t + \int_0^T\int_{\Gamma_{out}} p\phi Q\cdot n\,\mathrm{d}s\,\mathrm{d}t\\
&+\int_0^T\int_{\Gamma_3}\llbracket p\phi Q\cdot n\rrbracket\,\mathrm{d}s\,\mathrm{d}t\\
&+\int_0^T\int_\Omega -(H+z)\nabla\cdot(\mu_v\nabla p)\,\mathrm{d}x\,\mathrm{d}t\\
&+\int_0^T\int_{\Gamma_{out}}\left[\mu_v(H+z)\nabla p\cdot n - p\mu_v\nabla(H+z)\cdot n\right]\mathrm{d}s\,\mathrm{d}t\\
&+\int_0^T\int_{\Gamma_3}\left[\llbracket\mu_v\nabla(H+z)\cdot np\rrbracket - \llbracket\mu_v(H+z)\nabla p\cdot n\rrbracket\right]\mathrm{d}s\,\mathrm{d}t\\
&+\int_0^T\int_\Omega -\frac{\partial R}{\partial t}\cdot(\phi Q)\,\mathrm{d}x\,\mathrm{d}t + \int_\Omega\phi\left[Q(x,T)\cdot R(x,T) - Q_0\cdot R(x,0)\right]\mathrm{d}x\\
&+\int_0^T\int_\Omega -\phi\frac{Q}{H}\cdot\nabla R\cdot Q\,\mathrm{d}x\,\mathrm{d}t + \int_0^T\int_{\Gamma_{out}}\phi\frac{Q}{H}\cdot RQ\cdot n\,\mathrm{d}s\,\mathrm{d}t\\
&+\int_0^T\int_\Omega -\frac{1}{2}g\phi H^2\nabla\cdot R\,\mathrm{d}x\,\mathrm{d}t + \int_0^T\int_{\Gamma_{out}}\frac{1}{2}g\phi H^2R\cdot n\,\mathrm{d}s\,\mathrm{d}t\\
&+\int_0^T\int_{\Gamma_3}\llbracket\phi\frac{Q}{H}\cdot RQ\cdot n\rrbracket\,\mathrm{d}s\,\mathrm{d}t + \int_0^T\int_{\Gamma_3}\llbracket\frac{1}{2}g\phi H^2R\cdot n\rrbracket\,\mathrm{d}s\,\mathrm{d}t\\
&+\int_0^T\int_\Omega -Q\cdot\nabla\cdot(\mu_f\phi\nabla R)\,\mathrm{d}x\,\mathrm{d}t + \int_0^T\int_\Omega g\phi H\nabla z\cdot R\,\mathrm{d}x\,\mathrm{d}t\\
&+\int_0^T\int_\Gamma\left[\mu_f\phi Q\cdot\nabla R\cdot n - R\cdot(\mu_f\phi\nabla Q)\cdot n\right]\mathrm{d}s\,\mathrm{d}t\\
&+\int_0^T\int_{\Gamma_3}\left[\llbracket\mu_f\phi\nabla(Q)\cdot n\cdot R\rrbracket - \llbracket\mu_f\phi\nabla R\cdot Q\cdot n\rrbracket\right]\mathrm{d}s\,\mathrm{d}t\\
&-\int_0^T\int_\Omega g\frac{1}{2}H^2\nabla\phi\cdot R\,\mathrm{d}s\,\mathrm{d}t.\end{aligned}$$

Using the jump identity $\llbracket ab\rrbracket = \{\{a\}\}\llbracket b\rrbracket + \{\{b\}\}\llbracket a\rrbracket$ on boundary integrals over the interface Γ_3 and inserting boundary conditions (5.4) on Γ_1 and Γ_2 for terms that arise from the diffusive fluxes lead to

$$a(H,Q,p,R) = \int_0^T\int_\Omega -\frac{\partial p}{\partial t}\phi H\,\mathrm{d}x\,\mathrm{d}t + \int_\Omega\phi\left[H(x,T)p(x,T) - H_0p(x,0)\right]\mathrm{d}x -$$

$$
\begin{aligned}
&- \int_0^T \int_\Omega \phi Q \cdot \nabla p \,\mathrm{d}x \,\mathrm{d}t + \int_0^T \int_{\Gamma_2} \phi p Q \cdot n \,\mathrm{d}s \,\mathrm{d}t \\
&+ \int_0^T \int_{\Gamma_3} [\![p\phi Q \cdot n]\!] \,\mathrm{d}s \,\mathrm{d}t - \int_0^T \int_\Omega \frac{1}{2} g\phi H^2 \nabla \cdot R \,\mathrm{d}x \,\mathrm{d}t \\
&- \int_0^T \int_\Omega (H+z) \nabla \cdot (\mu_v \nabla p) \,\mathrm{d}x \,\mathrm{d}t + \int_0^T \int_{\Gamma_1} \mu_v (H+z) \nabla p \cdot n \,\mathrm{d}s \,\mathrm{d}t \\
&+ \int_0^T \int_{\Gamma_2} \mu_v H_1 \nabla p \cdot n \,\mathrm{d}s \,\mathrm{d}t + \int_0^T \int_{\Gamma_2} -p\mu_v \nabla (H_1 + z) \cdot n \,\mathrm{d}s \,\mathrm{d}t \\
&+ \int_0^T \int_{\Gamma_3} [\{\{\mu_v \nabla (H+z) \cdot n\}\} [\![p]\!] - \{\{H+z\}\} [\![\mu_v \nabla p \cdot n]\!]] \,\mathrm{d}s \,\mathrm{d}t \\
&- \int_0^T \int_\Omega \frac{\partial R}{\partial t} \cdot (\phi Q) \,\mathrm{d}x \,\mathrm{d}t + \int_\Omega \phi \left[Q(x,T) \cdot R(x,T) - Q_0 \cdot R(x,0) \right] \mathrm{d}x \\
&- \int_0^T \int_\Omega \phi \frac{Q}{H} \cdot \nabla R \cdot Q \,\mathrm{d}x \,\mathrm{d}t + \int_0^T \int_{\Gamma_2} \phi \frac{Q}{H_1} \cdot RQ \cdot n \,\mathrm{d}s \,\mathrm{d}t \\
&+ \int_0^T \int_{\Gamma_1} \frac{1}{2} g\phi H^2 R \cdot n \,\mathrm{d}s \,\mathrm{d}t + \int_0^T \int_{\Gamma_2} \frac{1}{2} g\phi H_1^2 R \cdot n \,\mathrm{d}s \,\mathrm{d}t \\
&+ \int_0^T \int_{\Gamma_3} [\![\phi \frac{Q}{H} \cdot RQ \cdot n]\!] \,\mathrm{d}s \,\mathrm{d}t + \int_0^T \int_{\Gamma_3} [\![\frac{1}{2} g\phi H^2 R \cdot n]\!] \,\mathrm{d}s \,\mathrm{d}t \\
&- \int_0^T \int_\Omega (Q) \cdot \nabla \cdot (\mu_f \phi \nabla R) \,\mathrm{d}x \,\mathrm{d}t + \int_0^T \int_{\Gamma_1, \Gamma_2} \mu_f \phi Q \nabla R \cdot n \,\mathrm{d}s \,\mathrm{d}t \\
&+ \int_0^T \int_{\Gamma_3} [\{\{\mu_f \phi \nabla (Q) \cdot n\}\} \cdot [\![R]\!] - \{\{Q\}\} \cdot [\![\mu_f \phi \nabla R \cdot n]\!]] \,\mathrm{d}s \,\mathrm{d}t \\
&+ \int_0^T \int_\Omega g\phi H \nabla z \cdot R \,\mathrm{d}x \,\mathrm{d}t - \int_0^T \int_\Omega g \frac{1}{2} H^2 \nabla \phi \cdot R \,\mathrm{d}x \,\mathrm{d}t.
\end{aligned}
$$

Differentiating for the state variable H leads to

$$
\begin{aligned}
\frac{\partial a(H,Q,p,R)}{\partial H} = &\int_0^T \int_\Omega -\frac{\partial \phi p}{\partial t} \,\mathrm{d}x \,\mathrm{d}t + \int_\Omega \phi p(x,T) \,\mathrm{d}x \\
&- \int_0^T \int_\Omega \nabla \cdot (\mu_v \nabla p) \,\mathrm{d}x \,\mathrm{d}t + \int_0^T \int_{\Gamma_1} [\mu_v \nabla p \cdot n] \,\mathrm{d}s \,\mathrm{d}t \\
&+ \int_0^T \int_{\Gamma_3} [\{\{\mu_v \nabla (H+z) \cdot n\}\}_H [\![p]\!] - \{\{H+z\}\}_H [\![\mu_v \nabla p \cdot n]\!]] \,\mathrm{d}s \,\mathrm{d}t \\
&- \int_0^T \int_\Omega \phi \frac{Q}{H^2} \cdot \nabla R \cdot Q \,\mathrm{d}x \,\mathrm{d}t \\
&- \int_0^T \int_{\Gamma_3} [\![\phi \frac{Q}{H^2} \cdot RQ \cdot n]\!] \,\mathrm{d}s \,\mathrm{d}t + \int_0^T \int_{\Gamma_3} [\![g\phi HR \cdot n]\!] \,\mathrm{d}s \,\mathrm{d}t \\
&- \int_0^T \int_\Omega -g\phi H \nabla \cdot R \,\mathrm{d}x \,\mathrm{d}t + \int_0^T \int_{\Gamma_1} g\phi HR \cdot n \,\mathrm{d}s \,\mathrm{d}t \\
&+ \int_0^T \int_\Omega g\phi \nabla z \cdot R \,\mathrm{d}x \,\mathrm{d}t - \int_0^T \int_\Omega gH \nabla \phi \cdot R \,\mathrm{d}x \,\mathrm{d}t
\end{aligned}
$$

and w.r.t. Q to

$$\begin{aligned}\frac{\partial a(H,Q,p,R)}{\partial Q} &= \int_0^T \int_\Omega -\frac{\partial \phi R}{\partial t}\,\mathrm{d}x\,\mathrm{d}t + \int_\Omega \phi R(x,T)\,\mathrm{d}x \\ &- \int_0^T \int_\Omega \phi \nabla p\,\mathrm{d}x\,\mathrm{d}t + \int_0^T \int_{\Gamma_2} \phi p n\,\mathrm{d}s\,\mathrm{d}t + \int_0^T \int_{\Gamma_3} [\![p\phi n]\!] \\ &- \int_0^T \int_\Omega \phi \frac{1}{H}(\nabla R)^T Q - \frac{1}{H}(Q\cdot\nabla)RQ\,\mathrm{d}x\,\mathrm{d}t \\ &+ \int_0^T \int_{\Gamma_2} \frac{\phi}{H_1}(Q\cdot n)R\,\mathrm{d}s\,\mathrm{d}t + \int_0^T \int_{\Gamma_2} \frac{\phi}{H_1}(QR)\cdot n\,\mathrm{d}s\,\mathrm{d}t \\ &+ \int_0^T \int_{\Gamma_3} [\![\frac{\phi}{H}(Q\cdot n)R]\!]\,\mathrm{d}s\,\mathrm{d}t + \int_0^T \int_{\Gamma_3} [\![\frac{\phi}{H}(QR)\cdot n]\!]\,\mathrm{d}s\,\mathrm{d}t \\ &- \int_0^T \int_\Omega \nabla\cdot(\mu_f \phi \nabla R)\,\mathrm{d}x\,\mathrm{d}t + \int_0^T \int_{\Gamma_1,\Gamma_2} \mu_f \phi \nabla R n\,\mathrm{d}s\,\mathrm{d}t \\ &+ \int_0^T \int_{\Gamma_3} [\{\{\mu_f \phi \nabla(Q)n\}\}_Q [\![R]\!] - \{\{Q\}\}_Q [\![\mu_f \phi \nabla R n]\!]]\,\mathrm{d}s\,\mathrm{d}t,\end{aligned}$$

where the subscripts denote differentiation for the respective state variable. Now if $\frac{\partial a(H,Q,p,R)}{\partial U} = -\frac{\partial J_1}{\partial U}$ then $\frac{\partial \mathcal{L}}{\partial U} = 0$ is fulfilled. From this we get the adjoint equations in strong form (6.33) and (6.34) with boundary conditions from equating boundary terms to zero. □

The porous SWE adjoint can be written in vector form as

$$-\phi\frac{\partial P}{\partial t} + \phi A P_x + \phi B P_y + \phi C P - \nabla\cdot(G(f(\phi,\mu))\nabla P) = S, \tag{6.41}$$

where

$$A = \begin{pmatrix} 0 & \frac{Q_1}{H^2} - gH & \frac{Q_1 Q_2}{H^2} \\ -1 & -2\frac{Q_1}{H} & -\frac{Q_2}{H} \\ 0 & 0 & -\frac{Q_1}{H} \end{pmatrix}, \quad B = \begin{pmatrix} 0 & \frac{Q_1 Q_2}{H^2} & \frac{Q_2^2}{H^2} - gH \\ 0 & -\frac{Q_2}{H} & 0 \\ -1 & -\frac{Q_1}{H} & -2\frac{Q_2}{H} \end{pmatrix} \tag{6.42}$$

and C originates from variations in the sediment and the porosity such that

$$C = \begin{pmatrix} 0 & g\frac{\partial z}{\partial x} - g\frac{H}{\phi}\frac{\partial \phi}{\partial x} & g\frac{\partial z}{\partial y} - g\frac{H}{\phi}\frac{\partial \phi}{\partial y} \\ 0 & 0 & 0 \\ 0 & 0 & 0 \end{pmatrix}. \tag{6.43}$$

Theorem 6.3. *(Shape Derivative) Assume that the parabolic PDE problem (6.20) is H^1-regular, so that its solution U is at least in $H^1(\Omega\times(0,T))^3$. Moreover, assume that the adjoint equations (6.41) admit a solution $P \in H^1(\Omega\times(0,T))^3$. Then the shape derivative of the objective J_1 at Ω in the direction V is given by*

$$
\begin{aligned}
DJ_1(\Omega)[V] = \int_0^T \int_\Omega \Big[& -(\nabla V)^T : \nabla(\phi Q)p - (\nabla V)^T : \nabla Q \frac{\phi Q}{H} \cdot R \\
& - (\nabla V Q \cdot \nabla)\frac{\phi Q}{H} \cdot R - gH(\nabla V)^T \nabla(\phi H) \cdot R \\
& - \mu_v \nabla(H+z)^T(\nabla V + \nabla V^T)\nabla p \\
& - \phi\mu_f \nabla Q \nabla V : \nabla R - \phi\mu_f \nabla Q \nabla V^T : \nabla R \\
& - g\phi H \nabla V^T \nabla z \cdot R + \frac{1}{2} g H^2 \nabla V^T \nabla \phi \cdot R \\
& + \operatorname{div}(V)\Big\{ \frac{\partial \phi H}{\partial t} p + \nabla \cdot (\phi Q)p + \frac{\partial \phi Q}{\partial t} \cdot R \\
& + \phi(Q \cdot \nabla)\frac{Q}{H} \cdot R + \nabla \cdot (\phi Q)\frac{Q}{H} \cdot R + \frac{1}{2} g \nabla(\phi H^2) \cdot R \\
& + g\phi H \nabla z \cdot R + \mu_v \nabla(H+z) \cdot \nabla p \\
& + \phi\mu_f \nabla Q : \nabla R - g\frac{1}{2} H^2 \nabla \phi \cdot R \Big\} \Big] \, \mathrm{d}x \, \mathrm{d}t.
\end{aligned}
\tag{6.44}
$$

Proof. Following the same arguments as in proof of theorem 4.4, we use the definition of the shape derivative (3.4) in terms of the Lagrangian, i.e.

$$
\begin{aligned}
& D\mathcal{L}(\Omega, U, P)[V] \\
& \quad = \lim_{\epsilon \to 0^+} \frac{\mathcal{L}(\Omega_\epsilon; U, P) - \mathcal{L}(\Omega; U, P)}{\epsilon} \\
& \quad = \frac{d}{d\epsilon} \mathcal{L}(\Omega_\epsilon, U, P)\big|_{\epsilon=0^+} = \frac{d}{d\epsilon} \mathcal{L}(\Omega_\epsilon, H, Q, p, R)\big|_{\epsilon=0^+}
\end{aligned}
$$

and apply the rule for differentiating domain integrals (3.28), where we split integrals for readability in to be added domain part, i.e.

$$
\begin{aligned}
\int_\Omega \Big[& \int_0^T -D_m\left(\frac{\partial p}{\partial t}\phi H\right) \mathrm{d}t + D_m\left(\phi H(x,T)p(x,T) - \phi H_0 p(x,0)\right) \\
& + \int_0^T -D_m\left(\frac{\partial R}{\partial t} \cdot \phi Q\right) \mathrm{d}t + D_m\left(\phi Q(x,T) \cdot R(x,T) - \phi Q_0 \cdot R(x,0)\right) \\
& + \int_0^T D_m\left(\nabla \cdot (\phi Q)p\right) \mathrm{d}t + \int_0^T D_m\left(\mu_v \nabla(H+z) \cdot \nabla p\right) \mathrm{d}t \\
& + \int_0^T D_m\left(\nabla \cdot \left(\phi \frac{Q}{H} \otimes Q\right) \cdot R\right) \mathrm{d}t + \int_0^T +D_m\left(\frac{1}{2} g \nabla(\phi H^2) \cdot R\right) \mathrm{d}t \\
& + \int_0^T D_m\left(\phi\mu_f \nabla Q : \nabla R\right) \mathrm{d}t + \int_0^T D_m\left(gH\nabla z \cdot R\right) \mathrm{d}t \\
& + \int_0^T -D_m\left(\frac{1}{2} g H^2 \nabla \phi \cdot R\right) \mathrm{d}t \\
& + \operatorname{div}(V)\Big(\int_0^T -\frac{\partial p}{\partial t}\phi H \, \mathrm{d}t + \phi H(x,T)p(x,T) - \phi H_0 p(x,0)
\end{aligned}
$$

$$
\begin{aligned}
&+\int_0^T -\frac{\partial R}{\partial t}\cdot(\phi Q)\,\mathrm{d}t+\phi Q(x,T)\cdot R(x,T)-\phi Q_0\cdot R(x,0)+\int_0^T \nabla Q\cdot p\,\mathrm{d}t\\
&+\int_0^T \mu_v\nabla(H+z)\cdot\nabla p\,\mathrm{d}t+\quad\int_0^T \nabla\cdot\Big(\phi\frac{Q}{H}\otimes Q\Big)\cdot R\,\mathrm{d}t\\
&+\int_0^T +\frac{1}{2}g\nabla(\phi H^2)\cdot R\,\mathrm{d}t+\int_0^T \phi\mu_f\nabla Q:\nabla R\,\mathrm{d}t+\int_0^T g\phi H\nabla z\cdot R\,\mathrm{d}t\\
&-\int_0^T gH^2\nabla\phi\cdot R\,\mathrm{d}t\Big)\Big]\,\mathrm{d}x
\end{aligned}
$$

and interior such as exterior boundary part, i.e.

$$
\begin{aligned}
&\int_{\Gamma_1}\Big[\frac{1}{2}\int_0^T D_m\Big([N(\hat U-\bar U)]^2\Big)+\mathrm{div}_{\Gamma_1}(V)[N(\hat U-\bar U)]^2\,\mathrm{d}t\Big]\,\mathrm{d}s\\
&-\int_{\Gamma_2}\Big[\int_0^T D_m\left(\mu_v\nabla(H_1+z)\cdot np\,\mathrm{d}t\right)+\mathrm{div}_{\Gamma_2}(V)\Big(\int_0^T \mu_v\nabla(H_1+z)\cdot np\,\mathrm{d}t\Big)\Big]\,\mathrm{d}s\\
&-\int_{\Gamma_3}\Big[\int_0^T D_m\left([\![\mu_v\nabla(H+z)\cdot np]\!]\right)\mathrm{d}t+\int_0^T D_m\left([\![\phi\mu_f\nabla Q\cdot n\cdot R]\!]\right)\mathrm{d}t\\
&+\mathrm{div}_{\Gamma_3}(V)\Big(\int_0^T [\![-\mu_v\nabla(H+z)\cdot np]\!]\,\mathrm{d}t+\int_0^T [\![-\phi\mu_f\nabla Q\cdot n\cdot R]\!]\,\mathrm{d}t\Big)\Big]\,\mathrm{d}s.
\end{aligned}
$$

Now the product rule (3.24) yields respectively for the domain part

$$
\begin{aligned}
&=\int_\Omega\Big[\int_0^T -D_m\left(\frac{\partial p}{\partial t}\right)\phi H-\frac{\partial p}{\partial t}D_m(\phi H)\,\mathrm{d}t\\
&+D_m(\phi H(x,T))p(x,T)+H(x,T)\dot p(x,T)-\phi H_0\dot p(x,0)\\
&+\int_0^T -D_m\left(\frac{\partial R}{\partial t}\right)\cdot(\phi Q)-\frac{\partial R}{\partial t}\cdot D_m(\phi Q)\,\mathrm{d}t+D_m(Q(x,T))\cdot R(x,T)\\
&+\phi Q(x,T)\cdot\dot R(x,T)-\phi Q_0\cdot\dot R(x,0)+\int_0^T \dot p\cdot\nabla(\phi Q)+p\cdot D_m(\nabla(\phi Q))\,\mathrm{d}t\\
&+\int_0^T (\mu_v D_m(\nabla(H+z))\cdot\nabla p+\mu_v\nabla(H+z)\cdot D_m(\nabla p))\,\mathrm{d}t\\
&-\int_0^T D_m\left(\nabla\cdot\Big(\phi\frac{Q}{H}\otimes Q\Big)\right)\cdot R\,\mathrm{d}t+\int_0^T \nabla\cdot\Big(\phi\frac{Q}{H}\otimes Q\Big)\cdot D_m\left(R\right)\mathrm{d}t\\
&+\int_0^T \Big(\frac{1}{2}gD_m(\nabla(\phi H^2))\cdot R+\frac{1}{2}g\nabla(\phi H^2)\cdot D_m(R)\Big)\,\mathrm{d}t\\
&+\int_0^T \left(D_m\left(\phi\mu_f\nabla Q\right):\nabla R+\phi\mu_f\nabla Q:D_m\left(\nabla R\right)\right)\mathrm{d}t\\
&+\int_0^T gD_m(\phi H)\nabla z\cdot R\,\mathrm{d}t+\int_0^T g\phi H D_m\left(\nabla z\right)\cdot R\,\mathrm{d}t+\int_0^T g\phi H\nabla z\cdot\dot R\,\mathrm{d}t\\
&-\int_0^T \frac{1}{2}gD_m(H^2)\nabla\phi\cdot R\,\mathrm{d}t-\int_0^T \frac{1}{2}gH^2D_m\left(\nabla\phi\right)\cdot R\,\mathrm{d}t-\int_0^T \frac{1}{2}gH^2\nabla\phi\cdot\dot R\,\mathrm{d}t\\
&+\mathrm{div}(V)\Big(\int_0^T -\frac{\partial p}{\partial t}\phi H\,\mathrm{d}t+\phi H(x,T)p(x,T)-\phi H_0p(x,0)
\end{aligned}
$$

$$
\begin{aligned}
&+\int_0^T -\frac{\partial R}{\partial t}\cdot(\phi Q)\,\mathrm{d}t+\phi Q(x,T)\cdot R(x,T)-\phi Q_0\cdot R(x,0)+\int_0^T \nabla Q\cdot p\,\mathrm{d}t\\
&+\int_0^T \mu_v\nabla(H+z)\cdot\nabla p\,\mathrm{d}t+\int_0^T \nabla\cdot\Big(\phi\frac{Q}{H}\otimes Q\Big)\cdot R\,\mathrm{d}t\\
&+\int_0^T \frac{1}{2}g\nabla(\phi H^2)\cdot R\,\mathrm{d}t+\int_0^T \phi\mu_f\nabla Q:\nabla R\,\mathrm{d}t+\int_0^T g\phi H\nabla z\cdot R\,\mathrm{d}t\\
&-\int_0^T gH^2\nabla\phi\cdot R\,\mathrm{d}t\Big)\Big]\,\mathrm{d}x
\end{aligned}
$$

and the boundary part

$$
\begin{aligned}
&\int_{\Gamma_1}\Big[\int_0^T[N(\hat U-\bar U)]\cdot\dot{\hat U}\,\mathrm{d}t+\mathrm{div}_{\Gamma_1}(V)\Big(\int_0^T[N(\hat U-\bar U)]^2\,\mathrm{d}t\Big)\Big]\,\mathrm{d}s\\
&+\int_{\Gamma_2}\Big[\int_0^T -\mu_v\nabla(H_1+z)\cdot n\dot p\,\mathrm{d}t+\mathrm{div}_{\Gamma_2}(V)\Big(\int_0^T -\mu_v\nabla(H_1+z)\cdot np\,\mathrm{d}t\Big)\Big]\,\mathrm{d}s\\
&+\int_{\Gamma_3}\Big[\int_0^T[\![-\mu_v D_m\left(\nabla(H+z)\right)\cdot np-\mu_v\nabla(H+z)\cdot n\dot p]\!]\,\mathrm{d}t\\
&+\int_0^T[\![-\phi\mu_f D_m(\nabla Q\cdot n)\cdot R-\phi\mu_f\nabla Q\cdot n\cdot\dot R]\!]\,\mathrm{d}t\\
&+\mathrm{div}_{\Gamma_3}(V)\Big(\int_0^T[\![-\mu_v\nabla(H+z)\cdot np]\!]\,\mathrm{d}t+\int_0^T[\![-\phi\mu_f\nabla Q\cdot n\cdot R]\!]\,\mathrm{d}t\Big)\Big]\,\mathrm{d}s.
\end{aligned}
$$

The combination of both integrals, the non-commuting of material and spatial derivatives (3.25), (3.26) and (3.27), integration by parts combined with the fact that sediment and porosity move alongside with the deformation, which ultimately lets the material derivative vanish, such as finally regrouping for the material derivatives of the state $U=(H,Q)$ and adjoint variables $P=(p,R)$, lead to three parts, where firstly

$$
\begin{aligned}
&\int_{\Gamma_1}\int_0^T[N(\hat U-\bar U)]\cdot\dot U\,\mathrm{d}t\,\mathrm{d}s+\int_\Omega\int_0^T\\
&\Big[\Big(-\phi\frac{\partial p}{\partial t}+\frac{\phi}{H^2}(Q\cdot\nabla)R\cdot Q-g\phi H(\nabla\cdot R)-\nabla\cdot(\mu_v\nabla p)+g\phi\nabla z\cdot R\Big)\dot H\\
&+\Big(-\phi\frac{\partial R}{\partial t}-\nabla p-\frac{\phi}{H}(Q\cdot\nabla)R-\frac{\phi}{H}(\nabla R)^TQ-(\nabla\cdot(\phi\mu_f\nabla R))\Big)\cdot\dot Q\\
&+\Big(\phi\frac{\partial H}{\partial t}+\nabla\cdot(\phi Q-\mu_v\nabla(H+z))\Big)\dot p\\
&+\Big(\phi\frac{\partial Q}{\partial t}+\nabla\cdot\Big(\phi\frac{Q}{H}\otimes Q+\frac{1}{2}g\phi H^2\mathbf{I}-\phi\mu_f\nabla Q\Big)+g\phi H\nabla z\Big)\cdot\dot R\,\mathrm{d}t\Big]\,\mathrm{d}x
\end{aligned}
$$

vanishes due to an evaluation the Lagrangian in its saddle point and secondly

$$
\begin{aligned}
&\int_{\Gamma_1}\int_0^T\Big[\mathrm{div}_{\Gamma_1}(V)[N(\hat U-\bar U)]^2\Big]\,\mathrm{d}t\,\mathrm{d}s\\
&+\int_{\Gamma_3}\Big[\int_0^T\Big([\![\frac{\phi\dot Q}{H}\cdot RQ\cdot n+\frac{\phi Q}{H}\cdot R\dot Q\cdot n+p\phi\dot Q\cdot n
\end{aligned}
$$

$$+\int_0^T \frac{1}{2} g D_m(\phi H^2) R \cdot n \rrbracket \Big) \,\mathrm{d}t \Big] \,\mathrm{d}s$$
$$+ \operatorname{div}_{\Gamma_3}(V) \Big(\int_0^T \llbracket -\mu_v \nabla (H+z) \cdot n p \rrbracket \,\mathrm{d}t + \int_0^T \llbracket -\phi \mu_f \nabla Q \cdot n \cdot R \rrbracket \,\mathrm{d}t \Big) \Big] \,\mathrm{d}s$$

vanishes since on the one hand outer boundaries are not variable and hence the deformation field V vanishes in small neighborhoods around Γ_1, Γ_2 such that the material derivative is zero and on the other due the continuity of state and fluxes corresponding material derivatives are continuous. Finally, this leaves us with the shape derivative in its final form (6.44). □

6.4 Numerical Implementation

We rely on the classical structure of adjoint and gradient-descent based shape optimization algorithms that were presented in Section 4.4 and Section 5.4.1, but including the notion of a well-balanced scheme for obtained DG-scheme that is discussed in Sections 6.4.1 and 6.4.2.

Algorithm 4 Shape Optimization Algorithm Porous SWE

Initialization
while $||DJ(\Omega_k)[V]|| > \epsilon_{TOL}$ **do**
1. Calculate SDF w_k [via Viscous Eikonal Equation (5.34) or AABBT]
2. Calculate State U_k [via $\tilde{U}_k$ of Section 6.4.2]
3. Calculate Adjoint P_k [via $\tilde{P}_k$ of Section 6.4.2]
4. Calculate Gradient W_k [via $DJ_{1,2,3,4}(\Omega)[V]$ & Linear Elasticity (4.54)]
5. Perform Linesearch for $\tilde{W}_k$
6. Calculate Ω_{k+1} [via $\tilde{W}_k$ and (3.33)]

end while

6.4.1 Derivation of DG-Scheme for Interface Conditions

The porous SWE (6.20) together with interface conditions on Γ_3 can be resolved in an SIPG scheme. Starting from the weak form (6.32) and integrating by parts on the advective terms, in addition to once more using the jump identity $\llbracket ab \rrbracket = \{\{a\}\}\llbracket b \rrbracket + \{\{b\}\}\llbracket a \rrbracket$ together with flux continuity for the diffusive and advective flux we obtain

$$\begin{aligned} a(H,Q,p,R) = &\int_0^T \int_\Omega -\frac{\partial p}{\partial t} \phi H \,\mathrm{d}x \,\mathrm{d}t + \int_\Omega \phi \left[H(x,T)p(x,T) - H_0 p(x,0) \right] \mathrm{d}x \\ &+ \int_0^T \int_\Omega -\phi Q \cdot \nabla p \,\mathrm{d}x \,\mathrm{d}t + \int_0^T \int_{\Gamma_{out}} p \phi Q \cdot n \,\mathrm{d}s \,\mathrm{d}t \\ &+ \int_0^T \int_{\Gamma_3} \{\{\phi Q \cdot n\}\} \llbracket p \rrbracket \,\mathrm{d}s \,\mathrm{d}t + \int_0^T \int_\Omega \mu_v \nabla (H+z) \cdot \nabla p \,\mathrm{d}x \,\mathrm{d}t \end{aligned}$$

$$
\begin{aligned}
&- \int_0^T \int_{\Gamma_{out}} [p\mu_v \nabla(H+z)\cdot n]\,\mathrm{d}s\,\mathrm{d}t - \int_0^T \int_{\Gamma_3} [\{\{\mu_v \nabla(H+z)\cdot n\}\}[\![p]\!]]\,\mathrm{d}s\,\mathrm{d}t \\
&- \int_0^T \int_\Omega -\frac{\partial R}{\partial t}\cdot(\phi Q)\,\mathrm{d}x\,\mathrm{d}t + \int_\Omega \phi\,[Q(x,T)\cdot R(x,T) - Q_0\cdot R(x,0)]\,\mathrm{d}x \\
&+ \int_0^T \int_\Omega -\phi\frac{Q}{H}\cdot\nabla R\cdot Q\,\mathrm{d}x\,\mathrm{d}t + \int_0^T \int_{\Gamma_{out}} \phi\frac{Q}{H}\cdot RQ\cdot n\,\mathrm{d}s\,\mathrm{d}t \\
&+ \int_0^T \int_\Omega -\frac{1}{2}g\phi H^2\nabla\cdot R\,\mathrm{d}x\,\mathrm{d}t + \int_0^T \int_{\Gamma_{out}} \frac{1}{2}g\phi H^2 R\cdot n\,\mathrm{d}s\,\mathrm{d}t \\
&+ \int_0^T \int_{\Gamma_3} \{\{\phi(\frac{Q}{H}\otimes Q)n\}\}\cdot[\![R]\!]\,\mathrm{d}s\,\mathrm{d}t + \int_0^T \int_{\Gamma_3} \{\{\frac{1}{2}g\phi H^2 n\}\}\cdot[\![R]\!]\,\mathrm{d}s\,\mathrm{d}t \\
&+ \int_0^T \int_\Omega \mu_f\phi\nabla Q : \nabla R\,\mathrm{d}x\,\mathrm{d}t + \int_0^T \int_\Omega g\phi H\nabla z\cdot R\,\mathrm{d}x\,\mathrm{d}t \\
&- \int_0^T \int_\Gamma [R\cdot\mu_f\phi\nabla Q\cdot n]\,\mathrm{d}s\,\mathrm{d}t - \int_0^T \int_{\Gamma_3} [\{\{\mu_f\phi\nabla Q\cdot n\}\}\cdot[\![R]\!]]\,\mathrm{d}s\,\mathrm{d}t \\
&- \int_0^T \int_\Omega g\frac{1}{2}H^2\nabla\phi\cdot R\,\mathrm{d}s\,\mathrm{d}t.
\end{aligned}
$$

Since this derivation does not make use of the continuity of the state (6.25), we weakly enforce it by adding the penalty term

$$\int_0^T \int_{\Gamma_3} \underline{\delta}(\hat{U}) : \underline{[\![P]\!]}\,\mathrm{d}s\,\mathrm{d}t \tag{6.45}$$

for

$$\underline{\delta}(\hat{U}) = C_{IP}\frac{k^2}{h}\{\{G(f(\phi,\mu))\}\}\underline{[\![\hat{U}]\!]}. \tag{6.46}$$

In addition, it appears natural to symmetrize the diffusive part by

$$-\int_0^T \int_{\Gamma_3} \{\{G(f(\phi,\mu))\nabla(P)\}\} : \underline{[\![\hat{U}]\!]}. \tag{6.47}$$

For the advective-flux we refer to upwinding as

$$\{\{\phi F(U)\cdot n\}\}_{Up} = \frac{1}{2}\left[\phi^+ F(U^+)\cdot n + \phi^- F(U^-)\cdot n\right]. \tag{6.48}$$

Finally, a complete SIPG-scheme over a conformal mesh is obtained by allowing discontinuous cell-transitions and performing integration by parts on each cell. If we allow alternation in the usage of the numerical flux function we obtain the SIPG-scheme in known form (5.30).

6.4.2 Well-Balancedness for DG and SIPG with Sources

In this section we derive the well-balanced property for the numerical scheme for the case of one-dimensional porous SWE, extending the approach in [183] to porous SWE

with diffusive terms. The two-dimensional formulation will follow immediately. Before starting, we explicitly state that our solver relies on variables

$$\tilde{U} = \begin{pmatrix} h \\ uh \end{pmatrix} = \begin{pmatrix} \phi H \\ \phi u H \end{pmatrix}. \tag{6.49}$$

Hence, we redefine the 1D porous SWE without diffusion in vector notation as

$$\partial_t(\tilde{U}) + \nabla \cdot (F(\tilde{U})) = S(\tilde{U}) + S_\phi(\tilde{U}) \tag{6.50}$$

for given flux matrix

$$F(\tilde{U}) = \begin{pmatrix} hu \\ hu^2 + \frac{1}{2}gh^2/\phi \end{pmatrix} \tag{6.51}$$

and as before a source regarding the variations in the sediment

$$S(\tilde{U}) = \begin{pmatrix} 0 \\ -gh\frac{\partial z}{\partial x} \end{pmatrix} \tag{6.52}$$

as well as variations in the porosity factor

$$S_\phi(\tilde{U}) = \begin{pmatrix} 0 \\ \frac{g}{2}\frac{h^2}{\phi^2}\frac{\partial \phi}{\partial x} \end{pmatrix}. \tag{6.53}$$

Well-balancing relies on incorporating the discretization of the source term in fluxes, such that members from Definition 2.58 used in (5.30) are redefined. Preserving still water stationary conditions means that $uh = 0$ for $h/\phi + z = c$ for all $t \in (0, T)$. For the contribution to time changes it should be justified that on each element $\kappa = [x_{j-1/2}, x_{j+1/2}] \in \mathcal{T}_h$ it holds that

$$\begin{aligned} R = &- \int_\kappa F(\tilde{U}_h(x,t)) \cdot \partial_x P_h(x)\,\mathrm{d}x + \mathcal{F}^L_{j+1/2} \cdot P_h(x^-_{j+1/2}) - \mathcal{F}^R_{j-1/2} \cdot P_h(x^+_{j-1/2}) \\ &- \int_\kappa S(\tilde{U}_h(x,t)) \cdot P_h(x)\,\mathrm{d}x - \int_\kappa S_\phi(\tilde{U}_h(x,t)) \cdot P_h(x)\,\mathrm{d}x = 0. \end{aligned} \tag{6.54}$$

In [183] it is stated that Equation (6.54) is fulfilled if,

i) $\mathcal{F}^L_{j+1/2} = F(\tilde{U}_h(x^-_{j+1/2}))$ and $\mathcal{F}^R_{j-1/2} = F(\tilde{U}_h(x^+_{j-1/2})$

ii) we are in a steady state and U_h is a numerical approximation of U, hence

$$\partial_x F(\tilde{U}_h) = \begin{pmatrix} 0 \\ g(h_h, z_h, \phi_h) \end{pmatrix}.$$

(a) $t = 0$ (b) $t = 1$

Figure 6.2: Lake at Rest for Continuous, Piecewise Polynomials z_h & ϕ_h

(a) $t = 0$ (b) $t = 1$

Figure 6.3: Lake not at Rest for Discontinuous, Piecewise Polynomials z_h & ϕ_h

The assumption above can be easily justified and shows the appropriateness of the unmodified scheme in case of a continuous piecewise sediment $z_h(x^-_{j+1/2}) = z_h(x^+_{j+1/2})$ and porosity coefficients $\phi_h(x^-_{j+1/2}) = \phi_h(x^+_{j+1/2})$ as it can be observed in Figure 6.2. However as before, this is certainly not enough in a discontinuous setting, since $\phi_h(x^-_{j+1/2}) \neq \phi_h(x^+_{j+1/2})$ and $z_h(x^-_{j+1/2}) \neq z_h(x^+_{j+1/2})$ lead to large numerical errors as displayed in Figure 6.3.

Situations with discontinuous sediment are dealt with by relying on the idea of redefining variables [18], i.e.

$$\begin{aligned} h^{+,*}_{h,j+1/2} &= \max\left(0, h^+_{h,j+1/2} + z^+_{h,j+1/2} - \max\left(z^+_{h,j+1/2}, z^-_{h,j+1/2}\right)\right) \\ h^{-,*}_{h,j+1/2} &= \max\left(0, h^-_{h,j+1/2} + z^-_{h,j+1/2} - \max\left(z^+_{h,j+1/2}, z^-_{h,j+1/2}\right)\right) \end{aligned} \tag{6.55}$$

which can be extended for varying porosity coefficient to

$$\begin{aligned} &h^{+,*}_{h,j+1/2} = \\ &\max\left(0, \frac{h^+_{h,j+1/2}}{\phi^+_{h,j+1/2}} + z^+_{h,j+1/2} - \max(z^+_{h,j+1/2}, z^-_{h,j+1/2})\right) \min\left(\phi^+_{h,j+1/2}, \phi^-_{h,j+1/2}\right) \end{aligned} \tag{6.56}$$

$$h^{-,*}_{h,j+1/2} = \max\left(0, \frac{h^-_{h,j+1/2}}{\phi^-_{h,j+1/2}} + z^-_{h,j+1/2} - \max(z^+_{h,j+1/2}, z^-_{h,j+1/2})\right) \min\left(\phi^+_{h,j+1/2}, \phi^-_{h,j+1/2}\right) \tag{6.57}$$

such that

$$\tilde{U}^{+,*}_{h,j+1/2} = \begin{pmatrix} h^{+,*}_{h,j+1/2} \\ uh^+_{h,j+1/2} \end{pmatrix}. \tag{6.58}$$

Theorem 6.4. *(Well-Balancedness) Redefining $\tilde{U}^{\pm,*}_{h,j+1/2}$ as in (6.58) in accordance with corrector-terms lead to a well-balanced scheme*

Proof. It holds that

$$\begin{aligned}\mathcal{F}^L_{j+1/2} =& \mathcal{F}(\tilde{U}^{-,*}_{h,j+1/2}, \tilde{U}^{+,*}_{h,j+1/2}) \\ &+ \begin{pmatrix} 0 \\ \frac{g}{2}(h^-_{h,j+1/2})^2/\phi^-_{h,j+1/2} - \frac{g}{2}(h^{-,*}_{h,j+1/2})^2/\min\left(\phi^+_{h,j+1/2}, \phi^-_{h,j+1/2}\right) \end{pmatrix} \\ =& F(\tilde{U}^-_{h,j+1/2})\end{aligned}$$

and similarly

$$\mathcal{F}^R_{j-1/2} = F(\tilde{U}^+_{h,j-1/2}).$$

□

Results of the redefinition and well-balancing can be observed in Figure 6.4. Ex-

(a) $t = 0$ (b) $t = 1$

Figure 6.4: Lake at Rest for Discontinuous, Piecewise Polynomials z_h & ϕ_h

tending results to two dimensions can be done by looking at the residual on an element $\kappa \in \mathcal{T}_h$, i.e.

$$\begin{aligned}R = &- \int_\kappa F(\tilde{U}_h(x,t)) : \nabla P_h(x)\,\mathrm{d}x + \int_{\partial\kappa} \mathcal{F}_{\partial\kappa}(U^+_h(x,t), U^-_h(x,t), n^+) \cdot P^+_h\,\mathrm{d}s \\ &- \int_\kappa S(\tilde{U}_h(x,t)) \cdot P_h(x)\,\mathrm{d}x - \int_\kappa S_\phi(\tilde{U}_h(x,t)) \cdot P_h(x)\,\mathrm{d}x = 0\end{aligned} \tag{6.59}$$

and relying on a flux modification on each elemental boundary as

$$\begin{aligned}\mathcal{F}_{\partial\kappa} =& \mathcal{F}(\tilde{U}^{-,*}_{h,\partial\kappa}, \tilde{U}^{+,*}_{h,\partial\kappa}, n^{+}_{\partial\kappa}) + \\ & G\begin{pmatrix} 0 \\ n^{+}_{0,\partial\kappa} \\ n^{+}_{1,\partial\kappa} \end{pmatrix} \begin{pmatrix} 0 \\ \frac{g}{2}(h^{+}_{h,\partial\kappa})^2/\phi^{+}_{h,\partial\kappa} - \frac{g}{2}(h^{+,*}_{h,\partial\kappa})^2/\min\left(\phi^{+}_{h,\partial\kappa}, \phi^{-}_{h,\partial\kappa}\right) \\ \frac{g}{2}(h^{+}_{h,\partial\kappa})^2/\phi^{+}_{h,\partial\kappa} - \frac{g}{2}(h^{+,*}_{h,\partial\kappa})^2/\min\left(\phi^{+}_{h,\partial\kappa}, \phi^{-}_{h,\partial\kappa}\right) \end{pmatrix},\end{aligned} \tag{6.60}$$

where

$$\tilde{U}^{+,*}_{h,\partial\kappa} = \begin{pmatrix} h^{+,*}_{h,\partial\kappa} \\ uh^{+}_{h,\partial\kappa} \\ vh^{+}_{h,\partial\kappa} \end{pmatrix}. \tag{6.61}$$

Remark. Adding diffusive terms in the form

$$\partial_t(\tilde{U}) + \nabla\cdot(F(\tilde{U})) - \nabla\cdot(G(f(\phi,\mu))\nabla\hat{U}) = S(\tilde{U}) + S_\phi(\tilde{U}),$$

where $\hat{U} = (z + h/\phi, uh, vh)$, does not disturb well-balancedness, since rest conditions cancel contributing terms.

Remark. Reformulation (6.49) requires eigenvalues in the form of (5.32) with $c = \sqrt{gh/\phi}$ to be used in the numerical flux function.

Remark. The numerical scheme used to handle discontinuous sediment and porosity coefficients forms the limit of a smoothed scenario, such that $U_\alpha \to U$ in $H^1((0,T)\times\Omega)^3$ where $\phi_\alpha \to \phi$ for $\alpha \to 0$ which is verified for one dimension numerically in Section 6.4.3.

For solving the adjoint we once more refer to the adjoint in vector notation, where we rewrite equations in vector-form i.e.

$$\phi\frac{\partial P}{\partial t} - \nabla\cdot(A\phi P, B\phi P) - \tilde{C}\phi P + \nabla\cdot(G(f(\phi,\mu))\nabla P) = -S, \tag{6.62}$$

where $\tilde{C}$ is defined to be

$$\tilde{C} = C - A_x - B_y. \tag{6.63}$$

and use once more that the eigenvalues of the obtained adjoint Jacobian $J^*_i := \partial_P F^*_i(P) = -\partial_P(\phi AP, \phi BP)$ equal the eigenvalues of the forward system. We rely computations on discontinuous variables

$$\tilde{P} = \begin{pmatrix} \tilde{p} \\ \tilde{r}_1 \\ \tilde{r}_2 \end{pmatrix} = \begin{pmatrix} \phi p \\ \phi R_1 \\ \phi R_2 \end{pmatrix}. \tag{6.64}$$

Then redefining

$$\tilde{p}^{+,*}_{h,j+1/2} = \frac{\tilde{p}^{+}_{h,j+1/2}}{\phi^{+}_{h,j+1/2}}\min\left(\phi^{+}_{h,j+1/2}, \phi^{-}_{h,j+1/2}\right) \tag{6.65}$$

$$\tilde{p}^{-,*}_{h,j+1/2} = \frac{\tilde{p}^{-}_{h,j+1/2}}{\phi^{-}_{h,j+1/2}} \min\left(\phi^{+}_{h,j+1/2}, \phi^{-}_{h,j+1/2}\right) \tag{6.66}$$

leads to a well-balanced adjoint scheme in two dimensions for fluxes defined as

$$\begin{aligned}\mathcal{F}_{\partial\kappa} =& \mathcal{F}(\tilde{P}^{-,*}_{h,\partial\kappa}, \tilde{P}^{+,*}_{h,\partial\kappa}, n^{+}_{\partial\kappa}) \\ &+ G \begin{pmatrix} 0 \\ n^{+}_{0,\partial\kappa} \\ n^{+}_{1,\partial\kappa} \end{pmatrix} \begin{pmatrix} 0 \\ (\tilde{p}^{+}_{h,\partial\kappa})^2/\phi^{+}_{h,\partial\kappa} - (\tilde{p}^{+,*}_{h,\partial\kappa})^2/\min\left(\phi^{+}_{h,\partial\kappa}, \phi^{-}_{h,\partial\kappa}\right) \\ (\tilde{p}^{+}_{h,\partial\kappa})^2/\phi^{+}_{h,\partial\kappa} - (\tilde{p}^{+,*}_{h,\partial\kappa})^2/\min\left(\phi^{+}_{h,\partial\kappa}, \phi^{-}_{h,\partial\kappa}\right) \end{pmatrix}.\end{aligned} \tag{6.67}$$

6.4.3 Numerical Convergence of the Smoothed Approach

As mentioned in Section 6.4.2 the numerical scheme used to handle discontinuous sediment and porosity coefficients forms the limit of a smoothed scenario. We numerically justify this by relying the smoothed porosity on smoothed step functions in one dimension, i.e. for discontinuities located at $x_0 < x_1 \in \mathbb{R}$ the smoothed porosity is obtained from

$$\phi_\alpha(x) = [1 - \psi(x, \alpha)]\, \phi_2 + \psi(x, \alpha)\phi_1, \tag{6.68}$$

where

$$\psi(x,\alpha) = \begin{cases} 1 & \text{if } x \leq x_0 - \alpha \wedge x \geq x_1 + \alpha \\ -\frac{1}{4}\left(\frac{x_0 - x}{\alpha}\right)^3 + \frac{3}{4}\frac{x_0 - x}{\alpha} + \frac{1}{2} & \text{if } x > x_0 - \alpha \wedge x < x_0 + \alpha \\ 1 - \left(-\frac{1}{4}\left(\frac{x_1 - x}{\alpha}\right)^3 + \frac{3}{4}\frac{x_1 - x}{\alpha} + \frac{1}{2}\right) & \text{if } x > x_1 - \alpha \wedge x < x_1 + \alpha \\ 0 & \text{if } x \geq x_0 + \alpha \wedge x \leq x_1 - \alpha. \end{cases} \tag{6.69}$$

We can observe exemplifications for varying α in Figure 6.5. We now define error norms

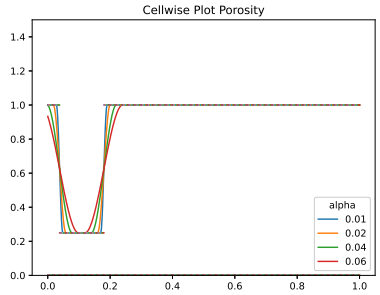

Figure 6.5: Smoothed Porosity for $\alpha \in \{0.01, 0.02, 0.04, 0.06\}$

for water height H and weighted velocity uH as

$$E_H = ||H - H_\alpha||_{L^2((0,T)\times\Omega)} = \left(\int_0^T \int_\Omega (H - H_\alpha)^2 \,\mathrm{d}x\,\mathrm{d}t\right)^{1/2} \tag{6.70}$$

$$E_{uH} = ||uH - uH_\alpha||_{L^2((0,T)\times\Omega)} = \left(\int_0^T \int_\Omega (uH - uH_\alpha)^2 \,\mathrm{d}x \,\mathrm{d}t \right)^{1/2}. \tag{6.71}$$

From construction of the well-balanced scheme it is obvious that steady state conditions $uH = 0$ for $H + z = c$ lead to zero error norms. We hence exemplifying investigate Gaussian initial conditions for the surface height H, i.e. $(H_0 + z, uH_0) = (1 + 0.3\exp(-100(x - 1/2)^2), 0)$, for final time $T = 0.4$ and step size $dt = 1\mathrm{e}{-3}$, where the discontinuities are located at $x_0 = 0.038$ and $x_1 = 0.18$. We can observe the convergence numerically, i.e. $U = \lim_{\alpha\to 0} U_\alpha$ for $\phi = \lim_{\alpha\to 0} \phi_\alpha$, as shown in table 6.1. At this point, we would like to emphasize that the convergence is limited by the grid size of the mesh, hence showing the limit decrease for $\alpha \to 0$ is only possible for $h_\kappa \to 0$.

α	$\|\|H - H_\alpha\|\|_{L^2((0,T)\times\Omega)}$	$\|\|uH - uH_\alpha\|\|_{L^2((0,T)\times\Omega)}$
0.06	3.45587	8.41055
0.04	2.05134	4.69693
0.03	1.40056	3.08506
0.02	0.81980	1.69824
0.01	0.3443	0.601958
0.005	0.17583	0.23194
0.001	0.10549	0.11108

Table 6.1: Error Norms E_H and E_{uH} for decreasing α

6.5 Numerical Results

In this Section we will verify theoretical results in two scenarios - the half circle (cf. to Section 5.4.2) in Section 6.5.1 and a representing mesh for the Mentawai islands, that are motivated in Section 1.1 and have not been investigated in this thesis yet, in Section 6.5.2.

6.5.1 Ex.1 The Half-Circled Mesh

In the first example for porous SWE, we look at the model problem - the half circle that was described in Section 6.2. The declaration of boundaries follows the description in Section 5.4.2. We will work with a rest height of the water at $\bar{H} = 1$, while targeting zeroed velocities. We penalize volume and thinness by setting $\nu_2 = 1\mathrm{e}{-4}$, $\nu_4 = 1\mathrm{e}{-2}$ and enforce a stronger regularization by $\nu_3 = 1\mathrm{e}{-4}$. The parameters in the porous shallow water system are set as follows: For the weight of the diffusion terms in the momentum equation we set $\mu_f = 1\mathrm{e}{-2}$. The mesh, displayed in Figure 6.6, was created using the finite element mesh generator GMSH [85], where the vertex density around the obstacle is increased to ensure a high resolution.

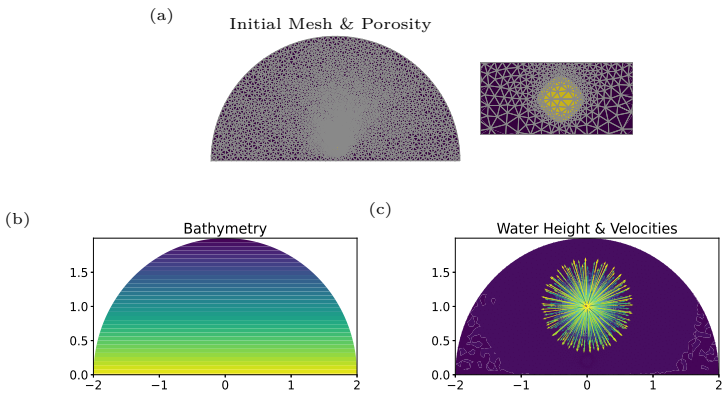

Figure 6.6: (a) Initial Mesh and Porosity with Enlarged Image Section, (b) Linear Bathymetry, (c) Field State at $t = 0.1$

The material coefficient is at $\phi_2 = 0.4$ in D and we obtain classical SWE on $\tilde{\Omega}$ by setting $\phi_1 = 1$. In addition, we employ Gaussian initial conditions as $(H_0 + z, uH_0, vH_0) = (1 + \exp(-15x^2 - 15(y-1)^2), 0, 0)$, which result into a wave traveling in time towards the boundaries. Solving the state equations requires the definition of the time-horizon $T = 2$, which is chosen to include the travel of a wave to and from the shore using a time-stepping size of $\Delta t = 2\text{e}{-3}$. Our calculations are performed for a linear decreasing time-constant sediment $z = 0.5 - 0.25y$. Having solved state and adjoint equations, the mesh deformation is performed for initial step size $\rho_{step} = 1.5$ as described in Section 5.4.1. Remaining parameters are chosen in accordance with Section 5.4.2. In Figure 6.7 the result of the shape optimization procedure is displayed after 24 iterations, where deformations appear to be symmetric.

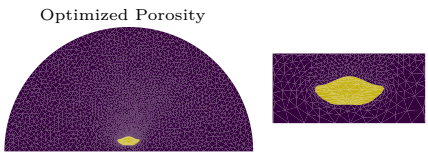

Figure 6.7: Optimized Porous Region with Enlarged Image Section

As we observe in Figure 6.8, we have achieved a decrease in the objective above 11%, which is notably smaller than in the preceding chapter and due to the transmission of the obstacle.

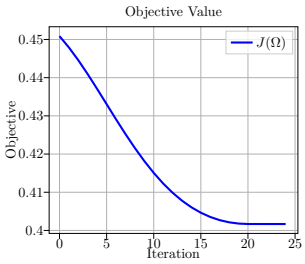

Figure 6.8: Objective Value per Iteration

6.5.2 Ex.2 The Mentawai Islands Mesh

The second example will take up one of the motivational examples of Section 1.1 - the Mentawai islands located in the south-west of Sumatra, Indonesia that turned out to be an effective shield in the 2010 tsunami for the mainland located behind [174]. Mentawai islands are threatened by rising sea levels and victim to massive floodings in the last decades and are hence offering itself for protective measures. For computational ease, we have decided to not consider smaller islands of a diameter less than 5km. Similar to the preceding example, we interpret Γ_1 as coastline of the mainland, Γ_2 as the open sea boundary such as Γ_3 as the interface boundary of the offshore islands. Assuming that islands are flooded, we represent them by a difference in the material coefficient, which shape is to be optimized. For this we set $\phi_2 = 0.5$ at D and $\phi_1 = 1$ on $\tilde{\Omega}$ (cf. to Figure 6.9, subfigure (a)). As before, we are in a tsunami-like setting and start with suitable Gaussian initial conditions for the height of the water. For simplicity, the sediment height is assumed to be zero on the whole domain. The remaining model-settings are similar to Section 5.4.2.

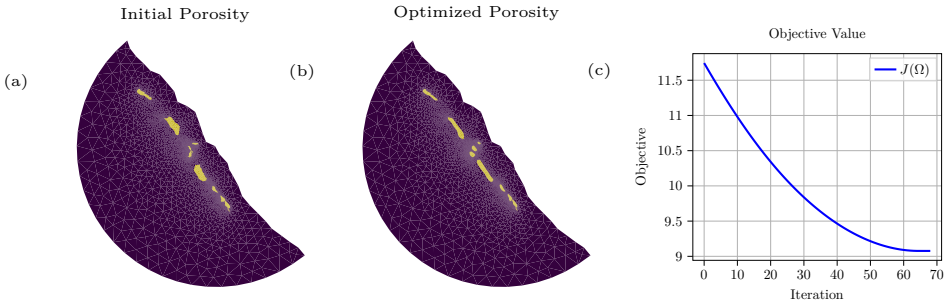

Figure 6.9: (a) Initial Porosity, (b) Optimized Porosity, (c) Objective Value per Iteration

We can once more observe convergence in the objective, after applying shape optimization on the porous region (cf. to Figure 6.9, subfigures (b) & (c)). It can be observed that obstacles are enlarged in perpendicular direction to the incoming sea wave.

Chapter 7

Shape Optimization for Coupled Shallow Water Equations

The following description completes for the time being investigations of fluids in the Eulerian setting based on shallowness assumptions. Instead of a fixed sediment in time, as it was investigated in Chapters 5 and 6, we assume that it moves and interacts with the fluid. For this reason we couple the SWE from before with a sediment transport formula of type Exner [116, 124, 77].
The chapter opens in Section 7.1 with an introduction of equations of type Exner, where an accurate definition of the sediment transport rate has employed physicists, geologists and oceanographers throughout the last decades [167, 121, 88]. We reduce to the model described in [88] for the following investigations. In Section 7.2 the PDE-constrained optimization problem from previous chapters is extended for the coupled SWE-Exner (SWEE). As before, continuous adjoint and shape derivative are derived as follow-up to Chapter 5. SWEE require specific attention in the numerical modeling as illustrated in Section 7.4, among other things we hereby firstly propose an Eulerian-Lagrangian coupling for the discretization. The chapter ends with numerical verifications in Section 7.5.

7.1 Exner-Type Sediment Transport Laws

In this work we are especially interested in the modeling of erosive phenomenons in the sediment transport. In contrast to the regular disposition of sand in regular flowing fluids, it describes the transport of bed material itself by a fluid moving over the surface. In practice, this leads to an additional law of conservation for the sediment mass. These types of equations are named after Austrian meteorologist Felix Maria Exner and can be described in a general form [73].

Definition 7.1. *(Exner-Type Equations) Sediment laws for the evolution of*

$z : \Omega \times (0,T) \to \mathbb{R}$ *of the form*

$$\frac{\partial z}{\partial t} = -\frac{1}{1-\phi}\nabla \cdot Q_s \quad \text{on } \Omega \times (0,T) \tag{7.1}$$

are called equations of type Exner.

In this definition $\phi \in [0,1)$ is said to be the porosity of the sediment and $Q_s : \Omega \times (0,T) \to \mathbb{R}^d$ is said to be the bedload sediment flux or the bedload sediment transport rate. Adjusting these terms for different sediment types is the delicate part of Exner equations.
One of the simplest definitions was given in [88].

Definition 7.2. *(Grass Sediment Transport) The Grass formula for the sediment transport formula is given by*

$$Q_s = A_d \frac{Q}{H} ||Q/H||_2^2, \tag{7.2}$$

where $0 \leq A_d \leq 1$.

Remark. A large coefficient in (7.2) results in a strong interaction between sediment and fluid. This formula is build such that the sediment immediately starts to move with the fluid itself. A_d is often only obtained from experimental data and correlates with the mean grain diameter $d_s > 0$ [88].

Additional formulae are most often based on the assumption that sediment starts to move once a critical shear stress threshold τ_{cr}^* is surpassed by the dimensionless bottom shear stress [167] that defines as

$$\tau_b^* = \frac{K||Q/H||_2^2 Q}{8H(s-1)gd_s}, \tag{7.3}$$

where $s = \rho_s/\rho > 0$ is the relative density of sediment in water, K some friction coefficient and g as before the gravitational acceleration. All these equations can be summarized in a single generalized form.

Definition 7.3. *(Shields-Type Sediment Transport) Sediment transport laws of the form*

$$Q_s = \begin{pmatrix} c\left(\tau_{b,1}^* - \tau_{cr}^*\right)_+^{p_E} \sqrt{(s-1)gd_s^3} \\ c\left(\tau_{b,2}^* - \tau_{cr}^*\right)_+^{p_E} \sqrt{(s-1)gd_s^3} \end{pmatrix} \tag{7.4}$$

are called of shields-type for to be determined constants $c > 0$ *and* $p_E > 0$.

Without claim for completeness the table below lists some of the most famous variants, which can be extended by various different sediment fluxes [42, 46, 135]:

Observer	p_E	c	τ^*_{cr}
Du Boys [93]	1	$\frac{1}{\sqrt{(s-1)gd_s^3}}$	0.047
Meyer-Peter & Müller [121]	3/2	8	0.047
Fernandez Luque & Van Beek [115]	3/2	5.7	0.047
Ribberink [151]	1.65	11	0.047

Table 7.1: Parameter for Shields-Type Sediment Transport

Remark. Due to its simplicity, the Grass model of Definition 7.2 is used in the following. Remaining laws of Definition 7.3 require a specific handle of non-differentiable functions, e.g. in Chapter 8 a smoothing of the *max*-function is proposed.

7.2 Model Formulation

We start by restating the model problem from Chapter 5, but since we are working with SWEE we redefine the the solution variable as $U = (H, Hu, Hv, z)$. Hence, we have increased the dimensionality of the problem and thus need to redefine flux matrices such as initial and boundary conditions. The SWEE initial boundary value problem requires us to calculate

$$\partial_t U + \nabla \cdot F(U) - \nabla \cdot (G(\mu)\nabla \hat{U}) = B_1(U)\frac{\partial U}{\partial x} + B_2(U)\frac{\partial U}{\partial y} \quad \text{on } \Omega \times (0,T), \tag{7.5}$$

where the flux matrix reads as

$$F(U) = \begin{pmatrix} Hu & vH \\ Hu^2 + \frac{1}{2}gH^2 & Huv \\ Huv & Hv^2 + \frac{1}{2}gH^2 \\ \frac{1}{1-\phi}Q_{s,1} & \frac{1}{1-\phi}Q_{s,2} \end{pmatrix} \tag{7.6}$$

and

$$B_1(U) = \begin{pmatrix} 0 & 0 & 0 & 0 \\ 0 & 0 & 0 & -gH \\ 0 & 0 & 0 & 0 \\ 0 & 0 & 0 & 0 \end{pmatrix}, \quad B_2(U) = \begin{pmatrix} 0 & 0 & 0 & 0 \\ 0 & 0 & 0 & 0 \\ 0 & 0 & 0 & -gH \\ 0 & 0 & 0 & 0 \end{pmatrix}. \tag{7.7}$$

Relying on the simplistic half-circled domain from Section 5.2, we define boundary conditions to be

$$\begin{aligned} &Q \cdot n = 0, \nabla H \cdot n = 0, \nabla Q_1 \cdot n = 0, \nabla Q_2 \cdot n = 0, \nabla z \cdot n = 0 && \text{on } \Gamma_1, \Gamma_3 \times (0,T) \\ &H = H_1, z = z_1, \nabla Q_1 \cdot n = 0, \nabla Q_2 \cdot n = 0 && \text{on } \Gamma_2 \times (0,T) \end{aligned} \tag{7.8}$$

and initial conditions as

$$U = U_0 \quad \text{in } \Omega \times \{0\}. \tag{7.9}$$

We obtain a PDE-constrained optimization problem by e.g. minimizing the four objectives of the preceding chapter with

$$J_1(\Omega) = \int_0^T \int_{\Gamma_1} \frac{1}{2} ||N(\hat{U}(t,x) - \bar{U}(t,x))||_2^2 \, \mathrm{d}s \, \mathrm{d}t, \tag{7.10}$$

where the objective in (7.10) is amended for the propagation of the sediment, i.e. $N \in \mathbb{R}^{4\times 4}$ is a diagonal matrix. To stabilize the solution we are again referring to SWE with artificial viscosity, where the diffusion in the mass conservation of the sediment can be motivated via viscous sedimentation models [184]. We control the amount of added diffusion as in Section 5.2 by diagonal matrix $G(\mu)$ with entries $\mu = (\mu_{v,1}, \mu_f, \mu_{v,2}) \in \mathbb{R}_+ \times \mathbb{R}_+^2 \times \mathbb{R}_+$ for $\hat{U} = (H + z, uH, vH, z)$.

7.3 Derivation of Adjoint & Shape Derivative

We will now derive adjoint equations such as the shape derivative. For this, we will mostly follow Section 5.3. The adjoint equations for the SWEE, solving for $P = (p, R, s)$, can be obtained from the following theorem based on the weak form of (7.5).

Theorem 7.4. *(Coupled SWE Adjoint) Assume that the solution U of (7.5) is at least in $H^1((0,T)\times\Omega)^4$, then is the adjoint in strong form given by*

$$\begin{aligned} -\frac{\partial p}{\partial t} + \frac{1}{H^2}(Q\cdot\nabla)R\cdot Q - gH(\nabla\cdot R) - \nabla\cdot(\mu_{v,1}\nabla p) + g\nabla z\cdot R \\ - \frac{1}{1-\phi}\frac{\partial Q_s}{\partial H}\cdot\nabla s = -N_{11}(H+z-\bar{H})_{\Gamma_1} \end{aligned} \tag{7.11}$$

such as

$$\begin{aligned} -\frac{\partial R}{\partial t} - \nabla p - \frac{1}{H}(Q\cdot\nabla)R - \frac{1}{H}(\nabla R)^T Q - (\nabla\cdot(G(\mu_f)\nabla(R)))^T \\ - \frac{1}{1-\phi}\frac{\partial Q_s}{\partial Q}\cdot\nabla s = -G(N_{22,33})(Q-\bar{Q})_{\Gamma_1} \end{aligned} \tag{7.12}$$

and

$$-\frac{\partial s}{\partial t} - \nabla\cdot(gHR) - \nabla\cdot(\mu_{v,2}\nabla s) = -N_{44}(z-\bar{z})_{\Gamma_1} - N_{11}(H+z-\bar{H})_{\Gamma_1} \tag{7.13}$$

with final conditions

$$\begin{aligned} p &= 0 \quad \text{in } \Omega\times\{T\} \\ R &= 0 \quad \text{in } \Omega\times\{T\} \\ s &= 0 \quad \text{in } \Omega\times\{T\} \end{aligned} \tag{7.14}$$

and boundary conditions as

$$\begin{aligned} R\cdot n = 0, \nabla p\cdot n = 0, \nabla R_1\cdot n = 0, \nabla R_2\cdot n = 0, \nabla s\cdot n = 0 \quad &\text{on } \Gamma_1, \Gamma_3\times(0,T) \\ pn + \frac{1}{H_1}(Q\cdot n)R + \frac{1}{H_1}(QR)\cdot n = 0, \nabla R_1\cdot n = 0, \nabla R_2\cdot n, \nabla s\cdot n = 0 \quad &\text{on } \Gamma_2\times(0,T). \end{aligned} \tag{7.15}$$

Proof. Integration by parts on the weak form of the SWEE and differentiating for the states $\frac{\partial a(H,Q,z,p,R,s)}{\partial H}$ and $\frac{\partial a(H,Q,z,p,R,s)}{\partial Q}$ is done according to the proof of the classical SWE adjoint of Theorem 5.2 e.g. for given additional partial derivatives as in (7.20). Furthermore, integration by parts and partial derivatives w.r.t. the sediment height $\frac{a(H,Q,z,p,R,s)}{\partial z}$ gives (7.13). Now if $\frac{\partial a(H,Q,z,p,R,s)}{\partial U} = -\frac{\partial J_1}{\partial U}$ then $\frac{\partial \mathcal{L}}{\partial U} = 0$ is fulfilled if the boundary conditions are suitably chosen. □

We can rewrite the adjoint of the coupled SWE (7.11)-(7.13) in vector form, on which we can build on finite element discretizations.

$$-\frac{\partial P}{\partial t} + AP_x + BP_y + CP - \nabla \cdot (G(\mu)\nabla P) = S, \tag{7.16}$$

where by the product rule follows

$$A = \begin{pmatrix} 0 & \frac{Q_1}{H^2} - gH & \frac{Q_1 Q_2}{H^2} & a_1 \\ -1 & -2\frac{Q_1}{H} & -\frac{Q_2}{H} & a_2 \\ 0 & 0 & -\frac{Q_1}{H} & a_3 \\ 0 & -gH & 0 & 0 \end{pmatrix}, \quad B = \begin{pmatrix} 0 & \frac{Q_1 Q_2}{H^2} & \frac{Q_2^2}{H^2} - gH & b_1 \\ 0 & -\frac{Q_2}{H} & 0 & b_2 \\ -1 & -\frac{Q_1}{H} & -2\frac{Q_2}{H} & b_3 \\ 0 & 0 & -gH & 0 \end{pmatrix} \tag{7.17}$$

and C originates from variations in the sediment in (7.7) such that

$$C = \begin{pmatrix} 0 & g\frac{\partial z}{\partial x} & g\frac{\partial z}{\partial y} & 0 \\ 0 & 0 & 0 & 0 \\ 0 & 0 & 0 & 0 \\ 0 & -g\frac{\partial H}{\partial x} & -g\frac{\partial H}{\partial y} & 0 \end{pmatrix}. \tag{7.18}$$

Here S is chosen as the right hand-side of (7.11)-(7.13). In addition, we denote partial derivatives of the Grass model as of Definition 7.2, that are used in the adjoint, by

$$\begin{aligned} a_1 &= \frac{1}{1-\phi}\frac{\partial Q_{s,1}}{\partial H}, & a_2 &= \frac{1}{1-\phi}\frac{\partial Q_{s,1}}{\partial Q_1}, & a_3 &= \frac{1}{1-\phi}\frac{\partial Q_{s,1}}{\partial Q_2} \\ b_1 &= \frac{1}{1-\phi}\frac{\partial Q_{s,2}}{\partial H}, & b_2 &= \frac{1}{1-\phi}\frac{\partial Q_{s,2}}{\partial Q_1}, & b_3 &= \frac{1}{1-\phi}\frac{\partial Q_{s,2}}{\partial Q_2}, \end{aligned} \tag{7.19}$$

where we have for $i, j \in \{1, 2\}$ with $i \neq j$ that

$$\begin{aligned} \frac{\partial Q_{s,i}}{\partial H} &= -A_d \frac{Q_i}{H^2}\left(\frac{Q_1^2}{H^2} + \frac{Q_2^2}{H^2}\right) - 2A_d \frac{Q_i}{H}\left(\frac{Q_1^2}{H^3} + \frac{Q_2^2}{H^3}\right) \\ \frac{\partial Q_{s,i}}{\partial Q_i} &= A_d\left(\frac{Q_1^2}{H^3} + \frac{Q_2^2}{H^3}\right) + 2A_d \frac{Q_i^2}{H^3} \\ \frac{\partial Q_{s,i}}{\partial Q_j} &= 2A_d \frac{Q_i Q_j}{H^3} \end{aligned} \tag{7.20}$$

For this model we need additional terms in the shape derivative compared to (5.27).

Theorem 7.5. *(SWEE Shape Derivative) Assume that the solution U of (7.5) is at least in $H^1((0,T)\times\Omega)^4$. Moreover, assume that the adjoint equation (7.15) admits a solution $P \in H^1((0,T)\times\Omega)^4$. Then the shape derivative of the objective $J_1(\Omega)$ at Ω in the direction V is given by*

$$DJ_1(\Omega)[V] = DJ_1^{SWE}(\Omega)[V] + \int_0^T \int_\Omega \Bigg[-\frac{1}{1-\phi}(\nabla V)^T : \nabla Q_s s - \mu_{v,2}\nabla z^T(\nabla V + \nabla V^T)\nabla s + \operatorname{div}(V)\left\{ \frac{\partial z}{\partial t}s + \frac{1}{1-\phi}\nabla\cdot Q_s s - \mu_{v,2}\nabla z\cdot\nabla s \right\}\Bigg] \mathrm{d}x\,\mathrm{d}t, \tag{7.21}$$

where $DJ_1^{SWE}(\Omega)[V]$ refers to the derived shape derivative of Theorem 5.3.

Proof. The shape derivative $DJ_1^{SWE}(\Omega)[V]$ is obtained by following the proof of Theorem 5.3. Using the same computations for the sediment transport equation with artificial viscosity yields the additional terms. □

7.4 Solutions to the Forward Problem

Obtaining numerical solutions to the SWEE system, following Chapters 5 and 6 is not straightforward. Difficulties arise due to the 4×4 Jacobian system and different speeds of the sediment and water propagation. In the literature commonly two approaches are presented to treat this problem, relying either on a coupled or a decoupled approach, obtained by operator splitting [177, Chapter 8]. The latter technique is attractive from the computational side, since deviating wave and sediment speeds can be easily dealt with. However, frequently numerical instabilities arise due to the bad approximation of the systems true eigenvalues [60]. In the following subsections we will describe each approach and in addition present a novel technique in the decoupled setting in an Eulerian-Lagrangian framework. For simplicity we restrict to hyperbolic SWE, the diffusive counterpart follows likewise.

Decoupled Eulerian Approach

Since the speed of the water surface is often much faster than the speed of the bottom topography, we potentially add a severe stability restriction on the size of the time steps. This can lead to excessive numerical diffusion for the sediment. In [51] an operator splitting is proposed [177, Chapter 8]. Hence, alternately the first and second systems are solved in $\Omega\times(0,T)$. In this setting the first system is defined in terms of solution variables $U:\Omega\times(0,T)\to\mathbb{R}\times\mathbb{R}^2$ and fixed sediment $z:\Omega\to\mathbb{R}$, i.e.

$$\begin{aligned} \partial_t U + \nabla\cdot F(U,z) &= S(U,z) \\ \partial_t z &= 0 \end{aligned} \tag{7.22}$$

with notion of fluxes and sources as in Section 5.2 and the second system for solution variable $z : \Omega \times (0,T) \to \mathbb{R}$, while fixing $U : \Omega \to \mathbb{R} \times \mathbb{R}^2$, i.e.

$$\begin{aligned} \partial_t z + \frac{1}{1-\phi} \nabla \cdot Q_s = 0 \\ \partial_t U = 0. \end{aligned} \tag{7.23}$$

This holds the evident advantage, that (7.22) leads to decreased solution variables for a hyperbolic system of equations that can be written in conservative form. However, in [104, 60, 148] it was shown, that this method may lead to a large overestimation in particular situations and to unphysical instabilities. A pseudocode with suitable step size evaluation can be taken from Algorithm 5.

Algorithm 5 Operator Splitting for SWEE in Eulerian-Eulerian Setting

Initialization
while $t < T$ **do**
1. Calculate Stable Timestep: Δt
2. Calculate Half Time-Step for First System $U_h(t + \Delta t/2)$ [via DG & Member of Theta-Methods]
3. Calculate Full Time-Step for Second System $z_h(t + \Delta t)$ [via DG & Member of Theta-Methods]
4. Calculate Half Time-Step for First System $U_h(t + \Delta t)$ [via DG & Member of Theta-Methods]
5. Set $t = t + \Delta t$

end while

Decoupled Eulerian-Lagrangian Approach

For pure advective movements Lagrangian fluid transport is known to be free of numerical diffusion [66]. As it will be central in Chapter 8, discretizations to Lagrangian descriptions are commonly obtained in a meshfree or particle-based setting. For the discretization of an Eulerian-Lagrangian coupling, using a splitted system as introduced before, we observe that we are in need to define particle-to-mesh and mesh-to-particle operations such that both systems are able to interconnect. We will follow the framework provided in [118]. A pseudocode is pictured below, where individual components are described in the following.

Algorithm 6 Operator Splitting for SWEE in Eulerian-Lagrangian Setting

Initialization
while $t < T$ **do**
1. Calculate Stable Timestep: Δt
2. Calculate Half Time-Step for First System $U_h(t + \Delta t/2)$ [via DG & Member of Theta-Methods]
3. Calculate Full Time-Step for Second System [via Particle Projection Step, $x_p(t)$ & $z_p(t + \Delta t)$]
4. Calculate Half Time-Step for First System $U_h(t+\Delta t)$ [via Mesh Projection Step, DG & Member of Theta-Methods]
5. Set $t = t + \Delta t$

end while

In this setting, we calculate a solution to the first system as explained in Chapter 5 and the decoupled Eulerian approach. The obtained discretized solution $U_h \in W_h \subset \mathcal{H}^1(\mathcal{T}_h \times (0,T))^3$ is translated in particle properties $(H_p(t), Q_p(t)) =: U_p(t) : (0,T) \to \mathbb{R} \times \mathbb{R}^2$ for each particle $p \in \{1, ..., N\}$ carrying its location $x_p(t) : (0,T) \to \Omega$, the required properties and a link to the reference cell [118]. In the following, analogously to preceding chapters we omit time-dependencies of variables for readability. In each time step we calculate a particle projection.

Definition 7.6. *(Particle Projection) The particle projection is defined by the solution to*

$$\min_{H_p} \sum_{p \in \{1,\dots,N\}} \frac{1}{2} \left(H_h(x_p) - H_p\right)^2 \tag{7.24}$$

for canonical finite element interpolation w.r.t. to the particle position as in (2.92) of $H_h(x_p)$.

In Definition 7.6 a trivial solution is obtained for $H_p = H_h(x_p)$ for all $p \in \{1, ..., N\}$. In this setting are particle vector quantities obtained via component-wise particle projection.

Definition 7.7. *(Particle Update Scheme) The particle position is determined via finite element interpolation of a sediment transport formula as in Definition 7.1, i.e.* $Q_{s_h} : \Omega \times (0,T) \to \mathbb{R}^2$, *such that*

$$\frac{dx_p}{dt} = \frac{1}{1-\phi} Q_{s_h}(x_p, t) \tag{7.25}$$

for each $t \in (0,T)$. *In this setting the particles move, while carried properties are fixed in time.*

Having calculated the new particle coordinate set, we can introduce the particle-to-mesh interaction, which can be stated as simple L^2-projection or more sophisticated as PDE-constrained optimization projection [118]

Definition 7.8. *(PDE-Constrained-Projection) The mesh field* $z_h \in W_h \subset \mathcal{H}^1(\mathcal{T}_h \times (0,T))$ *is obtained via*

$$\begin{aligned} \min_{z_h} & \sum_{p\in\{1,\dots,N\}} \frac{1}{2}\left(z_h(x_p) - z_p\right)^2 \\ s.t. & \ \frac{\partial z_h}{\partial t} + \frac{1}{1-\phi}\nabla \cdot Q_{s_h} = 0. \end{aligned} \tag{7.26}$$

where W_h *is a finite element approximation space from Section 2.3.1 and boundary conditions are defined in correspondence to the continuous problem.*

Remark. Since this Eulerian-Lagrangian coupling appears novel, we will shortly numerically exemplify the proceeding described above. We follow [118] from which LEoPart[1] an extension of the FEniCS package is obtained. We will start on a uniform rectangle mesh with a total number of 3200 elements. On this domain we initialize 1.102.500 particles. The setting can be taken from Figure 7.1. As in Section 5.4.2 we

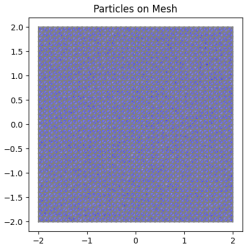

Figure 7.1: Scattered Plot of 1.102.500 Blue Particles on a Uniform Rectangle Mesh

initialize Gaussian initial conditions for the height of the water and the sediment, i.e. $H_0 + z_0 = 2 + \exp(-5x^2 - 5(y+0.2)^2)$ and $z_0 = 1.5\exp(-x^2 - (y+1)^2)$ alongside zeroed velocities. Initial fields are pictured in subfigures (a) and (b) of Figure 7.2. For the particle update scheme Definition 7.7 we rely on Grass-like velocities as in Definition 7.2. The resulting interaction of Eulerian waves and the Lagrangian particles can be observed in subfigure (c). We would like to highlight that the large number of particles certainly builds an impediment for the performance of the method. We have chosen the number in order not to obtain cells without particles during the propagation of the wave, which is currently not supported in the LEoPart software extension.

Coupled Eulerian Approach

Coupled SWE let us deal with hyperbolic and after stabilization possibly fully parabolic equations. We employ once more a SIPG method to discretize the coupled equations. As it was described before in Chapter 5, occurring numerical flux functions depend on wave speeds. In the literature it is either stated that it is not possible to find an explicit

[1] https://github.com/BinWang0213/3rdParty-LEoPart

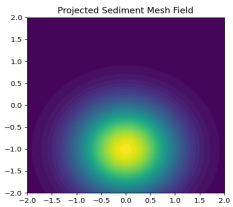

(a) Sediment Field z_h obtained from Particle Projections in $t = 0.1$

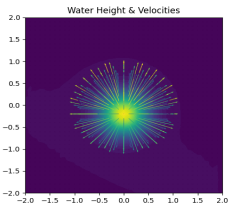

(b) Water Height H_h and Velocities Q_h in $t = 0.1$

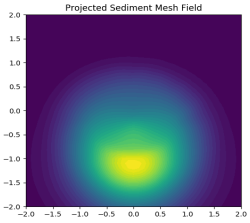

(c) Sediment Field z_h obtained from Particle Projections at $t = 2.0$

Figure 7.2: Eulerian-Lagrangian Model Simulation

expression for the eigenvalues of the 4×4 Jacobian matrix [146] or that it is not trivial nor effective to obtain a closed form [76]. In the following we will sketch the approach that utilizes the Cardano-Vieta formula as described in [98] and [47] to obtain eigenvalues to a resulting cubic polynomial.

We define a pseudo Jacobian matrix based on a reformulation of (7.5) without diffusive terms following [47], while introducing Jacobian $\mathcal{J}_i := \partial_U F_i(U)$, as

$$\frac{\partial U}{\partial t} + \sum_{i=1}^{2} \mathcal{J}_i \frac{\partial U}{\partial x_i} - B_i \frac{\partial U}{\partial x_i} = 0. \tag{7.27}$$

Then the pseudo Jacobian matrices $\tilde{\mathcal{J}}_1(U)$ and $\tilde{\mathcal{J}}_2(U)$ are obtained as

$$\tilde{\mathcal{J}}_1(U) = \mathcal{J}_1(U) - B_1(U) \quad = \begin{pmatrix} 0 & 1 & 0 & 0 \\ -\frac{Q_1^2}{H^2} + gH & 2\frac{Q_1}{H} & 0 & gH \\ -\frac{Q_1 Q_2}{H^2} & \frac{Q_2}{H} & \frac{Q_1}{H} & 0 \\ \frac{1}{1-\phi}\frac{\partial Q_{s,1}}{\partial H} & \frac{1}{1-\phi}\frac{\partial Q_{s,1}}{\partial Q_1} & \frac{1}{1-\phi}\frac{\partial Q_{s,1}}{\partial Q_2} & 0 \end{pmatrix} \tag{7.28}$$

and

$$\tilde{\mathcal{J}}_2(U) = \mathcal{J}_2(U) - B_2(U) \quad = \begin{pmatrix} 0 & 0 & 1 & 0 \\ -\frac{Q_1 Q_2}{H^2} & \frac{Q_2}{H} & \frac{Q_1}{H} & 0 \\ -\frac{Q_2^2}{H^2} + gH & 0 & 2\frac{Q_2}{H} & gH \\ \frac{1}{1-\phi}\frac{\partial Q_{s,2}}{\partial H} & \frac{1}{1-\phi}\frac{\partial Q_{s,2}}{\partial Q_1} & \frac{1}{1-\phi}\frac{\partial Q_{s,2}}{\partial Q_2} & 0 \end{pmatrix} \tag{7.29}$$

or equivalently

$$\tilde{\mathcal{J}}_1(U) = \begin{pmatrix} 0 & 1 & 0 & 0 \\ -u + gH & 2u & 0 & gH \\ -uv & v & u & 0 \\ \frac{1}{1-\phi}\frac{\partial Q_{s,1}}{\partial H} & \frac{1}{1-\phi}\frac{\partial Q_{s,1}}{\partial Q_1} & \frac{1}{1-\phi}\frac{\partial Q_{s,1}}{\partial Q_2} & 0 \end{pmatrix} \tag{7.30}$$

and

$$\tilde{\mathcal{J}}_2(U) = \begin{pmatrix} 0 & 0 & 1 & 0 \\ -uv & v & u & 0 \\ -v^2 + gH & 0 & 2v & gH \\ \frac{1}{1-\phi}\frac{\partial Q_{s,2}}{\partial H} & \frac{1}{1-\phi}\frac{\partial Q_{s,2}}{\partial Q_1} & \frac{1}{1-\phi}\frac{\partial Q_{s,2}}{\partial Q_2} & 0 \end{pmatrix}. \tag{7.31}$$

Here the partial derivatives of the sediment transport formula for the Grass method are obtained as in (7.20). A flux Jacobian matrix is finally obtained by $B(U,n) = \sum_{i=1}^{2} n_i \tilde{\mathcal{J}}_i(U)$ such that

$$B(U,n) = \begin{pmatrix} 0 & n_1 & n_2 & 0 \\ (-u+gH)n_1 - uvn_2 & 2un_1 + vn_2 & un_2 & gHn_1 \\ -uvn_1 - (v^2+gH)n_2 & vn_1 & un_1 + 2vn_2 & gHn_2 \\ \frac{1}{1-\phi}\frac{\partial Q_{s,1}}{\partial H}n_1 + \frac{1}{1-\phi}\frac{\partial Q_{s,2}}{\partial H}n_2 & \frac{1}{1-\phi}\frac{\partial Q_{s,1}}{\partial Q_1}n_1 + \frac{1}{1-\phi}\frac{\partial Q_{s,2}}{\partial Q_1}n_2 & \frac{1}{1-\phi}\frac{\partial Q_{s,1}}{\partial Q_2}n_1 + \frac{1}{1-\phi}\frac{\partial Q_{s,2}}{\partial Q_2}n_2 & 0 \end{pmatrix}. \tag{7.32}$$

We now follow [47] to obtain the eigenvalues to the associated 4×4 flux Jacobian matrix by relying on the Cardano-Vieta formula [43]. Hence, in [47] it is stated that the first eigenvalue to (7.32) can be found as

$$\lambda_1 = un_1 + vn_2, \tag{7.33}$$

which leaves us with the cubic polynomial [47]

$$P(\lambda) = \lambda^3 + c_1\lambda^2 + c_2\lambda + c_3 \tag{7.34}$$

for

$$\begin{aligned} c_1 &= -2(un_1 + vn_2) \\ c_2 &= (un_1 + vn_2)^2 - gH(1 + n_2 B_{4,3}(U,n) + n_1 B_{4,2}(U,n)) \\ c_3 &= gH\left(-B_{4,1}(U,n) + B_{4,2}(U,n)(-un_2^2 + vn_1n_2) + B_{4,3}(U,n)(-vn_1^2 + un_1n_2)\right). \end{aligned} \tag{7.35}$$

Defining $S = (3c_2 - c_1^2)/9$ and $R = (9c_1c_2 - 27c_3 - 2c_1^3)/54$ all the roots are real if $S^3 + R^2 < 0$ [47] and can be obtained by the Cardano-Vieta formula as [47]

$$\begin{aligned} \lambda_2 &= 2\sqrt{-S}\cos(\theta/3) - c_1/3 \\ \lambda_3 &= 2\sqrt{-S}\cos((\theta+2\pi)/3) - c_1/3 \\ \lambda_4 &= 2\sqrt{-S}\cos((\theta-2\pi)/3) - c_1/3 \end{aligned} \tag{7.36}$$

for $\theta = \arccos\left(R/\sqrt{-S^3}\right)$.

Remark. At this point we highlight, that wave speeds are differently obtained in the literature. Exemplifying in [170], it is referred to [177, Chapter 8] to state that wave-speeds of the multi-dimensional system in Cartesian coordinates are identical to the augmented one-dimensional problem, i.e. requiring to search the eigenvalues of either of the two matrices (7.30) or (7.31), whereas in [124] the eigenvalues are in contrast simplifying obtained for Jacobians without the inclusion of variations in the sediment.

7.5 Numerical Results for Shape Optimization for SWEE

Numerical results for shape optimization are obtained by relying on the coupled Eulerian approach described in the section before. It has the clear benefit that calculated eigenvalues from the forward system can be used in the numerical method for the adjoint system as derived in Theorem 5.4. As in previous chapters we calculate exemplifying results on the simplistic half-circled mesh. On this domain we rely on the same setting as in Section 5.4.2 for linear sediment, with the difference that the sediment is not fixed, but is determined by an Exner-type propagation law. In line with previous sections, the bedrock is transported for a Grass model with $A_d = 0.5$ and porosity $\phi = 0.2$ in Definition 7.2. In Figure 7.3 we have visualized the effect of tsunami-like waves on a linear sediment. We determine our objective (7.10) for the diagonal matrix

$$N = \begin{pmatrix} 1 & 0 & 0 & 0 \\ 0 & 1 & 0 & 0 \\ 0 & 0 & 1 & 0 \\ 0 & 0 & 0 & -0.1 \end{pmatrix} \tag{7.37}$$

with target water and sediment height such as velocities as

$$\bar{U} = \begin{pmatrix} 1 \\ 0 \\ 0 \\ 0 \end{pmatrix}. \tag{7.38}$$

This can be interpreted as the search for the rest height at the shore Γ_1 with zeroed velocities for increased sediment height. In Figure 7.4 , we can observe the deformed obstacle in addition to the decrease in the objective.

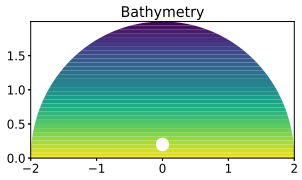

(a) $t = 0$

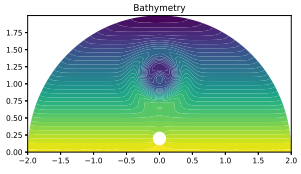

(b) $t = 0.5$

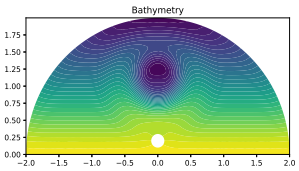

(c) $t = 1$

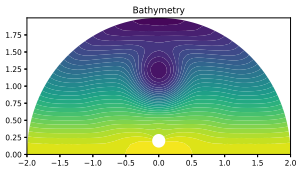

(d) $t = 1.5$

Figure 7.3: Visualization of a Sediment Propagation due to Water Heights & Velocities

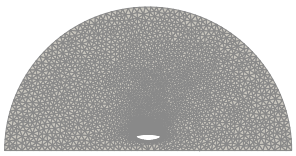

(a) Optimized Mesh & Obstacle

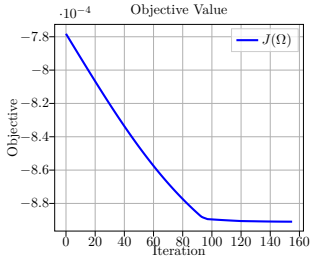

(b) Objective

Figure 7.4: Optimization Results

Chapter 8

Shape Optimization for Lagrangian Shallow Water Equations

Lagrangian particle movements appear to be the natural choice for solving sedimentation problems in oceanography, being generally free of diffusion. In contrast, inherent numerical diffusion in Eulerian methods can only affect the resolution of purely advective flows. It is therefore tempting to investigate shape optimization techniques for Lagrangian fluid flows. Typically, associated meshfree particle methods can be divided in two groups, the ones that approximate the weak form, e.g. the diffusive element [133], the element-free Galerkin [33] or the reproducing kernel method [113], such as the ones that approximate the strong form, e.g. the moving particle [108] or the vortex method [139]. In this chapter we investigate a particle flow that falls into the latter class - the smoothed particle hydrodynamics (SPH) [129].
We structure this as follows: We give a new derivation of adjoints for a general class of particle systems in Section 8.1. Before Section 8.2 will build the foundation for modeling the certain particle system described by SPH-fluids to discretize Lagrangian SWE, where the boundary interaction uncommonly for modeling but suitable for shape optimization follows [107]. Subsequently, Section 8.3 derives the discrete shape derivatives for this technique, based on adjoints that have been developed for the general case and verifies results numerically.

8.1 Adjoint for Particle Systems

In this section adjoints for a time-discretized system of particles are derived, we hence use the following definitions

Definition 8.1. *(Particle System) The system of states, i.e. the tuple consisting of position and velocities* $(x_k, u_k) \in \mathbb{R}^{dN} \times \mathbb{R}^{dN}$ *for time* $k \in \{1, ..., n\}$ *is called a particle system.*

Definition 8.2. *(Symplectic Euler) The iteration laws for force functions* $F : \mathbb{R}^{dN} \times \mathbb{R}^{dN} \times \Psi \to \mathbb{R}^{dN}$*, constant particle mass* $m > 0$*, fixed time-step* $\Delta t > 0$ *and to be determined control* $q \in \Psi$ *stated as*

$$\begin{aligned} u_k &= u_{k-1} + \frac{\Delta t}{m} F(u_{k-1}, x_{k-1}, q) \\ x_k &= x_{k-1} + \Delta t u_k \end{aligned} \tag{8.1}$$

are denoted as symplectic Euler.

The solution of the particle system constrains a time-dependent objective function $J : \mathbb{R}^{ndN} \times \mathbb{R}^{ndN} \times \Psi \to \mathbb{R}$, i.e.

$$J(u, x, q) = \sum_{k=1}^{n} J_k(u_k, x_k, q). \tag{8.2}$$

In this setting, we can derive the following theorem, consisting of recursively defined adjoints and an equation for the sensitivity calculation with respect to the control.

Theorem 8.3. *(Adjoint Particle System) Assume a particle system is solved iteratively using iteration (8.1), then sequences* $\{\delta_k\}_{k=1}^n$ *and* $\{\mu_k\}_{k=1}^n$ *required in adjoint computations are obtained from backward recursion, i.e.*

$$\delta_k = \delta_{k+1} + \frac{\Delta t}{m}(F^{x_k})^T \mu_{k+1} + \frac{\Delta t^2}{m}(F^{x_k})^T \delta_{k+1} + \left(J_k^{x_k}\right)^T \tag{8.3}$$

$$\mu_k = \mu_{k+1} + \frac{\Delta t}{m}(F^{u_k})^T \mu_{k+1} + \frac{\Delta t}{m}\delta_{k+1} + \frac{\Delta t^2}{m}(F^{u_k})^T \delta_{k+1} + \left(J_k^{u_k}\right)^T, \tag{8.4}$$

where the recursion starts at

$$\mu_n = J_n^{u_n} \quad \delta_n = J_n^{x_n}. \tag{8.5}$$

The sensitivity of the objective function with regards to the control q *are calculated as*

$$J^q = \sum_{k=1}^{n} J_k^q + \frac{\Delta t}{m}(F_{k-1}^q)^T \mu_k + \frac{\Delta t^2}{m}(F_{k-1}^q)^T \delta_k. \tag{8.6}$$

Proof. For simplicity we will rewrite the symplectic Euler by substitution of u_k in the second equation of (8.1)

$$\begin{aligned} u_k &= u_{k-1} + \frac{\Delta t}{m} F(u_{k-1}, x_{k-1}, q) \\ x_k &= x_{k-1} + \Delta t \left(u_{k-1} + \frac{\Delta t}{m} F(u_{k-1}, x_{k-1}, q) \right). \end{aligned} \tag{8.7}$$

The idea is related to [163] for adjoint calculations of iteration equations. We first sum up the products of iterates and unknown multipliers together with the objective (8.2)

$$\begin{aligned} 0 = &\sum_{k=1}^{n} \left[u_k - u_{k-1} - \frac{\Delta t}{m} F(u_{k-1}, x_{k-1}, q) \right]^T \mu_k \\ &+ \sum_{k=1}^{n} \left[x_k - x_{k-1} + \Delta t \left(u_{k-1} - \frac{\Delta t}{m} F(u_{k-1}, x_{k-1}, q) \right) \right]^T \delta_k \\ &+ J - \sum_{k=1}^{n} J_k \left(u_k, x_k, q \right). \end{aligned} \tag{8.8}$$

Differentiating w.r.t. the control leads to

$$\begin{aligned} 0 = &\sum_{k=1}^{n} \left[u_k^q - u_{k-1}^q - \frac{\Delta t}{m} F^{u_{k-1}} u_{k-1}^q - \frac{\Delta t}{m} F^{x_{k-1}} x_{k-1}^q - \frac{\Delta t}{m} F_{k-1}^q) \right]^T \mu_k \\ &+ \sum_{k=1}^{n} \left[x_k^q - x_{k-1}^q + \Delta t \left(u_{k-1}^q - \frac{\Delta t}{m} F^{u_{k-1}} u_{k-1}^q - \frac{\Delta t}{m} F^{x_{k-1}} x_{k-1}^q - \frac{\Delta t}{m} F_{k-1}^q) \right) \right]^T \delta_k \\ &+ J^q - \sum_{k=1}^{n} \left(J_k^{u_k} \right)^T u_k^q + \left(J_k^{x_k} \right)^T x_k^q + J_k^q. \end{aligned} \tag{8.9}$$

Using $x_0^q = u_0^q = 0$, shifting indices in sums and reorder terms for the unknowns x_k^q, u_k^q for $k \in \{1, ..., n\}$ yields

$$\begin{aligned} 0 = &\sum_{k=1}^{n-1} \left[\mu_k - \mu_{k+1} - \frac{\Delta t}{m} (F^{u_k})^T \mu_{k+1} - \frac{\Delta t}{m} \delta_{k+1} - \frac{\Delta t^2}{m} (F^{u_k})^T \delta_{k+1} - J_k^{u_k} \right]^T u_k^q \\ &+ \sum_{k=1}^{n-1} \left[-\frac{\Delta t}{m} (F^{x_k})^T \mu_{k+1} + \delta_k - \delta_{k+1} - \frac{\Delta t^2}{m} (F^{x_k}) \delta_{k+1} - J_k^{x_k} \right]^T x_k^q \\ &+ \left[\mu_n - J_n^{u_n} \right]^T u_n^q + \left[\delta_n - J_n^{x_n} \right]^T x_n^q \\ &+ J^q - \sum_{k=1}^{n} J_k^q - \frac{\Delta t}{m} (F_{k-1}^q)^T \mu_k - \frac{\Delta t^2}{m} (F_{k-1}^q)^T \delta_k. \end{aligned} \tag{8.10}$$

The recursion is finally obtained from the coefficients before the unknown partial derivatives, the terminal conditions follow from the third line. The sensitivity of the objective function with regards to the control q follows from the last line. □

Remark. In this chapter we will be concerned with a total of N particles in two dimensions such that $x_k, u_k \in \mathbb{R}^{2N}$. The recursion (8.4) can be written as

$$\begin{aligned} \mu_k &= \left(\mathbf{I}_{2N} + \frac{\Delta t}{m} F^{u_k} \right)^T (\mu_{k+1} + \Delta t \delta_{k+1}) + \left(J_k^{u_k} \right)^T \\ \delta_k &= \delta_{k+1} + \left(\frac{\Delta t}{m} F^{x_k} \right)^T (\mu_{k+1} + \Delta t \delta_{k+1}) + (J_k^{x_k})^T. \end{aligned} \tag{8.11}$$

In this form obtained adjoints equal the ones that have been derived earlier by different means [120, 182, 161].

Remark. In order to control a particle system, we only require the ability to calculate the matrix with partial derivatives of the forces. Further sensitivity calculations need to specify the particle system such as control q. We will restrict to the aforementioned SPH fluids in the following section, where the shape of an obstacle is optimized. The sensitivity is obtained in Section 8.3.1 by evaluating the discrete shape derivative $DJ(\Omega)[V_l]$ for domain Ω in direction V_l via formula (8.6).

8.2 Smoothed Particle Hydrodynamics

Before being concerned with optimization of the SPH-flow, Section 8.2.1 will discuss the basic idea, definitions and notations for this technique, while Section 8.2.2 is dealing with the numerical implementation of respectively fluid and boundary portion.

8.2.1 Basics of SPH

Central for SPH-particles traveling on a domain $\Omega \subset \mathbb{R}^d$ is the approximation of the delta-distribution by the usage of kernels. We hence first define

Definition 8.4. *(Dirac-Delta Distribution) In line with Definition 2.17, let $x' \in \Omega \subset \mathbb{R}^d$, then the Dirac-delta measure defines a distribution via mapping*

$$C_c^\infty(\Omega) \ni v \mapsto \delta_{x=x'}(v) = v(x'). \tag{8.12}$$

.

Remark. Although frequently done, it is not correct to write (8.12) as

$$\int_\Omega \delta(x - x')v(x)\,\mathrm{d}x = v(x'), \tag{8.13}$$

since there is no $\delta \in L^1_{Loc}(\Omega)$ that fulfills the equation above for all $v \in C_c^\infty(\Omega)$. Nonetheless, SPH-methods build around this idea, such that (8.15) is only understood symbolically with reservations on the validity.

Definition 8.5. *(Kernel) A function $W : \mathbb{R}^d \times \mathbb{R}_+ \to \mathbb{R}$ is defined as a valid kernel if it fulfils properties of*

i) $\int_\Omega W(x - x', h)\,\mathrm{d}x' = 1$

ii) $\lim_{h\to 0} \int_\Omega v(x')W(x - x', h)\,\mathrm{d}x' = \int_\Omega v(x')\delta(x - x')\,\mathrm{d}x'$

for $x, x' \in \Omega$.

Remark. The literature commonly denotes these two properties as normalization and Dirac-delta condition. These two properties are frequently accompanied by a positivity, symmetry and compact support condition, that are desirable from a computational point of view, i.e.

i) $W(x-x',h) \geq 0$

ii) $W(-x,h) = W(x,h)$

iii) $W(x-x',h) = 0 \quad$ for $||x-x'||_2 \geq h$.

With these definitions a field value $v : \Omega \to \mathbb{R}$ is written using the symbolical Dirac-delta identity and the Dirac-delta condition [129]

$$v(x) = \int v(x')\delta(x-x')\,\mathrm{d}x' = \lim_{h\to 0}\int v(x')W(x-x',h)\,\mathrm{d}x', \tag{8.14}$$

which in turn is intended to serve as a limiting object in the sense of

$$\lim_{h\to 0}\int v(x')W(x-x',h)\,\mathrm{d}x' = \lim_{h\to 0}\lim_{N\to\infty}\sum_{i=1}^{N} m^i\frac{v^i}{\rho^i}W(x-x^i,h). \tag{8.15}$$

Ultimately, the latter is approximated for fixed $h > 0$ and $N \in \mathbb{N}$, forming the basis of SPH-techniques. In the literature various valid kernel functions are defined, we restrict ourselves here to the original one, i.e.

Definition 8.6. *(Gaussian Kernel) The valid kernel defined defined for* $q := ||x-x'||_2/h$ *by*

$$W_G(x-x',h) = \sigma_G \exp\left[-q^2\right] \tag{8.16}$$

with normalization of

$$\begin{aligned} \sigma_G &= \frac{1}{\sqrt{\pi}h} && \text{for } d=1 \\ \sigma_G &= \frac{1}{\pi h^2} && \text{for } d=2 \\ \sigma_G &= \frac{1}{\pi^{3/2}h^3} && \text{for } d=3 \end{aligned} \tag{8.17}$$

is denoted as Gaussian kernel [130].

Remark. The Gaussian kernel comes with the advantage of belonging to class C^∞, we will use this fact in Section 8.3. In two dimensions is the gradient for this kernel given by

$$\nabla W_G = \begin{pmatrix} \frac{-2}{h^4\pi}\exp\left[-q^2\right](x-x') \\ \frac{-2}{h^4\pi}\exp\left[-q^2\right](y-y') \end{pmatrix}, \tag{8.18}$$

while the Laplacian reads

$$\begin{aligned} \nabla^2 W_G = &\frac{4}{h^6\pi}\exp\left[-q^2\right](x-x')^2 - \frac{2}{h^4\pi}\exp\left[-q^2\right] \\ &+\frac{4}{h^6\pi}\exp\left[-q^2\right](y-y')^2 - \frac{2}{h^4\pi}\exp\left[-q^2\right]. \end{aligned} \tag{8.19}$$

Remark. The Gaussian kernel lacks the compact support condition, which results in a summation over all particles in the domain. To counter this, often cut-off kernels are used.

Definition 8.7. *(Cubic Spline Kernel) The valid cut-off kernel defined for* $q := ||x - x'||_2/h$ *by*

$$W_C(x - x', h) = \sigma_C \begin{cases} 6(q^3 - q^2) + 1 & \text{for} \quad 0 \leq q \leq \frac{1}{2} \\ 2(1-q)^3 & \text{for} \quad \frac{1}{2} < q \leq 1 \\ 0 & \text{otherwise} \end{cases} \tag{8.20}$$

with normalization of

$$\begin{aligned} \sigma_C &= \frac{2}{3h} && \text{for } d = 1 \\ \sigma_C &= \frac{10}{7h^2} && \text{for } d = 2 \\ \sigma_C &= \frac{1}{\pi h^3} && \text{for } d = 3 \end{aligned} \tag{8.21}$$

is known as the cubic spline kernel [129].

Remark. In classical form cut-off kernels are not differentiable at the cut-off, but are attractive from computational side, as the summation is only performed over particles in the limited support radius.

Remark. A limited number of publications have been dealing with the convergence of SPH methods, based on joint particle limits $N \to \infty$ and smoothing limit $h \to 0$ as in (8.15). First attempts relied on spatial discretizations with time-continuous approximations [150] or at least the knowledge about exact particle trajectories [34]. In addition, convergence results have been presented for consecutive limits of discretization parameter and smoothing radius [68] or a selective choice of kernel functions [138].

8.2.2 Implementation Details of Lagrangian SWE SPH

Since we are interested in modeling fluids in this work, we will base the SPH in line with preceding chapters on the Lagrangian SWE in non-conservative form, which can be obtained from Theorem 5.1 and state as

Definition 8.8. *(Lagrangian Shallow Water Equations) In line with Definition 3.10 for notation as in (5.4) the viscous Lagrangian SWE are defined as*

$$D_m H = -H \nabla \cdot (Q/H) \tag{8.22}$$

$$D_m(Q/H) = -g \nabla (H + z) + \mu \nabla^2 (Q/H). \tag{8.23}$$

As it can be seen in (8.15) SPH methods allow for simplified density calculations, to utilize this benefit for Lagrangian SWE a density-water relation is used [173], i.e.

$$H = \frac{\rho}{\rho_0} \tag{8.24}$$

for reference density $\rho_0 > 0$. This definition gives only local conservation results, such that (8.22) and (8.23) hold only in the limit case of $h \to 0$, which is shown in [173] for inviscid Lagrangian SWE. Furthermore, for constant particle number and mass the continuity equation (8.22) is automatically fulfilled by reinterpretation of the density as height of the waves [173]. In this setting (8.23) reduces to regular SPH calculations for incompressible Navier-Stokes equations [130] with pressure and viscosity corresponding forcing terms such as an additional term that arises from variations in the sediment.
We will now in detail discuss the implementation of fluid and boundary particles via the SPH technique for Lagrangian SWE. Since the boundary interactions are the delicate and non-standard portion, our focus is on this very, following [107] that formulated rigid boundary interactions via density-fields for incompressible Navier-Stokes equations.

Fluid Interactions

The SPH algorithm for Lagrangian SWE without boundary and sediment interactions B builds around efficient implementations of different matrices for particle interactions, which is detailed in Appendix B for the interested reader. For a basic understanding we refer to Algorithm 7, alongside the following remarks.

Boundary Interactions

Since we are ultimately interested in shape optimization of particle systems, we need to specify the particle boundary interaction. In classical SPH methods, this is typically done via boundary particles [129]. The obvious drawback are increased computational efforts, undesired boundary frictions such as the inability to model complex geometries [107].
All SPH boundary techniques have the common idea to approximate the second integral below, which arises naturally when being restricted to a bounded domain $\Omega \subset D \subset \mathbb{R}^d$

$$\rho(x) = \lim_{h\to 0} \int_\Omega W(x - x', h)\rho(x')\,\mathrm{d}x' + \lim_{h\to 0} \int_{D\setminus\Omega} W(x - x', h)\rho(x')\,\mathrm{d}x'. \tag{8.25}$$

In the last decade various researchers addressed this problem e.g. by the usage of continuous boundary methods such as the boundary surface integral [109] or the signed distance field method [107]. This work will restrict to latter ideas and extends them for Lagrangian SWE with rigid and outflow boundary conditions. In [107] the boundary density portion is approximated as

$$\rho_D(x) = \lim_{h\to 0} \int_{D\setminus\Omega} \gamma(d_\Omega(x'))W(x - x', h)\,\mathrm{d}x', \tag{8.26}$$

where a modification of the signed distance function (5.15)

$$d_\Omega(x) = \begin{cases} d(x, \partial\Omega) & \text{if } x \in \Omega \\ 0 & \text{if } x \in \partial\Omega \\ -d(x, \partial\Omega) & \text{if } x \in D \setminus \Omega \end{cases} \tag{8.27}$$

is used with

$$\gamma(d_\Omega) = \begin{cases} \rho_0(1 - \frac{d_\Omega}{h}) & \text{if } d_\Omega \leq h \\ 0 & \text{otherwise.} \end{cases} \tag{8.28}$$

In addition to rigid boundaries and in analogy to preceding chapters, we implement in Section 8.3.2 open-sea boundaries. Due to this reason, we extend the idea of buffered layers for the modeling of outflow conditions, as introduced in [179] for SPH-based computations, to mesh-based signed distance maps. The idea is to create a collecting channel, in which the particle movement is decelerated. Suppose an additional layer as subdomain $\Omega_L \subset \mathbb{R}^d$ is introduced, that builds with Ω a conformal domain. Then as in (8.27), we require

$$d_{\Omega_L}(x) = \begin{cases} d(x, \partial\Omega_L) & \text{if } x \in (\Omega \cup D) \\ 0 & \text{if } x \in \partial\Omega \\ -d(x, \partial\Omega_L) & \text{if } x \in \Omega_L \setminus (\Omega \cup D). \end{cases} \tag{8.29}$$

Hence, outflow boundary conditions are created via subdomain-dependent modification of this very signed distance function, i.e.

$$\gamma^L(d_{\Omega_L}) = \begin{cases} \rho_0 d_{\Omega_L} & \text{if } x \in \Omega_L \\ 0 & \text{otherwise.} \end{cases} \tag{8.30}$$

In addition, we add a decelerating domain-dependent coefficient for the velocity in the particles iteration law of Definition 8.2, i.e. for $\epsilon > 0$

$$\phi := \begin{cases} \phi_1 = 1 \text{ in } \Omega \cup D \\ \phi_2 = \epsilon \text{ in } \Omega_L. \end{cases} \tag{8.31}$$

The implementation in the discretized setting is done, confer Definition 2.37, via interpolation for each particle and its position $\{x_k^i\}_{i,k=1}^{N,n}$ on a finite element mesh, e.g. consisting of Lagrangian elements κ, with $S = \dim(\mathbb{P}_p) = \frac{(d+p)!}{d!p!}$ nodal degrees of freedom for d dimensions, for polynomial space $P := \mathbb{P}_p$ of polynomial order $p \in \mathbb{N}$ with associated shape functions $\{N_1^p, ..., N_S^p\}$ in the finite element triplet of Definition 2.30, i.e.

$$\rho_D(x) = \sum_{s=1}^{S} m\gamma_s(d_\Omega)N_s^p(x) + \sum_{s=1}^{S} m\gamma_s^L(d_{\Omega_L})N_s^p(x). \tag{8.32}$$

The interpolation technique is then also used to compute the boundary forces by

$$F_D^{Height}(x) = \nabla\rho_D(x) = \sum_{s=1}^{S} \gamma_s(d_\Omega)\nabla N_s^p(x) + \sum_{s=1}^{S} \gamma_s^L(d_{\Omega_L})\nabla N_s^p(x). \tag{8.33}$$

Remark. The advantage in using this boundary representation lies in the possibility to precompute a solution field, allowing cheap finite element interpolations, whenever a particle is in the proximity of the boundary.
In same manner as the boundary density the sediment field $z : \Omega \to \mathbb{R}$ of Definition 8.8 can be created. In this setting, we can naturally identify domain boundaries via increased sediment elevations.

Remark. Rigid boundary contributions, as in (8.26), rely on the max-function, i.e.

$$\gamma(d_\Omega(x)) = \rho_0 \left(\max \left\{ 0, 1 - \frac{d_\Omega(x)}{h} \right\} \right),$$

since this is not differentiable for $x \in \Omega$ such that $d_\Omega(x) = h$, we will use a smoothed max-function $C^1(\Omega) \ni \max_\alpha : \Omega \to \mathbb{R}$ in the following section e.g. as [54]

$$\max_\alpha(d_\Omega) = \begin{cases} \max(0, 1 - \frac{d_\Omega}{h}) & \text{for } 1 - \frac{d_\Omega}{h} \in \mathbb{R} \setminus \left[-\frac{1}{\alpha}, \frac{1}{\alpha} \right] \\ \frac{\alpha}{4}(1 - \frac{d_\Omega}{h})^2 + \frac{1}{2}(1 - \frac{d_\Omega}{h}) + \frac{1}{4\alpha} & \text{otherwise} \end{cases} \tag{8.34}$$

for $\alpha > 0$ with derivative as

$$\max'_\alpha(d_\Omega) = \begin{cases} 0 & \text{for } 1 - \frac{d_\Omega}{h} \in \left(-\infty, -\frac{1}{\alpha} \right) \\ -\frac{\alpha}{2h}(1 - \frac{d_\Omega}{h}) - \frac{1}{2h} & \text{for } 1 - \frac{d_\Omega}{h} \in \left[-\frac{1}{\alpha}, \frac{1}{\alpha} \right] \\ -\frac{1}{h} & \text{for } 1 - \frac{d_\Omega}{h} \in \left(\frac{1}{\alpha}, \infty \right). \end{cases} \tag{8.35}$$

For outflow boundaries we rely on an analogous C^1-counterpart of the min-function as

$$\min_\alpha(d_{\Omega_L}) = \begin{cases} \min(0, d_{\Omega_L}) & \text{for } d_{\Omega_L} \in \mathbb{R} \setminus \left[-\frac{1}{\alpha}, \frac{1}{\alpha} \right] \\ -\frac{\alpha}{4} d_{\Omega_L}^2 + \frac{1}{2} d_{\Omega_L} - \frac{1}{4\alpha} & \text{otherwise} \end{cases} \tag{8.36}$$

with

$$\min'_\alpha(d_\Omega) = \begin{cases} 1 & \text{for } d_{\Omega_L} \in \left(-\infty, -\frac{1}{\alpha} \right) \\ -\frac{\alpha}{2}(d_{\Omega_L}) + \frac{1}{2} & \text{for } d_{\Omega_L} \in \left[-\frac{1}{\alpha}, \frac{1}{\alpha} \right] \\ 0 & \text{for } d_{\Omega_L} \in \left(\frac{1}{\alpha}, \infty \right). \end{cases} \tag{8.37}$$

The proceeding to calculate Lagrangian SWE SPH with boundary contributions can be obtained from Algorithm 7.

Remark. The following remarks should guide through Algorithm 7:

i) The neighbor search is only mentioned for completeness. For the Gaussian kernel (8.16) is the search for neighboring particles trivially omitted.

ii) Whenever quantities should be stored for subsequent computations the time step $k \in \{1, ..., n\}$ is explicitly mentioned.

Algorithm 7 2D SPH for Lagrangian SWE with Boundary Contribution

Initialize Particles carrying $(Q_0^i, x_0^i)_{i=1}^N$ with Constant Mass $m > 0$ and Step-Size $\Delta t > 0$
foreach *Time Step* $k \in \{1, ..., n\}$ **do**
  foreach *Particle* i **do**
    Find Neighbour Particles $M \subset \{1, ..., N\}$
  end foreach
  foreach *Particle* i **do**
    Compute Fluid Density ρ_F^i [via (8.15)]
    Compute Boundary Density ρ_D^i [via (8.32)]
    Compute Water Height H^i [via (8.24)]
  end foreach
  foreach *Particle* i **do**
    Calculate Forces:
    $F_k^i = F_i^{Height} + F_i^{Viscosity} + F_i^{Sediment}$
  end foreach
  foreach *Particle* i **do**
    Calculate States:
    $Q_{k+1}^i / H^i = Q_k^i / H^i + \Delta t F_k^i / m$
    $x_{k+1}^i = x_k^i + \Delta t Q_{k+1}^i / H^i$
  end foreach
end foreach

iii) The change from Lagrangian SWE to incompressible Navier-Stokes equations is remarkable easy for SPH-methods. Instead of computing water heights, a fluid pressure would be required as

$$p_F^i = B_T \left[\left(\frac{\rho_F^i}{\rho_0} \right)^{\xi} - 1 \right] \tag{8.38}$$

for $B_T, \xi > 0$ e.g. using Tait's law [32].

8.3 Adjoint-Based Shape Optimization for SPH Particles

Shape optimization for Lagrangian particle movement has been only rarely investigated. General approaches most often reduce to particle systems that are based on the weak form, introduced in order to enable large deformations, e.g. for the element-free Galerkin method [39] or the reproducing kernel particle method [89, 50]. Lately a one-way coupled, volume averaged transport model was used to circumvent the direct usage of the Lagrangian particle flow [97]. In particular for SPH-fluids only boundary contributions via ghost particles and the direct differentiation method to obtain optimal fluid-structure interactions have been investigated [92]. However, this method comes with the drawback of solving an additional problem for each design parameter, which can become costly for highly resolved obstacles. Hence, adjoint-based shape optimization for SPH-fluids and

accordingly also the usage in mitigation of coastal erosion appears novel. The following is devoted to the derivation the discrete shape derivative of an SPH-fluid with suitable boundary interaction in Section 8.3.1 and the numerical verification of results for various test cases in Section 8.3.2.

8.3.1 Derivation of the Shape Derivative

Suppose we are given an open domain $\Omega \subset \mathbb{R}^2$, which is split into disjoint subdomains, consisting of a connected, interior domain Ω_1 such that $\Gamma_1 \cup \Gamma_2 \cup \Gamma_3 := \Gamma := \partial\Omega_1$, a simply connected obstacle domain D and an exterior domain $\Omega_2 \cup \Omega_3 := \Omega \setminus \bar{\Omega}_1 \setminus D$, such that $\bar{\Omega}_1 \cup \Omega_2 \cup \Omega_3 \cup D = \Omega$. We assume the variable, interior boundary Γ_3 and the fixed outer $\Gamma_1 \cup \Gamma_2$ of interior domain Ω_1 to be at least Lipschitz. One simple example of such kind is visualized below in Figure 8.1.

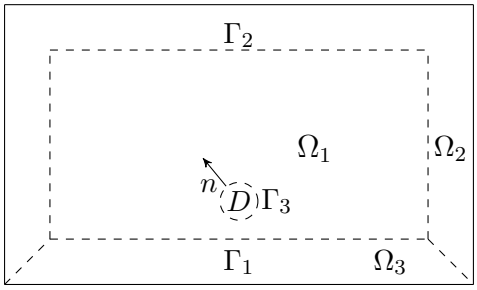

Figure 8.1: Illustrative Domain Ω with Initial Circled Obstacle D, Interior Domain Ω_1, Exterior Domains Ω_2, Ω_3 and Boundaries $\Gamma_1, \Gamma_2, \Gamma_3$

On this domain fluids will follow the laws of the Lagrangian SWE, i.e. Definition 8.8, subject to rigid boundary conditions on $\Gamma_1, \Gamma_3 \times (0, T)$, open boundary conditions on $\Gamma_2 \times (0, T)$ and suitable initial conditions on $\Omega \times \{0\}$. As in Section 6.2 our objective $J : \Omega \to \mathbb{R}$ is defined as

$$J(\Omega) = J_1(\Omega) + J_2(\Omega) + J_3(\Omega) + J_4(\Omega), \tag{8.39}$$

where the first part reduces for simplicity to be of tracking-type for a rest height along the shoreline Γ_1, i.e.

$$J_1(\Omega) = \int_0^T \int_{\Gamma_1} \frac{1}{2}(H - \bar{H})^2 \,\mathrm{d}s \,\mathrm{d}t. \tag{8.40}$$

In addition, the objective is accompanied by secondly a volume penalty (4.25), thirdly a perimeter regularization (4.26) and lastly a thinness penalty. Finally, with constraints of type (8.22)-(8.23) we obtain a PDE-constrained optimization problem, which is intended to be solved in a discretize-then-differentiate setting. The discretization is based on SPH as described in Section 8.2.1 with boundary interaction as in Section 8.2.2. From this we obtain a particle system, which provides us in two dimensions with states via tuple $(x_k, v_k) \in \mathbb{R}^{2N} \times \mathbb{R}^{2N}$. Here we interpret Ω_1 as fluid and $\Omega_2 \cup \Omega_3 \cup D$ as boundary

domain for the particles in reference to Section 8.2.2. Based on this we define the discrete counterpart to objective (8.40), i.e.

$$\begin{aligned} J_{1,h}(\Omega) &= \sum_{k=1}^{n} J_{1,h,k}(x_k, v_k, \Omega) \\ &= \sum_{(k,x)\in\{1,\dots,n\}\times\Gamma_{1,h}} \frac{1}{2}\Delta t \left(\frac{\rho(x)}{\rho_0} - \bar{H}(x)\right)^2 \\ &= \sum_{(k,x,j)\in\{1,\dots,n\}\times\Gamma_{1,h}\times\{1,\dots,N\}} \frac{1}{2}\Delta t \left(\frac{m}{\rho_0} W(x - x_k^j, h) - \bar{H}(x)\right)^2. \end{aligned} \tag{8.41}$$

Remark. In (8.41) and in what follows we are relying on a constant particle mass, in line with Section 8.1. Furthermore, we omit discretization indices for readability whenever it is clear from the context.

The sensitivity with respect to domain deformations is obtained from Theorem 8.3 as

$$\begin{aligned} DJ_1(\Omega)[V_l] &= \left.\frac{dJ_{1,h}(\Omega_\epsilon)}{d\epsilon}\right|_{\epsilon=0^+} \\ &= \left.\frac{d}{d\epsilon}\sum_{k=1}^{n} J_{1,h,k}(x_k, v_k, \Omega_\epsilon)\right|_{\epsilon=0^+} + \left.\frac{d}{d\epsilon}\sum_{k=1}^{n} (F_{k-1}^\epsilon)^T \left(\frac{\Delta t}{m}\mu_k + \frac{\Delta t^2}{m}\delta_k\right)\right|_{\epsilon=0^+}, \end{aligned} \tag{8.42}$$

where occurring functions are defined on the perturbed domain $\Omega_\epsilon \subset \mathbb{R}^d$. In need of deriving the shape derivative, we first state the following lemma, following [35].

Lemma 8.9. *For a finite element function $g \in W_h \subset H^1(\Omega)$, i.e. $g(x) = \sum_{s=1}^{S} g_s N_s^p(x)$ for finite element ansatz function N_s^p, whose restriction on an Lagrangian element κ is a polynomial of order $p \geq 1$, the shape derivative is derived as*

$$Dg[V_l] = \sum_{s=1}^{S} (Dg_s[V_l] N_s^p - g_s V_l \cdot \nabla N_s^p), \tag{8.43}$$

where $N_s^p(x_\epsilon) = N_s^p(\tau_\epsilon^{-1}(x_\epsilon))$ is moving alongside the deformation.

Proof. [35] Since $N_s^p(x)$ is moving along the deformation, the material derivative vanishes

$$D_m N_s^p = 0,$$

hence for the shape derivative it holds by (3.22)

$$DN_s^p[V_l] = -V_l \cdot \nabla N_s^p.$$

Since g_s is spatially constant, we conclude according to [35]

$$D_m g = \sum_{s=1}^{S} Dg_s[V_l] N_s^p$$

and therefore obtain the shape derivative as

$$Dg[V_l] = D_m g - V_l \nabla g = \sum_{s=1}^{S} \left(Dg_s[V_l] N_s^p - g_s V_l \cdot \nabla N_s^p \right).$$

□

Remark. For SPH boundary computations we recall the shape derivative of the signed distance function (5.28) for $x \notin \Sigma$

$$Dd_\Omega(x)[V] = -V(p_{\partial\Omega}(x)) \cdot n(p_{\partial\Omega}(x)). \tag{8.44}$$

In this sense, $Dd_{\Omega,s}[V_l]$ is its nodal discretized counterpart w.r.t. the l^{th} vertex perturbation.

Since the boundary contribution is driven by surface gradient forces, we require the shape derivative of the gradient of a finite element function (8.33).

Lemma 8.10. *For the gradient of a finite element function, i.e.* $\nabla g(x) = \sum_{s=1}^{S} g_s \nabla N_s^p(x)$ *for finite element ansatz function* N_s^p*, whose restriction on an Lagrangian element* κ *is a polynomial of order* $p \geq 2$*, the shape derivative is derived as*

$$D(\nabla g)[V_l] = \sum_{s=1}^{S} Dg_s[V_l] \nabla N_s^p - (\nabla V_l)^T \left(\sum_{s=1}^{S} g_s \nabla N_s^p \right) - \nabla \left(\sum_{s=1}^{S} g_s \nabla N_s^p \right) V_l. \tag{8.45}$$

Proof. The material derivative does not commute with the spatial derivative (3.25)

$$D_m(\nabla g) = \nabla(D_m g) - (\nabla V_l)^T \nabla g, \tag{8.46}$$

which equals by the same argument as in proof to Lemma 8.9

$$D_m(\nabla g) = \nabla \left(\sum_{s=1}^{S} Dg_s[V_l] N_s^p \right) - (\nabla V_l)^T \left(\sum_{s=1}^{S} g_s \nabla N_s^p \right). \tag{8.47}$$

Then we have for the shape derivative

$$\begin{aligned} D(\nabla g)[V_l] &= D_m(\nabla g) - \nabla(\nabla g) V_l \\ &= \nabla \left(\sum_{s=1}^{S} Dg_s[V_l] N_s^p \right) - (\nabla V_l)^T \left(\sum_{s=1}^{S} g_s \nabla N_s^p \right) - \nabla \left(\sum_{s=1}^{S} g_s \nabla N_s^p \right) V_l. \end{aligned} \tag{8.48}$$

□

Theorem 8.11. *Assume $\{x_k\}_{k=1}^n$ moves alongside the deformation, the shape derivative of objective $J_1(\Omega)$ is then given by*

$$\begin{aligned} DJ_1(\Omega)[V_l] =& \frac{d}{d\epsilon}\sum_{k=1}^{n} J_{1,k}(x_k, u_k, \Omega_t)\Big|_{\epsilon=0^+} + \frac{d}{d\epsilon}\sum_{k=1}^{n}(F_{k-1}^{\epsilon})^T\left(\frac{\Delta t}{m}\mu_k + \frac{\Delta t^2}{m}\delta_k\right)\Big|_{\epsilon=0^+} \\ =& \sum_{k=1}^{n}\sum_{i=1}^{N}\Bigg[\nabla\left(\sum_{s=1}^{S} D\gamma_s[V_l]N_s^p(x_k^i)\right) - \left(\nabla V_l(x_k^i)\right)^T\left(\sum_{s=1}^{S}\gamma_s\nabla N_s^p(x_k^i)\right) \\ & - \nabla\left(\sum_{s=1}^{S}\gamma_s\nabla N_s^p(x_k^i)\right)V_l(x_k^i)\Bigg]^T\left(\Delta t\mu_k^i + \Delta t^2\delta_k^i\right). \end{aligned} \tag{8.49}$$

where $D\gamma_s[V_l]$ is the nodal discretization w.r.t. the l^{th} vertex perturbation of

$$D\gamma(x)[V] = max'_{\alpha}(d_\Omega(x))(-V(p_{\partial\Omega}(x))\cdot n(p_{\partial\Omega}(x))). \tag{8.50}$$

Proof. Since Γ_1 is fixed, the objective (8.41) is independent of mesh deformations. Hence, the shape derivative is zero, i.e.

$$\frac{d}{d\epsilon}\sum_{k=1}^{n} J_{1,k}(x_k, u_k, \Omega_\epsilon)\Big|_{\epsilon=0^+} = 0.$$

We recall that for SPH-flows the fluid and boundary part are split up (8.25), i.e. for density of particle $i \in \{1, ..., N\}$ in each time step $k \in \{1, ..., n\}$

$$\rho(x_k^i) = \sum_{j=1}^{N} mW(x_k^i - x_k^j, h) + \sum_{s=1}^{S} mN_s(x_k^i)\gamma_s + \sum_{s=1}^{S} mN_s(x_k^i)\gamma_s^L.$$

The first sum is only dependent on the position of the particles, hence the respective shape derivatives vanish due to adjoints and we have

$$\frac{d}{d\epsilon}\sum_{j=1}^{N} mW(x_k^i - x_k^j, h)\Big|_{\epsilon=0^+} = 0.$$

The remainders follow from regarding terms w.r.t. the water gradient (8.33), Lemma 8.9 and 8.10 such as equation (8.49), by assuming that the particle position $\{x_k^i\}_{i,k=1}^{N,n}$ moves alongside the deformation in each time step. □

Remark. The assumption that $\{x_k^i\}_{i,k=1}^{N,n}$ moves along the deformation drastically simplifies calculations, otherwise we are required to perform low-level computations similar to works in [161].

Remark. Using (3.33) and the fact that nodal values are spatially constant we can rewrite (8.49) as

$$\begin{aligned} DJ_1(\Omega)[V_l] =& \frac{d}{d\epsilon} \sum_{k=1}^{n} (F_{k-1}^{\epsilon})^T \left(\frac{\Delta t}{m} \mu_k + \frac{\Delta t^2}{m} \delta_k \right) \Bigg|_{\epsilon=0^+} \\ =& \sum_{k=1}^{n} \sum_{i=1}^{N} \Bigg[\left(\sum_{s=1}^{S} D\gamma_s[V_l] \nabla N_s^p(x_k^i) \right) - \left(\delta x_l \nabla N_l^1(x_k^i) \right)^T \left(\sum_{s=1}^{S} \gamma_s \nabla N_s^p(x_k^i) \right) \\ & - \left(\sum_{s=1}^{S} \gamma_s \nabla \nabla N_s^p(x_k^i) \right) \delta x_l N_l^1(x_k^i) \Bigg]^T \left(\Delta t \mu_k^i + \Delta t^2 \delta_k^i \right). \end{aligned} \tag{8.51}$$

Here we highlight, that the product of ansatz functions is zero, whenever, $\{x_k^i\}_{i,k=1}^{N,n}$ is not in the support of shape functions N_s^p and N_l^1.

Remark. Factoring out the respective δx_l in (8.51) we can calculate the remaining quantities for each mesh vertex perturbation. All quantities can be collected in a vector $DJ_1(\Omega)[V_l]$ of size dL to apply some mesh deformation strategy as discussed in [126, Section 6.3]. Linear elasticity calculations as in [20] can be enabled, by choosing a basis of the test function space, calculating all occurring quantities and split vectorial contributions, as it is common in vector-valued finite element methods.

Remark. For completeness shape derivatives of the penalty terms are obtained as in (4.52) and (4.53), where the discretization and the subsequent usage in optimization routines follow naturally for standard finite element solvers.

8.3.2 Numerical Results

In this subsection we will first give details about the numerical implementation, before verifying results for a selected choice of test cases. In all the following examples we will work with a simple mesh in line with definitions given in Section 8.3.1, as it can be seen in Figure 8.2. The solution to the signed distance function is once more based on the

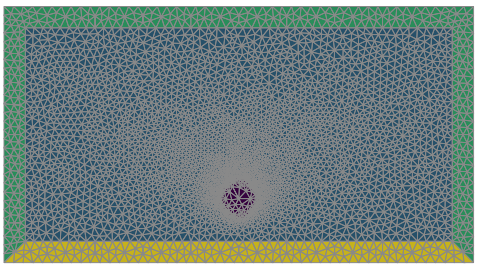

Figure 8.2: Initial Mesh with Colored Subdomains

solution of the Eikonal Equation with $f(x) = 1$, $q(x) = 0$ as in (5.33), for a viscous and stabilized version as in (5.34) or on AABBT [6]. Build on this solution, modifications as in (8.34) are exercised downstream by prescribing respective nodal values. The recursive

adjoints require the calculation of a matrix with partial derivatives w.r.t. the states. The partial derivatives matrix w.r.t. the positions is obtained by a $2N \times 2N$ matrix

$$\frac{\partial F}{\partial x} = \begin{pmatrix} \frac{\partial F_1^x}{\partial x^1} & \frac{\partial F_1^x}{\partial x^2} & \cdots & \frac{\partial F_1^x}{\partial x^N} & \frac{\partial F_1^x}{\partial y^1} & \frac{\partial F_1^x}{\partial y^2} & \cdots & \frac{\partial F_1^x}{\partial y^N} \\ \frac{\partial F_2^x}{\partial x^1} & \ddots & & \vdots & \frac{\partial F_2^x}{\partial y^1} & \ddots & & \vdots \\ \vdots & & \ddots & \vdots & \vdots & & \ddots & \vdots \\ \frac{\partial F_N^x}{\partial x^1} & \cdots & \cdots & \frac{\partial F_N^x}{\partial x^N} & \frac{\partial F_N^x}{\partial y^1} & \cdots & \cdots & \frac{\partial F_N^x}{\partial y^N} \\ \frac{\partial F_1^y}{\partial x^1} & \frac{\partial F_1^y}{\partial x^2} & \cdots & \frac{\partial F_1^y}{\partial x^N} & \frac{\partial F_1^y}{\partial y^1} & \frac{\partial F_1^y}{\partial y^2} & \cdots & \frac{\partial F_1^y}{\partial y^N} \\ \frac{\partial F_2^y}{\partial x^1} & \ddots & & \vdots & \frac{\partial F_2^y}{\partial y^1} & \ddots & & \vdots \\ \vdots & & \ddots & \vdots & \vdots & & \ddots & \vdots \\ \frac{\partial F_N^y}{\partial x^1} & \cdots & \cdots & \frac{\partial F_N^y}{\partial x^N} & \frac{\partial F_N^y}{\partial y^1} & \cdots & \cdots & \frac{\partial F_N^y}{\partial y^N} \end{pmatrix} \tag{8.52}$$

and the $2N \times 2N$ matrix of partial derivatives of the particle velocities as

$$\frac{\partial F}{\partial u} = \begin{pmatrix} \frac{\partial F_1^x}{\partial u^1} & \frac{\partial F_1^x}{\partial u^2} & \cdots & \frac{\partial F_1^x}{\partial u^N} & \frac{\partial F_1^x}{\partial v^1} & \frac{\partial F_1^x}{\partial v^2} & \cdots & \frac{\partial F_1^x}{\partial v^N} \\ \frac{\partial F_2^x}{\partial u^1} & \ddots & & \vdots & \frac{\partial F_2^x}{\partial v^1} & \ddots & & \vdots \\ \vdots & & \ddots & \vdots & \vdots & & \ddots & \vdots \\ \frac{\partial F_N^x}{\partial u^1} & \cdots & \cdots & \frac{\partial F_N^x}{\partial u^N} & \frac{\partial F_N^x}{\partial v^1} & \cdots & \cdots & \frac{\partial F_N^x}{\partial v^N} \\ \frac{\partial F_1^y}{\partial u^1} & \frac{\partial F_1^y}{\partial u^2} & \cdots & \frac{\partial F_1^y}{\partial u^N} & \frac{\partial F_1^y}{\partial v^1} & \frac{\partial F_1^y}{\partial v^2} & \cdots & \frac{\partial F_1^y}{\partial v^N} \\ \frac{\partial F_2^y}{\partial u^1} & \ddots & & \vdots & \frac{\partial F_2^y}{\partial v^1} & \ddots & & \vdots \\ \vdots & & \ddots & \vdots & \vdots & & \ddots & \vdots \\ \frac{\partial F_N^y}{\partial u^1} & \cdots & \cdots & \frac{\partial F_N^y}{\partial u^N} & \frac{\partial F_N^y}{\partial v^1} & \cdots & \cdots & \frac{\partial F_N^y}{\partial v^N} \end{pmatrix}. \tag{8.53}$$

with two-dimensional components $x = (x, y)$ and $u = (u, v)$. As in Chapters 4-7 a deformation scheme in the continuous setting can be obtained by regarding the Steklov-Poincaré type metric, such that a solution of the linear elasticity equation $W : \Omega \to \mathbb{R}^2$ can be used. In our discrete setting, the right hand-side in (4.54) is manually evaluated using (8.51) and the associated remark. The resulting vector is set to zero whenever the support is not in the interaction radius to the obstacle boundary. The full gradient-descent based shape optimization algorithm for SPH-flows is pseudocoded below.

Algorithm 8 Lagrangian SWE via SPH Shape Optimization Algorithm

Initialization Mesh, Particles

while $||DJ(\Omega_k)[V]|| > \epsilon_{TOL}$ **do**

1. Calculate Modified SDF γ_k [via Viscous Eikonal Eq. (5.34) or AABBT]
2. Calculate States x_k, u_k [via SPH Algorithm 7]
3. Calculate Adjoints δ_k, μ_k [via Section 8.1 & AD]
4. Calculate Gradient W_k [via (8.51-4.53) & Linear Elasticity (4.54)]
5. Perform Linesearch for $\tilde{W}_k$
6. Calculate Ω_{k+1} [via $\tilde{W}_k$ and (3.33)]

end while

Remark. Calculation of partial derivatives in (8.52) and (8.53) is manually possible, however results in a tremendous calculative effort, prone to errors. For circumvention we use automatic differentiation (AD) via the Autograd[1] library in either a forward or backward mode for the fluid portion, which is possible for code generated fully in Numpy[2]. Here we highlight for boundary terms as defined in (8.32) the partial derivative matrix for positional state is diagonal and zero for the velocity state. We also point out that derivatives of boundary contributions are fully implemented in FEniCS [6]. The manual evaluation of (8.49) in the fourth step is relying on multiple evaluations of finite element ansatz functions, where the FEniCS build-in function *evaluate_basis_derivatives_all* is used.

Example 1:

In the first example we model the propagation of two particles, i.e. $N = 2$, with initial position $x_0^1 = (0.5, 0.5)$ and $x_0^2 = (0.63, 0.5)$, towards the shore by prescribing initial velocities as $u_0 = (0, -3)^2$. This test case is deliberately kept simple to analyze the procedure. In Figure 8.3 we have visualized the particle movements for time snapshots $t \in \{0, 0.6, 0.12, 0.24\}$ for smoothing radius $h = 0.04$, particle mass $m = 1$, smoothing factor $\alpha = 100$ and reference density $\rho_0 = 10$. The particle propagation is performed using time steps of size $\Delta t = 0.008$ with end time $T = 0.24$. The red particle, with initial position x_0^1, travels towards the shore Γ_1 and effectively accounts for an increased objective in form of (8.41). In contrast, the blue particle contributes only marginally to the objective, starting from initial position x_0^2, being reflected from the obstacle and hence traveling back into the field and being collected in the outflow channel.

[1] https://github.com/HIPS/autograd
[2] https://numpy.org/

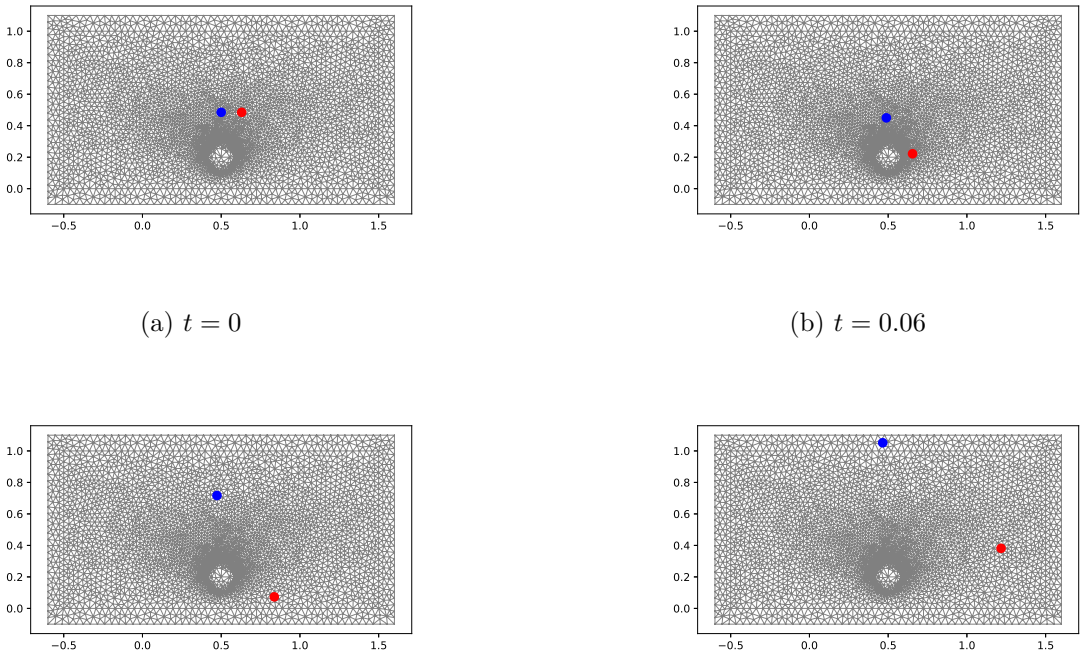

(a) $t = 0$ (b) $t = 0.06$

(c) $t = 0.12$ (d) $t = 0.24$

Figure 8.3: Ex.1 Particle Propagation

Both particles are within the interaction radius of the obstacle for a certain time frame, such that shape derivatives of boundary height forces are non-zero. However, as stated above, the objective contribution of blue ensures that adjoints $\{\delta_k^1\}_{k=1}^n$ and $\{\mu_k^1\}_{k=1}^n$ are vanishingly small. The initial deformation vector is hence predominantly activated in reds interaction region with the obstacle, as it can be observed in Figure 8.4 on the left. Relying on the shape optimization algorithm that we have presented before, for initial step-size $\rho_{step} = 1e{-}4$ and tolerance $\epsilon_{TOL} = 1e{-}9$, we are able to deform the obstacle setting $\mu_{min} = 10$ and $\mu_{max} = 100$ in the Poisson problem. The final mesh is able to decrease the objective up to a minimum, as it can be seen in Figure 8.4 in the middle and right part. We highlight, that even a small deformation is able to achieve these results in this simple setting.

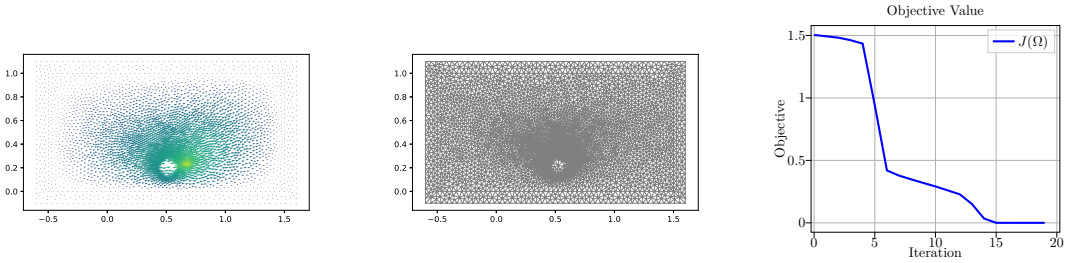

(a) Deformation Field (b) Optimized Mesh (c) Objective

Figure 8.4: Ex.1 Optimization Results

Example 2:

In the second example we increase the number of particles, i.e. $N = 180$, with initial positions drawn from a continuous uniform distribution as $x_0 = (0.6 + \mathcal{U}_{[0,0.35]}, 0.4 + \mathcal{U}_{[0,0.35]})^N$. The particles once more travel towards the shore driven by initial velocity as $u_0 = (0, -3)^N$. The remaining settings are chosen as in the first example. We can observe the movement in Figure 8.5.

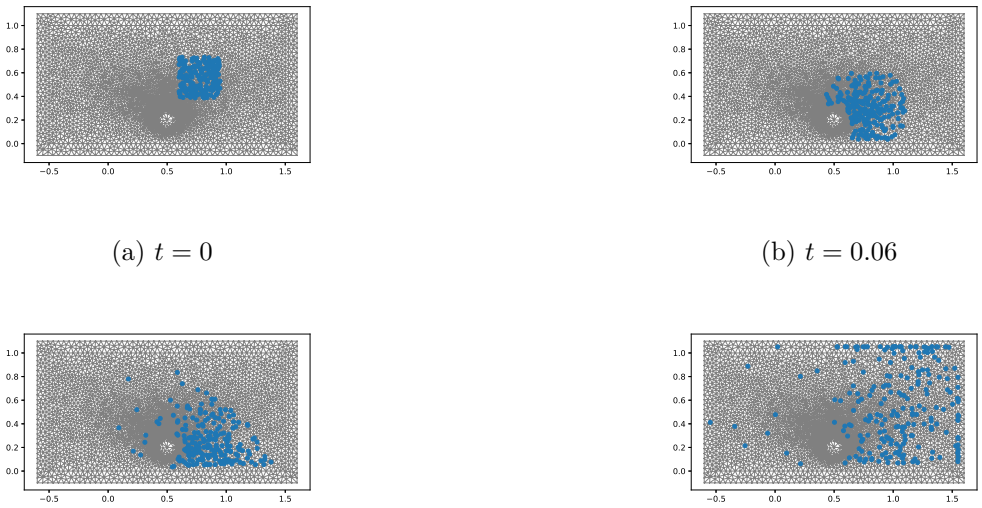

(a) $t = 0$ (b) $t = 0.06$

(c) $t = 0.12$ (d) $t = 0.24$

Figure 8.5: Ex.2 Particle Propagation

Once more relying on our shape optimization algorithm, we are able to deform the obstacle using resulting deformation fields, pictured in Figure 8.6 on the left for the first iteration. In this setting a larger deformation is necessary to effectively reduce the

objective as we see in the final mesh Figure 8.6 in the middle and on the right. We would like to highlight that the performance of the algorithm can be degrading by consecutive particle and boundary interactions, resulting from mesh deformations. Potentially this hinders us from obtaining improved results.

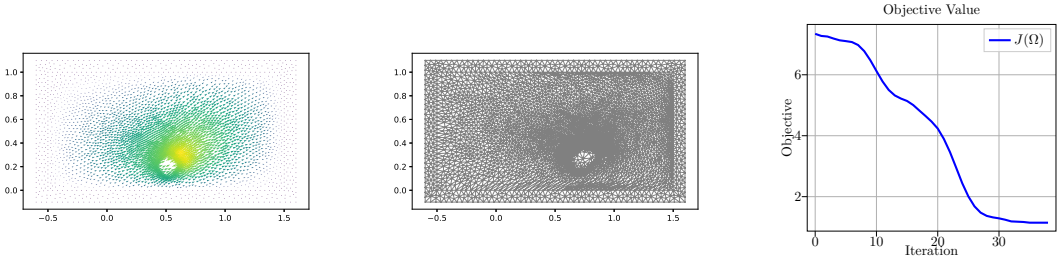

(a) Deformation Field (b) Optimized Mesh (c) Objective

Figure 8.6: Ex.2 Optimization Results

Chapter 9

Future Directions & Conclusion

This chapter should pave the way to possible future investigations in shape optimization for the mitigation of coastal erosion. It is divided in three distinct sections. In Section 9.1 we refer to selected improvements in the simulation of propagating waves and sediment interactions in relation with equations that have been presented in Chapters 5,6 and 7. In Section 9.2, we refer to alternative wave and sediment descriptions and possible treatments in the shape optimization context. Finally the chapter ends with overall conclusions in Section 9.3.

9.1 Numerical Improvements for SWE

In this section we will provide simulative improvements for equations that have been presented in Chapters 5,6 and 7. In this light, we will first deal with the wetting-drying phenomenon that was first mentioned in Chapter 5. To this, we will present extensions potentially suitable for the use in shape optimization. In the following, we will look at alternative boundary conditions, that may prove useful in a non-tsunami like setting.

Wetting & Drying

Accurate simulations of wetting-drying processes play a significant role in numerical investigations of predictive models for near-coastal flows. Difficulties are hereby manifold e.g. as implementations quickly result in instabilities alongside wet and dry interfaces or in a loss of the conservation of mass property [87]. In the last decades various approaches have been presented e.g. using flux limiters [87] or relying on alternative formulations via variable sediment [103] or as variational inequality [38]. In the following we refer to the latter approaches that are potentially well-suited for investigations in shape optimizations. In the early works of Bermudez [38] the domain is divided in variable regions

classified as wet, dry or interface, i.e.

$$\begin{aligned}\Omega^+ &= \{(x,t) \in \Omega \times (0,T) : H(x,t) > 0\} \\ \Omega^- &= \{(x,t) \in \Omega \times (0,T) : H(x,t) \leq 0\} \\ \Sigma &= \partial\Omega_t^-\end{aligned} \tag{9.1}$$

In all calculated examples in Chapters 5-7 the water height was implicitly assumed to be positive. However, wetting and drying allows for negative heights, provided an algorithmic handle is used for specific regions without relying on general wave speeds of (5.32). Subdomains (9.1) can be used to redefine the SWE from Theorem 5.1, on which all currently proposed treatments rely on, i.e.

$$\begin{aligned}\frac{\partial H}{\partial t} + \nabla \cdot Q = 0 \qquad & \text{in } \Omega^+ \\ \frac{\partial Q}{\partial t} + \nabla \cdot \left(\frac{Q}{H} \otimes Q\right) + \frac{g}{2}\nabla(H^2) = -gH\nabla z \qquad & \text{in } \Omega^+ \\ Q = 0, \quad H = 0 \qquad & \text{in } \Omega^-,\end{aligned} \tag{9.2}$$

alongside a Hamilton-Jacobi equation for the tracking of the interface (cf. to Definition 3.19),

$$\frac{\partial \phi}{\partial t} + \nabla\phi \cdot Q = 0, \quad H = 0 \quad \text{at } \Sigma. \tag{9.3}$$

In [38] it is proposed to start from the time discrete counterpart of (9.2), that can then be written as variational inequality of second kind and is reformulated for the setting of a zero reference height as in Theorem 5.1, i.e.

$$\begin{aligned}&\frac{1}{\Delta t}\int_\Omega Q^{k+1}(R - Q^{k+1})\,\mathrm{d}x + g\Delta t \int_\Omega \nabla \cdot Q^{k+1}\nabla z \cdot (R - Q^{k+1})\,\mathrm{d}x \\ &+\frac{g}{2\Delta t}(\Psi(H^k - \Delta t\nabla \cdot R) - \Psi(H^k - \Delta t\nabla \cdot Q^{k+1})) \geq \langle \tilde{L}^k, R - Q\rangle, \forall R \in V\end{aligned} \tag{9.4}$$

where

$$\Psi(z) = \int_\Omega \psi(x,H)\,\mathrm{d}x, \quad \psi(x,H) = \begin{cases}\frac{1}{3}H^3 & \text{if } H \geq 0 \\ +\infty & \text{otherwise,}\end{cases} \tag{9.5}$$

and the source is defined in terms of the evolution of a volume element and the sedimental variation, i.e.

$$\tilde{L}^k = (1/\Delta t)J^kQ^k[X^k] - gH^k\nabla z$$

for suitable function space V as in [117]. Solutions as well as optimization strategies can then rely on the sub-differential such as Moreau-Yosida regularizations of the integrand in (9.5) [38, 117]. However, techniques for adjoint-based shape optimization for variational inequalities of second kind still require pioneering work as approaches so far reduce to variational inequalities of first kind [114].

More frequently solutions to (9.2) are based on switches, e.g. a smoothed version relying on a variable sediment height is presented in [103]. We reformulate this in the following for the setting of a zero reference height as in Theorem 5.1.

$$\begin{aligned} \frac{\partial H}{\partial t} + \frac{\partial f(H)}{\partial t} + \nabla \cdot \left(\tilde{H} u\right) &= 0 \\ \frac{\partial \tilde{Q}}{\partial t} + \nabla \cdot \left(\frac{\tilde{Q}}{\tilde{H}} \otimes \tilde{Q}\right) + \frac{g}{2} \nabla(\tilde{H}^2) &= g \tilde{H} \nabla z \end{aligned} \tag{9.6}$$

for solution variables $(\tilde{H}, \tilde{Q}) = (H + f(H), u\tilde{H}, v\tilde{H})$ and $f \in C^1(\Omega \times (0,T))$ that can be characterized as smoothed *max*-function, e.g. as in (8.34) of the preceding chapter. System (9.6) is motivated by the observation that $\frac{\partial H}{\partial t} + \frac{\partial f(H)}{\partial t} = (1 + f'(H))\frac{\partial H}{\partial t}$ where the coefficient is a smooth indicator of wet and dry zones with $0 < 1 + f'(H) < 1$. This formulation offers itself for immediate shape sensitivity evaluations as it has been conducted in the discretize-then-differentiate setting in [80].

Wave Maker Boundary

We will now concentrate on boundary conditions that allow to deviate from the tsunami-like setting in Chapters 5-7, i.e. instead of resulting waves due to difference in the initial water height, propagating waves are the consequence of suitable boundary conditions. From the analytical point of view this was covered in [140, 2]. In our discrete setting (5.30), where the boundary terms are specified as

$$\begin{aligned} N_{\Gamma,h}(U_h, P_h) = &\int_0^T \int_\Gamma \mathcal{F}(U_h^+, U_\Gamma(U_h^+), n) \cdot P_h^+ \,\mathrm{d}s\,\mathrm{d}t \\ &+ \int_0^T \int_{\Gamma_n} \Big[\underline{\delta}_\Gamma(\hat{U}_h^+) : P_h \otimes n + G(\mu^+) \nabla_h (\hat{U}_h^+) : P_h^+ \otimes n \\ &- G(\mu^+) \nabla_h V_h^+ : (\hat{U}_h^+ - U_\Gamma(\hat{U}_h^+)) \otimes n \Big] \,\mathrm{d}s\,\mathrm{d}t, \end{aligned} \tag{9.7}$$

randomized wave-maker boundary conditions can be implemented by

$$\begin{aligned} U_\Gamma(U_h^+) = (&H_{\Gamma,h}^+ + \mathbb{1}_{\mathcal{T}}(t) X, \\ &\mathrm{sgn}(n_1) \max(Q_{\Gamma,1}^+ \mathrm{sgn}(n_1), 0) + \mathbb{1}_{\mathcal{T}}(t) Y, \\ &\mathrm{sgn}(n_2) \max(Q_{\Gamma,2}^+ \mathrm{sgn}(n_2), 0) + \mathbb{1}_{\mathcal{T}}(t) Y) \end{aligned}$$

for outward-pointing normal n, time point of wave occurrence $\mathcal{T} = \{t_0, t_1, ...\}$ and random variable $X \sim \mathcal{N}(p_1, p_2)$ drawn e.g. from normal-distribution to signify a randomized initial wave height from an interval $(p_1, p_2) \subset \mathbb{R}$ with $0 < p_1 < p_2$ and randomized initial directed wave acceleration $Y \sim \mathcal{N}(r_1, r_2)$ from an interval $(r_1, r_2) \subset \mathbb{R}$ with $0 < r_1 < r_2$. In this formulation shape sensitivities are the easiest captured in a discretize-then-differentiate setting as the continuous counterpart is not immediately available. In Figure 9.1 resulting waves are visualized for the one-dimensional representative.

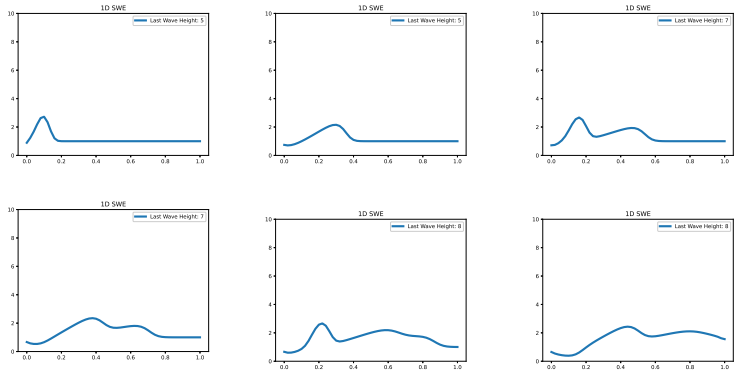

Figure 9.1: Visualization of 1D Waves created by Wave Maker Traveling from Left to Right Boundary for $t \in \{0, 0.5, 1, 1.5, 2, 2.5\}$

9.2 Related Propagation Laws

This section will introduce two promising wave formulations, that encounter weaknesses of proposed methods and equations in Chapters 5-8. In this light, we firstly introduce porous layered SWE in Section 9.2, that account for the fact that obstacles in contrast to presented simulations are often limited not only in width but also in height. Secondly, we restate equations for the long-term dynamics of sand dunes [74], which are potentially useful in modeling long-term effects in sedimentation problems, whereas we have focused on short-term, impactful and rare events.

Porous Layered Shallow Water Equations

Various types of fluid flows can be approximated as layered systems that consist of two shallow fluids of distinct densities. One common interpretation lies in the identification of an upper clear water layer over a dense mixture of water and moving grains [17]. We hereby propose an additional porosity factor for the lower layer, which can be identified as a geotextile tube as investigated in Chapter 6, which effect is limited in height due to the second layer. We state the porous layered SWE consisting of the first layer

$$
\begin{aligned}
\frac{\partial H_1}{\partial t} &+ \frac{\partial H_1 u_1}{\partial x} + \frac{\partial H_1 v_1}{\partial y} &&= 0 \\
\frac{\partial H_1 u_1}{\partial t} &+ \frac{\partial H_1 u_1^2 + 1/2 g H_1^2}{\partial x} + \frac{\partial H_1 u_1 v_1}{\partial y} &&= -gH_1 \frac{\partial z + H_2}{\partial x} \\
\frac{\partial H_1 v_1}{\partial t} &+ \frac{\partial H_1 u_1 v_1}{\partial x} + \frac{\partial H_1 u_1^2 + 1/2 g H_1^2}{\partial y} &&= -gH_1 \frac{\partial z + H_2}{\partial y}
\end{aligned}
$$

for solution variable $U_1 : \Omega\times(0,T) \to \mathbb{R}\times\mathbb{R}^2$ denoted by $U_1 = (H_1, Q_1) = (H_1, H_1u_1, H_1v_1)$ and the second porous layer

$$\begin{aligned}
\phi\left[\frac{\partial H_2}{\partial t} + \frac{\partial H_2u_2}{\partial x} + \frac{\partial H_2v_2}{\partial y}\right] &= 0\\
\phi\left[\frac{\partial H_2u_2}{\partial t} + \frac{\partial H_2u_2^2 + 1/2gH_2^2}{\partial x} + \frac{\partial H_2u_2v_2}{\partial y}\right] &= -g\phi H_2\frac{\partial z + \frac{\rho_1}{\rho_2}H_1}{\partial x} + g\frac{H_2^2}{2}\frac{\partial \phi}{\partial x}\\
\phi\left[\frac{\partial H_2v_2}{\partial t} + \frac{\partial H_2u_2v_2}{\partial x} + \frac{\partial H_2u_2^2 + 1/2gH_2^2}{\partial y}\right] &= -g\phi H_2\frac{\partial z + \frac{\rho_1}{\rho_2}H_1}{\partial y} + g\phi\frac{H_2^2}{2}\frac{\partial \phi}{\partial y}
\end{aligned}$$

for solution variable $U_2 : \Omega\times(0,T) \to \mathbb{R}\times\mathbb{R}^2$ denoted by $U_2 = (H_2, Q_2) = (H_2, H_2u_2, H_2v_2)$ such as densities $\rho_1, \rho_2 > 0$, which define the interaction of both layers via source contribution. Continuous adjoints and shape derivatives for layered SWE can be calculated in the same manner as for classical and porous SWE in Chapters 5 and 6 with the addition of artificial viscosity. The shape derivative of each individual layer is then extended by the additional source terms. Solutions to porous, layered SWE are obtained from the system's vector form, where the delicate part lies in the derivation of wave speeds. Investigations so far have only dealt with the one-dimensional 4×4 system of governing equations, which however is already known to possess numerical hindrances, e.g. a loss of hyperbolicity is exhibited under certain flow configurations [101].

Long-Term-Dynamics of Sand Dunes

This part will discuss possible long-term computations that can be performed with SWEE. For this, we derive the sediment dynamics, called long-term dynamics of sand-dunes (LTDD) following [74] and the coupled hydrodynamics as in [21]. We hereby discuss difficulties in obtaining numerical solutions and applications in shape optimization.

The derivation in [74] of long-term Exner-type sediment laws, starts by looking at Van Rijns sediment transport formula [152], that is a representative of equations characterized in Definition 7.1. Based on this, the equation is non-dimensionalized, using a scaling argument for independent and dependent variables such as derivative operators. Finally, using simple reformulations an equation in terms of non-dimensional solution counterparts is ultimately obtained, which can form the basis for the investigation of different time horizons, e.g. in [74] short-, mid- and longterm dynamics are derived. In the latter case the homogenized parameter $\epsilon > 0$, obtained from a 16-years reciprocal

$$\epsilon := \frac{1}{192} \tag{9.8}$$

leads to the final form of the LTDD, which are a viscous sedimentation formula as in [184], using dimensionless parameters (a_1, b_1, c_1) and omitting ϵ-dependency of variables

$$\frac{\partial z}{\partial t} - \frac{c_1}{\epsilon^2}\nabla\cdot\left((1-b_1\epsilon H)||Q/H||_2^3\nabla z\right) = \frac{a_1}{\epsilon^2}\nabla\cdot((1-b_1\epsilon H)||Q/H||_2^2 Q/H). \tag{9.9}$$

Based on this, a coupling with shallow water equations can be obtained as introduced in Chapter 7 after performing non-dimensionalization in the same manner for the SWE system [21], which gives for dimensionless parameters (a_2, b_2, c_2)

$$\begin{aligned} \frac{\partial H}{\partial t} + \frac{a_2}{\epsilon^4}\nabla \cdot Q = 0 \\ \frac{\partial Q}{\partial t} + \frac{a_2}{\epsilon^4}\nabla \cdot \left(\frac{Q}{H} \otimes Q\right) + \frac{b_2}{2\epsilon^4}\nabla(H^2) + \frac{c_2}{2\epsilon^4} H\nabla z = 0 \\ \frac{\partial z}{\partial t} - \frac{a_1}{\epsilon^2}\nabla \cdot ((1 - b_1\epsilon H)||Q/H||_2^2 Q/H) - \frac{c_1}{\epsilon^2}\nabla \cdot \Big((1 - b_1\epsilon H)||Q/H||_2^3 \nabla z\Big) = 0. \end{aligned} \tag{9.10}$$

As it has been done before in Chapters 5-7, numerical solutions can be based on the vector notation of (9.10), which is different to [21], where an operator splitting as in Section 7.4 is proposed. We obtain for the advective part

$$\partial_t U + \frac{1}{\epsilon^4}\nabla \cdot F(U) = \frac{1}{\epsilon^4} B_1 \frac{\partial U}{\partial x} + \frac{1}{\epsilon^4} B_2 \frac{\partial U}{\partial y}, \tag{9.11}$$

where

$$\tilde{U} = (H, Hu, Hv, z) \tag{9.12}$$

and

$$F = (F_1, F_2) = \begin{pmatrix} a_2 Hu & a_2 Hv \\ a_2 Hu^2 + b_2/2H^2 & a_2 Huv \\ a_2 Huv & a_2 Hv^2 + b_2/2H^2 \\ -\epsilon^2 a_1(1 - b_1\epsilon H)||Q/H||_2^2 u & -\epsilon^2 a_1(1 - b_1\epsilon H)||Q/H||_2^2 v \end{pmatrix} \tag{9.13}$$

and

$$B_1 = \begin{pmatrix} 0 & 0 & 0 & 0 \\ 0 & 0 & 0 & c_2 H \\ 0 & 0 & 0 & 0 \\ 0 & 0 & 0 & 0 \end{pmatrix} \quad B_2 = \begin{pmatrix} 0 & 0 & 0 & 0 \\ 0 & 0 & 0 & 0 \\ 0 & 0 & 0 & c_2 H \\ 0 & 0 & 0 & 0 \end{pmatrix}. \tag{9.14}$$

Using the coupled LTTD-SWE in optimization requires us in the simplest case to rewrite equations obtaining fully parabolic equations. Hence, diffusion is added, relying once more on scaled and non-dimensionalized parameters, such that it holds

$$\begin{aligned} \frac{\partial H}{\partial t} + \frac{a_2}{\epsilon^4}\nabla \cdot Q - \frac{d_2}{\epsilon^4}\nabla \cdot (\mu_v \nabla(H + z)) = 0 \\ \frac{\partial Q}{\partial t} + \frac{a_2}{\epsilon^4}\nabla \cdot \left(\frac{Q}{H} \otimes Q\right) + \frac{b_2}{2\epsilon^4}\nabla(H^2) + \frac{c_2}{2\epsilon^4} H\nabla z - \frac{d_2}{\epsilon^4}\nabla \cdot (G(\mu_f)\nabla Q) = 0 \\ \frac{\partial z}{\partial t} - \frac{a_1}{\epsilon^2}\nabla \cdot ((1 - b_1\epsilon H)||Q/H||_2^2 Q/H) - \frac{c_1}{\epsilon^2}\nabla \cdot \Big((1 - b_1\epsilon H)||Q/H||_2^3 \nabla z\Big) = 0. \end{aligned} \tag{9.15}$$

Adjoints and shape derivatives for the SWE-LTDD can be obtained as for the simple SWEE of Chapter 7. However, in numerical implementations the CFL-condtion [56,

Chapter 3] poses a severe time restriction, driven by the square of the homogenization parameter [21]. Possible cures alongside implicit time-stepping schemes can rely on the numerical-two-scale method [79] or on homogenized results [22]. However, it appears that an SWE coupling is ill-suited for shape optimization algorithms relying on classical gradient-descent schemes, which require an iteration-wise solution to system (9.15) over a predefined time-frame.

9.3 Conclusion

This dissertation has intended to utilize shape optimization for the mitigation of coastal erosion. In this light, various wave and sediment descriptions, from either the Eulerian or the Lagrangian viewpoint, have been proposed and successfully applied in a shape optimization framework, which is detailed in the following:
In the Eulerian framework we have investigated a broad range of time-independent and time-dependent equations in Chapters 4-7.
In a first simplistic description of wave propagation in Chapter 4, we have derived the stationary continuous adjoint such as shape and topology derivative for Helmholtz scattering with suitable boundary conditions and objectives for near-shore flows. Results are tested using a gradient-descent based algorithm on a two-dimensional simplistic domain and a comprehensive domain representing the LdB coastal section with a single artificial offshore island. We have seen that the optimized shape is strongly affected by the incoming wave and by the respective surrounding coastal section that is to be protected. In the second part we have exploited an alternative description of a local minimum description in an algorithm to perform topology optimization. As these techniques are commonly used for variants of elasticity equations, this forms an additional field of application. However, since the Helmholtz equation in form of a mild-slope equation only provides a very basic, time-harmonic description of propagating waves the informative value of results is limited.
In Chapters 5-7 we have targeted this weakness by relying on various forms of the sophisticated SWE with physically motivated boundary conditions and objectives. In all three chapters we have derived the time-dependent continuous adjoint and shape derivative of the SWE in volume form and tested results for different meshes.
More precisely, SWE in the classical form have been investigated in Chapter 5. The focus is hereby on numerical investigations, firstly proposing a SIPG method to obtain discretized solutions to state and adjoint equations under the addition of artificial viscosity. In the LdB case it is observed that an optimizer, placed on the three offshore islands, proposes to build back the islands in its original form. In addition, we have introduced techniques for global shore protection in an immersed manifold setting. Once more it is observed that the optimized shape strongly orients itself to the wave direction and to the mesh region that is to be protected. The approach can be easily adjusted for arbitrary meshes, objective functions and different wave properties driven by initial and boundary conditions. In comparison to Chapter 4, topological calculations are open to further investigations, as solutions are time-dependent, vector-valued and nonlinear.

Chapter 6 extends the preceding formulation by a discontinuous porosity coefficient to represent obstacles with permeability. For the addition of diffusive terms, we have firstly derived viscous and porous shallow water equations. Solution methods are once more based on the SIPG method, which provides a novelty compared to previous constant cell-based approximations. In this setting, numerical solutions necessary rely on a well-balanced scheme that ensures validity under rest-conditions and due to this reason a redefinition of variables is proposed. Numerical investigations extend the application field to Mentawai islands, that served as effective shields in former rare but atrocious tsunamis.
The investigation of shallow flows in an Eulerian framework is finalized in Chapter 7 utilizing a coupling with Exner-type equations. Numerical difficulties occur in this setting due to the enlarged system size. For this, we have presented three solution approaches and firstly propose an Eulerian-Lagrangian coupling. As before, we have verified results numerically.
In the Lagrangian framework in Chapter 8 we have derived the discrete adjoint for a general symplectic Euler particle class. In addition, for an SWE SPH representative, based on novel and non-standard boundary interactions by signed distance fields, the discrete shape derivative is derived, that reduces to the shape derivative of a finite element interpolator. Results have been verified on a sample mesh inspired by practical applications to mitigate effects of coastal erosion. We point out that this can only serve as a first feasibility study, since the number of particles is still low and meshes are simplified. In future, convergence results for the solution of forward, adjoint and shape derivative calculations, for simultaneous limit behavior of particles (cf. to [150]) and mesh-refinement appear of interest. In this light, relations and comparisons between shape optimization in an Eulerian, cf. to Chapter 4-7, and an Lagrangian framework 8, such as an Eulerian-Lagrangian coupling as proposed in Section 7.4, build exciting fields of research.
Summarizing we are given a first feasibility study in the application of shape optimization in the mitigation of coastal erosion, without any claim to completeness. As we have seen in Section 9.1 and 9.2 multiple adjustments and improvements for accurate wave descriptions are evident. Ultimately, practical implementations would require the collaboration of experts in different fields of research ranging from computer and material scientists to oceanologists and physicists.

List of Figures

Bibliography

[1] Pierre-Antoine Absil, Robert Mahony, and Rodolphe Sepulchre. *Optimization Algorithms on Matrix Manifolds*. Vol. 78. Princeton University Press, Dec. 2008. DOI: 10.1515/9781400830244.

[2] Valery I. Agoshkov, A. Quarteroni, and F. Saleri. "Recent Developments in the Numerical Simulation of Shallow Water Equations I: Boundary Conditions". In: *Applied Numerical Mathematics* 15.2 (1994), pp. 175–200. DOI: https://doi.org/10.1016/0168-9274(94)00014-X.

[3] Vadym Aizinger and Clint Dawson. "A Discontinuous Galerkin Method for Two-Dimensional Flow and Transport in Shallow Water". In: *Advances in Water Resources* 25.1 (2002), pp. 67–84. DOI: https://doi.org/10.1016/S0309-1708(01)00019-7.

[4] Grégoire Allaire, François Jouve, and Georgios Michailidis. "Thickness Control in Structural Optimization via a Level Set Method". In: *Structural and Multidisciplinary Optimization* 53 (June 2016). DOI: 10.1007/s00158-016-1453-y.

[5] Grégoire Allaire, François Jouve, and Anca-Maria Toader. "A Level-Set Method for Shape Optimization". In: *Comptes Rendus Mathematique* 334.12 (2002), pp. 1125–1130. DOI: https://doi.org/10.1016/S1631-073X(02)02412-3.

[6] Martin S. Alnæs et al. "The FEniCS Project Version 1.5". In: *Archive of Numerical Software* 3.100 (2015). DOI: 10.11588/ans.2015.100.20553.

[7] Hans Wilhelm Alt. *Lineare Funktionalanalysis. eine anwendungsorientierte Einführung*. ger. 5. Berlin; Heidelberg: Springer, 2006, XIV, 431 S.

[8] Lino Alvarez-Vázquez et al. "An Optimal Shape Problem Related to the Realistic Design of River Fishways". In: *Ecological Engineering* (June 2006).

[9] Samuel Amstutz. "An introduction to the topological derivative". In: *Engineering Computations* ahead-of-print (Sept. 2021). DOI: 10.1108/EC-07-2021-0433.

[10] Samuel Amstutz. "Regularized Perimeter for Topology Optimization". In: *SIAM Journal on Control and Optimization* 51 (Dec. 2010). DOI: 10.1137/100816997.

[11] Samuel Amstutz. “Topological Sensitivity Analysis for some Nonlinear PDE Systems”. In: *Journal de Mathématiques Pures et Appliquées* 85.4 (2006), pp. 540–557. DOI: https://doi.org/10.1016/j.matpur.2005.10.008.

[12] Samuel Amstutz and Heiko Andrä. “A New Algorithm for Topology Optimization using a Level-Set Method”. In: *Journal of Computational Physics* 216.2 (2006), pp. 573–588. DOI: https://doi.org/10.1016/j.jcp.2005.12.015.

[13] Samuel Amstutz, Charles Dapogny, and Alex Ferrer Ferre. “A Consistent Approximation of the Total Perimeter Functional for Topology Optimization Algorithms”. In: *ESAIM: Control, Optimisation and Calculus of Variations* (Jan. 2022). DOI: 10.1051/cocv/2022005.

[14] Samuel Amstutz and Nicolas Van Goethem. “Topology Optimization Methods With Gradient-Free Perimeter Approximation”. In: *Interfaces and Free Boundaries* 14 (Oct. 2012), pp. 401–430. DOI: 10.4171/IFB/286.

[15] Douglas Arnold. “An Interior Penalty Finite Element Method with Discontinuous Elements”. In: *SIAM Journal on Numerical Analysis* 19.4 (1982), pp. 742–760.

[16] Douglas Arnold et al. “Unified Analysis of Discontinuous Galerkin Methods for Elliptic Problems”. In: *SIAM Journal on Numerical Analysis* 39 (Jan. 2002). DOI: 10.1137/S0036142901384162.

[17] Emmaniel Audusse. “A Multilayer Saint-Venant Model: Derivation and Numerical Validation”. In: *Discrete and Continuous Dynamical Systems-series B - Discrete Contin. Dyn. Sys.-Ser.* 5 (May 2005), pp. 189–214. DOI: 10.3934/dcdsb.2005.5.189.

[18] Emmanuel Audusse, Christophe Chalons, and Philippe Ung. “A Simple Three-Wave Approximate Riemann Solver for the Saint-Venant–Exner Equations”. In: *International Journal for Numerical Methods in Fluids* (Sept. 2015). DOI: 10.1002/fld.4500.

[19] Alexandros Avdis et al. “Meshing Ocean Domains for Coastal Engineering Applications”. In: *VII European Congress on Computational Methods in Applied Sciences and Engineering*. June 2016. DOI: 10.7712/100016.1830.7712.

[20] Timothy J. Baker and Peter A. Cavallo. “Dynamic Adaptation for Deforming Tetrahedral Meshes”. In: *14th Computational Fluid Dynamics Conference*. 1999.

[21] Mouhamadou Baldé and Diaraf Seck. “Coupling the Shallow Water Equation with a Long Term Dynamics of Sand Dunes”. In: *Discrete and Continuous Dynamical Systems - Series S* 9 (Oct. 2016), pp. 1521–1551. DOI: 10.3934/dcdss.2016061.

[22] Mouhamadou A.M.T. Baldé and Diaraf Seck. “Homogenization and Corrector Result for a Coupled Parabolic Hyperbolic System”. In: *Journal of Mathematical Analysis and Applications* 484.1 (2020), p. 123677. DOI: https://doi.org/10.1016/j.jmaa.2019.123677.

[23] Adhémar-Jean-Claude Barré de Saint-Venant. “Théorie du Mouvement Non-Permanent des Eaux, avec Application aux Crues des Rivières et è l’Introduction des Marées dans leur Lit”. In: *C. R. Acad Sci Paris* (Aug. 1871).

[24] Garrett E. Barter and David L. Darmofal. “Shock Capturing with PDE-based Artificial Viscosity for DGFEM: Part I. Formulation”. In: *Journal of Computational Physics* 229.5 (2010), pp. 1810–1827. DOI: https://doi.org/10.1016/j.jcp.2009.11.010.

[25] Timothy J. Barth and Dennis C. Jespersen. “The Design and Application of Upwind Schemes on Unstructured Meshes”. In: *AIAA 27th Aerospace Sciences Meeting*. 1989.

[26] Francesco Bassi and Stefano Rebay. “A High-Order Accurate Discontinuous Finite Element Method for the Numerical Solution of the Compressible Navier–Stokes Equations”. In: *Journal of Computational Physics* 131.2 (1997), pp. 267–279. DOI: https://doi.org/10.1006/jcph.1996.5572.

[27] Harry Bateman. “Some Recent Researches on the Motion of Fluids”. In: *Monthly Weather Review* 43 (1915), pp. 163–170.

[28] Martin Bauer, Philipp Harms, and Peter W. Michor. “Sobolev Metrics on Shape Space of Surfaces”. In: *Journal of Geometric Mechanics* 3.4 (2011), pp. 389–438. DOI: 10.3934/jgm.2011.3.389.

[29] Carlos Erik Baumann and J. Tinsley Oden. “A Discontinuous hp Finite Element Method for Convection-Diffusion Problems”. In: *Computer Methods in Applied Mechanics and Engineering* 175.3 (1999), pp. 311–341. DOI: https://doi.org/10.1016/S0045-7825(98)00359-4.

[30] Richard M. Beam, Robert F. Warming, and H. C. Yee. “Stability analysis of numerical boundary conditions and implicit difference approximations for hyperbolic equations”. In: *Journal of Computational Physics* 48 (1982), pp. 200–222.

[31] Eliane Becache, Anne-Sophie Bonnet-Ben Dhia, and Guillaume Legendre. “Perfectly Matched Layers for the Convected Helmholtz Equation”. In: *SIAM J. Numerical Analysis* 42 (Jan. 2004), pp. 409–433. DOI: 10.1137/S0036142903420984.

[32] Markus Becker and Matthias Teschner. “Weakly Compressible SPH for Free Surface Flows”. In: *Eurographics/SIGGRAPH Symposium on Computer Animation*. Ed. by Dimitris Metaxas and Jovan Popovic. The Eurographics Association, 2007. DOI: 10.2312/SCA/SCA07/209-218.

[33] Ted Belytschko, Y. Y. Lu, and L. Gu. “Element-Free Galerkin Methods”. In: *International Journal for Numerical Methods in Engineering* 37.2 (1994), pp. 229–256. DOI: https://doi.org/10.1002/nme.1620370205.

[34] Bachir Ben Moussa and Jean Paul Vila. “Convergence of SPH Method for Scalar Nonlinear Conservation Laws”. In: *SIAM Journal on Numerical Analysis* 37.3 (2000), pp. 863–887. DOI: 10.1137/S0036142996307119.

[35] Martin Berggren. “A Unified Discrete-Continuous Sensitivity Analysis Method for Shape Optimization”. In: *CSC 2010*. 2010.

[36] Juri C.W. Berkhoff. “Computation of Combined Refraction-Diffraction”. In: *Coastal Engineering Proceedings* 1.13 (Jan. 1972), p. 23. DOI: 10.9753/icce.v13.23.

[37] Juri C.W. Berkhoff. “Mathematical Models for Simple Harmonic Linear Water Waves: Wave Diffraction and Refraction”. PhD thesis. Delft Hydraulics Lab, 1976.

[38] Alfredo Bermudez, Carmen Rodríguez, and M. Vilar. “Solving Shallow Water Equations by a Mixed Implicit Finite Element Method”. In: *Ima Journal of Numerical Analysis* 11 (Jan. 1991), pp. 79–97. DOI: 10.1093/imanum/11.1.79.

[39] Florin Bobaru. “Meshless Approach to Shape Optimization of Linear Thermoelastic Solids”. In: *International Journal for Numerical Methods in Engineering* 53 (Feb. 2002), pp. 765–796. DOI: 10.1002/nme.311.

[40] Dietrich Braess. *Finite Elements: Theory, Fast Solvers, and Applications in Solid Mechanics*. 3rd ed. Cambridge University Press, 2007. DOI: 10.1017/CBO9780511618635.

[41] Martin Burger, Benjamin Hackl, and Wolfgang Ring. “Incorporating Topological Derivatives into Level Set Methods”. In: *Journal of Computational Physics* 194 (July 2004), pp. 344–362. DOI: 10.1016/j.jcp.2003.09.033.

[42] Benoit Camenen and Magnus Larson. “A General Formula for Non-Cohesive Bed-Load Sediment Transport”. In: *Estuarine, Coastal and Shelf Science* 63 (Apr. 2005), pp. 249–260. DOI: 10.1016/j.ecss.2004.10.019.

[43] Girolamo Cardano and T. Richard Witmer. *Ars Magna or the Rules of Algebra*. Dover, 1993.

[44] Christian Kanzow Carl Geiger. *Numerische Verfahren zur Lösung unrestringierter Optimierungsaufgaben*. Springer Berlin, Heidelberg, 1999. DOI: https://doi.org/10.1007/978-3-642-58582-1.

[45] Ana Carpio and Maria-Luisa Rapun. “Solving Inhomogeneous Inverse Problems by Topological Derivative Methods”. In: *Inverse Problems* 24 (July 2008), p. 045014. DOI: 10.1088/0266-5611/24/4/045014.

[46] Manuel Castro, Enrique Fernández-Nieto, and Ana Ferreiro. “Sediment Transport Models in Shallow Water Equations and Numerical Approach by High Order Finite Volume Methods”. In: *Computers & Fluids* 37 (Mar. 2008), pp. 299–316. DOI: 10.1016/j.compfluid.2007.07.017.

[47] Manuel Castro et al. “Two-Dimensional Sediment Transport Models in Shallow Water Equations. A Second Order Finite Volume Approach on Unstructured Meshes”. In: *Computer Methods in Applied Mechanics and Engineering* 198 (July 2009), pp. 2520–2538. DOI: 10.1016/j.cma.2009.03.001.

[48] Carlo Cattaneo and Joseph Kampé de Fériet. *Sur une forme de l’équation de la chaleur éliminant le paradoxe d’une propagation instantanée*. Gauthier-Villars, Paris, 1958.

[49] Jean Cea. “Conception optimale ou identification de formes, calcul rapide de la dérivée directionnelle de la fonction coût”. In: *ESAIM: M2AN* 20.3 (1986), pp. 371–402. DOI: 10.1051/m2an/1986200303711.

[50] J. Chen and Nam Kim. “Meshfree Method and Application to Shape Optimization”. In: *Optimization of Structural and Mechanical Systems*. World Scientific, Sept. 2007, pp. 389–414. DOI: 10.1142/9789812779670_0014.

[51] Alina Chertock, Alexander Kurganov, and Tong Wu. “Operator Splitting Based Central-Upwind Schemes For Shallow Water Equations With Moving Bottom Topography”. In: *Communications in Mathematical Sciences* (2019).

[52] Kyung K. Choi. “Shape Design Sensitivity Analysis and Optimal Design of Structural Systems”. In: *Computer Aided Optimal Design: Structural and Mechanical Systems*. Ed. by Carlos A. Mota Soares. Springer Berlin Heidelberg, 1987, pp. 439–492.

[53] Ven Te Chow. *Open-Channel Hydraulics*. The Blackburn Press, 1959.

[54] Constantin Christof et al. “Optimal Control of a Non-Smooth Semilinear Elliptic Equation”. In: *Mathematical Control and Related Fields* 8 (May 2017), pp. 247–276. DOI: 10.3934/mcrf.2018011.

[55] Philippe G. Ciarlet. “Basic Error Estimates for Elliptic Problems”. In: *Finite Element Methods (Part 1)*. Vol. 2. Handbook of Numerical Analysis. Elsevier, 1991, pp. 17–351. DOI: https://doi.org/10.1016/S1570-8659(05)80039-0.

[56] Bernardo Cockburn. “An introduction to the Discontinuous Galerkin method for convection-dominated problems”. In: 1998.

[57] Bernardo Cockburn, George E. Karniadakis, and Chi-Wang Shu. *Discontinuous Galerkin Methods*. Springer Berlin, Heidelberg, 2000.

[58] Bernardo Cockburn, San-Yih Lin, and Chi-Wang Shu. “TVB Runge-Kutta Local Projection Discontinuous Galerkin Finite Element Method for Conservation Laws III: One-Dimensional Systems”. In: *Journal of Computational Physics* 84.1 (1989), pp. 90–113. DOI: https://doi.org/10.1016/0021-9991(89)90183-6.

[59] David Colton and Rainer Kress. *Inverse Acoustic and Electromagnetic Scattering Theory*. Springer New York, NY, 1992.

[60] Stéphane Cordier, Minh H. Le, and Tomas Morales De Luna. “Bedload Transport in Shallow Water Models: Why Splitting (may) Fail, how Hyperbolicity (can) Help”. Nov. 2010.

[61] Rafael Correa and Alberto Seeger. “Directional Derivative of a Minmax Function”. In: *Nonlinear Analysis-theory Methods & Applications* 9 (Jan. 1985), pp. 13–22. DOI: 10.1016/0362-546X(85)90049-5.

[62] Michael G. Crandall, Lawrence C. Evans, and Pierre-Louis Lions. “Some Properties of Viscosity Solutions of Hamilton-Jacobi Equations.” In: *Transactions of the American Mathematical Society* 282 (1984), pp. 487–502.

[63] Juan De los Reyes. *Numerical PDE-Constrained Optimization*. Springer Cham, Mar. 2015. DOI: 10.1007/978-3-319-13395-9.

[64] Michel C. Delfour. "Control, Shape, and Topological Derivatives via Minimax Differentiability of Lagrangians". In: *Numerical Methods for Optimal Control Problems*. Ed. by Maurizio Falcone et al. Cham: Springer International Publishing, 2018, pp. 137–164. DOI: 10.1007/978-3-030-01959-4_7.

[65] Michel C. Delfour and Jean-Paul Zolésio. *Shapes and Geometries*. Second. Society for Industrial and Applied Mathematics, 2011. DOI: 10.1137/1.9780898719826.

[66] Bishnu H. Devkota and Jörg Imberger. "Lagrangian Modeling of Advection-Diffusion Transport in Open Channel Flow". In: *Water Resources Research* 45.12 (2009). DOI: https://doi.org/10.1029/2009WR008364.

[67] Benjamin Dewals et al. "Porosity Models for Large-Scale Urban Flood Modelling: A Review". In: *Water* 13.7 (2021). DOI: 10.3390/w13070960.

[68] Roberto Di Lisio, Emmanuel Grenier, and Mario Pulvirenti. "The Convergence of the SPH Method". In: *Computers & Mathematics with Applications* 35.1 (1998), pp. 95–102. DOI: https://doi.org/10.1016/S0898-1221(97)00260-5.

[69] Alexandre Ern and Jean-Luc Guermond. *Theory and Practice of Finite Elements*. Springer New York, NY, 2004.

[70] Martin Ester et al. "A Density-Based Algorithm for Discovering Clusters in Large Spatial Databases with Noise". In: *KDD'96: Proceedings of the Second International Conference on Knowledge Discovery and Data Mining*. AAAI Press, 1996, pp. 226–231.

[71] Tommy Etling et al. "First and Second Order Shape Optimization based on Restricted Mesh Deformations". In: *Methods and Algorithms for Scientific Computing* (Oct. 2018).

[72] Lawrence Evans. *Partial Differential Equations*. American Mathematical Society, Jan. 2010.

[73] Felix Maria Exner. *Über die Wechselwirkung zwischen Wasser und Geschiebe in Flüssen*. Hölder-Pichler-Tempsky, A.-G., 1925.

[74] Ibrahima Faye, Emmanuel Frénod, and Diaraf Seck. "Long Term Behaviour of Singularly Perturbed Parabolic Degenerated Equation". In: *Journal of Nonlinear Analysis and Application* 2016 (May 2011). DOI: 10.5899/2016/jnaa-00297.

[75] Gonzalo Feijóo, Assad Oberai, and Peter Pinsky. "An Application of Shape Optimization in the Solution of Inverse Acoustic Scattering Problems". In: *Inverse Problems* 20.1 (Dec. 2003), pp. 199–228. DOI: 10.1088/0266-5611/20/1/012.

[76] Enrique Fernández-Nieto, Manuel Castro, and C. Madroñal. "On an Intermediate Field Capturing Riemann Solver Based on a Parabolic Viscosity Matrix for the Two-Layer Shallow Water System". In: *Journal of Scientific Computing* 48 (July 2011), pp. 117–140. DOI: 10.1007/s10915-011-9465-7.

[77] Enrique Fernández-Nieto et al. “Formal Deduction of the Saint-Venant-Exner Model including Arbitrarily Sloping Sediment Beds and Associated Energy”. In: *ESAIM: Mathematical Modelling and Numerical Analysis* 51 (Mar. 2016). DOI: 10.1051/m2an/2016018.

[78] Clive A. J. Fletcher. *Computational Techniques for Fluid Dynamics 1*. Berlin, Heidelberg: Springer Berlin Heidelberg, 1998, pp. 17–46. DOI: 10.1007/978-3-642-58229-5_2.

[79] Emmanuel Frénod, Ibrahima Faye, and Diaraf Seck. “Two-Scale Numerical Simulation of Sand Transport Problems”. In: *Discrete and Continuous Dynamical Systems - Series S* 8 (Oct. 2013). DOI: 10.3934/dcdss.2015.8.151.

[80] Simon W. Funke, P.E. Farrell, and Matthew D. Piggott. “Tidal Turbine Array Optimisation using the Adjoint Approach”. In: *Renewable Energy* 63 (2014), pp. 658–673. DOI: https://doi.org/10.1016/j.renene.2013.09.031.

[81] Emilio Gagliardo. “Caratterizzazioni delle tracce sulla frontiera relative ad alcune classi di funzioni in n variabili”. it. In: *Rendiconti del Seminario Matematico della Università di Padova* 27 (1957), pp. 284–305.

[82] P. Gangl and K. Sturm. “Automated computation of topological derivatives with application to nonlinear elasticity and reaction–diffusion problems”. In: *Computer Methods in Applied Mechanics and Engineering* 398 (Aug. 2022), p. 115288. DOI: 10.1016/j.cma.2022.115288.

[83] Stéphane Garreau, Philippe Guillaume, and Mohamed Masmoudi. “The Topological Asymptotic for PDE Systems: The Elasticity Case”. In: *SIAM J. Control and Optimization* 39 (Apr. 2001), pp. 1756–1778. DOI: 10.1137/S0363012900369538.

[84] Caroline Geiersbach, Estefanía Loayza, and Kathrin Welker. *PDE-constrained shape optimization: towards product shape spaces and stochastic models*. July 2021.

[85] Christophe Geuzaine and Jean-François Remacle. “Gmsh: A 3-D Finite Element Mesh Generator with Built-in Pre- and Post-Processing Facilities”. In: *International Journal for Numerical Methods in Engineering* 79 (Sept. 2009), pp. 1309–1331. DOI: 10.1002/nme.2579.

[86] Andrew Giuliani and Lilia Krivodonova. “A Moment Limiter for the Discontinuous Galerkin Method on Unstructured Triangular Meshes”. In: *SIAM Journal on Scientific Computing* 41 (Jan. 2019), A508–A537. DOI: 10.1137/17M1159038.

[87] Olivier Gourgue et al. “A Flux-Limiting Wetting–Drying Method for Finite-Element Shallow-Water Models, with Application to the Scheldt Estuary”. In: *Advances in Water Resources* 4 (Oct. 2009). DOI: 10.1016/j.advwatres.2009.09.005.

[88] Arnold Jules Grass. “Sediment Transport by Waves and Currents”. In: *SERC London Cent. Mar. Technol. Report* (1981).

[89] Iulian Grindeanu et al. “Design Sensitivity Analysis of Hyperelastic Structures Using a Meshless Method”. In: *Aiaa Journal - AIAA J* 36 (Apr. 1998), pp. 618–627. DOI: 10.2514/2.414.

[90] Oksana Guba et al. “The Spectral Element Method on Variable-Resolution Grids: Evaluating Grid Sensitivity and Resolution-Aware Numerical Viscosity”. In: *Geoscientific Model Development Discussions* 7 (June 2014). DOI: 10.5194/gmdd-7-4081-2014.

[91] Vincent Guinot and Sandra Soares-Frazão. “Flux and Source Term Calculation inTwo-Dimensional Shallow Water Models with Porosity on Unstructured Grids”. In: *International Journal for Numerical Methods in Fluids* 50 (Jan. 2006), pp. 309–345. DOI: 10.1002/fld.1059.

[92] Youn Doh Ha et al. “Shape Design Optimization of SPH Fluid–Structure Interactions Considering Geometrically Exact Interfaces”. In: *Structural and Multidisciplinary Optimization* 44 (Sept. 2011), pp. 319–336. DOI: 10.1007/s00158-011-0645-8.

[93] Willi H. Hager. “Du Boys and Sediment Transport”. In: *Journal of Hydraulic Research* 43 (May 2005), pp. 227–233. DOI: 10.1080/00221680509500117.

[94] Ralf Hartmann. *Numerical Analysis of Higher Order Discontinuous Galerkin Finite Element Methods*. Oct. 2008.

[95] Edwin Shields Hewitt and Robert E. Hewitt. “The Gibbs-Wilbraham Phenomenon: An Episode in Fourier Analysis”. In: *Archive for History of Exact Sciences* 21 (1979), pp. 129–160.

[96] Ralf Hiptmair, A. Paganini, and Sahar Sargheini. “Comparison of Approximate Shape Gradients”. In: *BIT Numerical Mathematics* 55 (June 2014). DOI: 10.1007/s10543-014-0515-z.

[97] Raphael Hohmann and Christian Leithäuser. *Gradient-Based Shape Optimization for the Reduction of Particle Erosion in Bended Pipes*. 2019.

[98] Justin Hudson. *Numerical Techniques for Morphodynamic Modelling*. University of Reading, 2001.

[99] Michael Isaacson and Shiqin Qu. “Waves in a Harbour with Partially Reflecting Boundaries”. In: *Coastal Engineering* 14.3 (1990), pp. 193–214. DOI: https://doi.org/10.1016/0378-3839(90)90024-Q.

[100] Kazufumi Ito, Karl Kunisch, and Gunther H. Peichl. “Variational approach to shape derivatives”. In: *ESAIM: COCV* 14.3 (2008), pp. 517–539. DOI: 10.1051/cocv:2008002.

[101] Nouh Izem, Mohammed Seaid, and Mohamed Wakrim. “A Discontinuous Galerkin Method for Two-layer Shallow Water Equations”. In: *Mathematics and Computers in Simulation* (May 2015).

[102] Mostafa Kadiri. “Shape Optimization and Applications to Hydraulic Structures Mathematical Analysis and Numerical Approximation”. Doctoral Thesis. Université de Caen Normandie, 2019.

[103] Tuomas Kärnä et al. “A Fully Implicit Wetting–Drying Method for DG-FEM Shallow Water Models, with an Application to the Scheldt Estuary”. In: *Computer Methods in Applied Mechanics and Engineering* 200.5 (2011), pp. 509–524. DOI: https://doi.org/10.1016/j.cma.2010.07.001.

[104] David Kelly and Nicholas Dodd. “Beach-Face Evolution in the Swash Zone”. In: *Journal of Fluid Mechanics* 661 (Oct. 2010), pp. 316–340. DOI: 10.1017/S0022112010002983.

[105] Moritz Keuthen and D. Kraft. “Shape Optimization of a Breakwater”. In: *Inverse Problems in Science and Engineering* 24 (Sept. 2015). DOI: 10.1080/17415977.2015.1077522.

[106] Andreas Klöckner, Tim Warburton, and Jan Hesthaven. “Viscous Shock Capturing in a Time-Explicit Discontinuous Galerkin Method”. In: *Mathematical Modelling of Natural Phenomena* 6 (Feb. 2011). DOI: 10.1051/mmnp/20116303.

[107] Dan Koschier and Jan Bender. “Density maps for improved SPH boundary handling”. In: *Proceedings of the ACM SIGGRAPH / Eurographics Symposium on Computer Animation* (2017).

[108] Seiichi Koshizuka and Yoshiaki Oka. “Moving-Particle Semi-Implicit Method for Fragmentation of Incompressible Fluid”. In: *Nuclear Science and Engineering* 123 (1996), pp. 421–434.

[109] Sivakumar Kulasegaram et al. “A Variational Formulation based Contact Algorithm for Rigid Boundaries in 2D SPH Applications”. In: *Computational Mechanics* 33 (Mar. 2004), pp. 316–325. DOI: 10.1007/s00466-003-0534-0.

[110] Dmitri Kuzmin. “A Vertex-Based Hierarchical Slope Limiter for p-Adaptive Discontinuous Galerkin Methods”. In: *Journal of Computational and Applied Mathematics* 233.12 (2010), pp. 3077–3085. DOI: https://doi.org/10.1016/j.cam.2009.05.028.

[111] Horace Lamb. *Hydrodynamics*. Cambridge: University Press, 1895.

[112] Antoine Laurain and Kevin Sturm. *Domain Expression of the Shape Derivative and Application to Electrical Impedance Tomography*. Preprint: Weierstraß-Institut für Angewandte Analysis und Stochastik. WIAS, 2013.

[113] Wing Kam Liu, Sukky Jun, and Yi Fei Zhang. “Reproducing Kernel Particle Methods”. In: *International Journal for Numerical Methods in Fluids* 20.8-9 (1995), pp. 1081–1106. DOI: https://doi.org/10.1002/fld.1650200824.

[114] Daniel Luft, Volker Schulz, and Kathrin Welker. “Efficient Techniques for Shape Optimization with Variational Inequalities Using Adjoints”. In: *SIAM Journal on Optimization* 30.3 (Jan. 2020), pp. 1922–1953. DOI: 10.1137/19m1257226.

[115] R. Fernandez Luque and R. Van Beek. "Erosion And Transport Of Bed-Load Sediment". In: *Journal of Hydraulic Research* 14.2 (1976), pp. 127–144. DOI: 10.1080/00221687609499677.

[116] DA Lyn and Mustafa Altinakar. "Saint Venant–Exner Equations for Near-Critical and Transcritical Flows". In: *Journal of Hydraulic Engineering-asce* 128 (June 2002). DOI: 10.1061/(ASCE)0733-9429(2002)128:6(579).

[117] Jorge Macías, Carlos Pares, and Manuel J. Castro. "Improvement and generalization of a finite element shallow-water solver to multi-layer systems". In: *International Journal for Numerical Methods in Fluids* 31.7 (1999), pp. 1037–1059. DOI: https://doi.org/10.1002/(SICI)1097-0363(19991215)31:7<1037::AID-FLD909>3.0.CO;2-V.

[118] Jakob M. Maljaars, Chris N. Richardson, and Nathan Sime. "LEoPart: A Particle Library for FEniCS". In: *Computers & Mathematics with Applications* (May 2020). DOI: 10.1016/j.camwa.2020.04.023.

[119] Gianni Maso. *An Introduction to Γ-Convergence*. Birkhäuser Boston, MA.

[120] Antoine McNamara et al. "Fluid Control Using the Adjoint Method". In: *ACM Trans. Graph.* 23.3 (Aug. 2004), pp. 449–456. DOI: 10.1145/1015706.1015744.

[121] E. Meyer-Peter and R. Müller. "Formulas for Bed-Load transport". In: *IAHSR 2nd meeting, Stockholm, appendix 2* (1948).

[122] Peter W. Michor and David Mumford. "Riemannian Geometries on Spaces of Plane Curves". In: *Journal of the European Mathematical Society* (2003). DOI: 10.48550/ARXIV.MATH/0312384.

[123] Peter W. Michor and David Mumford. *Vanishing Geodesic Distance on Spaces of Submanifolds and Diffeomorphisms*. 2005.

[124] Craig Michoski et al. "Fully Coupled Methods for Multiphase Morphodynamics". In: *Advances in Water Resources* 59 (Sept. 2013), pp. 95–110. DOI: 10.1016/j.advwatres.2013.05.002.

[125] Bijan Mohammadi and Afaf Bouharguane. "Optimal Dynamics of Soft Shapes in Shallow Waters". In: *Computers & Fluids* 40 (Jan. 2011), pp. 291–298. DOI: 10.1016/j.compfluid.2010.09.031.

[126] Bijan Mohammadi and Olivier Pironneau. "Applied Shape Optimization in Fluids". In: *Applied Shape Optimization for Fluids* (May 2001). DOI: 10.1093/acprof:oso/9780199546909.001.0001.

[127] Bijan Mohammadi et al. "Optimal Shape Design of Coastal Structures Minimizing Coastal Erosion". In: *Extended Proceedings of Workshop on Inverse Problems*. CIRM, Jan. 2005.

[128] Bijan Mohammadi et al. "Shape Optimization of Geotextile Tubes for Sandy Beach Protection". In: *International Journal for Numerical Methods in Engineering* 74 (May 2008), pp. 1262–1277. DOI: 10.1002/nme.2209.

[129] Joseph Monaghan. “SPH Compressible Turbulence”. In: *Monthly Notices of the Royal Astronomical Society* 335 (Apr. 2002). DOI: 10.1046/j.1365-8711.2002.05678.x.

[130] Joseph John Monaghan and John Lattanzio. “A Refined Particle Method for Astrophysical Problems”. In: *Astronomy and Astrophysics* 149 (1985), pp. 135–143.

[131] Peter Marvin Müller et al. *A Novel p-Harmonic Descent Approach Applied to Fluid Dynamic Shape Optimization*. 2021. DOI: 10.48550/ARXIV.2103.14735.

[132] Charles B. Morrey Murray H. Protter. *Intermediate Calculus*. Springer New York, NY, 1971.

[133] Bernard Nayroles, Gilbert Touzot, and Pierre Villon. “Generalizing the Finite Element Method: Diffuse Approximation and Diffuse Elements”. In: *Computational Mechanics* 10 (1992), pp. 307–318.

[134] John Von Neumann and Robert D. Richtmyer. “A Method for the Numerical Calculation of Hydrodynamic Shocks”. In: *Journal of Applied Physics* 21 (1950), pp. 232–237.

[135] Peter Nielsen. *Coastal Bottom Boundary Layers and Sediment Transport*. English. Includes bibliographical references (p. 299-308) and indexes. Singapore; River Edge, N.J. : World Scientific, 1992.

[136] Antonio André Novotny and Jan Sokolowski. *Topological Derivatives in Shape Optimization*. Springer, Jan. 2013.

[137] Antonio André Novotny, Jan Sokolowski, and Antoni Zochowski. “Topological Derivatives of Shape Functionals. Part I: Theory in Singularly Perturbed Geometrical Domains”. In: *Journal of Optimization Theory and Applications* 180 (Feb. 2019). DOI: 10.1007/s10957-018-1417-z.

[138] Karl Oelschläger. *On the Connection Between Hamiltonian Many-particle Systems and the Hydrodynamical Equations*. Universität Heidelberg. SFB 123, 1991.

[139] Yoshifumi Ogami and Teruaki Akamatsu. “Viscous Flow Simulation using the Discrete Vortex Model—the Diffusion Velocity Method”. In: *Computers & Fluids* 19.3 (1991), pp. 433–441. DOI: https://doi.org/10.1016/0045-7930(91)90068-S.

[140] Joseph Oliger and Arne Sundström. “Theoretical and Practical Aspects of Some Initial Boundary Value Problems in Fluid Dynamics”. In: *SIAM Journal on Applied Mathematics* 35.3 (1978), pp. 419–446. DOI: 10.1137/0135035.

[141] Stanley Osher and Fadil Santosa. “Level Set Methods for Optimization Problems Involving Geometry and Constraints: I. Frequencies of a Two-Density Inhomogeneous Drum”. In: *Journal of Computational Physics* 171 (July 2001), pp. 272–288. DOI: 10.1006/jcph.2001.6789.

[142] Stanley Osher and James Sethian. “Fronts Propagating with Curvature-Dependent Speed: Algorithms based on Hamilton-Jacobi Formulations”. In: *Journal of Computational Physics* 79.1 (1988), pp. 12–49. DOI: https://doi.org/10.1016/0021-9991(88)90002-2.

[143] Ilhan Özgen, Dongfang Liang, and Reinhard Hinkelmann. “Shallow Water Equations with Depth-Dependent Anisotropic Porosity for Subgrid-Scale Topography”. In: *Applied Mathematical Modelling* 40.17 (2016), pp. 7447–7473. DOI: https://doi.org/10.1016/j.apm.2015.12.012.

[144] Guozheng Yan; Peter Y.H. Pang. “The Uniqueness of the Inverse Obstacle Scattering Problem with Transmission Boundary Conditions”. In: *Pergamon Computers Math. Applic. Vol. 36* (1997).

[145] Brice Anselme et Yves-François Thomas Paul Durand. “L’impact de l’ouverture de la brèche dans la langue de Barbarie à Saint-Louis du Sénégal en 2003 : un changement de nature de l’aléa inondation?” In: *European Journal of Geography* (2010). DOI: DOI:https://doi.org/10.4000/cybergeo.23017.

[146] Marica Pelanti, François Bouchut, and Anne Mangeney. “A Roe-Type Scheme for Two-Phase Shallow Granular Flows over Variable Topography”. In: *ESAIM Mathematical Modelling and Numerical Analysis* 42 (Sept. 2008), pp. 851–885. DOI: 10.1051/m2an:2008029.

[147] Per-Olof Persson and J. Peraire. “Sub-Cell Shock Capturing for Discontinuous Galerkin Methods”. In: *AIAA paper* 2 (Jan. 2006). DOI: 10.2514/6.2006-112.

[148] Matteo Postacchini et al. “A Multi-Purpose, Intra-Wave, Shallow Water Hydro-Morphodynamic Solver”. In: *Advances in Water Resources* 38 (Mar. 2012), pp. 13–26. DOI: 10.1016/j.advmatres.2011.12.003.

[149] A. C. Radder. “On the Parabolic Equation Method for Water-Wave Propagation”. In: *Journal of Fluid Mechanics* 95 (1978), pp. 159–176.

[150] Pierre-Arnaud Raviart. “An Analysis of Particle Methods”. In: *Numerical Methods in Fluid Dynamics*. Ed. by Franco Brezzi. Berlin, Heidelberg: Springer Berlin Heidelberg, 1985, pp. 243–324.

[151] Jan S. Ribberink and Abdullah A. Al-Salem. “Sediment Transport in Oscillatory Boundary Layers in cases of Rippled Beds and Sheet Flow”. In: *Journal of Geophysical Research: Oceans* 99.C6 (1994), pp. 12707–12727. DOI: https://doi.org/10.1029/94JC00380.

[152] Leo C. van Rijn. “Sediment Transport, Part I: Bed Load Transport”. In: *Journal of Hydraulic Engineering* 110.10 (1984), pp. 1431–1456. DOI: 10.1061/(ASCE)0733-9429(1984)110:10(1431).

[153] Béatrice Rivière and Mary Wheeler. “Improved Energy Estimates for Interior Penalty, Constrained and Discontinuous Galerkin Methods for Elliptic Problems I”. In: *Comput. Geosci.* 3 (Jan. 1999), pp. 337–360. DOI: 10.1023/A:1011591328604.

[154] Marie Rognes et al. “Automating the Solution of PDEs on the Sphere and other Manifolds in FEniCS 1.2”. In: *Geoscientific Model Development* 6 (Dec. 2013). DOI: 10.5194/gmd-6-2099-2013.

[155] Thomas Rowan. “Advances in Modelling and Numerical Simulation of Sediment Transport in Shallow Water Flows”. PhD thesis. Durham University, 2019.

[156] Brett F. Sanders, Jochen E. Schubert, and Humberto A. Gallegos. “Integral Formulation of Shallow-Water Equations with Anisotropic Porosity for Urban Flood Modeling”. In: *Journal of Hydrology* 362.1 (2008), pp. 19–38. DOI: https://doi.org/10.1016/j.jhydrol.2008.08.009.

[157] Luka Schlegel and Volker Schulz. “Shape Optimization for the Mitigation of Coastal Erosion via Porous Shallow Water Equations”. In: *International Journal for Numerical Methods in Engineering* (2022). DOI: 10.1002/nme.7074.

[158] Luka Schlegel and Volker Schulz. *Shape Optimization for the Mitigation of Coastal Erosion via Shallow Water Equations*. 2021. DOI: 10.48550/ARXIV.2107.09464.

[159] Luka Schlegel and Volker Schulz. *Shape Optimization for the Mitigation of Coastal Erosion via Smoothed Particle Hydrodynamics*. 2022. DOI: 10.48550/ARXIV.2203.09916.

[160] Luka Schlegel and Volker Schulz. *Shape Optimization for the Mitigation of Coastal Erosion via the Helmholtz Equation*. 2021. DOI: 10.48550/ARXIV.2107.10038.

[161] René Schneider and Peter Jimack. “On the Evaluation of Finite Element Sensitivities to Nodal Coordinates”. In: *Electronic Transactions on Numerical Analysis. Volume* 32 (Jan. 2008), pp. 134–144.

[162] Steven H Schot. “Eighty Years of Sommerfeld’s Radiation Condition”. In: *Historia Mathematica* 19.4 (1992), pp. 385–401. DOI: https://doi.org/10.1016/0315-0860(92)90004-U.

[163] Volker Schulz. *Numerical Optimization of the Cross-Sectional Shape of Turbine Blades*. 1996.

[164] Volker Schulz and Martin Siebenborn. “Computational Comparison of Surface Metrics for PDE Constrained Shape Optimization”. In: *Computational Methods in Applied Mathematics* (2015).

[165] Volker Schulz, Martin Siebenborn, and Kathrin Welker. “Structured Inverse Modeling in Parabolic Diffusion Processess”. In: *SIAM Journal on Control and Optimization* 53 (Sept. 2014). DOI: 10.1137/140985883.

[166] Volker Schulz, Martin. Siebenborn, and Kathrin. Welker. “Efficient PDE Constrained Shape Optimization Based on Steklov–Poincaré-Type Metrics”. In: *SIAM Journal on Optimization* 26.4 (2016), pp. 2800–2819. DOI: 10.1137/15M1029369.

[167] Adrian Matthew Shields. “Anwendung der Aehnlichkeitsmechanik und der Turbulenzforschung auf die Geschiebebewegung”. PhD thesis. Preussische Versuchsanstalt für Wasserbau, 1936.

[168] Joseph J. Shirron and Ivo Babuška. "A Comparison of Approximate Boundary Conditions and Infinite Element Methods for Exterior Helmholtz Problems". In: *Computer Methods in Applied Mechanics and Engineering* 164.1 (1998). Exterior Problems of Wave Propagation, pp. 121–139. DOI: https://doi.org/10.1016/S0045-7825(98)00050-4.

[169] Ole Sigmund and J. Petersson. "Numerical instabilities in topology optimization: A survey on procedures dealing with checkerboards, mesh-dependencies and local minima". In: *Structural Optimization* 16 (Aug. 1998), pp. 68–75. DOI: 10.1007/BF01214002.

[170] Sandra Soares-Frazão and Yves Zech. "HLLC Scheme with Novel Wave-Speed Estimators Appropriate for Two-Dimensional Shallow-Water Flow on Erodible Bed". In: *International Journal for Numerical Methods in Fluids* 66 (July 2011), pp. 1019–1036. DOI: 10.1002/fld.2300.

[171] Jan Sokolowski and Antoni Zochowski. "On the Topological Derivative in Shape Optimization". In: *SIAM Journal on Control and Optimization* 37 (May 1999). DOI: 10.1137/S0363012997323230.

[172] Jan Sokolowski and Jean Paul Zolésio. *Introduction to Shape Optimization: Shape Sensitivity Analysis*. Springer series in computational mathematics. Springer-Verlag, 1992.

[173] Barbara Solenthaler et al. "SPH Based Shallow Water Simulation". In: *Workshop in Virtual Reality Interactions and Physical Simulation*. Ed. by Jan Bender, Kenny Erleben, and Eric Galin. The Eurographics Association, 2011. DOI: 10.2312/PE/vriphys/vriphys11/039-046.

[174] T. S. Stefanakis et al. "Can Small Islands Protect Nearby Coasts from Tsunamis? An Active Experimental Design Approach". In: *Proceedings of the Royal Society A: Mathematical, Physical and Engineering Sciences* 470.2172 (Dec. 2014), p. 20140575. DOI: 10.1098/rspa.2014.0575.

[175] Roland Stoffel. "Structural Optimization of Coupled Problems". doctoralthesis. Universität Trier, 2014. DOI: 10.25353/ubtr-xxxx-a6ec-394d/.

[176] Kevin Sturm. "Lagrange method in shape optimization for non-linear partial differential equations : A material derivative free approach". In: 2013.

[177] Eleuterio Toro. *Riemann Solvers and Numerical Methods for Fluid Dynamics: A Practical Introduction*. Springer Berlin, Heidelberg, Jan. 2009. DOI: 10.1007/b79761.

[178] Fredi Tröltzsch. "Optimal control of partial differential equations. Theory, methods and applications". In: 112 (Jan. 2010). DOI: 10.1090/gsm/112.

[179] Renato Vacondio et al. "SPH Modeling of Shallow Flow with Open Boundaries for Practical Flood Simulation". In: *Journal of Hydraulic Engineering* 138 (June 2012), pp. 530–541. DOI: 10.1061/(ASCE)HY.1943-7900.0000543.

[180] Venkat Venkatakrishnan. “Convergence to Steady State Solutions of the Euler Equations on Unstructured Grids with Limiters”. In: *Journal of Computational Physics* 118.1 (1995), pp. 120–130. DOI: https://doi.org/10.1006/jcph.1995.1084.

[181] Kathrin Welker. “Efficient PDE Constrained Shape Optimization in Shape Spaces”. doctoralthesis. Universität Trier, 2017. DOI: 10.25353/ubtr-xxxx-6575-788c/.

[182] Chris Wojtan, Peter Mucha, and Greg Turk. “Keyframe Control of Complex Particle Systems using the Adjoint Method”. In: *SCA ’06*. 2006.

[183] Yulong Xing and Chi-Wang Shu. “A New Approach of High Order Well-Balanced Finite Volume WENO Schemes and Discontinuous Galerkin Methods for a Class of Hyperbolic Systems with Source”. In: *Communications in Computational Physics* 1 (Feb. 2006).

[184] Jean Zabsonré, Carine Lucas, and Enrique Fernández-Nieto. “An Energetically Consistent Viscous Sedimentation Model”. In: *Mathematical Models and Methods in Applied Sciences* 19 (Mar. 2009). DOI: 10.1142/S0218202509003504.

Appendices

Appendix A

SWE Derivation

The SWE can be derived by depth-integrating the three dimensional Navier-Stokes equations [23, 155], that state as

Definition A.1. *(Navier-Stokes Equations) Suppose $\Omega \subset \mathbb{R}^3$, then the Navier-Stokes equations are defined to be the system consisting of continuity and three conservation of momentum equations, i.e. on $\Omega \times (0,T)$ it holds*

$$\frac{\partial u}{\partial x} + \frac{\partial v}{\partial y} + \frac{\partial w}{\partial z} = 0 \tag{A.1}$$

$$\rho\left(\frac{\partial u}{\partial t} + u\frac{\partial u}{\partial x} + v\frac{\partial u}{\partial y} + w\frac{\partial u}{\partial z}\right) = F_x - \frac{\partial p}{\partial x} + \nu\left[\frac{\partial^2 u}{\partial^2 x} + \frac{\partial^2 u}{\partial^2 y} + \frac{\partial^2 u}{\partial^2 z}\right] \tag{A.2}$$

$$\rho\left(\frac{\partial v}{\partial t} + u\frac{\partial v}{\partial x} + v\frac{\partial v}{\partial y} + w\frac{\partial v}{\partial z}\right) = F_y - \frac{\partial p}{\partial y} + \nu\left[\frac{\partial^2 v}{\partial^2 x} + \frac{\partial^2 v}{\partial^2 y} + \frac{\partial^2 v}{\partial^2 z}\right] \tag{A.3}$$

$$\rho\left(\frac{\partial w}{\partial t} + u\frac{\partial w}{\partial x} + v\frac{\partial w}{\partial y} + w\frac{\partial w}{\partial z}\right) = F_z - \frac{\partial p}{\partial z} + \nu\left[\frac{\partial^2 w}{\partial^2 x} + \frac{\partial^2 w}{\partial^2 y} + \frac{\partial^2 w}{\partial^2 z}\right]. \tag{A.4}$$

for velocity components $u, v, w : \Omega \times (0,T) \to \mathbb{R}$, and viscosity weight $\nu > 0$, pressure and density field $p, \rho : \Omega \times (0,T) \to \mathbb{R}$ and coordinate-wise forcing terms $F = (F_x, F_y, F_z)$ consisting of additional forces.

In assuming incompressibility for the fluid in Definition A.1 we can write equations in terms of a mean density. Due to shallow assumptions we have that vertical velocity component w is to a large factor smaller than horizontal u and v. Furthermore terms in the z-direction are vanishingly small compared to the gravity and pressure terms. A scaling argument such as substitution $\nu = \mu\rho$ and dividing by ρ for the second and third momentum equations leads us to regard

$$\frac{\partial u}{\partial x} + \frac{\partial v}{\partial y} + \frac{\partial w}{\partial z} = 0 \tag{A.5}$$

$$\frac{\partial u}{\partial t} + u\frac{\partial u}{\partial x} + v\frac{\partial u}{\partial y} + w\frac{\partial u}{\partial z} = \frac{1}{\rho}F_x - \frac{1}{\rho}\frac{\partial p}{\partial x} + \frac{\partial}{\partial x}\left(\mu\frac{\partial u}{\partial x}\right) + \frac{\partial}{\partial y}\left(\mu\frac{\partial u}{\partial y}\right) + \frac{\partial}{\partial z}\left(\mu\frac{\partial u}{\partial z}\right) \tag{A.6}$$

$$\frac{\partial v}{\partial t} + u\frac{\partial v}{\partial x} + v\frac{\partial v}{\partial y} + w\frac{\partial v}{\partial z} = \frac{1}{\rho}F_y - \frac{1}{\rho}\frac{\partial p}{\partial y} + \frac{\partial}{\partial x}\left(\mu\frac{\partial v}{\partial x}\right) + \frac{\partial}{\partial y}\left(\mu\frac{\partial v}{\partial y}\right) + \frac{\partial}{\partial z}\left(\mu\frac{\partial v}{\partial z}\right) \tag{A.7}$$

$$0 = -\rho g - \frac{\partial p}{\partial z}. \tag{A.8}$$

The last equation (A.8) implies a hydrostatic pressure distribution in vertical direction. The strategy for deriving SWE can be summarized as specifying boundary conditions, performing averaged depth-integrating and applying boundary conditions from before. We choose hereby non-negative sediment and water-heights from a zero datum as shown in Figure 5.2. Hence, at the bottom $z = z_0$ we pose no normal flow conditions [155]

$$w\big|_{z=z_0} = \frac{D(z_0)}{Dt} := \frac{\partial(z_0)}{\partial t} + u\big|_{z=z_0}\frac{\partial(z_0)}{\partial x} + v\big|_{z=z_0}\frac{\partial(z_0)}{\partial y}. \tag{A.9}$$

At the free surface height $z_0 + H$ we have no relative normal flow, i.e.

$$w\big|_{z=z_0+H} = \frac{D(z_0+H)}{Dt} := \frac{\partial(z_0+H)}{\partial t} + u\big|_{z=z_0+H}\frac{\partial(z_0+H)}{\partial x} + v\big|_{z=z_0+H}\frac{\partial(z_0+H)}{\partial y}. \tag{A.10}$$

Starting depth-integrating the continuity equation, we have

$$\begin{aligned} 0 &= \int_{z_0}^{z_0+H}\left(\frac{\partial u}{\partial x} + \frac{\partial v}{\partial y} + \frac{\partial w}{\partial z}\right)\mathrm{d}z \\ &= \int_{z_0}^{z_0+H}\frac{\partial u}{\partial x}\,\mathrm{d}z + \int_{z_0}^{z_0+H}\frac{\partial v}{\partial y}\,\mathrm{d}z + \int_{z_0}^{z_0+H}\frac{\partial w}{\partial z}\,\mathrm{d}z. \end{aligned} \tag{A.11}$$

The Leibniz integration rule [132, Chapter 8] and the fundamental theorem of calculus [132, Chapter 3] lead to

$$\begin{aligned} 0 =& \frac{\partial}{\partial x}\int_{z_0}^{z_0+H} u\,\mathrm{d}z + \frac{\partial}{\partial x}\int_{z_0}^{z_0+H} v\,\mathrm{d}z \\ &+ \left[u\frac{\partial z_0}{\partial x} + v\frac{\partial z_0}{\partial y} - w\right]\Big|_{z=z_0} - \left[u\frac{\partial(z_0+H)}{\partial x} + v\frac{\partial(z_0+H)}{\partial y} - w\right]\Big|_{z=z_0+H} \end{aligned} \tag{A.12}$$

applying the boundary conditions (A.9) and (A.10) for the terms in the brackets we obtain

$$0 = -\frac{\partial z_0}{\partial t} + \frac{\partial(z_0+H)}{\partial t} + \frac{\partial}{\partial x}\int_{z_0}^{z_0+H} u\,\mathrm{d}z + \frac{\partial}{\partial y}\int_{z_0}^{z_0+H} v\,\mathrm{d}z. \tag{A.13}$$

From this we obtain the conservation of mass equation

$$\frac{\partial H}{\partial t} + \frac{\partial \bar{u}H}{\partial x} + \frac{\partial \bar{v}H}{\partial y} = 0, \tag{A.14}$$

by relying on depth-averaged variables, i.e.

$$\bar{u} = \frac{1}{H}\int_{z_0}^{z_0+H} u\,\mathrm{d}z \quad \text{and} \quad \bar{v} = \frac{1}{H}\int_{z_0}^{z_0+H} v\,\mathrm{d}z. \tag{A.15}$$

.

The x-momentum equation (A.6) is dealt with in the following. We start with the left-hand side

$$\begin{aligned}&\int_{z_0}^{z_0+H}\left(\frac{\partial u}{\partial t} + u\frac{\partial u}{\partial x} + v\frac{\partial u}{\partial y} + u\frac{\partial w}{\partial z}\right)\mathrm{d}z \\ =&\int_{z_0}^{z_0+H}\frac{\partial u}{\partial t}\,\mathrm{d}z + \int_{z_0}^{z_0+H}\frac{\partial u^2}{\partial x}\,\mathrm{d}z + \int_{z_0}^{z_0+H}\frac{\partial uv}{\partial y}\,\mathrm{d}z + \int_{z_0}^{z_0+H}\frac{\partial uw}{\partial z}\,\mathrm{d}z.\end{aligned} \tag{A.16}$$

Once more the Leibniz integration rule on the first three integrals and the fundamental theorem of calculus on the last lead to

$$\begin{aligned}=&\frac{\partial}{\partial t}\int_{z_0}^{z_0+H} u\,\mathrm{d}z + \frac{\partial}{\partial x}\int_{z_0}^{z_0+H} u^2\,\mathrm{d}z + \frac{\partial}{\partial x}\int_{z_0}^{z_0+H} uv\,\mathrm{d}z \\ &+u\big|_{z=z_0}\left[\frac{\partial z_0}{\partial t} + u\big|_{z=z_0}\frac{\partial z_0}{\partial x} + v\big|_{z=z_0}\frac{\partial z_0}{\partial y} - w\big|_{z=z_0}\right] \\ &-u\big|_{z=z_0+H}\left[\frac{\partial (z_0+H)}{\partial t} + u\big|_{z=z_0+H}\frac{\partial (z_0+H)}{\partial x} + v\big|_{z=z_0+H}\frac{\partial (z_0+H)}{\partial y} - w\big|_{z=z_0+H}\right].\end{aligned} \tag{A.17}$$

By the same notation as before we obtain

$$= \frac{\partial H\bar{u}}{\partial t} + \frac{\partial (H\bar{u}^2)}{\partial x} + \frac{\partial (H\bar{u}\bar{v})}{\partial y}. \tag{A.18}$$

The pressure term in (A.6) is also depth-integrated, while using $p = \rho g(z_0 + H - z)$ as implication of the hydrostatic pressure distribution (A.8)

$$\begin{aligned}-\frac{1}{\rho}\int_{z_0}^{z_0+H}\frac{\partial p}{\partial x}\,\mathrm{d}z &= -\int_{z_0}^{z_0+H}\frac{\partial}{\partial x}\left(g(z_0+H-z)\right)\mathrm{d}z \\ &= -\int_{z_0}^{z_0+H}\frac{\partial}{\partial x}\left(g(z_0+H)\right)\mathrm{d}z \\ &= -gH\frac{\partial z_0}{\partial x} - gH\frac{\partial H}{\partial x}.\end{aligned} \tag{A.19}$$

Viscous terms are treated in the same way by depth-integration, i.e.

$$\int_{z_0}^{z_0+H}\left[\frac{\partial}{\partial x}\left(\mu\frac{\partial u}{\partial x}\right) + \frac{\partial}{\partial y}\left(\mu\frac{\partial u}{\partial y}\right) + \frac{\partial}{\partial z}\left(\mu\frac{\partial u}{\partial z}\right)\right]\mathrm{d}z \tag{A.20}$$

and the usage of the Leibniz rule, the fundamental theorem of calculus and depth-

averaged variables, such that

$$
\begin{aligned}
=&\frac{\partial}{\partial x}\left(H\mu\frac{\partial \bar{u}}{\partial x}\right)+\frac{\partial}{\partial y}\left(H\mu\frac{\partial \bar{u}}{\partial y}\right)\\
&+\mu\frac{\partial u}{\partial x}\bigg|_{z=z_0}\frac{\partial z_0}{\partial x}+\mu\frac{\partial u}{\partial y}\bigg|_{z=z_0}\frac{\partial z_0}{\partial y}-\mu\frac{\partial u}{\partial z}\bigg|_{z=z_0}\\
&-\mu\frac{\partial u}{\partial x}\bigg|_{z=z_0+H}\frac{\partial (z_0+H)}{\partial x}-\mu\frac{\partial u}{\partial y}\bigg|_{z=z_0+H}\frac{\partial (z_0+H)}{\partial y}+\mu\frac{\partial u}{\partial z}\bigg|_{z=z_0+H}.
\end{aligned}
\tag{A.21}
$$

Performing a stress balance at the surface and at the bottom, it can be shown for the last two lines that

$$
\mu\frac{\partial u}{\partial x}\bigg|_{z=z_0}\frac{\partial z_0}{\partial x}+\mu\frac{\partial u}{\partial y}\bigg|_{z=z_0}\frac{\partial z_0}{\partial y}-\mu\frac{\partial u}{\partial z}\bigg|_{z=z_0}=-\frac{\tau_x^b}{\rho}
\tag{A.22}
$$

and

$$
-\mu\frac{\partial u}{\partial x}\bigg|_{z=z_0+H}\frac{\partial (z_0+H)}{\partial x}-\mu\frac{\partial u}{\partial y}\bigg|_{z=z_0+H}\frac{\partial (z_0+H)}{\partial y}+\mu\frac{\partial u}{\partial z}\bigg|_{z=z_0+H}=\frac{\tau_x^s}{\rho}
\tag{A.23}
$$

for surface and bottom shear stress, defined in terms of shear stresses τ_{ij} on the i,j-plane and

$$
\tau_x^s=-\frac{1}{\rho}\left[\tau_{xx}\frac{\partial H+z_0}{\partial x}+\tau_{xy}\frac{\partial H+z_0}{\partial y}-\tau_{xz}\right]
\tag{A.24}
$$

$$
\tau_x^b=-\frac{1}{\rho}\left[\tau_{xx}\frac{\partial z_0}{\partial x}+\tau_{xy}\frac{\partial z_0}{\partial y}-\tau_{xz}\right]
\tag{A.25}
$$

such that neglecting additional forces F_x and analogous operation for the y-momentum gives us the two momentum equations.

Appendix B

Fluid Particle Implementation

The SPH fluid interaction is build to predominantly rely on matrix operations to enable efficient computational implementations. Suppose starting from a total number of $N > 1$ particles in $d \geq 1$ dimensions, then all density-based calculations depend on spatial distances of the particles to one another. Hence, exemplifying for $d = 2$ we obtain spatial matrices $\Delta x, \Delta y \in \mathbb{R}^{2N \times 2N}$ as

$$\Delta x = \begin{pmatrix} x^1 - x^1 & x^1 - x^2 & \dots & x^1 - x^N \\ x^2 - x^1 & \ddots & & \vdots \\ \vdots & & \ddots & \vdots \\ x^N - x^1 & \dots & \dots & x^N - x^N \end{pmatrix} \tag{B.1}$$

and

$$\Delta y = \begin{pmatrix} y^1 - y^1 & y^1 - y^2 & \dots & y^1 - y^N \\ y^2 - y^1 & \ddots & & \vdots \\ \vdots & & \ddots & \vdots \\ y^N - y^1 & \dots & \dots & y^N - y^N \end{pmatrix}. \tag{B.2}$$

Relying on kernel specifications as in Definition 8.6 or 8.7, the density matrix $\rho_M \in \mathbb{R}^{2N \times 2N}$ is obtained by

$$\rho_M = \begin{pmatrix} m^1 W^{11} & m^2 W^{12} & \dots & m^N W^{1N} \\ m^1 W^{21} & \ddots & & \vdots \\ \vdots & & \ddots & \vdots \\ m^1 W^{N1} & \dots & \dots & m^N W^{NN} \end{pmatrix}, \tag{B.3}$$

where we have used the abbreviating superscripts w.r.t. the chosen kernel function as

$$W^{ij} = W((x^i - x^j, y^i - y^j), h) \quad \text{for } i, j \in \{1, ..., N\}. \tag{B.4}$$

The density matrix allows us to compute particle-wise densities via the respective row sum, i.e.

$$\begin{pmatrix} \rho^1 \\ \vdots \\ \rho^N \end{pmatrix} = \begin{pmatrix} \sum_{i=1}^N m^i W^{1i} \\ \vdots \\ \sum_{i=1}^N m^i W^{Ni} \end{pmatrix}. \tag{B.5}$$

Using analytical versions of the kernel gradient, e.g. for (8.18), associated computations rely on one $2N \times 2N$ matrix per direction, i.e.

$$\nabla W_M = \left(\tfrac{-2}{h^2} \rho_M \odot \Delta x, \tfrac{-2}{h^2} \rho_M \odot \Delta y \right), \tag{B.6}$$

where we have used the Hadamard product for element-wise multiplication.
The described procedure for full reliance on matrix representatives carries over to all required quantities w.r.t. the interaction of fluid particles.